

50376  
1993  
12

50376  
1993  
12

N° d'ordre H 58

Université des Sciences et Technologies de Lille

Travaux présentés par

Jean-Luc DEUZE

en vue de l'obtention de

L'HABILITATION A DIRIGER DES RECHERCHES  
EN SCIENCES PHYSIQUES

APPORT DE LA POLARISATION A  
LA CARACTERISATION DES AEROSOLS.  
PREPARATION DE L'EXPERIENCE POLDER

Soutenance le 26 février 1993

devant le jury composé de:

J. LENOBLE	Professeur à l'Université de Lille	Président
A. DOLLFUS	Astronome Titulaire à l'Observatoire de Paris	Rapporteur
J.W. HOVENIER	Professeur à l'Université d'Amsterdam	Rapporteur
V. VANDERBILT	Research Senior Scientist à la NASA	Rapporteur
M. HERMAN	Professeur à l'Université de Lille	Examineur
J.M. MARTINUZZI	Ingénieur CNES, Chef de projet POLDER	Examineur
R. SANTER	Professeur à l'Université du Littoral	Examineur
D. TANRE	Directeur de Recherches au CNRS, Lille	Examineur

U.F.R de Physique Fondamentale

Laboratoire d'Optique Atmosphérique



SCD LILLE 1



D 030 258925 1

## INTRODUCTION

### CHAPITRE I

P1 Saharan Aerosols over South of France: Characterization Derived from Satellite Data and Ground Based Measurements.1988.

J.L. Deuzé, C. Devaux, M. Herman and D. Tanré.

J. of Appl. Meteo.,Vol. 27, No. 5, May 1988.

P2 SPOT Calibration at La Crau Test Site (France).(1992)

R. Santer, X.F. Gu, G. Guyot, J.L. Deuzé, C. Devaux, E. Vermote and M. Verbrughe.

Remote Sens. Environ. 41:227-237

### CHAPITRE II

P3 Photopolarimetric Observations of Aerosols and Clouds from Balloon.(1989)

J.L. Deuzé, C. Devaux, M. Herman, R. Santer, J.Y. Balois, L. Gonzalez, P. Lecomte and C. Verwaerde.

Remote Sens. Environ. 29:93-109

P4 Fourier Series Expansion of the Transfer Equation in the Atmosphere-Ocean System.(1989)

J.L. Deuzé, M. Herman and R. Santer.

J. Quant. Spectrosc. Radiat. Transfer. Vol. 41, No. 6, pp. 483-494,

P5 Polarization of the solar light scattered by the Earth-Atmosphere system as observed from the U.S. Shuttle.

J.C. Roger, R. Santer, M. Herman and J.L. Deuzé.

Accepted in Remote Sens. Environ.

### CHAPITRE III

P6 The POLDER Mission: Instrument Characteristics and Scientific Objectives.

F.M. Bréon, A. Bricaud, J.C. Buriez, P.Y. Deschamps, J.L. Deuzé, M. Herman, M. Leroy, A. Podaire, G. Séze.

Submitted to IEEE Trans. on Geosciences and Remote Sensing.

P7 Analysis of the POLDER (POLarization and Directionality of Earth's Reflectances) Airborne Instrument Observations. over Land

J.L. Deuzé, F.M. Bréon, P.Y. Deschamps, C. Devaux, M. Herman, A. Podaire and J.L. Roujean.

Remote Sens. Environ. In press.

P8 Analysis of the POLDER Airborne Instrument Observations over Cloud Covers.

P. Goloub, J.L. Deuzé, P.Y. Deschamps, Y. Fouquart and M. Herman.

Submitted to IEEE Trans. on Geosciences and Remote Sensing.

Ce présent travail porte sur l'interaction du rayonnement solaire avec notre planète Terre: de telles études sont surtout intéressantes depuis l'avènement des satellites artificiels qui permettent une couverture globale et le suivi temporel des processus se déroulant sur l'ensemble de la surface terrestre. Si la terre a toujours été le siège de modifications, aux changements naturels il faut maintenant ajouter ceux liés à l'activité humaine qui, à terme, peuvent bouleverser les équilibres de la planète et oblitérer sa survie. Les exemples récents les plus connus sont sans doute

- dans l'atmosphère: l'augmentation des gaz à effet de serre ( $\text{CO}_2$ ,  $\text{CH}_4$ ,  $\text{NO}_2$ ...), la diminution de l'ozone stratosphérique liée à la présence des chlorofluorocarbones, l'acidification de la basse atmosphère dans les régions fortement industrialisées.

- dans les océans: les rejets de déchets polluants qui modifient le biotope naturel et influent sur les capacités des échanges océan-atmosphère.

- sur les terres émergées: la déforestation, l'urbanisation et l'augmentation des terres cultivées conduisant à une modification de l'albédo du sol et de l'hydrologie et renforçant l'érosion des sols.

Les réponses de notre environnement à ces agressions doivent être suivies et évaluées avec le plus grand soin de façon à prévenir dès que possible les conséquences humaines et économiques qu'elles induiront. Ces études rentrent dans le cadre de grands programmes internationaux tels PMRC (Programme Mondial de Recherche sur le Climat) et PIGB (Programme International Géosphère-Biosphère). La compréhension et la modélisation des différents processus évoqués ci-dessus passent par l'observation globale de la planète qui ne peut être réalisée qu'à l'aide des satellites.

Le rayonnement solaire qui arrive au sommet de l'atmosphère est directionnel et non polarisé: il est défini par son éclairement spectral  $E_s(\lambda)$ . Le champ de rayonnement diffus qu'il génère après interaction avec la Terre est défini, dans une direction donnée, par la luminance monochromatique  $L(\lambda)$ , le taux de polarisation linéaire  $P$  et la direction du plan de polarisation. Les mécanismes d'interaction sont multiples (diffusion, absorption, réflexion, réfraction) et susceptibles de se manifester simultanément. L'étude du rayonnement permet d'identifier ces mécanismes et d'en tirer des informations sur l'atmosphère et les surfaces.

Dans mon travail, j'ai plus particulièrement cherché à utiliser les informations liées à l'état de polarisation du rayonnement, complémentaires des informations liées à la dépendance spectrale et directionnelle.

Il y a très longtemps que des mesures en polarisation avaient été réalisées sur les planètes: en particulier dès 1929 Lyot (1) avait mesuré le taux de polarisation intégré de Vénus en fonction de l'angle de phase, et ensuite Dollfus (2, 3) avait étendu le domaine spectral à l'ultraviolet et au proche infrarouge et effectué des mesures de polarisation localisée. L'interprétation de telles mesures restait cependant quasi-impossible à cette époque et se réduisait à des comparaisons avec des échantillons terrestres faute de moyens de calculs permettant de résoudre les problèmes de transfert radiatif dans les atmosphères.

Sur le plan théorique, la diffusion avait été abordée à la fin du 19ème siècle par Lord Rayleigh en assimilant les molécules à des dipôles oscillants sous l'effet du champ électromagnétique. Ce premier modèle expliquait la distribution angulaire et spectrale (bleu du ciel) de la lumière diffuse du ciel. La description du rayonnement diffusé, éventuellement absorbé, par des particules de petites

dimensions avait été faite théoriquement par Mie (4) à partir des équations de Maxwell: ces calculs, même appliqués au cas simple d'une seule particule, supposée sphérique, étaient déjà très difficiles à résoudre numériquement.

L'équation de transfert n'était résolue qu'en 1950 par Chandrasekhar (5) dans le cas particulier de l'atmosphère moléculaire. Pour le cas général de la diffusion de Mie, de nombreuses méthodes de résolution avaient été proposées, (Lenoble (6)), mais pratiquement c'était le développement des calculateurs qui allait permettre leur mise en oeuvre.

C'est ce que j'ai fait dans ma thèse de 3<sup>ème</sup> cycle (7) en mettant au point un code numérique de résolution de l'équation de transfert, basé sur la méthode des ordres successifs de diffusion (SOS : Successive Orders of Scattering) et permettant de tenir compte de la polarisation. Hansen et Hovenier (8) avaient montré l'intérêt de la polarisation pour la caractérisation de l'atmosphère vénusienne. A l'aide de mon code, j'ai pu simuler le taux de polarisation de Vénus en fonction de l'angle phase à partir de leurs résultats. C'est à cette époque que nous avons engagé une collaboration avec A. Dollfus qui disposait de nombreuses mesures de la polarisation localisée de Vénus dont l'interprétation devenait possible.

Après ma thèse, je me suis longuement absenté pour me consacrer à des tâches d'enseignement à l'étranger mais la collaboration avec A. Dollfus devait se poursuivre avec succès avec R. Santer et donner lieu à plusieurs publications sur la polarisation des planètes (9).

Dans la deuxième partie de la décennie 70, le Laboratoire d'Optique Atmosphérique (LOA) était passé des études planétaires à l'observation de la Terre dans le cadre d'expériences embarquées sur satellites: le laboratoire fut impliqué dans l'étude du capteur océanique CZCS, Coastal Zone Color Scanner (10), et dans la préparation de SPOT (11). Ces nouveaux axes de recherche nécessitaient le développement de codes de simulation du signal satellitaire - méthode de Monte-Carlo, logiciel 5S (12)- permettant d'établir des bilans de flux précis avant le lancement des capteurs, et de préparer les algorithmes d'inversion des données. Parallèlement une station-sol de mesures atmosphériques était développée pour valider des mesures satellitaires ou pour aider à l'interprétation d'expériences entreprises par le laboratoire à partir de ballons stratosphériques (Expériences Radibal et Pirat). Lors de mon retour au laboratoire, je me suis donc intéressé à ces manipulations qui incluaient des mesures de polarisation.

La première partie de mon travail a concerné, après 1984 et en collaboration avec C. Devaux et R. Santer, l'interprétation des mesures de la station-sol en essayant plus particulièrement de dégager l'apport de la polarisation pour préciser les caractéristiques des aérosols ou corriger leur influence. Certains des résultats obtenus à l'aide de cette station sont exposés dans la partie I de ce travail, en particulier un cas d'étude d'un nuage de poussières sahariennes au-dessus de la France (P.1).

Par ailleurs, les mesures de la station-sol, associées à des mesures de réflectance du sol permettant de simuler le signal au niveau d'un satellite, cette méthode était mise en oeuvre pour étalonner les capteurs de SPOT 1. Ce travail a fait l'objet de plusieurs contrats (13), sous la responsabilité de R. Santer, entre le CNES et notre laboratoire depuis 1987 et a donné lieu à une collaboration avec l'INRA d'Avignon, chargé des mesures de réflectance de sol. Un contrat commencé avec les capteurs de SPOT1 a été prolongé pour SPOT2. Les résultats concernant la première campagne SPOT1 sont présentés dans la publication P2. Depuis, de nombreuses campagnes ont été menées et j'ai largement participé à leur dépouillement. Compte tenu des résultats positifs, cet étalonnage passera en phase opérationnelle en 1993 pour SPOT2, à raison d'une campagne par an, et un nouveau contrat du CNES sera engagé pour SPOT3.

Parallèlement, pour tester l'apport de la polarisation à la télédétection des aérosols troposphériques, le Laboratoire avait développé une expérience embarquée sur ballon stratosphérique, PIRAT (Polarisation Infra-Rouge du Rayonnement Atmosphérique). Le but était de mesurer les réflectances et taux de polarisation de la lumière solaire diffuse dans un plan vertical, le radiomètre étant porté par un ballon stratosphérique. Pour éviter les problèmes liés aux surfaces terrestres (réflectances élevées et spatialement très variables), l'expérience était conduite au-dessus de l'océan. J'ai pris la responsabilité de l'analyse de ces vols PIRAT. Les mesures ont mis en évidence la polarisation de la lumière diffuse des aérosols au-dessus de l'océan et celle des nuages sur un large banc de stratus.

L'interprétation de cette expérience, présentée dans la publication P3, a nécessité l'extension du code de transfert dont nous disposions en introduisant comme condition limite une surface océanique agitée qui présente une forte anisotropie en réflectance (phénomène du glitter): ce travail a été fait en respectant la structure des ordres successifs de diffusion et en utilisant une décomposition semi-analytique du couplage océan-atmosphère (P 4) ce qui allège les calculs numériques.

Cette méthode est applicable à d'autres problèmes comme la réflexion sur les feuilles d'un couvert végétal; j'ai pu aider G. Rondeaux à mettre au point un calcul de transfert radiatif dans un couvert végétal qui est basé sur une méthode très proche de celle des ordres successifs de diffusion et qui est exposé dans sa thèse (14).

La lourdeur des études systématiques justifiait le développement de codes approchés de calcul que j'ai mis au point pour le taux de polarisation et la réflectance au-dessus de l'océan. Ces modélisations approchées, basées sur les différentes contributions au signal global présentaient un certain intérêt pour aborder l'inversion des mesures expérimentales.

Les codes, exact ou approché, ont permis de préciser l'état de polarisation du rayonnement à l'entrée des capteurs satellitaires dans diverses conditions d'observation (géométries et cibles différentes) et d'en déduire l'erreur en réflectance introduite par la polarisation propre de l'instrument. Une telle étude systématique a d'abord été réalisée à la demande du CNES pour les capteurs HRV et Végétation de SPOT4 dans le cadre d'un contrat de deux ans dont j'ai assuré la responsabilité scientifique (15). Une étude de même type, mais limitée à des visées océaniques, a ensuite été reprise par E. Vermote dans le cadre d'un contrat avec l'ESA pour l'instrument MERIS (Medium Range Imaging Spectrometer)(16). Afin de valider certaines hypothèses sur la polarisation des sols et de compléter l'étude précédente par des observations, le CNES proposait au LOA l'analyse de photographies en polarisation prises depuis la navette spatiale américaine (17).

Cette étude qui a débouché sur la publication P5, commençait la préparation de l'expérience POLDER (POLarization and Directionality of the Earth Reflectance) dans laquelle sont réalisées des mesures spectrales, bidirectionnelles et polarisées. Cette expérience qui avait été proposée par le LOA et le LERTS a été retenue sur la plate-forme japonaise ADEOS (Advanced Device of Earth Observing System): le lancement est prévu en 1996, le CNES étant le maître d'oeuvre pour la réalisation de l'instrument spatial.

Depuis 1989, la partie essentielle de mes activités est consacrée à cette expérience d'un type nouveau, par ses mesures directionnelles et de polarisation. Ce travail est reporté dans la partie III du présent document.

Les objectifs mission, développés dans la publication P6, portent sur les nuages, l'océan et les terres émergées mais aussi sur les aérosols qui devraient être mieux détectés à l'aide des mesures réalisées par POLDER. en particulier on espère préciser la granulométrie des aérosols et leur indice de réfraction. C'est ce que j'ai montré dans une étude théorique réalisée dans le cadre d'un contrat passé avec le

CNES (LERTS) sur la télédétection des aérosols au-dessus de l'océan (18). Ceci devrait améliorer le suivi de ces aérosols et améliorer les corrections atmosphériques sur la couleur de l'eau.

L'accès à des produits utilisables à partir des mesures brutes effectuées par POLDER implique des traitements de données élaborés et je suis largement impliqué dans la mise au point des algorithmes utilisant les mesures de polarisation, plus particulièrement dans la télédétection des aérosols au-dessus des terres émergées et au-dessus des océans qui posent deux types de problèmes assez différents. Dans le cadre de la préparation de la mission, j'ai enfin participé à différentes études contractuelles concernant le modèle radiométrique et l'inter-étalonnage.

De façon à simuler les mesures du futur instrument spatial, à mieux appréhender les problèmes posés par le nouveau concept instrumental et à tester les algorithmes, une version aéroportée de POLDER a été réalisée au laboratoire. Depuis juin 1990 plusieurs campagnes ont été effectuées avec des objectifs divers: deux publications concernant respectivement les mesures au-dessus des terres émergées (P7) et des nuages (P8) sont présentées et complétées par quelques résultats obtenus au-dessus de l'océan.

C'est dans le cadre de cette préparation de la mission POLDER que j'ai encadré le stage de DEA de F. El Tahan (19), sur les images POLDER prises depuis le sol, participé au suivi du DEA de B. Toubbé (20) et de la thèse de P. Goloub (21) en collaboration avec M. Herman. Actuellement je suis le stage de DEA de T. Croquelois et je partage l'encadrement de la thèse de G. Perry, boursier CNES, qui travaille sur les algorithmes Polder.

## PARTIE I

Une première partie de mon travail a porté sur l'analyse de la polarisation du rayonnement du ciel, mesuré à partir du sol. Cette mesure est l'une de celles réalisées par la station-sol, développée au laboratoire depuis plusieurs années et actuellement sous la responsabilité de C. Devaux. Ces mesures optiques qui permettent de caractériser les aérosols ont été utilisées avec différents objectifs:

- qualifier l'effet des aérosols dans l'imagerie satellite.
- étudier les aérosols pour eux-mêmes, ce qui a été fait en particulier lors de campagnes spécifiques sur les aérosols sahariens à Dakar (Tanré, 1987) et sur les aérosols marins dans l'océan Indien (Devaux, 1990).
- quantifier leur influence sur les mesures satellitaires en particulier lors des étalonnages sur site de capteurs (HRV de SPOT).
- servir de vérité-terrain à des expériences ballon (Pirat) ou avion (Polder).

La station-sol utilise d'abord des mesures de transmission, par visée directe du soleil (de 400 à 1650 nm), et d'auréole à 850 nm de façon à minimiser l'influence des molécules. Ces mesures fournissent respectivement la variation spectrale de l'épaisseur optique des aérosols et leur indicatrice de diffusion avant (angle de diffusion inférieur à 30°). Ceci permet d'accéder à la granulométrie des particules.

Ces mesures sont complétées par des mesures dans le proche infra-rouge de la luminance et du taux de polarisation de la lumière diffuse du ciel, faites dans le plan principal de façon à couvrir un large domaine d'angles de diffusion avec un soleil bas sur l'horizon. Ces données permettent d'atteindre le taux de polarisation des aérosols dans les directions de rétrodiffusion ce qui est très intéressant car cette grandeur est très sensible à l'indice de réfraction des aérosols.

J'ai effectué l'analyse de ces mesures sur plusieurs campagnes en collaboration avec C. Devaux; cette analyse consiste, connaissant la granulométrie, à préciser l'indice de réfraction à partir du diagramme directionnel du taux de polarisation, en simulant le signal à l'aide du code des ordres successifs.

Un premier exemple est présenté dans la publication P1: il s'agissait de l'observation d'un nuage d'aérosols sahariens dans le sud-est de la France. L'interprétation est surtout basée sur les mesures de transmission car l'utilisation de l'auréolemètre fut compromise par un fort vent dégradant la précision des pointés. Le radiomètre polarisé, qui opérait pour la première fois, a donné des indications qualitatives bien corrélées à la grosseur des particules. Les résultats de cette expérience sont cohérents mais l'analyse des données de la station-sol revêt ici un caractère préliminaire compte tenu du manque d'informations sur les plus grosses particules.

Depuis, de nombreuses campagnes de la station-sol se sont déroulées et leur dépouillement s'est affiné. L'adjonction d'un radiomètre, régulièrement étalonné sur ballon stratosphérique, a rendu plus fiables les mesures d'épaisseurs optiques. La granulométrie des aérosols est maintenant obtenue par l'inversion simultanée des données de transmission et d'auréole (22). Nous présentons ci-dessous quelques résultats relatifs à des mesures réalisées par C. Devaux dans l'océan Indien. Les granulométries de la fig.1 qui restituent parfaitement les données d'épaisseurs optiques et d'auréole, sont obtenues en fixant a priori l'indice de réfraction. Les mesures de polarisation présentées sur les figures 2 et 3 respectivement à 865 nm et à 1650 nm, permettent de préciser l'indice de réfraction et la nature de l'aérosol, ici sans doute océanique, ce qu'il est important de connaître dans une climatologie des aérosols.

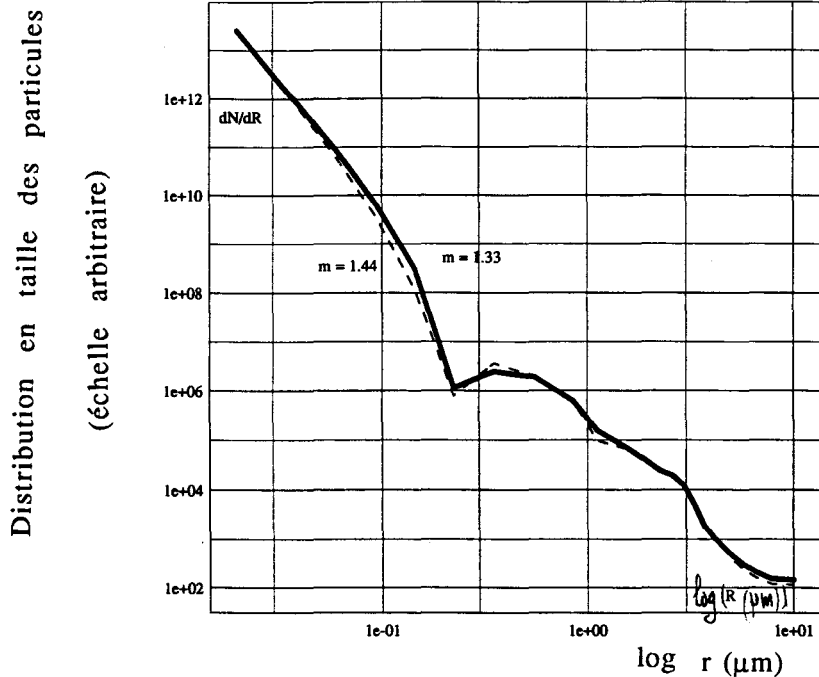
Un autre exemple d'utilisation des mesures de la station-sol est présenté dans le cadre de l'étalonnage des capteurs de SPOT au-dessus de la plaine de La Crau. Le

principe de l'étalonnage, exposé dans la publication P2, consiste à comparer le signal mesuré par le capteur au signal prévu à partir de mesures in-situ. Le site français de La Crau a été choisi pour ses caractéristiques de stabilité et d'homogénéité, mais sa réflectance n'est pas très élevée, comparée par exemple à celle de White Sands (USA), si bien que les mesures atmosphériques revêtent une grande importance dans la qualité de l'étalonnage, d'autant plus que les situations atmosphériques sont assez variables (continentale ou maritime suivant l'orientation des vents).

Je participe activement, avec C. Devaux, à l'analyse de ces campagnes d'étalonnage qui ont fait l'objet d'un contrat (13) avec le CNES sous la responsabilité de R. Santer.

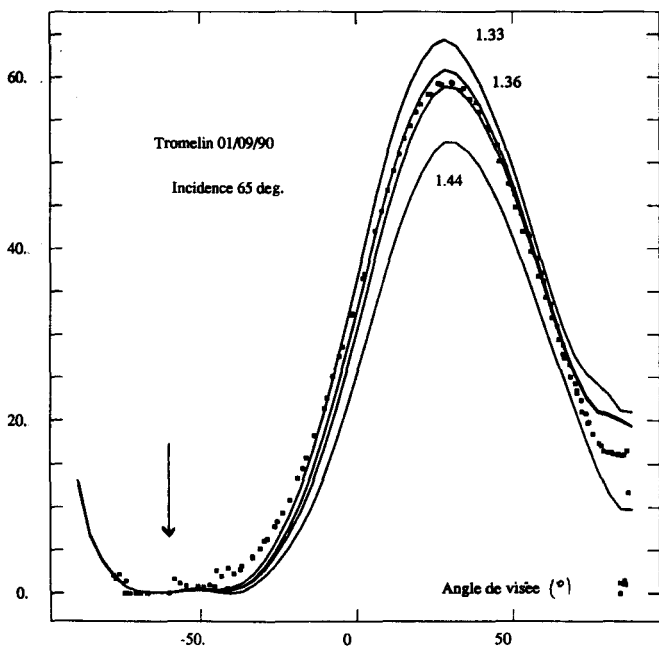
Nous présentons sur la figure 4 les granulométries obtenues à partir des mesures de la station-sol sur La Crau en janvier 1992: l'inversion des mesures a été essayée pour différents indices de réfraction ( 1.33, 1.44 et 1.50 avec une partie imaginaire égale à 0.005) mais une bonne restitution des diagrammes directionnels du taux de polarisation et de la luminance du ciel implique qu'on prenne des indices de réfraction égaux à  $1.50 - 0.01.i$  à 850 nm et  $1.40 - 0.005.i$  à 1650 nm (Figs. 5 et 6). Cette diminution d'indice de réfraction de 850 à 1650 nm se retrouve sur certains modèles connus d'aérosols troposphériques (23): on note toutefois un accroissement de la partie imaginaire qui n'apparaît pas dans nos résultats.

Une synthèse des résultats pour SPOT2, est présentée sur la figure 7:; il s'agit de la bande centrée sur 550 nm. On a porté, en fonction du temps écoulé depuis le lancement, les coefficients d'étalonnage, ceci toutes méthodes confondues (lampes à bord, sites français et américains). On voit que les résultats déduits des campagnes La Crau sont compatibles avec ceux obtenus sur les sites américains. Ces résultats sur site ont permis de recalibrer les étalonnages-bord affectés par le vieillissement des lampes.



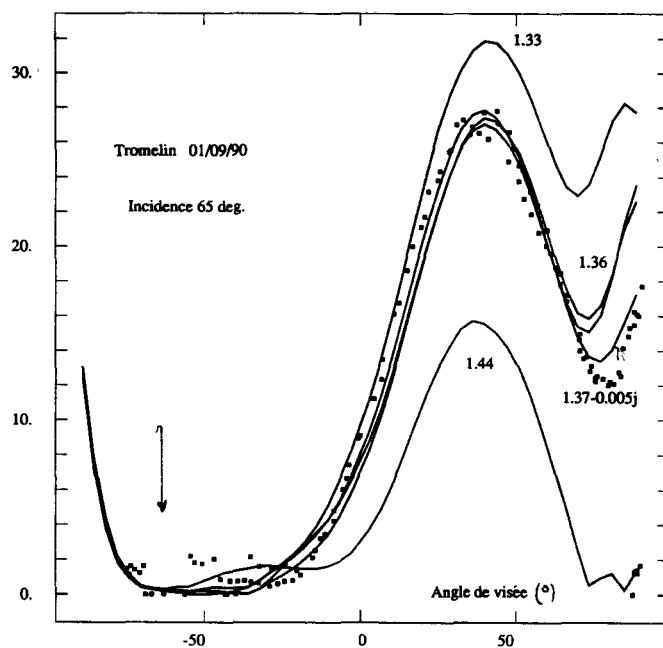
-1- Distributions en taille des particules déduites des mesures de la station-sol en prenant successivement deux indices de réfraction  $m$  ( Tromelin, 01/09:1990)

Taux de polarisation à 865 nm



2

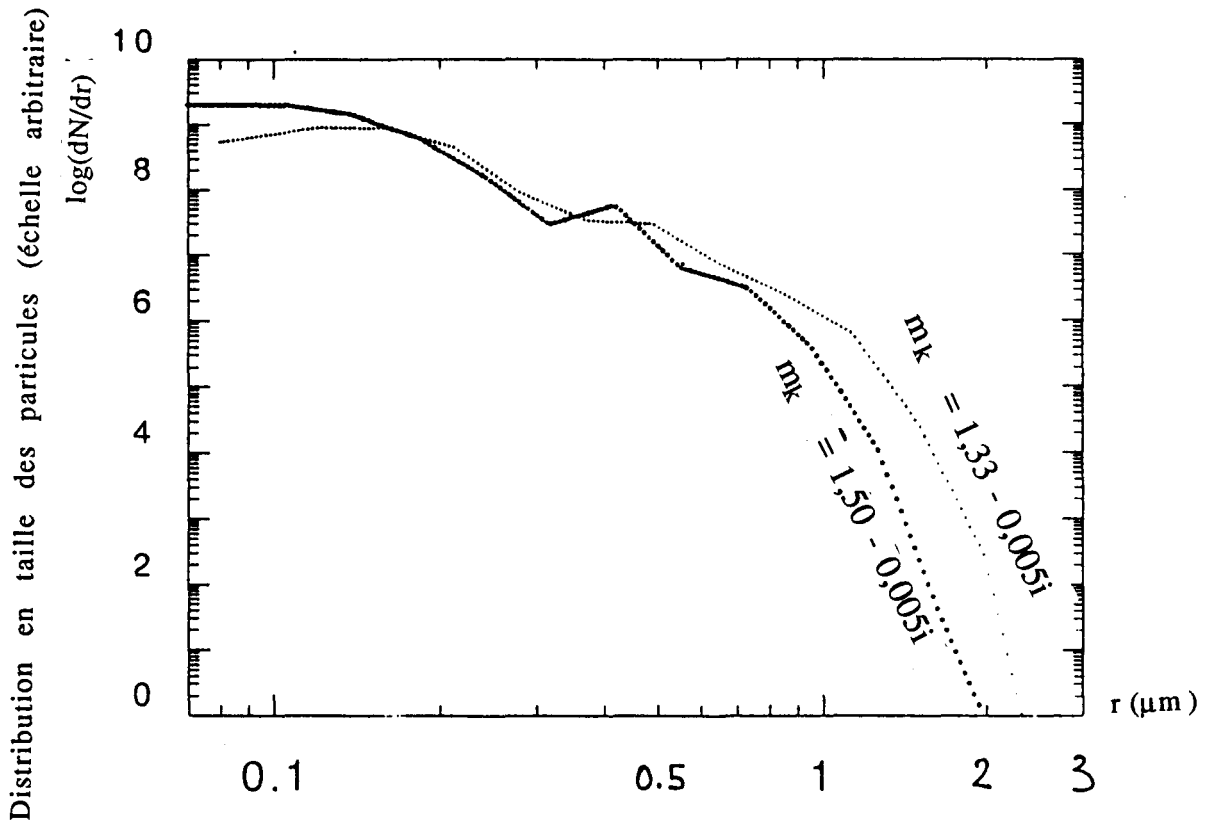
Taux de polarisation à 1650 nm



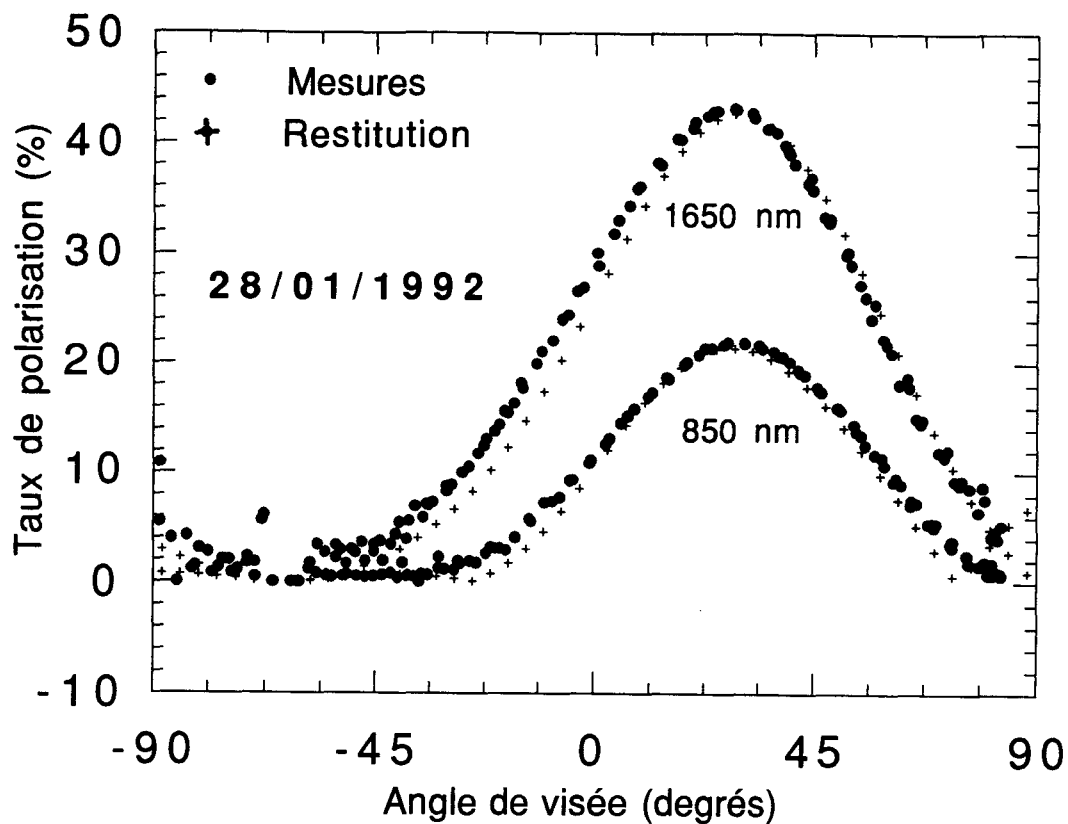
3

-2- Restitution du taux de polarisation du rayonnement du ciel à 850 nm. La meilleure restitution est obtenue pour l'indice de réfraction  $m = 1,36$ , ceci indépendamment de la granulométrie choisie (voir figure 1)

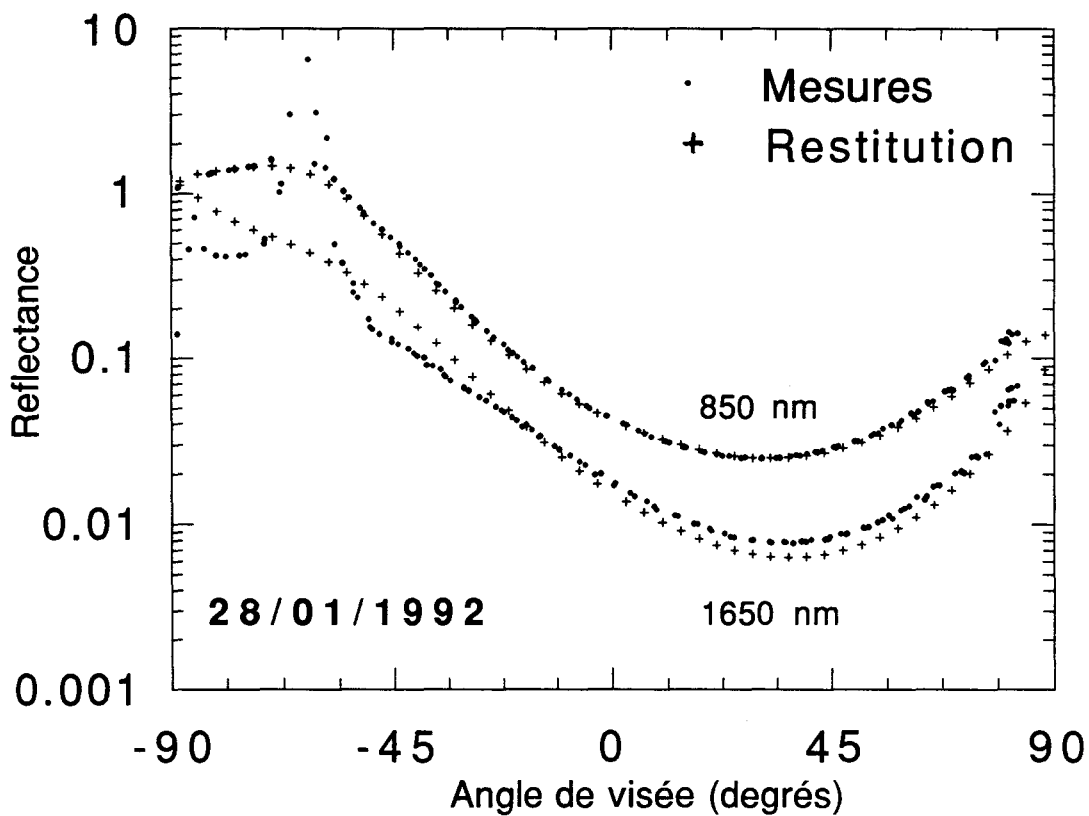
-3- Même légende que sur la figure 2, mais dans le canal 1650 nm. On a également tracé le résultat obtenu avec  $m = 1,37 - 0,005i$ , indice qui donne une meilleure restitution vers les incidences élevées.



-4- Distributions en taille des particules déduites des mesures de la station-sol en prenant successivement deux indices de réfraction  $m$ .

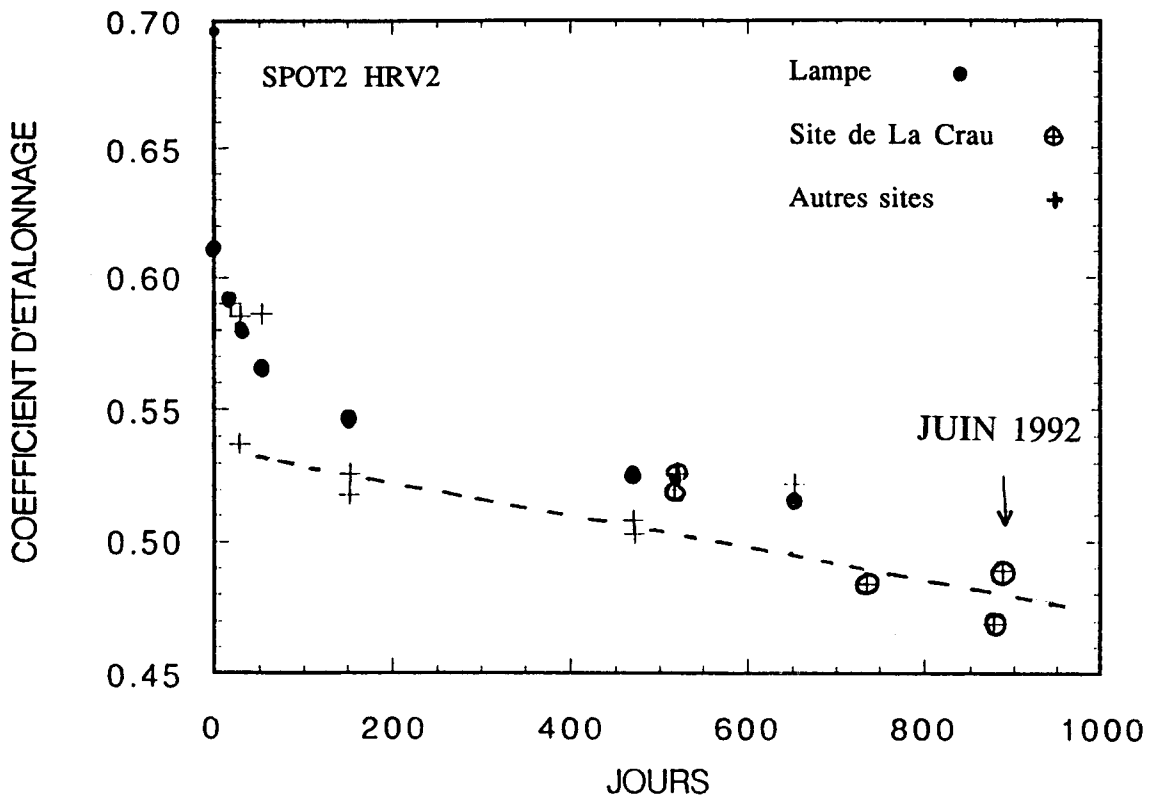


(a)



(b)

-5- Restitution du taux de polarisation (a) et de la réflectance diffuse du ciel (La Crau, janvier 1992) avec un indice de réfraction égal à  $1,49 - 0,01i$  à 850 nm et  $1,37 - 0,02i$  à 1650 nm..



-6- Evolution temporelle du coefficient d'étalonnage du capteur HRV de SPOT2 dans le canal 550 nm. On compare ici différents méthodes d'étalonnage.

## Partie II

Pour confirmer l'intérêt des mesures polarisation directionnelles dans l'observation de la terre depuis l'espace, le LOA avait développé, à partir de 1982, un polarimètre embarqué sur ballon stratosphériques (24). Cette expérience, appelée RADIBAL, d'abord dédiée à l'étude des aérosols stratosphériques, consistait à mesurer dans un plan horizontal la réflectance et le taux de polarisation de la lumière solaire diffuse: l'analyse directionnelle était obtenue par la rotation de la nacelle portant le capteur sous le ballon.

Le succès de RADIBAL a amené à transformer ce système dans l'expérience PIRAT (POLarisation dans l'Infra-rouge du Rayonnement ATMosphérique) dont j'ai assuré l'interprétation avec M. Herman et R. Santer (P3); L'objectif était la caractérisation des aérosols troposphériques depuis ballon. L'instrument Radibal fut donc transformée pour observer le rayonnement renvoyé vers l'espace, en adjoignant au polarimètre RADIBAL un miroir de renvoi. Pour que l'analyse du rayonnement soit praticable, il fallait survoler une surface homogène à l'échelle d'un balayage (soit environ deux fois l'altitude du ballon soit 50 km). Les vols ont donc été faits au-dessus de l'océan. Pour réaliser cette expérience, la section ballon du CNES a développé une technique particulière de vol, dit vol-boomerang, qui permet d'envoyer, et surtout de récupérer, une charge au-dessus de l'océan. Pour des lancers depuis Aire sur l'Adour (sud-ouest de la France), la technique consistait à utiliser le vent stratosphérique d'est à l'aller et à effectuer le retour grâce aux vents troposphériques d'ouest. Trois vols de ce type ont eu lieu entre 1985 et 1988.

Pour dépouiller cette expérience, il a été nécessaire d'adapter le code de transfert en introduisant, à la place d'une surface lambertienne, la réflexion sur les vagues de l'océan en utilisant le modèle de Cox et Munk (25). A cette occasion des codes de calculs approchés ont été développés pour analyser les données et mettre en oeuvre des procédures d'inversion des mesures.

Le premier vol nous a permis de valider les mesures de polarisation directionnelle réalisées pour la première fois dans des conditions proches de l'observation spatiale. Les résultats de ce vol, présentés dans la publication P3, ont porté sur les points suivants:

- observation du glitter et validation du modèle de Cox et Munk en polarisation (Fig. 7).

- observation des aérosols: les aérosols troposphériques ont d'abord été observés au-dessus des sols, avec un soleil bas sur l'horizon ce qui minimise l'influence de la surface. Au-dessus de l'océan, malgré la présence perturbatrice du glitter, on a constaté que la signature en polarisation de ces aérosols subsistait en rétrodiffusion (Fig. 7).

- observation des nuages: durant le vol, un large banc de stratus a été survolé: les réflectances qui présentaient peu d'effets directionnels, excepté au limbe, ont été utilisées dans l'inter-étalonnage des deux canaux proche infra-rouge. Au contraire, les mesures du taux de polarisation exhibaient dans l'arc-en-ciel un maximum caractéristique de la diffusion par des goutellettes d'eau (fig. 8).

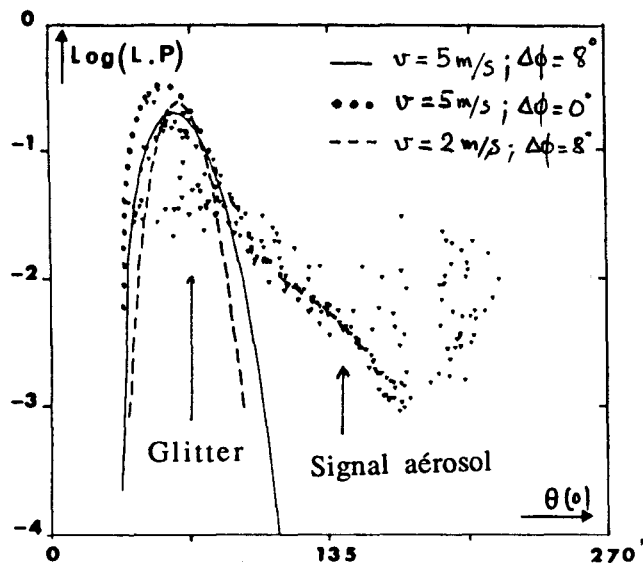
Bon nombre des idées développées à l'occasion du dépouillement de ce vol Pirat ont été reprises dans l'expérience POLDER et seront exposées dans la partie III.

Les travaux de modélisation développés pour l'expérience Pirat ont été utilisés par ailleurs, dans le cadre d'un contrat avec le CNES dont j'ai eu la charge (15), pour étudier l'impact de la polarisation sur les mesures des capteurs satellitaires en particulier pour HRV (High Radiometer Visible) et le passager Végétation de SPOT4. Une étude similaire a été reprise ensuite par E. Vermote (16) pour l'instrument MERIS dédié à la couleur de l'océan.

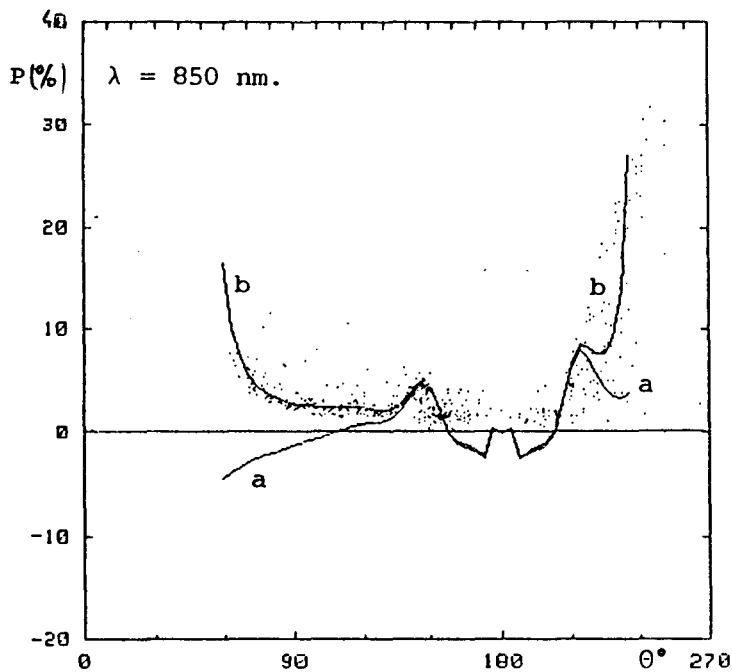
L'erreur en réflectance  $\Delta\rho$  introduite par la polarisation propre P de l'optique d'un capteur s'écrit  $\Delta\rho = P \cdot \rho_{pol}$  où  $\rho_{pol}$  est la réflectance polarisée en entrée du capteur. L'étude que j'ai conduite consistait à évaluer  $\Delta\rho$  dans différentes conditions d'observation et pour différentes cibles. Une première modélisation a porté sur le cas particulier de l'atmosphère moléculaire, au-dessus d'un sol lambertien puis au-dessus de l'océan, glitter et diffusion moléculaire aux courtes longueurs d'onde étant les cibles qui donnent les plus fortes luminances polarisées.

D'autres cibles ont ensuite été introduites dans l'étude: sable, neige et végétation, dont les caractéristiques de polarisation ont été déduites de mesures tirées de la littérature ou de modélisations rudimentaires. Pour tester certaines de ces hypothèses sur la polarisation, le CNES nous a proposé par la suite une étude visant à interpréter des images en polarisation prises depuis la navette spatiale: ce contrat (17), pris en charge par R. Santer et J.C. Roger, a débouché sur la publication P5. La prise de ces photographies ne faisant pas partie des missions "officielles" de l'équipage de la navette, aucun protocole de mesure n'avait été défini pour cette expérience ce qui a rendu singulièrement compliquée son interprétation. De nombreuses informations sont manquantes et ne sont estimées que très difficilement (étalonnage photométrique, polarisation des hublots) et au prix de suppositions expérimentales (ouvertures des diaphragmes, directions de visée, axe des polariseurs ...).

Malgré tout, outre les études spécifiques à la polarisation de diverses cibles, cette expérience a permis de tester des méthodes d'étalonnage qui seront reprises pour POLDER: étalonnage absolu des canaux courtes longueurs d'onde en utilisant la diffusion moléculaire, inter-étalonnage sur le glitter et les nuages. Par ailleurs, on a pu caractériser une situation très particulière avec des aérosols provenant de feux de forêt.



-7- Luminance polarisée à 850 nm: mesures et simulations utilisant le modèle de pente de vagues de Cox et Munk.



-8- Taux de polarisation mesuré au-dessus d'un banc de nuages, en fonction de l'angle de diffusion  $\theta$ . Les courbes représentent des simulations au-dessus d'un nuage de type C1, en tenant compte (a) ou non (b) de l'atmosphère libre au-dessus du nuage.

### PARTIE III

Cette dernière partie est essentiellement consacrée à l'instrument POLDER ( POLARization and Directionality of the Earth's Reflectances) qui devrait être placé sur orbite en 1996 sur la plate-forme japonaise ADEOS ( ADvanced Earth Observing System). Cet instrument, réalisé grâce à l'apparition des matrices de détecteurs C.C.D. (Charged Coupled Device), synthétise les concepts présentés dans les chapitres précédents à savoir les visées spectrales, directionnelles et polarisées. Les principaux objectifs- mission relèvent des programmes PMRC et PIGB; ils sont exposés dans la publication P6 et concernent les points suivants:

pour l'atmosphère: caractérisation, sources, transport et rôle climatique des aérosols; propriétés directionnelles, altitude et phase des nuages; contenu en vapeur d'eau.

sur l'océan: couleur de l'eau et cycle du carbone.

sur les terres émergées: propriétés directionnelles des sols et production primaire.

Mon travail sur POLDER s'est développé autour de quatre axes principaux, menés parallèlement:

- la mise au point du prototype aéroporté développé au laboratoire.
- l'analyse des premières campagnes en m'intéressant plus particulièrement aux aérosols aussi bien au-dessus des terres qu'au-dessus des océans.
- la préparation des algorithmes qui seront intégrés dans le segment sol Polder et qui permettront de transformer les données du capteur en produits géophysiques utilisables par la communauté scientifique.
- et diverses études techniques, en particulier sur l'inter-étalonnage.

Ce travail qui traduit une large collaboration avec M. Herman, se retrouve partiellement dans les travaux (DEA et thèses) d'étudiants que j'ai co-dirigés, P. Goloub, B. Toubbé, G. Perry, ou dirigé, F El Tahan.

Le premier point concernait le développement du modèle radiométrique de l'instrument Polder ce qui consistait à prendre en compte les différents défauts de l'optique liés à l'ouverture grand champ de l'instrument, aux transmissions des polariseurs et filtres, aux différences de sensibilités entre les détecteurs de la C.C.D. Ce premier point est résumé dans un rapport interne (26) et détaillé dans la thèse de P. Goloub (21) qui a pris la responsabilité de ce travail. Dans le même but de mise au point, les premiers essais de Polder depuis le sol, développés dans le cadre du DEA de F. El Tahan (19), ont montré l'intérêt de la polarisation pour détecter les aérosols.

Dans le cadre des études techniques, j'ai analysé la possibilité d'utiliser le glitter pour inter-étalonner l'instrument, supposé étalonné en absolu sur la diffusion moléculaire aux plus courtes longueurs d'onde ( Rapport interne Herman, Deuzé). Ce travail a été approfondi par P. Goloub (27) puis par B. Toubbé avec qui nous étudions la possibilité d'utiliser la polarisation du glitter pour retrouver des informations sur les aérosols.

Dans le cadre d'un contrat CNES (18), j'ai également réalisé une étude montrant la possibilité d'une meilleure caractérisation des aérosols au-dessus des océans en utilisant les mesures polarisées de la version satellitaire de Polder.

Le simulateur aéroporté Polder a volé pour la première fois en juin 1990 au-dessus de La Crau; il a été depuis impliqué dans plusieurs expériences thématiques énumérées ci-dessous:

Date	Campagne	Lieu	Thème
06/1990	La Crau	France S-E	Aérosols et sols
08/1990	Landes	France S-O	Aérosols et sols
06/1991	La Crau	France S-E	Aérosols et sols
07/1991	Orgeval	France Centre	Végétation
03 et 04/1991	Medimar	Méditerranée	Eau, aérosols
05/1991	Cleopatra	Allemagne	Nuages
12/1991	Racer	Antarctique	Eau, aérosols
05/1992	Astex	Açores	Nuages
08 au 10/1992	Hapex	Niger	Aérosols et sols

Une analyse préliminaire du premier vol (28) a permis de vérifier le bon fonctionnement (mécanique et électrique) de l'instrument ainsi que l'acquisition correcte des données (transferts de la CCD aux mémoires, enregistrement sur bande magnétique, relecture). Nous avons montré qu'au cours de ce premier vol l'instrument restituait des signatures classiques, telles celle du glitter, de la réflectance bidirectionnelle de La Crau, du hot-spot ou encore de l'atmosphère au-dessus de lacs, ce qui établissait la faisabilité de l'expérience.

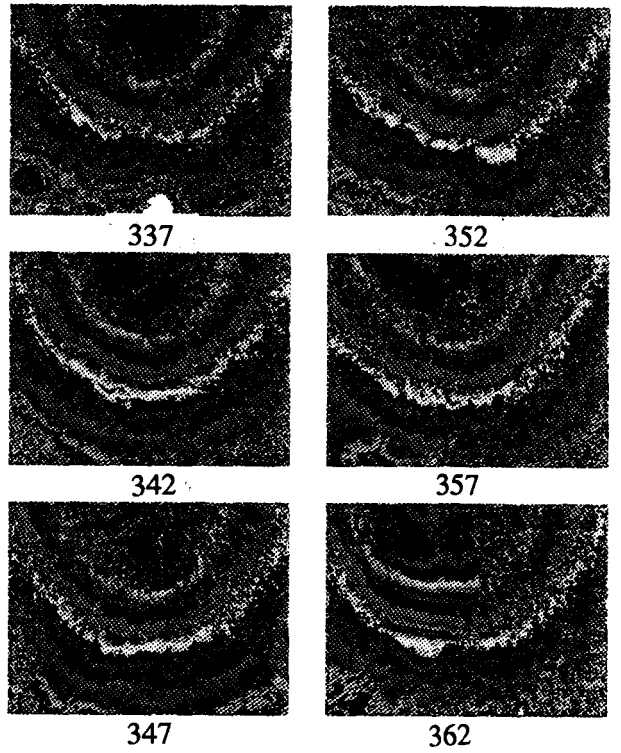
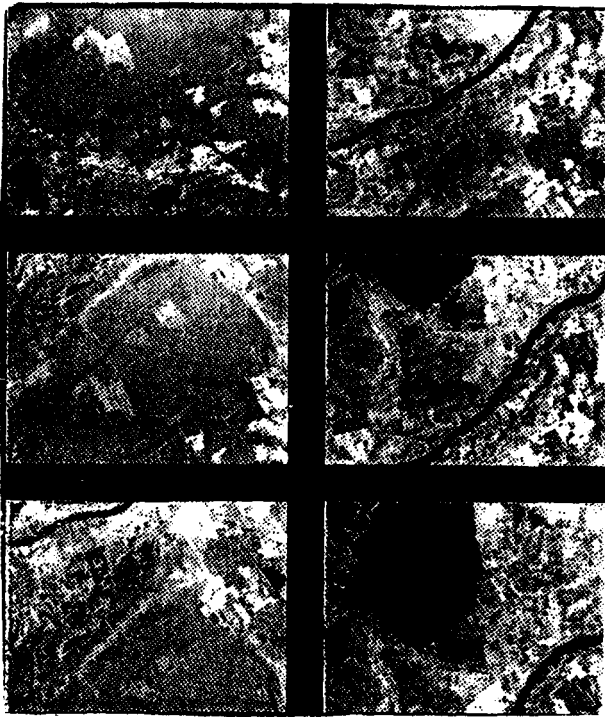
Par la suite, l'étude des propriétés bidirectionnelles des sols a été reprise par F.M. Bréon alors que P. Goloub prenait en charge celle des propriétés des nuages (phase et altimétrie) à partir des mesures de polarisation (publication P8).

Je détaillerai essentiellement le travail de détection des aérosols dans l'imagerie POLDER: ce travail dont je suis responsable, constitue un point important de la mission pour le suivi des aérosols et l'amélioration attendue des corrections atmosphériques. L'approche est fort différente suivant que les observations se font au-dessus de l'océan ou des terres émergées.

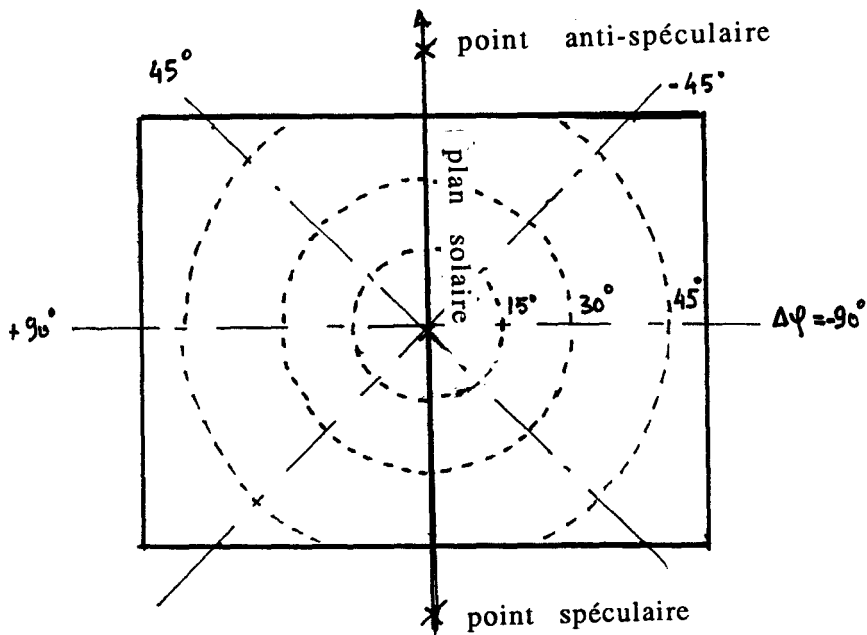
Dans ce dernier cas, on sait que la grande variabilité et le niveau élevé des réflectances des sols rendent très difficile la détection des aérosols en utilisant la seule réflectance. Au contraire, nous avons montré que la réflectance polarisée, principalement générée par l'atmosphère, était une grandeur permettant de détecter les aérosols et sans doute de les caractériser. Ceci est illustré sur la figure 9 représentant une série d'images Polder au-dessus de La Crau: on observe distinctement à gauche, sur les images prises en réflectance, différentes scènes facilement identifiables (végétation, lacs...) alors qu'à droite, en réflectance polarisée, la même allure se retrouve d'une image à l'autre, indépendamment de la surface, et traduit donc une information atmosphérique pure. La géométrie de l'observation est expliquée sur la figure 10. La réflectance polarisée s'écrit en première approximation:

$$\rho_{pol} = (\delta_a \cdot p_a(\Theta) \cdot P_a(\Theta) + \delta_m \cdot p_m(\Theta) \cdot P_m(\Theta)) / (4 \cdot \cos \theta_s \cos \theta_v)$$

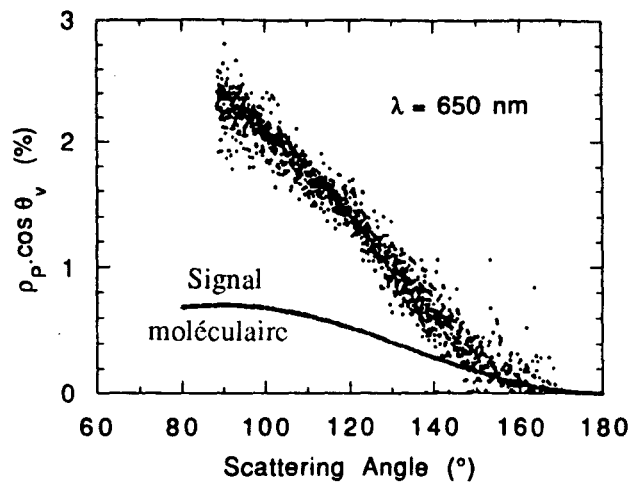
où  $\delta$  représente l'épaisseur optique,  $p(\Theta)$  la fonction de phase dépendant de l'angle de diffusion  $\Theta$ ,  $P(\Theta)$  le taux de polarisation primaire des aérosols, indicé "a", ou des molécules, indicé "m".  $\theta_s$  est l'angle d'incidence solaire et  $\theta_v$  l'angle de visée. Pour une même image, la quantité  $\cos \theta_v \rho_{pol}$  ne dépend donc que de l'angle de diffusion  $\Theta$ . C'est effectivement ce que nous observons en traçant  $\cos \theta_v \rho_{pol}$  en fonction de  $\Theta$  (fig.11). Sur cette figure, nous avons également porté le signal moléculaire, la différence entre les deux courbes correspondant alors à la contribution des aérosols.



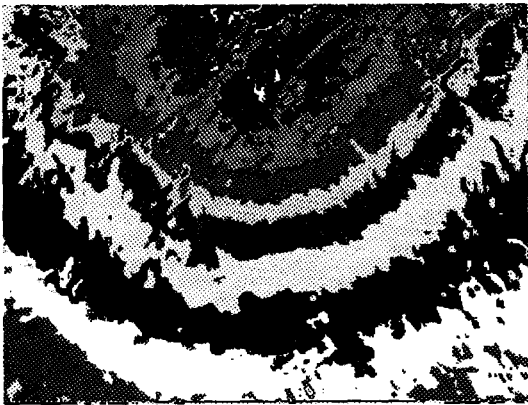
-9- Série d'images POLDER prises au-dessus de La Crau (17/06/1990) en réflectance dans le canal 850 nm (a) et en réflectance polarisée à 550 nm (b). Cette séquence représente des images prises de 5 en 5, l'avion gardant le même cap.



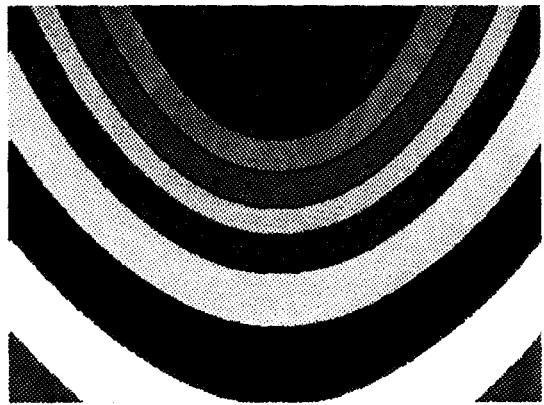
-10- Géométrie de l'observation pour les images de la figure 9.



-11- On a tracé sur cette figure la quantité  $\rho_{\text{pol}} \cdot \cos \theta_v$  en fonction de l'angle de diffusion  $\theta$  pour toutes les observations d'une prise de vue POLDER à 650 nm.



Mesures



Simulations

-12- Comparaison entre les mesures et les simulations de réflectance polarisée à 650 nm. Les simulations sont faites avec le modèle d'aérosol déduit des mesures de la station-sol (La Crau, 17/06/1990).

Le modèle d'aérosols déduit des mesures de la station-sol permet de simuler la réflectance polarisée à l'altitude de l'avion, ici 6 km: la comparaison entre mesures et simulations (Fig. 12) est tout à fait satisfaisante; sur certaines images, on note parfois de légers écarts pour les visées autour du point spéculaire, directions dans lesquelles la polarisation de la surface intervient.

L'inversion des mesures est en cours dans le cadre du DEA de T. Croquelois: la méthode consistera à comparer les réflectances polarisées mesurées à des valeurs précalculées pour différents modèles d'aérosols caractérisés par leur coefficient d'Angström, traduisant la dépendance spectrale, leur indice de réfraction et différentes épaisseurs optiques.

Les premières images POLDER au-dessus de l'eau ont été obtenues au cours de la campagne POLDER qui s'est déroulée en Méditerranée, au large de Banyuls, en mars-avril 1991. Pour ces campagnes océaniques, seuls les canaux 850 et 450 étaient équipés de polariseurs, trois autres canaux étant utilisés pour la couleur de l'eau. La figure 13a représente une image en réflectance prise à 850 nm le 01 avril, avec un angle d'incidence solaire égal à 39°, ce qui explique la présence de la tache du glitter dans le champ de l'instrument. La forme et l'intensité de cette tache, qui est une gêne pour l'étude des aérosols et de la couleur de l'eau, donnent une idée de la vitesse du vent estimée ici à 12 m/s, valeur qui introduit une réflectance d'écume égale à 0,003. On retrouve, figure 14a, le même phénomène sur le taux de polarisation, grandeur qui convient ici pour l'étude, tout comme la réflectance polarisée, car la surface océanique est uniforme. Hors du glitter, on note la présence de zéros de polarisation isolés et situés en dehors du plan solaire: ces zéros apparaissent localement et non pour tous les pixels correspondant à un même angle de diffusion: ceci montre que le taux de polarisation ne dépend pas uniquement de l'angle de diffusion  $\Theta$ , comme c'était le cas pour la réflectance polarisée au-dessus des sols. Le problème est ici plus compliqué car la lumière polarisée résulte de trois contributions: le signal atmosphérique, le signal correspondant à la lumière réfléchi sur l'océan puis diffusée dans l'atmosphère et enfin celui correspondant à la réflexion de la lumière diffuse. Ces composantes s'ajoutent directement en réflectance mais pas en réflectance polarisée car leurs directions de polarisation ne sont pas les mêmes.

Pour amorcer l'inversion des mesures aéroportées, on utilise dans un premier temps les réflectances en évaluant, hors glitter, un coefficient d'Angström  $\alpha$  entre 850 et 650 nm: sur cette image, nous avons trouvé  $\alpha = 1,50$  alors que la valeur déduite des épaisseurs optiques mesurées sur le navire océanographique opérant au moment du passage donnait  $\alpha = 1,53$ . A partir de la théorie de Mie, il est facile de trouver les modèles granulométriques qui, pour un indice de réfraction  $m$ , restituent le coefficient  $\alpha$ . Avec une loi de distribution log-normale à deux paramètres, nous avons trouvé:

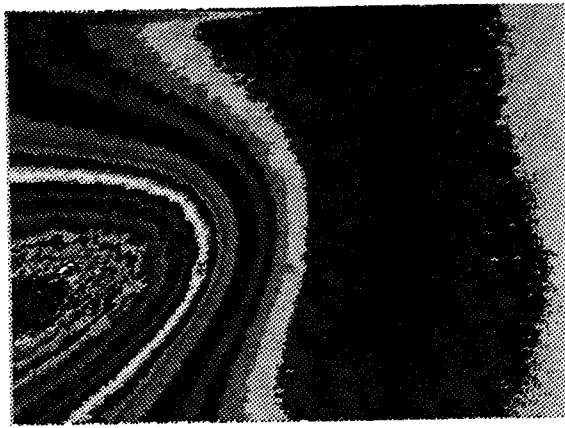
pour $m = 1,33$	$r_{\text{eff}} = 0,02 \mu\text{m}$	et	$\sigma = 0,40$
pour $m = 1,50$	$r_{\text{eff}} = 0,02 \mu\text{m}$	et	$\sigma = 0,38$

L'épaisseur optique  $\delta_a$  des aérosols à 850 nm, est obtenue par tâtonnement, en simulant le signal sur toute l'image à l'aide du code des ordres successifs et en comparant aux mesures de réflectance. Nous avons trouvé  $\delta_a = 0,17$  pour  $m = 1,33$  et  $\delta_a = 0,10$  pour  $m = 1,50$  alors que la valeur mesurée au bateau était  $\delta_a = 0,12$ . Le résultat de ces deux simulations est présenté sur les figures 13b et c pour les réflectances, et sur les figures 14b et c pour les taux de polarisation. On constate que l'indice  $m = 1,33$  restitue mieux l'allure générale du taux de polarisation que  $m = 1,50$  qui fait apparaître une polarisation nulle dans le plan solaire, ce qui est lié à une inversion du taux de polarisation primaire. La simulation avec l'indice  $m = 1,33$  restitue des zéros de polarisation isolés, comme sur les mesures, même s'ils ne sont

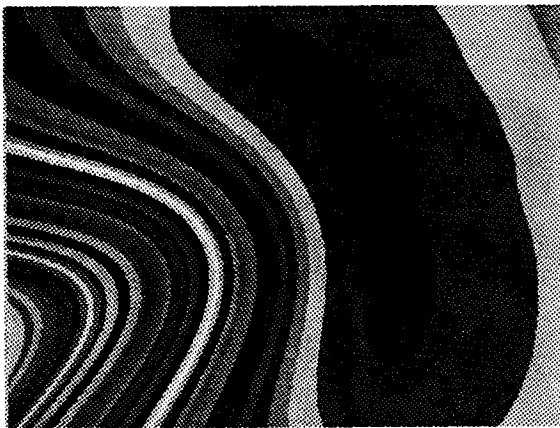
pas parfaitement positionnés. La polarisation apporte donc un complément intéressant pour la détermination des caractéristiques des aérosols. Nous avons également porté sur la figure 15 l'angle  $\beta$  repérant la direction du plan de polarisation: la comparaison entre les mesures et les simulations confirme le meilleur accord pour  $m = 1,33$ .

Les simulations réalisées dans le canal 450 nm avec  $m = 1,33$  ne restituent correctement le signal en réflectance qu'en introduisant une réflectance d'eau de mer bien supérieure à celle mesurée in-situ. Nous avons représenté sur la figure 16 les mesures en réflectance (a), respectivement en taux de polarisation (b), et leur restitution (c), respectivement (d). Le mauvais résultat relatif à la réflectance de l'eau ne peut être attribué en totalité aux défauts d'étalonnage: il est plutôt lié aux corrections atmosphériques entre 850 et 450 nm et à la détermination imparfaite du modèle d'aérosol qui ne restitue que qualitativement les mesures à 850 nm. Un meilleur accord passe sans doute par une plus grande complexité du modèle d'aérosol (multi-modalités, absorption propre et échelle de hauteur des particules) et par une prise en compte plus réaliste des effets de surface (dépendance en azimut de la réflexion sur l'océan, modèle d'écume).

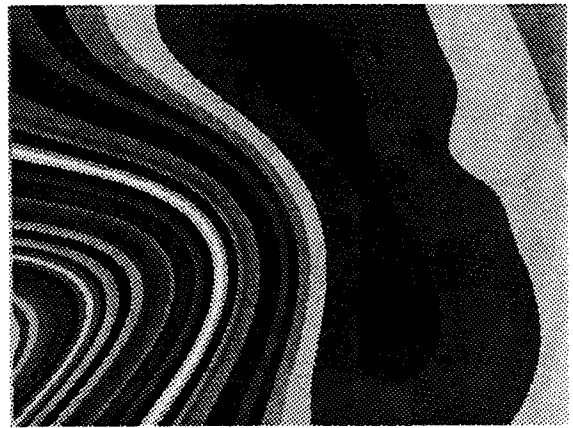
La méthode présentée pour retrouver le modèle d'aérosol, à partir des mesures de réflectance et de polarisation à 850 nm, a également été appliquée aux mesures RACER (28). Même si elle a besoin d'être améliorée, comme nous l'avons vu ci-dessus, elle constitue une première approche des algorithmes d'inversion des aérosols au-dessus des océans, algorithmes du segment-sol POLDER sur lesquels je travaille actuellement avec M. Herman et G. Perry.



a) Mesures en réflectance (850 nm)



b) Simulations avec  $m = 1,33$



c) Simulations avec  $m = 1,50$

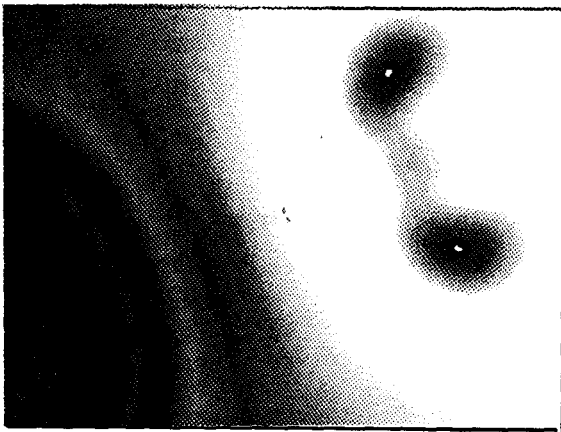


-13- Images POLDER en réflectance à 850 nm.

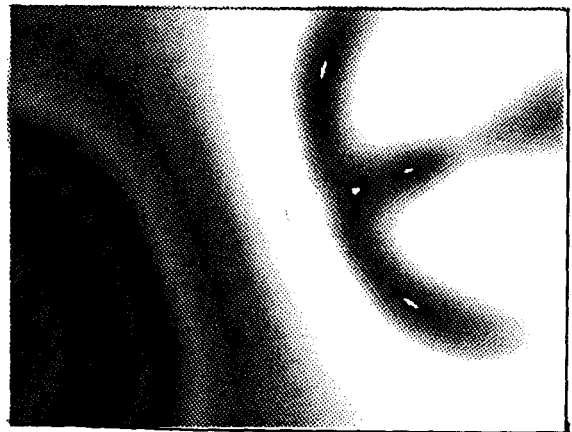
- a) Mesures prises en Méditerranée ( MEDIMAR 01/04/1991).
- b) Simulations avec un indice de réfraction  $m = 1.33$  (voir texte)
- c) Simulations avec un indice de réfraction  $m = 1.50$  (voir texte)



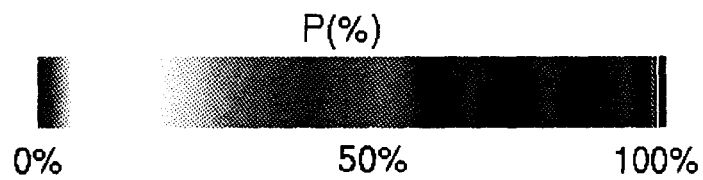
a) Mesures du taux de polarisation (850 nm)



b) Simulations avec  $m = 1,33$



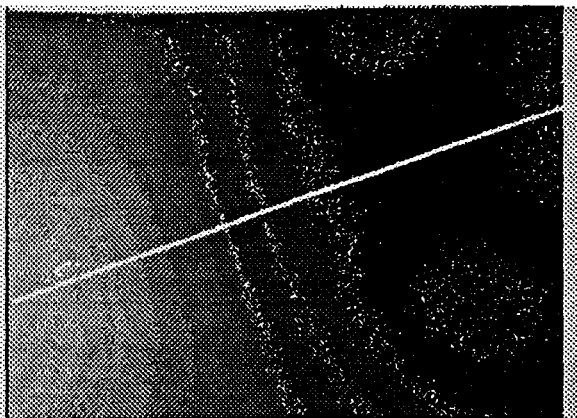
c) Simulations avec  $m = 1,50$



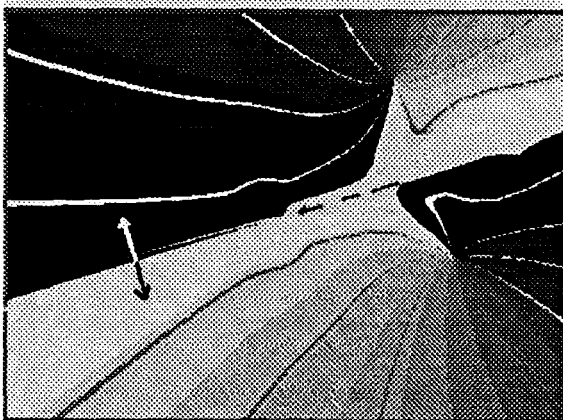
-14- Même légende que sur la figure 13, mais pour le taux de polarisation.



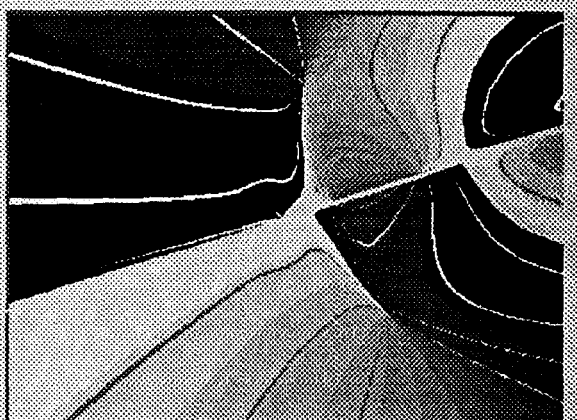
Mesures de  $\beta$



Taux de polarisation



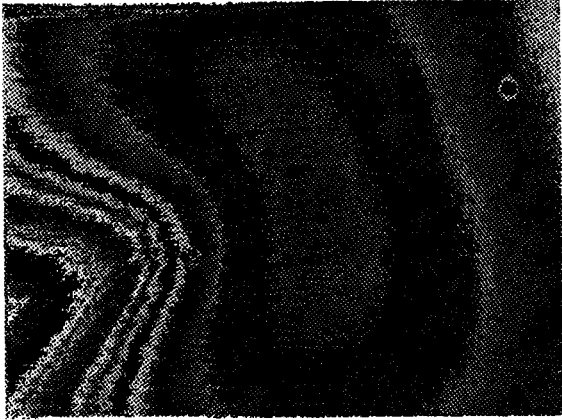
Simulations de  $\beta$  (  $m = 1,33$  )



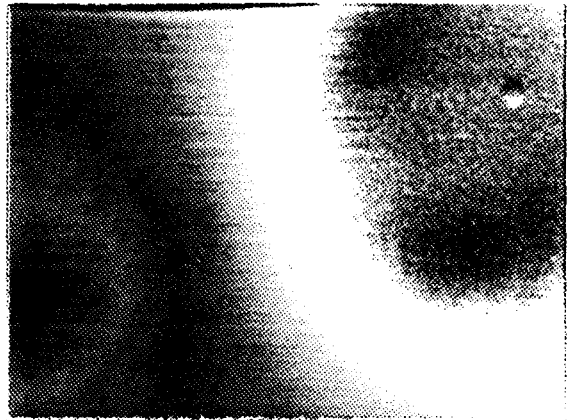
Simulations de  $\beta$  (  $m = 1,50$  )



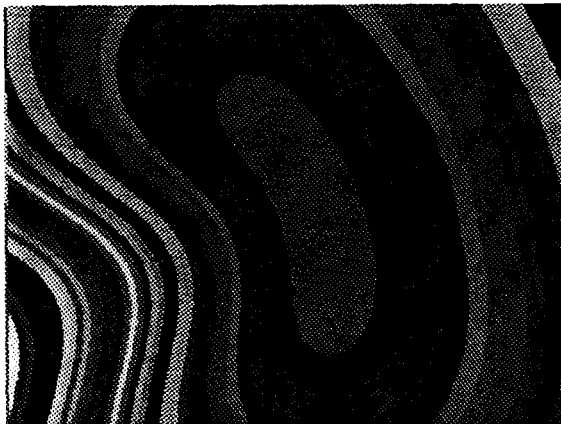
-15- Même légende que sur la figure 13, mais pour l'angle  $\beta$  repérant la direction du plan de polarisation par rapport au plan solaire.



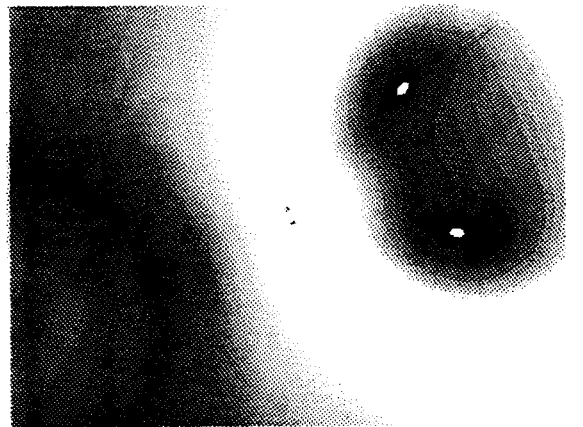
a) Mesures en réflectance (450 nm)



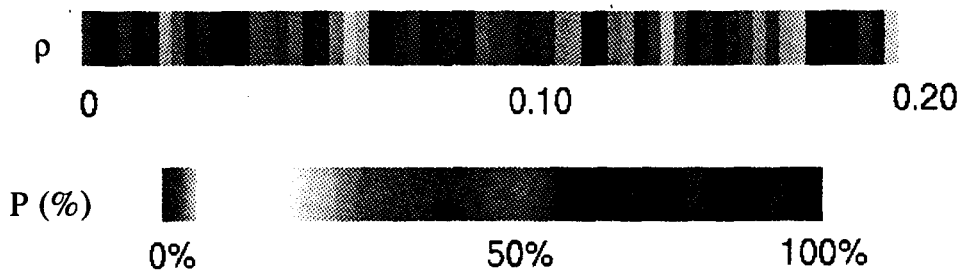
b) Mesures du taux de polarisation



c) Simulations de la réflectance



d) Simulations du taux de polarisation



-16- Mesures en réflectance (a) et en taux de polarisation (b) à 450 nm. Restitution de la réflectance (c) et du taux de polarisation (d) avec l'indice de réfraction  $m = 1.33$  et en tenant compte de la réflexion propre de l'eau de mer ( voir texte).

## CONCLUSION

Dans le présent travail, j'ai montré l'intérêt de la polarisation pour la caractérisation des aérosols en présentant différents résultats expérimentaux.

Dans le cadre des vérités-terrain réalisées avec la station-sol du Laboratoire, les mesures de polarisation du rayonnement diffus complètent celles de transmission et d'auréole en permettant d'accéder à l'indice de réfraction des particules, comme nous l'avons montré sur différentes situations (la Crau, Tromelin ). L'étude est à étendre aux aérosols désertiques qui ne sont plus tout à fait sphériques et dont la dimension moyenne est plus grande.

Les expériences effectuées depuis ballon stratosphérique (PIRAT) et la Navette Spatiale ont prouvé la possibilité d'observer les aérosols depuis l'espace au-dessus de l'océan et ont souligné l'intérêt des visées directionnelles aussi bien en réflectance qu'en polarisation. Ces possibilités d'analyse directionnelle et en polarisation, complément des informations spectrales, constituent la spécificité de l'instrument POLDER: nous avons présenté les objectifs de la mission spatiale et des résultats acquis grâce aux mesures de polarisation durant les campagnes aéroportées du simulateur POLDER. De telles mesures permettent en particulier d'évaluer l'altitude du sommet des nuages et de préciser leur phase, liquide ou non. Au-dessus des océans, les premières analyses montrent qualitativement l'intérêt de la polarisation pour accéder à l'indice de réfraction: un travail important reste à faire pour affiner le modèle d'aérosols. Un résultat très intéressant a été obtenu au-dessus des terres émergées où il devient possible, grâce à la polarisation, de séparer les contributions du sol et de l'atmosphère.

La détermination des aérosols depuis l'espace est un objectif important de la mission POLDER tout d'abord pour le suivi et la caractérisation de ces aérosols (sources, nature, transport...) et ensuite pour les corrections atmosphériques qui conditionneront la qualité des produits de surface tels la réflectance propre de l'eau ou des sols. L'amélioration escomptée de ces produits devrait permettre un meilleur suivi spatio-temporel des productions primaires océanique et terrestre.

L'obtention des produits POLDER nécessite la mise au point d'algorithmes de traitement qui seront implantés dans le segment-sol. Je participe actuellement au développement des algorithmes concernant les aérosols et les corrections atmosphériques: ce travail sera poursuivi dans l'avenir et partiellement validé sur les campagnes aéroportées dont le dépouillement continue. L'étape suivante sera de préparer et d'effectuer la validation des différents produits après le lancement. Enfin des programmes plus généraux restent à définir pour utiliser et exploiter les produits POLDER dans des analyses géophysiques globales.

## Bibliographie

- 1- Lyot, B., 1929: Recherches sur la polarisation de la lumière des planètes et de quelques substances terrestres. Ann. Observ. Paris (Meudon), 8, 161pp.
- 2a- Dollfus, A., 1968: Synthesis on the ultraviolet survey of clouds in Venus' atmosphere; The atmospheres of Venus and Mars, J.C. Brandt and M.E. McElroy, Eds, New York, Gordon and Breach, 133-146.
- 2b- Dollfus, A., and D.L. Coffeen, 1970: Polarization of Venus. I. Disk observations. Astron. Astrophys , 8, 251-266.
- 3- Lord Rayleigh. 1881: Phil. Mag., 12, 81. Sci. Papers.
- 4- Mie, G., 1908: Beiträge zur Optik Trüber Medien, speziell kolloidaler Metallösungen. Ann. Phys., 25, 377-445.
- 5- Chandrasekhar, S., 1950: Radiative Transfer. London, Oxford University Press.
- 6- Lenoble, J, 1985: Radiative transfer in scattering and absorbing atmospheres: Standard computational procedures. Deepak. Hampton.
- 7- Deuzé, J.L., 1974: Etude de la polarisation du rayonnement par les milieux diffusants. Application à la polarisation localisée de Vénus. Thèse de 3ème cycle. Université de Lille. France.
- 8- Hansen, J.E., and J.W. Hovenier: Interpretation of the polarization of Venus. J. Atmos. Sci., 31, 1137-1160.
- 9- Santer, R, 1984: Caractérisation des aérosols à partir de la polarisation du rayonnement solaire diffusé. Application aux atmosphères de la Terre, de Vénus et de Saturne. Thèse d'état. Université de Lille. France.
- 10- Deschamps P.Y, M. Viollier. 1987. Algorithm for ocean color from space and applications to CZCS data. Adv. Space Res. 7, (2),11-19.
- 11- Tanré D., M. Herman, P.Y. Deschamps, A. de Leffe. 1979: Atmospheric modeling for space measurements of ground reflectances, including bidirectional properties. Appl. Optics, 18,21, 3587-3594.
- 12- Tanré D., C. Deroo, P; Duhaut et al. 1990: Description of a computer code to simulate the satellite signal in the solar spectrum: The 5S code. Int. J. Remote Sens. 11: 659-668.
- 13- Santer R., J.L. Deuzé, C. Devaux, E. Vermote, G. Guyot, X. Gu, M. Verbrugghe. 1990. Etalonnage de HRV (SPOT1) sur le site de La Crau. Contrat CNES 883/CNES/89/5935/00.
- 14- Rondeaux G. 1990: Polarisation de la lumière réfléchie par un couvert végétal. Thèse de doctorat. Université de Paris VII. France.
- 15- Deuzé, J.L., M.. Herman, R. Santer. 1989  
Modélisation de l'état de polarisation du rayonnement atmosphérique ascendant:  
partie 1. Atmosphère limitée par un sol lambertien.  
partie 2: Atmosphère limitée par un océan agité.  
partie 3: Atmosphère limitée par un sol polarisant.  
Contrat 833/CNES/87/4689/00

- 16- Vermote E., M. Herman, P.Y. Deschamps, J.L. Deuzé, R. Santer. 1990: Polarization Assessment for MERIS. ESA Contract 110237.
- 17- Roger J.C., R. Santer, M. Herman, J.L. Deuzé. 1990: Analyse des images en lumière polarisée prises depuis la navette spatiale américaine. Contrat CNES 833/CNES/88/5527/00.
- 18- Deuzé J.L. et M.Herman. 1990: Simulations des observations de POLDER. Détection des aérosols: étude de faisabilité. Contrat CNES 836/89/5994/00.
- 19- El Tahan F. 1991: Analyse du rayonnement du ciel mesuré par l'instrument POLDER. Rapport de D.E.A.. Université de Lille. France.
- 20- Toubbé B. 1992: Inter-étalonnage des canaux POLDER à partir de la tache du glitter. Rapport de D.E.A.. Université de Lille. France.
- 21- Goloub P.. 1992: Modèle radiométrique du polarimètre imageur grand champ POLDER. Analyses des observations en lumière polarisée. Thèse de l'Université des Sciences de Lille. France.
- 22- Devaux C., M. Herman, R. Santer, D. Tanré. 1988: On the complementarity of the solar transmission and aureole measurements to derive the aerosol size distribution: Application to desert aerosol characteristics retrievals. International Radiation Symposium. Lille. France. pp 557-560.
- 23- Fen, R.W., S.A. Clough, W.O. Gallery et al.. 1985: Optical and infrared properties of the atmosphere, Handbook Geophys. 18(9) 18-25.
- 24- Santer R., Herman M., Tanre D., Lenoble J. 1988: Characterisation of stratospheric aerosol from polarization measurements. J.G.R., 93, D1,14209-14221.
- 25- Cox, C., and W.H. Munk. 1954: The measurement of the roughness of the sea surface from photographs of the sun glitter. J. Opt. Soc. Am. 44, 838-850.
- 26- M. Herman, J.L. Deuze, P. Goloub. 1991. Etalonnage du prototype POLDER: analyse de l'optique. Rapport interne POL-LOA-MOR-300-01
- 27- P. Goloub, J.L. Deuze, M. Herman. 1992. POLDER Interband Calibration, using the sunglint. Rapport interne POL-LOA-BET-301-01.
- 28- Deuzé J.L., J.Y. Balois, C. Devaux, L. Gonzalez, M. Herman, P. Lecomte, C. Verwaerde. 1991: Aircraft simulations of the POLDER experiment: First results. ISPRS meeting. Courchevel. France.
- 29- Deuzé J.L., P. Goloub, M. Herman, R. Frouin. 1992: Retrieval of aerosols over the Gerlache Strait from aircraft polarimetric observations. Antarctic Journal of U.S. In press.

Reprinted from JOURNAL OF APPLIED METEOROLOGY, Vol. 27, No. 5, May 1988  
American Meteorological Society

**Saharan Aerosols over the South of France: Characterization Derived from Satellite Data  
and Ground Based Measurements**

J. L. DEUZE, C. DEVAUX, M. HERMAN, R. SANTER AND D. TANRE

## Saharan Aerosols over the South of France: Characterization Derived from Satellite Data and Ground Based Measurements

J. L. DEUZE, C. DEVAUX, M. HERMAN, R. SANTER AND D. TANRE

*Laboratoire d'Optique Atmosphérique, Université des Sciences et Techniques de Lille, France*

20 May 1987 and 28 September 1987

### ABSTRACT

In July 1983, the summer transport of Saharan aerosols across the Mediterranean Sea was observed. The dust cloud was particularly dense and was clearly detected in A.V.H.R.R. and METEOSAT imageries. Optical thicknesses and Angström coefficients have been derived from these pictures. During the same period, ground based observations—transmission, aureole and polarization measurements—were performed at the Observatoire de Haute Provence (southeast of France). Measured aerosol optical thicknesses at 550 nm were as large as about 1.5.

The optical thicknesses and Angström coefficients derived from the two experiments are compared and are in good agreement.

### 1. Introduction

In summertime, westward migrations of saharan dust clouds over the tropical North Atlantic Ocean are commonly observed from satellite imagery. Local and time variations of the dust have been described by Carlson and Prospero (1972). The aerosol optical thickness has been derived from satellite data in the visible range (Carlson et al. 1977; Norton et al. 1980; Griggs 1979; Koepke and Quenzel 1979). The integrated mass of dust was obtained by Fraser (1976). Dust outbreaks have also been observed over the eastern Mediterranean Sea by Mekler et al. (1977) and Otterman et al. (1982). These dust clouds have also appeared during nighttime in the METEOSAT IR channel (Legrand et al. 1985).

During July 1983, ground based measurements were planned at the O.H.P. ("Observatoire de Haute Provence", about 80 km from the mediterranean coast with an altitude of 1900 m) in order to observe the El Chichon stratospheric layer. This objective was disturbed by the occurrence of a saharan dust outbreak, which provided the opportunity to characterize this dust cloud from ground measurements.

This event was looked for in the AVHRR (on NOAA-7) and METEOSAT imageries over the Mediterranean Sea. Thus, we have the interesting possibility of comparing aerosol characterization derived from satellite imagery with a more detailed characterization derived from ground observations. We will show that

the aerosol thickness ( $\tau_a$ ) and the Angström coefficient deduced from satellite data are in good agreement with the ground measurements.

### 2. The ground based measurements

#### *a. Presentation of the measurements, from 26 July to 29 July 1983*

Extinction measurements were performed with two multispectral radiometers. The first one has a silicium detector and covers the range from 440 to 1100 nm; the second has a PbS detector, and performs measurements up to 3000 nm. The two radiometers had been previously calibrated, (April 1983), using Langley plots. The seven band measurements are centered at 445, 551, 648, 864, 1040, 1586 and 2208 nm.

In the wavelength range of our band measurements, water vapor and ozone absorption is simply a corrective term. This gaseous absorption was merely computed from LOWTRAN-5 code (Kneizys et al. 1980), by using the climatologic value of London et al. (1976) for the ozone content, and the midlatitude summer model of Mc Clatchey et al. (1970) for the water vapor content. The Rayleigh optical thickness was estimated from the pressure measurements. By subtracting Rayleigh scattering and gaseous absorption components from the total optical thickness, we obtained the aerosol optical thickness  $\tau_a$ . Figure 1 gives  $\tau_a$  versus the UTC time, at  $\lambda = 550$  nm, for the 4 observation days. On the morning of 26 July, the aerosol content was almost constant and Langley plots drawn from these data confirmed the previous calibration. Despite the high altitude of the site (1900 m),  $\tau_a$  was always very large, with a maximum of 1.7 on 27 July, which is quite an un-

*Corresponding author address:* Dr. J. L. Deuze, Laboratoire D'Optique Atmosphérique, Université Des Sciences Et Techniques De Lille, 59655 Villeneuve D'Ascq Cedex, France.

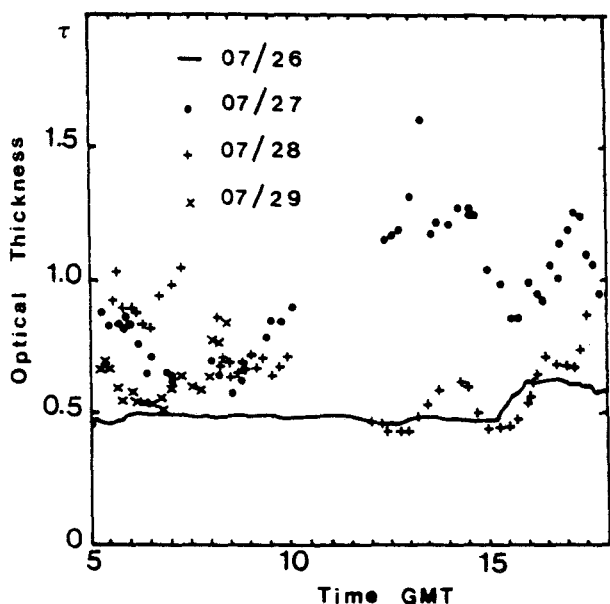


FIG. 1. Instantaneous aerosol optical thickness  $\tau_a$ , at 550 nm, for the 4 days. A full line has been drawn through the smooth measurements obtained on 26 July. The symbols for other days are included on the figure. It was initially planned that the traditional Langley technique would be used to derive  $\tau_a$ , so that no extinction measurements were performed around noon, when the air mass did not vary; this explains the lack of information, from 1000 to 1300 UTC, in Fig. 1.

usual value. Note that it is unlikely that cirrus clouds could explain these large values of  $\tau_a$ . The sky was routinely observed around the sun disk, using cross-

polaroids in order to attenuate the sun irradiance, and no cirrus clouds were observed during the campaign.

The spectral dependence of the aerosol optical thickness,  $\tau_a(\lambda)$ , proved to be nearly constant for a given day, but exhibited large variations from day to day. Figure 2 shows the  $\tau_a(\lambda)$  behavior observed for the 4 days. On 27 July, the aerosol optical thickness increased largely in the blue range. For the other days, the spectral variation was more flat, mainly on 29 July where the optical thickness was almost constant in the visible range, and decreased slowly at near-IR wavelengths. Figure 2 shows that, through the large investigated spectral range, the  $\tau_a(\lambda)$  behavior could not be accounted for with a single Angström coefficient. Therefore, the log-log plots of  $\tau_a(\lambda)$  versus  $\lambda$ , in Fig. 2, were crudely fitted by two linear laws, from 445 to 668 nm and from 668 to 1650 nm, thus providing two Angström coefficients, hereafter noted  $\alpha_v$  and  $\alpha_{IR}$ , respectively. In Table 1, we reported for the 4 days the values obtained for  $\alpha_v$  and  $\alpha_{IR}$ . The large value of  $\alpha_v$  proves the presence of small particles on 29 July, whereas larger particles were predominant on 29 July. The mean deviations  $\Delta\alpha_v$  (or  $\Delta\alpha_{IR}$ ) (see Table 1) showed fairly good stability of the aerosol size distribution for a given day, as noted previously. Deviations of the Angström coefficients were somewhat larger in near-IR than in the visible, as a result of the larger measurement errors.

Aureole measurements were performed at  $\lambda = 850$  nm, using a silicium detector with an aperture angle of  $1^\circ$ . About 5 min were needed to scan scattering angles from  $2^\circ$  to  $30^\circ$ ; the observations were performed

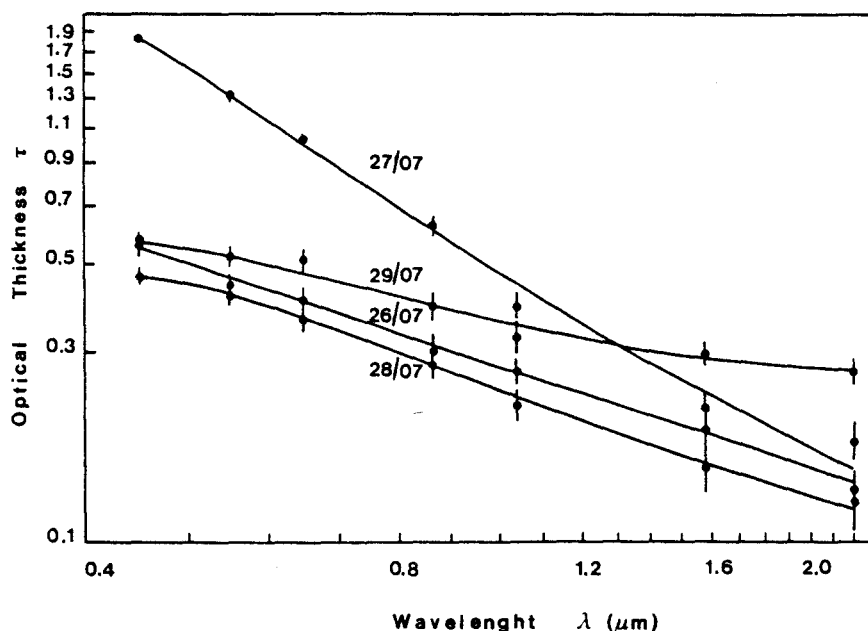


FIG. 2. Aerosol optical thickness as a function of the wavelength for the 4 days. The circles correspond to the measurements, and bars indicate the estimated errors. The solid lines represent the optical thickness spectral dependence computed with the retrieved size distribution.

TABLE 1. Summary of the ground-based measurements (see text):  $P_{\max}$ , maximum value of the polarization ratio, and  $\rho(\theta)$ , particle phase function.

Variable	26 July	27 July	28 July	29 July
$\alpha_v$	0.70	1.42	0.46	0.18
$\alpha_{IR}$	1.24	2.06	0.91	0.63
$\Delta\alpha_v$	0.01	0.02	0.02	0.01
$\Delta\alpha_{IR}$	0.07	0.08	0.06	0.08
$P_{\max}$ 850 nm	22	51	/	18
$P_{\max}$ 1650 nm	16	41	/	18
$\rho(2^\circ)/\rho(10^\circ)$	4.39	/	6.32	7.91

in the amulcantar region, and corrections for multiple scattering were applied, according to Weinman et al. (1975), using the optical thickness measured during the scan.

Unfortunately, the aureole metre rotation speed was subject to large uncertainties due to high wind speeds during the observations. Although the measurements are only indicative, the increase of the forward scattering from 26 to 29 July (see Table 1) is well correlated with the Angström coefficient variation, and confirms the presence of larger particles on 29 July.

Finally, polarization measurements were performed

at near-infrared wavelengths (850 and 1650 nm). The polarimeter scanned the sun incident plane, at low solar elevations to reach backscattering directions. The polarization ratios are reported in Fig. 3, versus the scattering angle. On 27 July, a large contamination by small particles was made evident by the large polarization ratios, whereas both the measurements on 26 and 29 July corresponded to larger particles. Thus, polarization measurements were consistent with the extinction and aureole measurements.

#### b. Interpretation of the measurements

The aerosol size distribution was retrieved from the optical thicknesses measured in the seven channels, from 445 to 2208 nm, by using the constrained linear inversion scheme developed by King et al. (1978). Six classes of abundance were derived, within the range 0.1–4  $\mu\text{m}$  for 26 and 27 July, and within the range 0.15–6  $\mu\text{m}$  for the 2 last days, to take into account the increase of the large particles. According to the estimates of Patterson et al. (1977), the real part of the refractive index of desert aerosols lies in about 1.55. Desert aerosols are absorbing (WMO 1986), but the imaginary part of their refractive index is probably no more than

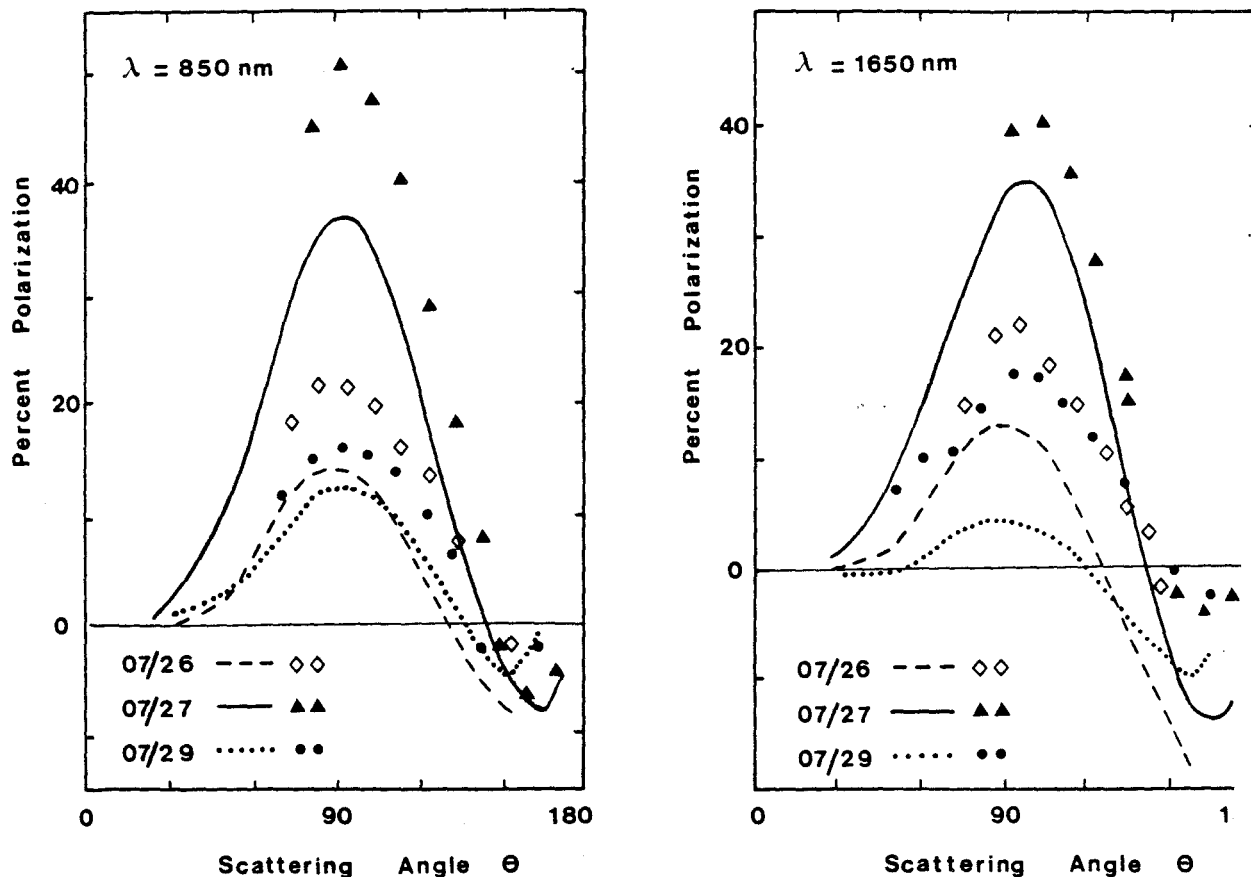


FIG. 3. Percent of polarization as a function of the scattering angle at two wavelengths (850 and 1650 nm) for 3 days (26, 27 and 29 July). The symbols correspond to the measurements, the solid lines to the theoretical computations.

0.005 (Fouquart et al. 1986). Mie calculations prove that so slight an absorption has negligible effect on the spectral dependence of  $\tau_a(\lambda)$  and on the polarization ratio for single scattering (Santer 1984), and the inversion was run for an assumed real refractive index,  $m = 1.55$ .

The results are reported in Fig. 4. The vertical scale applies to the results for 29 July (uppermost curve), and the curves for the other days have been successively displaced downward by a factor of 10 to avoid confusing superposition of the plots. From 26 to 27 July, the particle abundance in the first class increased by one order of magnitude. The large optical thicknesses observed on 27 July thus corresponded to a large addition of small particles of about  $0.1 \mu\text{m}$  radius. The size distributions were quite similar on 26 and 28 July. On 29 July, Fig. 4 shows the occurrence of a bimodal structure of the aerosol size distribution.

As noted previously, the poor quality of the aureole measurements prevents quantitative analysis of these

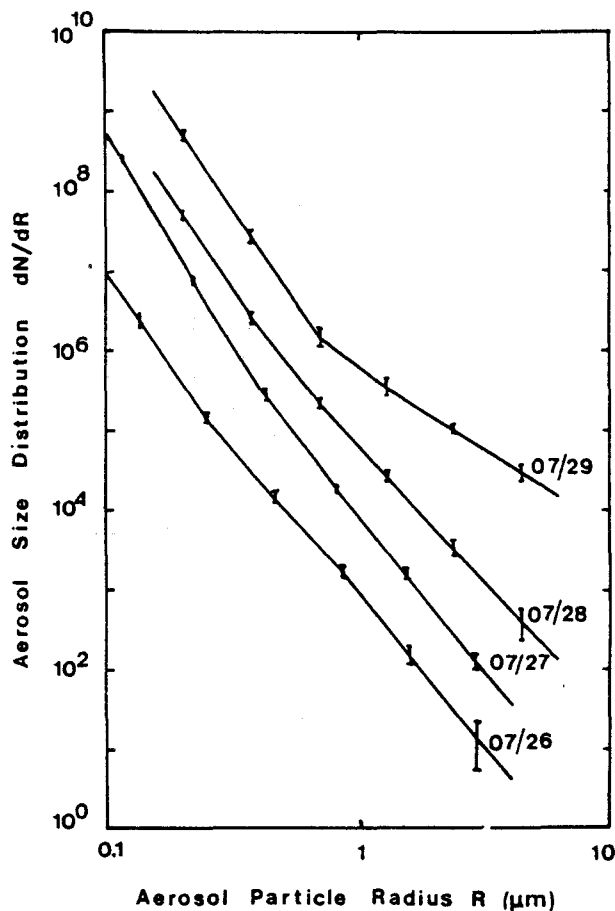


FIG. 4. Aerosol size distributions inverted from the aerosol spectral optical thickness,  $\tau_a(\lambda)$ . The date is labeled for each curve. The vertical scale applies to the results of 29 July (uppermost curve), and the curves corresponding to the other days have been successively translated downward by a factor of 10. The error bars correspond to the errors on  $n(r)$  resulting, in the inversion method, from the experimental errors on  $\tau_a(\lambda)$  (error bars in Fig. 2).

data. On the other hand, the polarimeter was operated for the first time on this occasion and the polarization data deserve some caution. Nevertheless, they have been compared tentatively with the transmission measurements as follows.

Radiative transfer calculations for polarized light were performed for atmosphere models including the appropriate Rayleigh scattering and ground reflectance, and the aerosol component derived from the transmission measurement. The ground-based station was set up in a mountain site with a patchy landscape of bare soils, rocks and meadows, whose mean reflectance was estimated to be about 0.2. As a matter of fact, polarization measurements were performed with low solar elevations, and, thus, with low ground illuminations, so that large inaccuracy in the ground reflectance would have very small influence on the calculated polarization of the sky light. For the aerosol component, the size distribution was fixed according to Fig. 4, the optical thickness was fixed according to the  $\tau_a(\lambda)$  measurements performed during the polarimeter scanning and we considered conservative particles. The computed polarization ratios have been reported in Fig. 3 to be compared with the measurements.

The agreement is not at all perfect, and large discrepancies appear, both near the polarization maxima and in backward scattering directions. In fact, by slightly modifying either the particle refractive index or the particle size distribution (particularly, by extrapolating differently  $n(r)$  outside the radius range,  $0.1 \mu\text{m} - 4 \mu\text{m}$ , in Fig. 4), the observations may be matched more closely in Fig. 3. Such improvements, however, are questionable and raise difficult problems which are beyond the scope of this paper. On the other hand, despite their defects, the predicted polarization ratios are very consistent with the main observed features, especially concerning the time variations and the small particle event on 27 July, and this semiquantitative agreement is encouraging.

Although the aureole and polarization measurements performed during the experiment were very preliminary and were only partly successful, they look promising. Such observations may certainly complement transmission measurement for aerosol characterization. Concerning the main objective of this paper, i.e., the ground validation of satellite observations, the consistency of the whole set of measurements gives an improved confidence in the optical thickness determination.

There may be different explanations, including differences in the source region, for the observed variations of the aerosol characteristics. But, even for a given source area (probably around Chad lake, at this period), the aerosol size distribution may change in connection with the importance of the dust storm. During the ECLATS field experiment, Fouquart et al. (1987) pointed out a clear correlation between the aerosol abundance and their size distribution, with an unexpected amount of small particles for the most turbid

days. We note that this is in accordance with the present observations corresponding to the 27 July event.

### 3. Satellite data

Desert aerosols are known to be a climatic parameter and it seems valuable to obtain their spatial and time variations at climatic scales in order to include these data in general circulation models. It seems interesting to derive these informations from B2 METEOSAT products, which have been set up to support the International Satellite Cloud Climatology Project (ISCCP). The B2 data are sampled at 3-h intervals and the spatial resolution is  $30 \text{ km} \times 30 \text{ km}$ . We are developing an algorithm in order to detect dust storms over oceans and estimate their optical thickness from such imagery. This algorithm was applied to the METEOSAT data for 27 July over the Mediterranean Sea. Moreover, as AVHRR images were available for 29 July over the same area, we derived the dust Angström

coefficient from these AVHRR data. They are in a good agreement with the ground based measurements.

#### a. METEOSAT imagery

The problem is to deduce a quantitative estimate of the aerosol loading from satellite pictures. That is easy over ocean surfaces for cloudless conditions, since the atmospheric radiance then depends mainly on the aerosol optical thickness.

By chance no clouds appeared in the METEOSAT imagery of 27 July, so that we were able to localize easily the dust cloud in the pictures. As an example Fig. 5 displays the METEOSAT picture of 1130 UTC. The figure corresponds to the full resolution of the B2 data, with every pixel labeled according to its digital count, as indicated. The picture looks very clear; Sardinia, Corsica, Sicilia and the entire coastal areas are clearly recognizable. However, from the coasts towards a maximum located west of Sardinia, the reflectance



FIG. 5. The figure shows the METEOSAT picture of 27 July at 1130 UTC, over the Mediterranean Sea. Every B2 pixel has been displayed, with different label according to its digital count. The W label corresponds to a digital count larger than 60, and no label corresponds to a digital count smaller than 20 (clear sky). The coasts are well recognizable and no cloud structure appear with sharp edges and large reflectances. The reflectance behavior in the middle of the picture indicates the large and smooth saharan dust cloud.

increases weakly but distinctly. The smoothness and the weakness of the reflectance behavior clearly does not correspond to a cloud structure, but to a dust haze. Therefore, any pixel over the sea which had a digital count (CN) equal or greater than 20 (for the 8-bit-count; i.e., two times the radiance corresponding to the molecular scattering and the mean ocean reflectance) was selected and was considered as corresponding to the aerosol cloud.

The above treatment provided localization of the dust cloud. In order to quantify the phenomena, we first converted digital counts to radiance values, by using the calibration coefficients given by Koepke (1982). Then we corrected these radiances from the Rayleigh scattering contribution and from the gaseous atmosphere effect, by assuming the same previous atmosphere model. Finally, the optical thickness  $\tau_a$  was derived from these corrected radiances  $L_a$ . Here,  $L_a$  mainly correspond to single scattered radiation and provide with a good accuracy

$$\tau_a = \frac{4\pi\mu_v L_a}{p_a(\theta)E_0} \quad (1)$$

as shown by Deschamps et al. (1983). In Eq. (1),  $E_0$  is the solar irradiance,  $\theta$  the scattering angle,  $\mu_v = \cos\theta_v$  the cosine of the viewing direction, and  $p_a(\theta)$  the aerosol phase function, which was computed from the desert aerosol model defined by the international radiation commission (WMO 1986).

The above procedure was applied to the METEOSAT pictures of 27 July. The spatial distributions of the aerosol optical thickness derived for the three pictures (0830, 1130 and 1430 UTC) have been drawn in Fig. 6. We have drawn optical depths isolines for  $\tau = 0.5, 1.0$  and  $1.5$ . Each picture provides a well-defined geographical repartition of the cloud. The cloud evolution from one picture to the next is very coherent, and the time evolution is consistent with the wind speed ( $20 \text{ km h}^{-1}$ ) measured at the Meteorological Office of Nimes-Courbessac. The cloud observed at 0830 UTC is retrieved in the two other scenes (1130 and 1430 UTC) at distances consistent with this speed. Moreover, we selected a fixed point, P, over the sea, located about 120 km south from the OHP; P is marked by a cross in the maps of Fig. 5. The time evolution of the optical thicknesses observed, respectively over this point P from METEOSAT and over the OHP from the ground measurements, are compared in Fig. 7. The two measurements are very consistent since the cloud takes 6 hours to reach the OHP, with respect to the overpass pixel hour.

#### b. AVHRR imagery

A visible spectral study from AVHRR on NOAA-7 has also been completed. The study was used to obtain an idea of the type of particles through the Angström coefficient. The polar orbiting satellite, named "NOAA series", contains the Advanced Very High Resolution Radiometer (AVHRR) which includes two visible and

three infrared channels. We considered only the 0.55–0.90 and 0.725–1.10  $\mu\text{m}$  visible channels (Malila and Anderson 1986).

Unfortunately, during the dust event, we only had data for 29 July; the data for 26 and 27 July were not available and those for 28 July were very contaminated by the glitter effect. By the same method as for the METEOSAT study, we derived the aerosol reflectance by correcting data for Rayleigh and gaseous effects.

From these two reflectances,  $\rho_a(\lambda_1)$  and  $\rho_a(\lambda_2)$ , we inferred an Angström coefficient  $\alpha_a$ :

$$\alpha_a = -\frac{\log(\rho_a(\lambda_1)/\rho_a(\lambda_2))}{\log(\lambda_1/\lambda_2)} \quad (2)$$

In Eq. (2),  $\lambda_1$  and  $\lambda_2$  are the centroid wavelengths  $\lambda_C$  defined by

$$\lambda_C = \frac{\int_0^\infty \lambda E_0(\lambda)R(\lambda)d\lambda}{\int_0^\infty E_0(\lambda)R(\lambda)d\lambda} \quad (3)$$

where  $R(\lambda)$  is the spectral response of the sensor. Therefore, for NOAA-7,  $\lambda_1 = 633 \text{ nm}$  and  $\lambda_2 = 848 \text{ nm}$ .

The order of magnitude of  $\alpha_a$  retrieved by this method is  $\alpha_a = 0.57$ . This small value confirms the

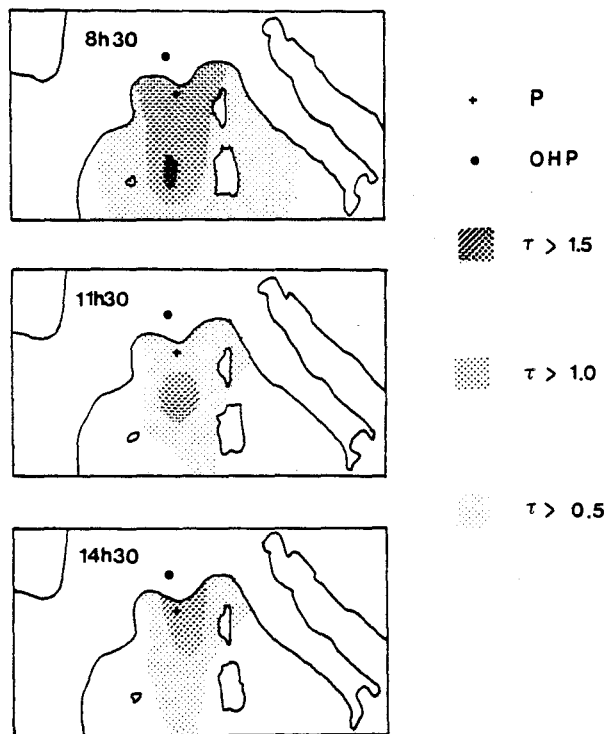


FIG. 6. Maps of the aerosol cloud over the Mediterranean Sea retrieved from METEOSAT data for 0830, 1130 and 1430 UTC. The dust outbreak maximum is observed on the first map, where the area located west of Sardinia presents optical thicknesses larger than 1.5. The importance of the dust outbreak decreases slightly all along the day, but the main features of the optical thickness isolines are similar from map to map, with a motion towards the North.

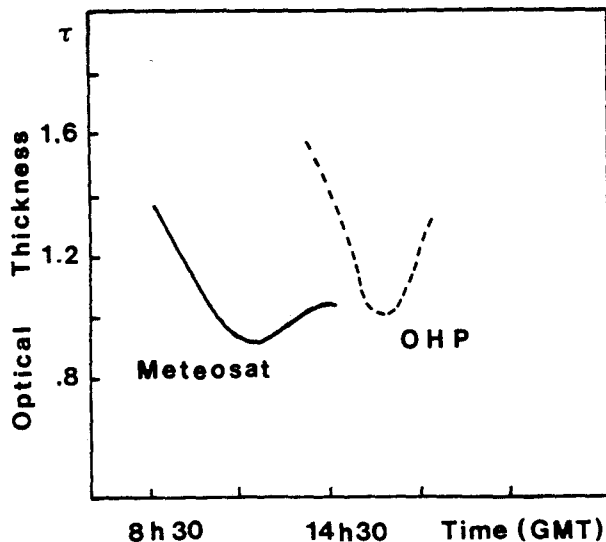


FIG. 7. Time evolution of the aerosol optical thickness derived from METEOSAT data at point P (solid line), and measured at the OHP (dashed line), on 27 July. The curve "METEOSAT" was roughly interpolated from the values of  $\tau_a$  at P, at 0830, 1130 and 1430 UTC, derived from the maps in Fig. 5. The curve "OHP" was interpolated from the  $\tau_a$  measurements (Fig. 1) performed at the OHP from 1330 to 1730 UTC. The two curves are consistent, taking into account the 6 h needed for the dust cloud to go from P to the OHP, a distance of about 120 km according to the observed wind speed of  $20 \text{ km h}^{-1}$ .

presence of large particles and is close to the value derived from the ground measurements. The  $\tau_a(\lambda)$  measurements reported in Fig. 2 for 29 July at 648 and 864 nm (i.e., quite near from the AVHRR centroid wavelengths) provide an Angström coefficient  $\alpha_a = 0.66$  (close to the  $\alpha_{IR}$  figure reported in Table 1). The good agreement between the two estimates indicates that  $\alpha_a$  might be deduced from AVHRR data and could provide some information on the particle dimension evolution.

#### 4. Conclusion

A dust cloud was observed with a photometric station from the ground, and, simultaneously, from two satellite imageries (METEOSAT and AVHRR). The optical thicknesses derived from the two experiments (ground and METEOSAT data) lead to good agreement. The Angström coefficient derived from the AVHRR data seems valid. It indicates a large mode of particles, also observed at the ground station. The METEOSAT B2 data allowed the dust outbreak to be seen and, also, the aerosol mass to be quantified by an estimation of the optical thickness. A climatology of Saharan dust using METEOSAT B2 data at climatic scales is now being developed.

*Acknowledgments.* This work was partly supported by the "Centre National de la Recherche Scientifique" (CNRS) and by the "Centre National d'Etudes Spatiales" (CNES).

#### REFERENCES

- Carlson, T. N., and J. M. Prospero, 1972: The large scale movements of Saharan air outbreaks over the equatorial North Atlantic. *J. Appl. Meteor.* **11**, 289-297.
- , and P. Wendling, 1977: Reflected radiance measured by NOAA 3 AVHRR as a function of optical depth for Saharan dust. *J. Appl. Meteor.* **16**, 1368-1371.
- Deschamps, P. Y., M. Herman and D. Tanré, 1983: Modeling of the atmospheric effects, and its application to the remote sensing of ocean color. *Appl. Opt.* **22**, 3751-3758.
- Fouquart, Y., B. Bonnel, M. Chaoui Roquai, R. Santer and A. Cerf, 1987: Observation of Saharan aerosols: results of ECLATS field experiment, Part I: Optical properties and aerosol size distributions. *J. Climate Appl. Meteor.* **26**, 28-37.
- Fraser, R. S., 1976: Satellite measurements of mass of Saharan dust in the atmosphere. *Appl. Opt.* **15**, 2471-2479.
- Griggs, M., 1979: Satellite observations of atmospheric aerosols during the EOMET Cruise. *J. Atmos. Sci.* **36**, 695-698.
- Herman, M., J. Y. Balois, L. Gonzalez, P. Lecomte, J. Lenoble, R. Santer and C. Verwaerde, 1986: Stratospheric aerosol observations from a balloon-borne polarimetric experiment. *Appl. Opt.* **25**, 3573-3584.
- King, M. D., D. M. Byrne, B. M. Herman and J. A. Reagan, 1978: Aerosol size distribution obtained by inversion of spectral optical depth measurements. *J. Atmos. Sci.* **35**, 2153-2167.
- Kneizys, F. Y., E. P. Shettle, W. O. Gallery, J. H. Chetwind, Jr., L. W. Abren, J. E. A. Selby, R. W. Fenn and R. A. Mc Clatchey, 1980: Atmospheric transmittance/radiance: Computer code LOWTRAN 5, Rep. AFGL-TR-80-0067, 233 pp.
- Koepke, P., 1982: Calibration of the vis-channel of Meteosat-2. *Adv. Space Res.* **2**, 93-96.
- , and H. Quenzel, 1979: Turbidity of the atmosphere determined from satellite: Calculation of optimum viewing geometry. *J. Geophys. Res.* **84**, 7847-7856.
- Legrand, M., J. J. Bertrand and M. Desbois, 1985: Dust clouds over West Africa: A characterization by satellite data. *Ann. Geophys.* **3**, 777-784.
- London, J., R. D. Bojkov, S. Oltmans and J. I. Kelley, 1976: *Atlas of the Global Distribution of Total Ozone July 1957-June 1967*. NCAR Tech. Note, NCAR/TN/113+STR, pp 276.
- Mc Clatchey, R. A., R. W. Fenn, J. E. A. Selby, F. E. Volz and J. S. Garing, 1971: Optical properties of the atmosphere. Rep. AFCRL-71-0279, pp 85.
- Maiika, W. A., and D. M. Anderson, 1986: Satellite data availability and calibration documentation for land surface climatology studies. Contract NAS5-28715, NASA, Goddard Space Flight Center, pp 214.
- Mekler, Y., H. Quenzel, G. Ohring and J. Marcus, 1977: Relative atmospheric aerosol content from ERTS observations. *J. Geophys. Res.* **82**, 967-970.
- Norton, C. C., F. R. Mosher, B. Hinton, D. W. Martin, D. Santek and W. Kuklow, 1980: A model for calculating desert aerosol turbidity over the oceans from geostationary satellite data. *J. Appl. Meteor.* **19**, 633-644.
- Otterman, J., R. S. Fraser and O. P. Bahethi, 1982: Characterization of tropospheric desert aerosols at solar wavelengths by multi-spectral radiometry from Landsat. *J. Geophys. Res.* **82**, 1270-1278.
- Patterson, E. M., D. A. Gillette and B. M. Stockton, 1977: Complex index of refraction between 300 and 700 nm for Saharan aerosols. *J. Geophys. Res.* **82**, 3153-3160.
- Santer, R., 1984: Caractérisation des aérosols à partir de la polarisation du rayonnement solaire diffusé. Application aux atmosphères de la Terre, de Vénus et de Saturne. Thèse de Doctorat es Sciences Physiques. Université des Sciences et Techniques de Lille.
- Weinman, J. A., J. T. Twitty, J. R. Browning and B. M. Herman, 1975: Derivation of phase functions from multiply scattered sunlight transmitted through a hazy atmosphere. *J. Atmos. Sci.* **32**, 577-583.
- World Meteorological Organization, 1986: A preliminary cloudless standard atmosphere for radiation computation. WCP-112, WMO/TD-n°24, pp 53.

## SPOT Calibration at the La Crau Test Site (France)

R. Santer,\* X. F. Gu,<sup>†</sup> G. Guyot,<sup>†</sup> J. L. Deuzé,\* C. Devaux,\*  
E. Vermote,\* and M. Verbrugge<sup>†</sup>

\*Laboratoire d'Optique Atmosphérique, Université de Lille I, Villeneuve d'Ascq, France

<sup>†</sup>INRA Bioclimatologie, Montfavet, France

*In-flight calibrations of SPOT1 were performed in 1989 using a French site located in La Crau (southeastern France). A full description of the procedure is presented which includes both the characterization of the ground and of the atmosphere. To predict the radiance at the satellite level, we take into account the nonlambertian properties of the test site and the surrounding contribution. A detailed error budget is carefully conducted; the overall error of the method is around  $\pm 3\%$ . The three calibrations performed are self-consistent and are in close agreement with calibration data obtained by CNES for XS2 and XS3. A discrepancy of 8% is observed for XS1 and its origin is under study.*

### INTRODUCTION

In France, the National Center for Space Studies (CNES) is highly concerned with the calibration of HRV instruments aboard SPOT. From the preflight calibration (Begni, 1985), two internal calibration devices (Dinguirard and Maisonneuve, 1980), using respectively the Sun and a lamp as

light sources, can be used to follow the sensitivity loss of the system. Moreover, an in-flight calibration has been conducted by Slater's team throughout the lifetime of SPOT1 using the method developed for Landsat TM calibration (Slater et al., 1987). This method combines the measurement of the reflectance of a test site (White Sands in New Mexico or Edward Base in California) with the characterization of the atmosphere at the time of the satellite overpass. Using an atmospheric transfer code, the incoming radiance at the sensor is predicted and compared to digital counts registered over the test site.

For the preparation of SPOT 4 and 5 missions, CNES wished to develop an alternative calibration site in Europe. The choice of the site was the object of a previous investigation divided into two successive steps. From a first study performed on satellite data, several potential sites over Europe and Northern Africa were compared (Rouquet, 1987) and the site at La Crau was selected. Ground-based and airborne reflectance measurements of La Crau enabled us to define the position of the test site and to characterize its bidirectional properties and its spatial and temporal variabilities (Gu et al., 1990).

The aim of this article is to present the results of the last step of the analysis and the results of two SPOT calibration campaigns conducted in 1989 in order to validate the methodologies used.

Address correspondence to Dr. Xing-Fa Gu, INRA Bioclimatologie, BP 91, 84143 Montfavet Cedex, France.

Received 1 March 1992.

## GROUND REFLECTANCE MEASUREMENTS

The calibration site, a  $400 \times 400 \text{ m}^2$  area, is located in the center of "La Crau Seche," a  $60 \text{ km}^2$  flat pebbly area in southeastern France (longitude:  $4.87^\circ\text{E}$ , latitude:  $43.50^\circ\text{N}$ ), on the eastern bank of the Rhone river and about 50 km northwest of Marseille (Gu et al., 1990). This area has a dry and sunny Mediterranean climate. The soil is mainly composed of pebbles and is sparsely covered by a low vegetation. Its optical properties vary little within the year.

A detailed description of the measurement procedure is reported by Gu et al. (1992). SPOT simulation radiometers (Guyot et al., 1984) simultaneously measure the reflected directional radiance and the incident hemispherical irradiance in the SPOT channels. The ground bidirectional reflectance is obtained by ratioing the two measurements and a calibration is done, using a halon panel. Departures of the irradiance head and of the reflectance panel from the cosine law have been measured and the corresponding corrections are introduced in the data reduction (Gu, 1991). The analysis of the sampling variance of the  $400 \text{ m} \times 400 \text{ m}$  test site enabled us to define the number of measurements necessary for obtaining a given accuracy (Dagnelie, 1970). With 100 samples (0.6 m in diameter) the error on the ground reflectance is lower than  $\pm 2\%$  for SPOT Channels 1 (XS1) and 2 (XS2) and lower than  $\pm 1\%$  for Channel 3 (XS3) (Gu et al., 1990). For the direct-direct path, nadir reflectance measurements were performed at the time of satellite overpass (within  $\pm 30$  min). For SPOT off-nadir viewing a correction was applied using a set of bidirectional measurements (Guyot et al., 1989). As these measurements are performed with a mobile boom and are time-consuming, they were restricted to a few samples. In order to reduce the error due to the view angle correction, the future ground-level reflectance measurements will be performed using a new support enabling measurement of the ground radiance with the same geometry as SPOT (Gu et al., 1992).

Two measurement campaigns were performed in March and June 1989. All the available SPOT windows were recorded, and only three dates were used considering the atmospheric conditions: 22 March, 7 and 13 June. For these experimental calibration campaigns, only multispectral images were acquired with the HRV2 instrument.

Table 1 gives the geometrical conditions of the observations. Table 2 reports, for each date, the number of samples, the mean value of the reflectance measured in the SPOT channels, and their standard deviations. It must be pointed out that the number of measurements is limited and the accuracy of the reflectance estimate is reduced as compared to an ideal figure of 400 samples allowing an accuracy better than  $\pm 1\%$  (Gu et al., 1990). For these measurements only one radiometer was available and 100 measurements required about 1 h. Moreover, on 7 June, cloudy conditions occurring before the SPOT overpass reduced this number.

## ATMOSPHERIC MEASUREMENTS

In order to apply the atmospheric corrections, it is necessary to characterize the aerosols and also the amount of gases which absorb and scatter the light in the SPOT bands. The characteristics of the aerosols (size distribution function, spectral optical thickness) and the atmospheric gas transmission are determined from passive optical measurements at ground level and radiosonde data. The Rayleigh scattering due to gas molecules, which depends on atmospheric pressure and wavelength, is deduced from barometric measurements at ground level.

Table 1. Geometric Conditions of the SPOT Observations<sup>a</sup>

Date	Time of Overpass (U.T.)	$\theta_s$ ( $^\circ$ )	$\phi_s$ ( $^\circ$ )	$\theta_v$ ( $^\circ$ )	$\phi_v$ ( $^\circ$ )
22-03	10.42	45.9	156.6	2.7	99
07-06	11.01	22.4	156.4	25.5	279
13-06	10.46	33.8	155.8	3.7	99

<sup>a</sup>  $\theta$  = zenith angle;  $\phi$  = azimuth angle;  $s$  = sun angle;  $v$  = view angle.

Table 2. Mean Reflectances ( $\rho$ ) of la Crau in the Three SPOT-HRV Bands and Their Standard Deviations ( $\sigma$ )<sup>a</sup>

Date	Parameters	XS1	XS2	XS3
22-03	$\rho$	12.3	17.7	29.8
(106)	$\sigma$	1.3	1.8	1.6
07-06	$\rho$	14.2	19.8	27.7
(56)	$\sigma$	1.1	1.4	1.4
13-06	$\rho$	16.0	22.2	30.0
(108)	$\sigma$	1.1	1.3	1.1

<sup>a</sup> The number of measurements is indicated in parentheses under the date.

## Description of the Measurements

Different radiometers measure the extinction of the solar beam in the range 0.45–2.2  $\mu\text{m}$ . A single wavelength radiometer (at 450 nm) (ETAL) was calibrated on the extraterrestrial irradiance during stratospheric flights at an altitude higher than 25 km. The other radiometers are cross-calibrated directly in the blue band. For the other channels, the calibration is initialized using the classical Langley–Bouguer plotting with a linear regression on the logarithm of the radiometer output voltage  $V(\lambda)$  and the air mass  $M$ :

$$\log V(\lambda) = \log V_s(\lambda) - \delta(\lambda)M. \quad (1)$$

Equation (1) provides the intercept  $V_s(\lambda)$  and the slope  $\delta(\lambda)$  corresponding to the total atmospheric optical thickness. It is well known that the stability of the atmosphere, required for this method, is a first approximation. The suggested improvement consists in monitoring the variation of the optical thickness as a function of the time  $t$  (from the Langley plot) with the assumption that it is mainly due to variations of the aerosol optical thickness,  $\delta_a(t)$ . We then obtain

$$\frac{\Delta\delta_a(t,\lambda)}{\delta_a(\lambda)} = \frac{\Delta\delta_a(t,450 \text{ nm})}{\delta_a(450 \text{ nm})}. \quad (2)$$

Assuming that the aerosols are stable in nature, the mean value of  $\delta_a$  at  $\lambda$  and 450 nm is derived from the Langley linear regression after removing the Rayleigh contribution. The instantaneous variations of the aerosol optical thickness at 450 nm are measured by the calibrated radiometer ETAL. Plotting of  $\log V(\lambda) + \Delta\delta_a(t,\lambda) \cdot M$  gives a better estimate of  $V_s(\lambda)$  and  $\delta_a(\lambda)$ .

Aureole measurements are also performed at  $\lambda = 850$  nm. The radiometer with  $1^\circ$  field of view initially aims at the Sun. Then a small rotation in azimuth allows collection of measurements in the range of the scattering angle, between  $2^\circ$  and  $30^\circ$ . The diffuse radiance is proportional to the atmosphere phase function from which a first estimate of the aerosol phase function can be deduced. This first estimate is then used to correct for the effect of multiple scattering, using a simple iterative method proposed by Weinman et al. (1975).

The last measurements consist of scans in the principal plane of the radiance and of the polarization ratio. The photopolarimeter described by Herman et al. (1986) has two bands at 850 nm

and 1650 nm in order to minimize the Rayleigh scattering contribution.

## Aerosol Characterization

To apply the atmospheric corrections, the aerosols must be characterized with three parameters: their optical thickness  $\delta_a(\lambda)$ , their size distribution  $n(r)$ , and their refractive index ( $m - ik$ ). The aerosol thickness is the fundamental parameter directly produced by the extinction measurements. The main problem consists in the determination of the last two parameters.

We are not concerned with the actual complexity of the aerosols, by either their composition and or their vertical distribution. We just need a convenient description of the medium which allows us to retrieve the optical properties in order to apply the atmospheric corrections. The aerosol model used corresponds to a "modified" Junge size distribution with

$$\begin{aligned} n(r) &= Cr_0^\nu & \text{if } r \leq r_0, \\ n(r) &= Cr^\nu & \text{if } r > r_0, \end{aligned} \quad (3)$$

and a particle refractive index ( $m - ik$ ) independent of the size.

It is then necessary to define our strategy concerning the inversion. As demonstrated by Santer (1984), the inversion of the polarization and of the radiance at two wavelengths permits retrieval of the main optical properties of the medium. The inversion is conducted as follows: First we use a simple but accurate approximate of the signal (Deuzé et al., 1987), which includes the Rayleigh scattering, the multiple scattering, and a boundary condition, corresponding to a lambertian reflector. Then, for a given refractive index  $m$  and a set of  $r_0$  values, we adjust the polarization ratio at 1650 nm. Finally the 850 nm retrieval provides a unique solution ( $r_0, \nu$ ).

As an example, we give the restitution of polarization measurements (Fig. 1) and the radiance (Fig. 2) performed on 7 June, around 6:00 a.m., when the sun was low. The restitution of the polarization can be achieved regardless of the particle refractive index. To retrieve the polarization ratio around  $\theta = 100^\circ$ , it is necessary to introduce larger particle size when the refractive index decreases. Conversely, the aureole measurements are not sensitive to the refractive index (major contribution of the diffraction) but highly dependent upon the particle size. The comple-

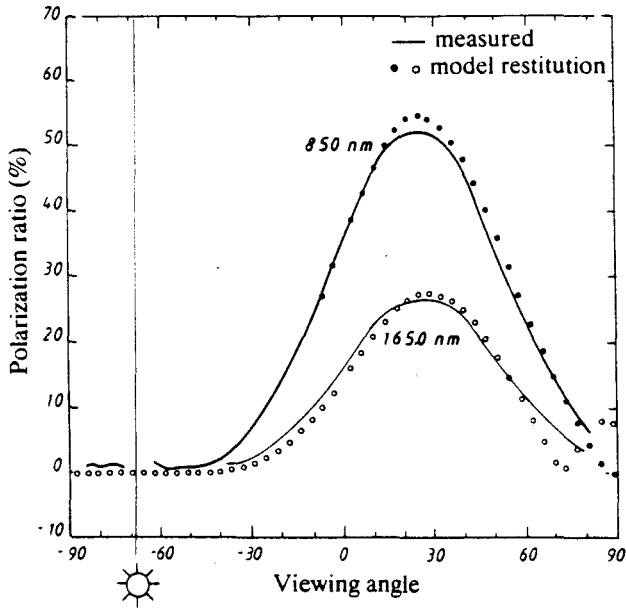


Figure 1. Measured polarization ratio compared to the restitution with an aerosol model defined by  $r_0 = 0.15 \mu\text{m}$ ,  $\nu = -3.7$ ,  $m = 1.50$ , and  $\delta_a^{850} = 0.056$ . The measurements were performed with a low sun at 6:00 a.m. on 7 June 1989.

mentarity between polarization and aureole measurements is illustrated in Figure 3, where a typical value of  $m = 1.50$ , characteristic of continental materials, appears to be suitable.

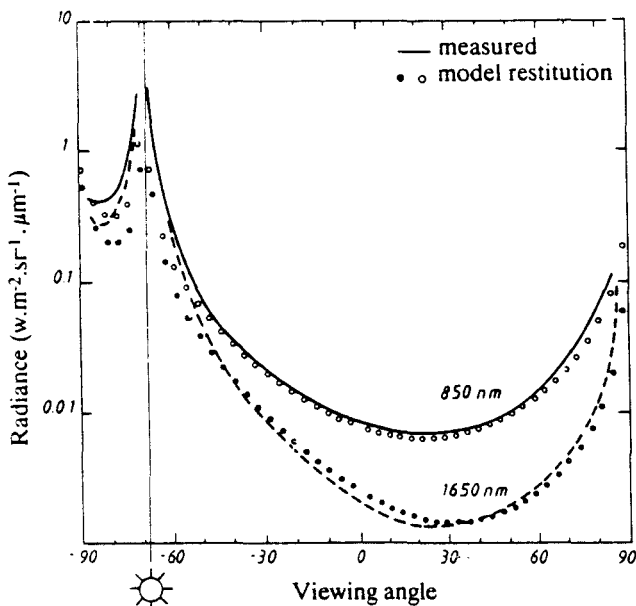


Figure 2. Measured radiance compared to the restitution with an aerosol model defined by  $r_0 = 0.15 \mu\text{m}$ ,  $\nu = -3.7$ ,  $m = 1.50$ , and  $\delta_a^{850} = 0.056$ . The measurements were performed with a low sun at 6:00 a.m. on 7 June 1989.

### Gaseous Contents

At a given place, the ozone amount can be determined with an acceptable accuracy, from the seasonal values given by London et al. (1976). For the water vapor content, two weather stations bound the site: Marignane (10 km SE of the site) and Nimes (40 km NW). From the two stations we obtain temperature and relative humidity (under screen) from which we derive, by linear interpolation, the water vapor density at ground level on the test site. We have also radiosoundings at midnight and noon performed at Nimes. The integrated water vapor content on the site, at the time of the SPOT overpass, is the result of linear spatiotemporal interpolations between the ground level measurements and the radiosoundings.

In fact, the ground-based station can control this information. The extinction measurements, including the Chapuis band and the aerosol model, is sufficiently defined to predict, from outside measurements, their contribution in this band (Biggar et al., 1990). In the same way, a differential technique (Frouin and Gautier, 1987) associates a broad and a narrow band filter in the water vapor band at 950 nm to derive the integrated amount (Table 3).

### Results

Table 4 gives, for three days of measurements, the aerosol optical thickness as measured in the SPOT bands; the two flexible parameters ( $r_0, \nu$ ) of the Junge size distribution are derived from the polarization measurements, and the refractive index is the result of the aureole retrieval for 22 March and 7 June. For 13 June, the characterization of the aerosols was done only by extinction measurements with a portable sun-radiometer working between 0.45  $\mu\text{m}$  and 0.85  $\mu\text{m}$ . The slope of the Junge size distribution follows the spectral dependence of  $\delta_a(\lambda)$  while the refractive index value determined on 7 June is used.

We have to point out that the aerosol model is close to the standard continental model (Deirmendjian, 1964) defined by  $r_0 = 0.1 \mu\text{m}$ ,  $\nu = -4$ ,  $m = 1.50$ . The extremely good visibilities observed on 22 March and 7 June correspond to a Mistral regime, the continental dry wind which blows in the Rhone valley.

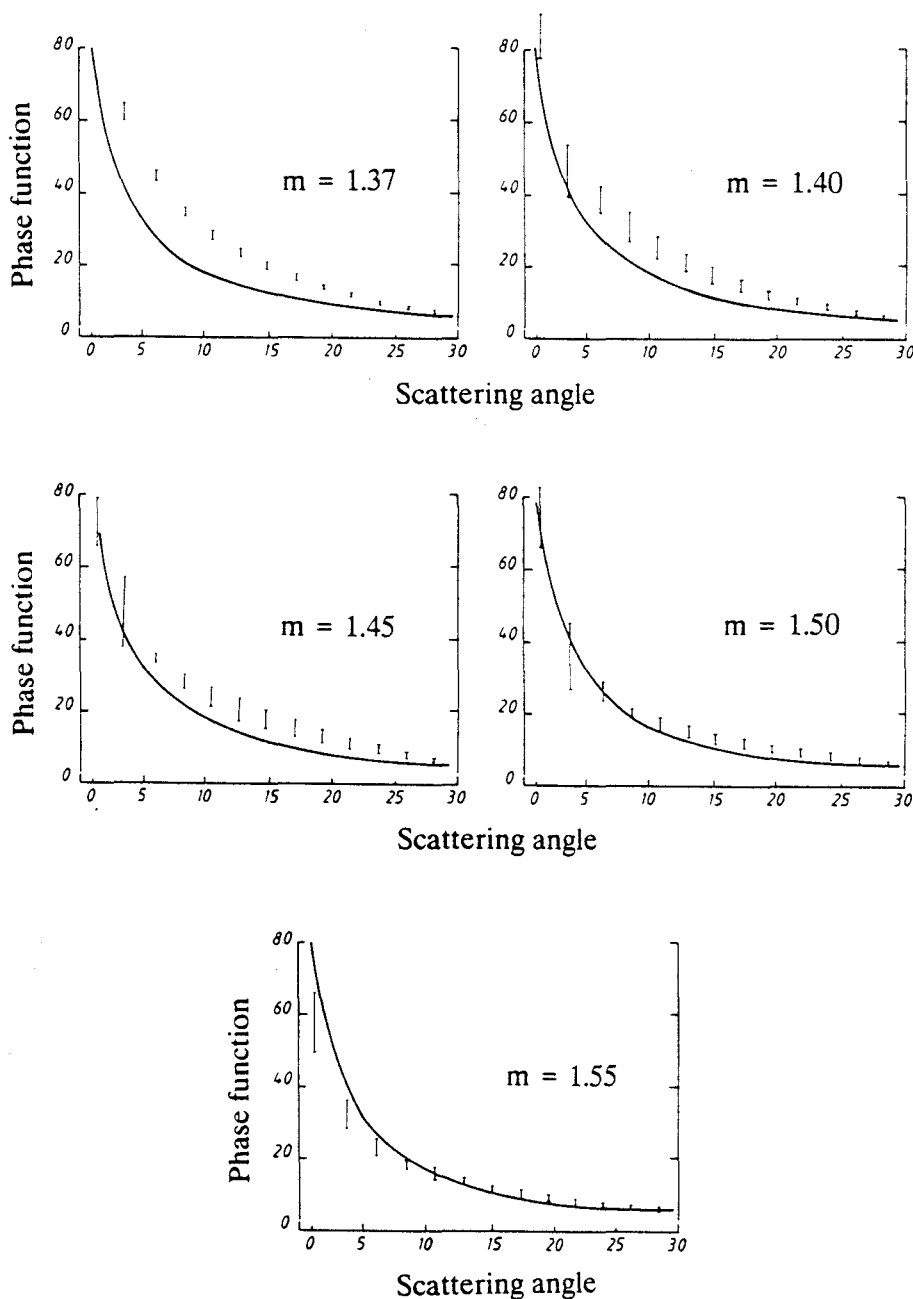


Figure 3. Restitution of the aureole for the measurements on 7 June. Aureole measurements are converted into phase function (continuous line) and compared to phase function computed for models deduced from the inversion of the polarization at different refractive indices. Error bars result from inaccuracies introduced in the measurements. The computations are normalized at  $\theta = 30^\circ$  and the increase of the error bars in the forward scattering is a direct consequence.

COMPUTATION OF THE SIGNAL

Standard Computation

To express the apparent reflectance  $\rho^*_i$  in Channel  $i$ , we uncouple absorption and scattering with

$$\rho^*_i = T_g^i \rho_i^0 \tag{4}$$

The gaseous transmittance  $T_g^i$  is computed using the "5S" code (Tanré et al., 1990). The spectral response of the SPOT internal filters  $R_\lambda^i$  are pro-

vided by CNES and the other inputs for ozone and water vapor are the integrated values. The reflectance  $\rho_i^0$  corresponds to the reflectance observed over a lambertian reflector  $\rho_g$  for a nonab-

Table 3. Atmospheric Water Content and Ozone Concentration for the Three Days of Measurements

Date	$U_{H_2O}$ ( $g\ cm^{-2}$ )	$U_{O_3}$ ( $cm\ atm$ )
22-03	1.83	0.390
07-06	1.27	0.383
13-06	1.27	0.388

Table 4. Aerosol Characteristics

Date	Optical Thickness			Size Distribution		Refraction Index (m)
	XS1	XS2	XS3	$r_0$	$\nu$	
22-03	0.049	0.042	0.032	0.10	-4.0	1.50
07-06	0.072	0.065	0.056	0.15	-3.7	1.50
13-06	0.334	0.285	0.218	0.10	-4.0	1.50

sorbing atmosphere. The computation is achieved using the method of successive orders of scattering (Deuzé et al., 1989). The inputs are the inverted aerosol model ( $r_0$ ,  $\nu$ ,  $m$ ,  $\delta_a^i$ ), mixed with the Rayleigh scattering, assuming a scale length of 2 km for the aerosols and the ground reflectance  $\rho_g$ .

The computation is monochromatic and the Rayleigh and aerosol optical thickness  $\delta$  have been integrated over the filter response:

$$\delta = \frac{\int_0^\infty E_s(\lambda) R_\lambda^i \delta(\lambda) \delta\lambda}{\int_0^\infty E_s^\lambda R_\lambda^i \delta\lambda}, \quad (5)$$

with

$R_\lambda^i$  = spectral responsivity of the sensor,  
 $E_s^\lambda$  = equivalent solar irradiance.

The spectral dependence of  $\delta$  is in  $\lambda^{-4}$  for the Rayleigh and in  $\lambda^{-\alpha}$  for the aerosols where the Angström coefficient  $\alpha$  is derived from the measurements.

This basic version of the solution of the radiative transfer equation in a plane-parallel atmosphere does not take into account the actual non-lambertian properties of the surface and the spectral inhomogeneity of the target.

### Departures from the Lambertian Approximation

The bidirectional properties of La Crau have been measured by Gu et al. (1991). For example, during summer, at the SPOT overpass time, the bidirectional reflectance decreases by about 10% in the specular direction and increases by 20% in the hot spot, compared to nadir measurements. The successive order transfer code is based on a Fourier series decomposition of the signal, and a suitable expansion of the boundary condition is

$$\rho(\mu_v, \mu_s, \phi_v - \phi_s) = \sum_{s=0}^4 \rho^s(\mu_v, \mu_s) \cos(\phi_v - \phi_s), \quad (6)$$

with  $\mu = \cos \theta$ .

Since the surface reflection is quite isotropic, the Fourier series expansion is restricted to five terms. The components  $\rho^s(\mu_v, \mu_s)$  are computed in a polynomial form for a complete set of bidirectional measurements at different solar elevations. The principle of reciprocity is used to double the available points. Figure 4 reports the relative error on  $\rho^0$  if we neglect the bidirectionality of the reflectance. These computations, versus the view angle  $\nu_v$ , are done for three solar zenith angles, 30°, 50°, and 60°, for  $\phi_v - \phi_s = 50^\circ$ , which closely corresponds to the SPOT azimuth angle (see Table 1).

The errors depend slightly upon the viewing angles and decrease with the increasing wavelength and with the decreasing atmospheric effects. Since they can be as high as 3%, the bidirectional effects have to be included in the calibration process. Fortunately the properties of the ground are quite stable with time, mainly in their angular distribution. We can then add extensive data collected prior to those collected the day of a SPOT calibration.

### Effect of the Environment

If La Crau is reduced in size (about 10 km in diameter), the contribution of the surroundings

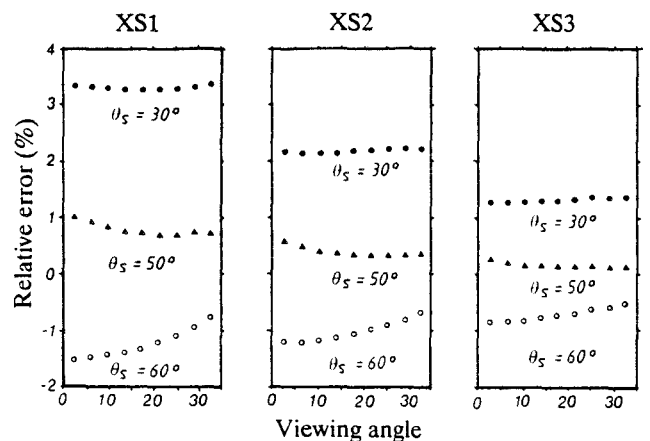


Figure 4. Relative difference between a Lambertian target and La Crau in the vertical plane, perpendicular to the sun azimuth. The continental aerosol model is used with a visibility of 50 km. The simulations correspond to three sun zenith angles for each SPOT band.

may then be significant. A simple case is proposed for computation in 5S: homogeneous disk surrounded by homogeneous ground. An immediate modification can be done by dividing the surroundings into elementary coronets. Figure 5 gives the average digital counts for coronets 200 m thick as measured by SPOT in the three bands. As reported in the Appendix, from the contrast of the digital counts between the target and its environment, and for a given atmosphere, we can derive the environmental effect. For example, for a visibility of 50 km with continental aerosols and a solar zenith angle of 30°, the environment, as shown in Figure 5, decreases the reflectance by 2% in XS1, 1.7% in XS2, and 0.4% in XS3, compared to a spatially uniform ground. Again it appears necessary to include this effect in a calibration procedure.

**CALIBRATION AND RELATED ERRORS**

**Calibration Coefficients**

The incoming parameter at the sensor is the integrated radiance

$$L_i = \int_0^\infty R_i^\lambda L_\lambda d\lambda \quad (w \text{ m}^{-2} \text{ sr}^{-1} \mu\text{m}^{-1}) \quad (7)$$

with  $L_\lambda$  = monochromatic radiance at the sensor.

Generally, in order to be independent of the absolute amplitude of the spectral response, the integrated radiance  $L_i$  is transformed into an equivalent radiance  $L_i^e$ :

$$L_i^e = \frac{L_i}{\int_0^\infty R_i^\lambda d\lambda} \quad (8)$$

Since the detection is linear, the calibration equation is

$$DC_i = A_i L_i^e, \quad (9)$$

$DC_i$  being the digital count and  $A_i$  the calibration coefficient (counts per  $w \text{ m}^{-2} \text{ sr}^{-1} \mu\text{m}^{-1}$ ). However, the viewing gain of SPOT HRV  $m_i$  can have eight integer values,  $1 \leq m_i \leq 8$ , associated with the signal amplifier. For this reason an absolute calibration coefficient  $A_i$  is defined and will be used in this study:

$$DC_i = A_i \cdot 1.3^{(m_i - 3)} L_i^e. \quad (10)$$

The digital count corresponds here to the aver-

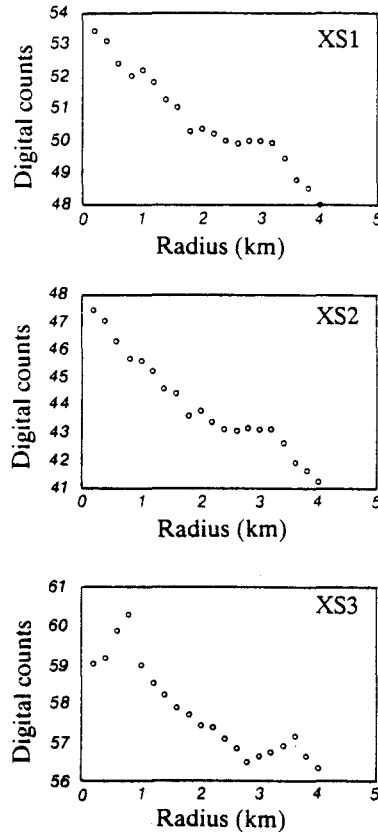


Figure 5. Variation of the mean digital counts of the SPOT image, as a function of the diameter of the circle centred on the test site, for the three SPOT channels.

age value for the  $20 \times 20$  pixels of the test site reported in Table 5. The transfer code produces the apparent reflectance  $\rho_i^*$  related to  $L_i^e$  by

$$L_i^e = \mu_s E_s^i \rho_i^* / (\pi d^2), \quad (11)$$

where  $E_s^i$  is the equivalent solar irradiance (1845,

Table 5. Digital Counts Observed for the Three SPOT Bands

Date	Parameters	XS1	XS2	XS3
22-03	Mean	67.7	66.6	61.9
	Minimum	59	58	58
	Maximum	73	72	65
	Standard deviation	2.1	2.1	1.1
07-06	Mean	88.8	95.2	75.9
	Minimum	82	88	73
	Maximum	94	99	78
	Standard deviation	1.9	2.0	1.0
13-06	Mean	93.1	100.5	77.4
	Minimum	88	94	75
	Maximum	97	105	80
	Standard deviation	1.6	1.9	0.9

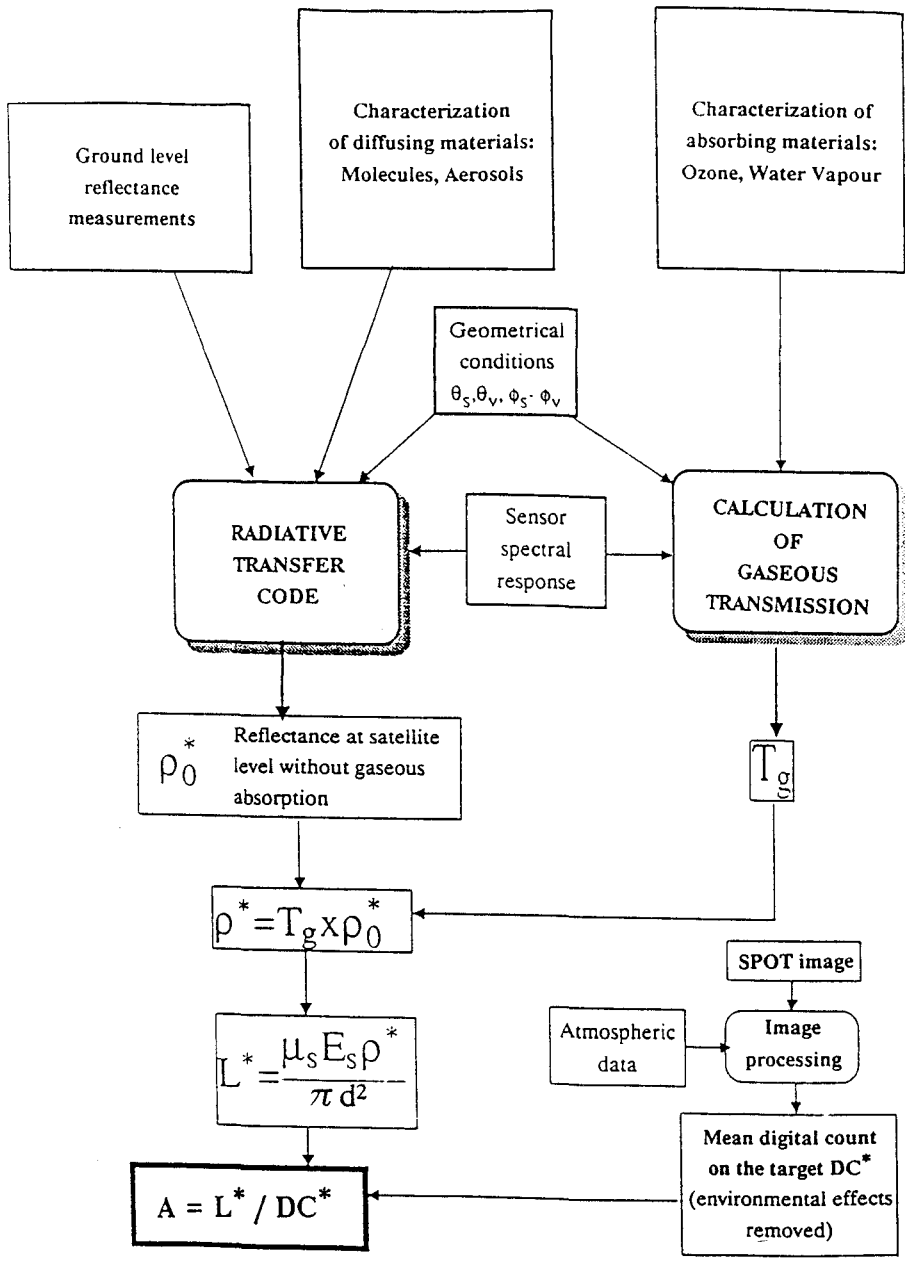


Figure 6. Flow chart representing the calibration procedure.

1575, and 1040 W m<sup>-2</sup> μm<sup>-1</sup> for SPOT1-HRV2 channels XS1, XS2, and XS3, respectively) and *d* the Earth-Sun distance (expressed in u.a.).

The flow chart reported in Figure 6 illustrates the complete calibration procedure. Ignoring the gaseous transmission, the apparent reflectance is computed with the optical parameters as first inputs. The boundary conditions correspond, for the direct to direct path, to the average measured values of the reflectances on the calibration site and, for the other terms, to an up-dated experi-

mental description of the bidirectional function expended in a Fourier series. The gaseous transmission is computed separately using the "5S" code to balance the former result. The apparent reflectance is transformed into radiance. On the other hand, since the evolution of the environmental effect is achieved on the digital counts, we deconvolute the average value of the test site instead of correcting this surrounding effect on the predicted value of the outgoing radiance.

For the three dates, the calibration coeffi-

coefficients are reported in Table 6. We also reported the coefficients proposed by CNES (Dingirard and Briottet, 1989) and also the relative difference between the two sets. For XS2 and XS3, the agreement is quite good and obviously within the error domains. The large discrepancies in XS1 are under investigation. One explanation lies in a possible yellowing of the lamp used for SPOT internal calibration. On the other hand, the calibration method applied to SPOT1 HRV1 and Landsat5 TM give consistent results compared with the calibration performed by Slater's team with a difference ranging between 0% and 6% (Gu, 1991).

### Error Budget

Table 7 gives a detailed error budget for 7 June. The uncertainties on  $R_{\lambda}^i$  correspond to CNES specifications. The impacts of  $R_{\lambda}^i$  inaccuracies are on the determination of  $E_{\lambda}^i$  and on the computation of the signal (mainly on gaseous transmission). The instrumental noises are proportional to  $\mu_s$ . The errors on the reflectance of the ground are computed according to Gu et al. (1991), taking into account the spectral response of the radiometer and the actual number of samples. The apparent contribution of the surface is weighted by the atmospheric transmittances, which reduce, in the same way, the error in the estimation of ground contribution. As expected, errors concerning the gaseous content are more significant in XS1 for  $O_3$  and XS3 for  $H_2O$ . Uncertainties of the barometric pressure ( $\delta h_p$ ) have been introduced for the Rayleigh scattering. For the aerosols, the error budget is more complex, resulting from errors in mea-

Table 6. Comparison of SPOT1-HRV2 Calibration Coefficients Determined from La Crau and from the Internal Calibration (CNES)

Date	Origin	XS1	XS2	XS3
22-03	Crau	0.518	0.376	0.555
	CNES	0.469	0.381	0.567
	Difference (%)	+10.4	-1.3	-2.3
07-06	Crau	0.505	0.391	0.562
	CNES	0.466	0.380	0.567
	Difference (%)	+8.4	+2.9	-0.9
13-06	Crau	0.495	0.389	0.561
	CNES	0.466	0.380	0.567
	Difference (%)	+6.2	+2.4	-1.1

Table 7. Detailed Error Budget on 7 June

Origin	Relative Error (%)		
	XS1	XS2	XS3
Spectral response	0.60	0.90	0.60
Instrumental noise	1.60	1.45	1.05
Apparent refl. of the target	1.95	1.97	1.60
Water vapor	0.30	0.31	0.52
Ozone	0.58	0.47	0.00
Molecules	0.12	0.05	0.01
Aerosols	0.61	0.48	0.36
$E_{\lambda}$ variation	0.20	0.20	0.20
$E_{\lambda}$ determination	1.00	1.00	1.00
Sun zenith angle	0.14	0.14	0.14
Surrounding effect	0.50	0.50	0.10

surements of the optical thickness, the polarization ratio, and the aureole. Moreover, since our inversion scheme is not sensitive to the imaginary part of the refractive index, we introduced this parameter as arbitrarily defined as  $5 \times 10^{-3}$ . The transformation of the reflectance into radiance is affected by uncertainties in  $\theta_s$  and  $E_{\lambda}^i$  with its natural variation (within 0.2%), plus a systematic bias of 1%, depending on the data source. At last, we saw how to correct for the environmental effects and a residual inaccuracy appears.

Finally, Table 8 gives the errors as a quadratic sum. The errors are of the order of 3% except on 13 June because the visibility was low. Moreover, the atmospheric measurements were reduced to visible extinction measurements, and the error budget was adapted consequently.

### CONCLUSIONS

The utility of La Crau as a calibration site for SPOT has been demonstrated. This site should be used on a routine basis at a biannual rate. For further campaigns some improvements are planned. The number of samples of the target reflectance will be increased by using a second radiometer. Moreover, the radiometers will be

Table 8. Relative Error (%) on Calibration Coefficients

Date	XS1	XS2	XS3
22-03	3.2	3.1	2.0
07-06	3.0	3.0	2.4
13-06	6.3	4.4	5.0

tilted in the SPOT viewing direction and measurements will be performed in the same azimuthal plane. For atmospheric measurements, global and diffuse measurements are planned in order to control the absorption of the aerosols.

The 1991 campaign at La Crau has been integrated in the European NASA ER2 campaign with special attention paid to intercalibration with AVIRIS, the JPL spectroimager, and with POLDER, a photopolarimetric camera developed at Lille. For more general purposes, the Appendix provides a suitable tool for introducing the surrounding effect from the image content.

## APPENDIX

As proposed by Tanré et al. (1990), the upward reflectance is the sum of three different contributors:

1. The atmospheric path radiance  $\rho_a$ .
2. The contribution of the pixel of reflectance  $\rho$ :

$$T(\mu_s)\rho e^{-\delta/\mu_v} \quad (12)$$

where  $T(\mu_s)$  is the total transmittance (i.e., the downward global irradiance divided by the solar incident flux) and where  $e^{-\delta/\mu_v}$  describes the attenuation on the direct atmospheric path.

3. The surrounding effect which can be expressed as

$$T(\mu_s)\langle\rho\rangle t_d(\mu_v), \quad (13)$$

where  $T_d$  is the diffuse transmittance and where  $\langle\rho\rangle$  is the mean reflectance of the environment, expressed as

$$\langle\rho\rangle = \int_0^\infty \rho(r)f(r) dr. \quad (14)$$

The environment function  $f(r)$  describes the probability for a photon reflected by the ground at a distance  $r$  from the target center to be scattered within the solid angle  $\Omega$ .

Finally, the sum of the contributions gives

$$\rho^0 = \rho_a + \frac{T(\mu_s)[\rho e^{-\delta/\mu_v} + \langle\rho\rangle t_d(\mu_v)]}{1 - \langle\rho\rangle s} \quad (15)$$

where the multiple interactions between the ground and the atmosphere, introduced in the

denominator, involved the spherical albedo  $s$ . We have to point out that Eq. (14) corresponds to a nadir observation. According to Tanré et al. (1990), this formulation is still valid up to a viewing angle of  $30^\circ$ , which is suitable for SPOT observations. The atmospheric functions  $\rho_a$ ,  $T$ ,  $t_d$ , and  $s$  are computed using the successive orders of scattering method for the relevant inputs.

The *in situ* measurements are restricted to the calibration site. The computation of the environmental effect is then based on the contrast

$$C(r) = DC(r) / DC(o) \quad (16)$$

between the digital counts observed at a distance  $r$  from the target and for the target. From Eqs. (14)–(16), it can be demonstrated that (Vermote, 1990)

$$\langle\rho\rangle = \frac{\rho_a(P-1) + P\rho T(\mu_s)e^{-\delta/\mu_v}}{s\rho_a(P-1) + T(\mu_s)[T(\mu_v) - Pt_d(\mu_v)]}, \quad (17)$$

where

$$P = \int_0^\infty f(r)C(r) dr. \quad (18)$$

*This study was supported by the Centre National d'Etudes Spatiales (CNES) under Contract n° 833/89/5935/00. We thank M. Herman (LOA) and M. Leroy (CNES) for helpful discussions.*

## REFERENCES

- Begni, G. (1985), The radiometric calibration of the SPOT HRV sensors, in *Acta Polytechnica Scandinavia* (T. Friberg and Pirkko Oittinen, eds.), Proc. Image Science, Vol. 2, pp. 10–11.
- Biggar, S. F., Santer, R. P., and Slater P. N. (1990), Irradiance-based calibration of imaging sensors, in *Proc. IGARSS '90*, Washington DC, May 1990, pp. 507–510.
- Dagnelie, P. (1970), *Théorie et Méthodes Statistiques*, (J. Duclot S.A., ed.), Les Presses Agronomiques de Gembloux, A.S.B.S.L., Gembloux, Belgium, Vol. 2, 451 pp.
- Deirmendjian, D. (1964), Scattering and polarization properties of water clouds and hazes in the visible and infrared. *Appl. Opt.* 3:187–196.
- Deuzé, J. L., Herman, M. and Santer, R. (1987), Modélisation de l'état de polarisation du rayonnement atmosphérique ascendant. Partie 1 Atmosphère limitée par un sol lambertien, Rapport Contrat CNES.
- Deuzé, J. L., Herman, M., and Santer, R. (1989), Fourier series expansion of the transfer equation in the atmosphere-ocean system, *J. Quant. Spectrosc. Transfer* 41:483–494.

- Dinguirard, M., and Briottet, X. (1989), Bilan d'étalonnage absolu SPOT1. Troisième bilan semestriel, Rapport CNES S-NT-OB1-561-CN.
- Dinguirard, M., and Maisoneuve, J. M. (1980), Description du dispositif d'étalonnage absolu de la caméra HRV, Rapport CNES Toulouse (France) S-NT-OB1-0090-CN.
- Frouin, R., and Gautier, C. (1987), Calibration and NOAA-7 AVHRR, GOES-5, and GOES-6 VISSR / VAS solar channels, *Remote Sens. Environ.* 22:73-101.
- Gu, X. F. (1991), Etalonnage et intercomparaison des données satellitaires en utilisant le site test de la Crau, Thèse doctorat, Université Paris VII, 260 pp.
- Gu, X. F., Guyot, G., and Verbrugge, M. (1990), Analyse de la variabilité spatiale d'un site test -Exemple de la Crau (France), *Photo-Interprétation* 90-1(5):39-52.
- Gu, X. F., Guyot, G., and Verbrugge, M. (1992), Evaluation of measurement errors in ground surface reflectance for satellite calibration, *Int. J. Remote Sens.*, forthcoming.
- Guyot, G., Hanocq, J. F., Buis, J. P., and Saint, G. (1984), Mise au point d'un radiomètre de simulation de SPOT, *Second International Colloquium on Spectral Signatures of Objects in Remote Sensing*, Bordeaux, France, 12-16 September 1983, Ed. INRA Publ., Les Colloques de l'INRA n° 23, pp. 233-242.
- Guyot, G., Gu, X. F., and Verbrugge, M. (1989), Caractérisation des propriétés optiques du site de la Crau, Rapport Final Contrat 833 / CNES / 87 / 4891 / 00, INRA Bioclimatologie, Montfavet, France, 79 pp.
- Herman, M., Balois, J. Y., Gonzalez, L., et al. (1986), Stratospheric aerosols observation from a balloon-borne polarimetric experiment, *Appl. Opt.* 25:3573-3584.
- London, J., Bojkov, R. J., Oltmans, S., Kelley, J. I. (1976), Atlas of the global distribution of total ozone July 1957-June 1967, NCAR Technical Note No. 113 + STR.
- Rouquet, M. C. (1987), Faisabilité de la calibration HRV-SPOT sur des cibles tests, Rapport Contrat CNES, Toulouse, France, 833 / CNES / 87 / 4891 / 00.
- Santer, R. (1984), Caractérisation des aérosols à partir de la polarisation du rayonnement solaire diffusé. Application aux atmosphères de la Terre de Vénus et de Saturne, Thèse d'Etat, Lille.
- Slater, P. N., Biggar, S. F., Holm R. D., et al. (1987), Reflectance and radiance-based methods for the in-flight absolute calibration of multispectral sensors, *Remote Sens. Environ.* 22:11-37.
- Tanré, D., Deroo, C., Duhaut, P., et al. (1990), Description of a computer code to simulate the satellite signal in the solar spectrum: The 5S code, *Int. J. Remote Sens.* 11:659-668.
- Vermote, E. (1990), Effects d'atmosphère en télédétection, Thèse Doctorat, Université des Sciences et Techniques de Lille Flandres Artois (France).
- Weinmann, J. A., Twilley, J. T., Browning, S. R., and Herman, B. M. (1975), Derivation of phase function from multiple scattered sunlight transmitted through a hazy atmosphere, *J. Atmos. Sci.* 32:577.

# Photopolarimetric Observations of Aerosols and Clouds from Balloon

J. L. Deuzé, C. Devaux, M. Herman, R. Santer, J. Y. Balois,  
L. Gonzalez, P. Lecomte, and C. Verwaerde

Laboratoire d'Optique Atmosphérique, Université de Lille-Flandres-Artois,  
59655 Villeneuve d'Ascq Cedex, France

*This paper presents a balloon-borne experiment for directional observations of the radiance and of the polarization ratio of the light reflected toward the space by the earth-atmosphere system. A first flight was conducted on 5 July, 1985 over the Bay of Biscay (SW of France). The goal was to monitor the tropospheric aerosols by taking advantage of the black surface offered by the ocean at near infrared wavelengths. During the first part of the flight, remote sensing of the aerosols was disturbed by fair weather cumulus, but cloudless observations could be selected, which exhibit typical features of the sunglint and of scattering by aerosols. The inversion of these measurements allows a characterization of the optical properties of the aerosols. During the second part of the flight, the balloon drifted over a huge cloud deck. There, the observed radiance provides a determination of the optical thickness of the cloud, and the polarization ratio is illustrative of scattering by large cloud droplets.*

## INTRODUCTION

The polarizing properties of planetary atmospheres have been discussed by many authors, mainly for Venus where the analysis is simplified on account of the sphericity of the aerosols and the large optical thickness of the haze layer (Hansen and Hovenier, 1974). For Mars, during clear periods, Mars-5 Orbiter polarization measurements have been used to describe the surface properties (Dollfus et al., 1983). The use of polarization measurements appears more complicated when both the signatures of the atmosphere and of the surface are present in the measurements as for Mars or the Earth. To emphasize the atmospheric effect, limb measurements have been investigated, from the Soviet Mars-5 Orbiter to deduce the particulate properties in the atmosphere of Mars (Santer et al., 1985), or from stratospheric balloons, to describe the Earth stratospheric layers (Herman et al., 1986). For Mars and for the Earth, cloud characterization has been obtained largely from polarization measurements (Santer et al., 1986; Hansen, 1972). But only a few polarization experiments have been conducted to study the global Earth-atmosphere system from space.

Concerning the theoretical aspect of the problem, most of the authors developed radiative trans-

---

Received 1 March 1988; revised 14 March 1989.

0034-4257/89/\$3.50

©Elsevier Science Publishing Co. Inc., 1989  
655 Avenue of the Americas, New York, NY 10010

fer codes for oceanic observations (Kattawar et al., 1973; Plass et al., 1975; Ahmad and Fraser, 1982), where the boundary condition is well known. The depolarization of the sunglint has been used by Prosch et al. (1982) to deduce the aerosol optical thickness, by assuming depolarization arises only from the aerosol scattering. Some polarization signatures observed over the ocean have been also reported by Takashima and Masuda (1985). Extensive measurements of the polarizing properties of natural terrestrial surfaces have been performed (Walraven and Coulson, 1972; Egan, 1985; Vanderbilt and Grant, 1984). The first attempt to measure the polarization of the light reflected by the Earth-atmosphere system was done by Nagaraja Rao (1969); balloon-based measurements, performed over the White Sands area (New Mexico), exhibited depolarization of the Rayleigh scattering by a lambertian ground. The only extensive measurements of atmospheric and surface polarization have been done during four Shuttle missions, and a preliminary presentation has been made by Coulson and Whitehead (1986).

A balloon-borne polarimetric device was developed for the observation of the stratospheric aerosols (Herman et al., 1986). This apparatus has been adapted to observe, at near infrared wavelengths and as a function of the direction, the polarized radiance emerging from the Earth-atmosphere system. As a first goal, the experiment was designed to monitor the tropo-

spheric aerosols from balloon overflights of the ocean. There, near infrared observations are free from the seawater scattering contamination, due to the water absorption, and a preliminary study (Santer et al., 1983) showed that retrieval of the aerosol characteristics from polarization measurements was possible.

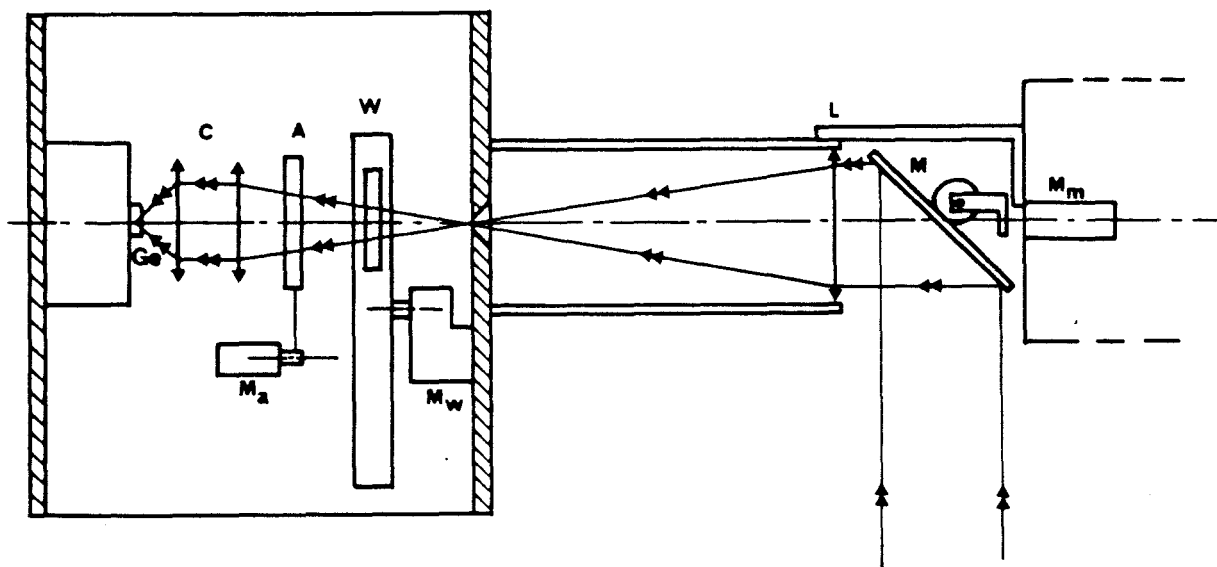
The first flight of the experiment was conducted in July 1985. Although the observations were largely disturbed by different cloud systems, the polarization signatures were proved to be meaningful, and the typical features of the sunglint, of scattering by aerosols, and of scattering by cloud droplets are recognizable and may be analyzed in a quantitative manner.

## EXPERIMENTAL PROCEDURE

### Description of the Polarimeter

The polarimeter, which was designed for balloon-borne polarization measurements in the stratosphere, has been described in Herman et al. (1986). A schematic description of the instrument is given in Fig. 1. The radiometer is a  $2^\circ$  field of view Cassegrain telescope, using a cooled germanium photodiode. A rotating wheel contains two filters, with respective central wavelengths of 850 and 1650 nm, and respective bandwidths of 30 and 150 nm. The signal is modulated by the rotation of an

Figure 1. Schematic of the polarimeter: M, mirror; L, objective lens; W, rotatable filter wheel; A, rotatable analyzer; C, condenser; Ge, germanium photodiode; Mm, Mw, Ma, mirror, filter wheel, and analyzer motors providing the respective 1/60, 1, and 48 Hz rotation rates.



analyzer. It is sampled after a first amplification stage, and then an on-board microprocessor computes its mean value and its mean deviation. The spin rate of the filter wheel is one rps and, every second, for the two filters and for a dark position, the mean value and the mean deviation of the signal are transmitted to the ground based reception station. After removing the dark signal, we get the polarization ratio. A preflight calibration gives the conversion factor of the digital counts into equivalent radiance, i.e.,

$$L = \pi \frac{\int_0^\infty L(\lambda) R(\lambda) d\lambda}{\int_0^\infty E_s(\lambda) R(\lambda) d\lambda}, \quad (1)$$

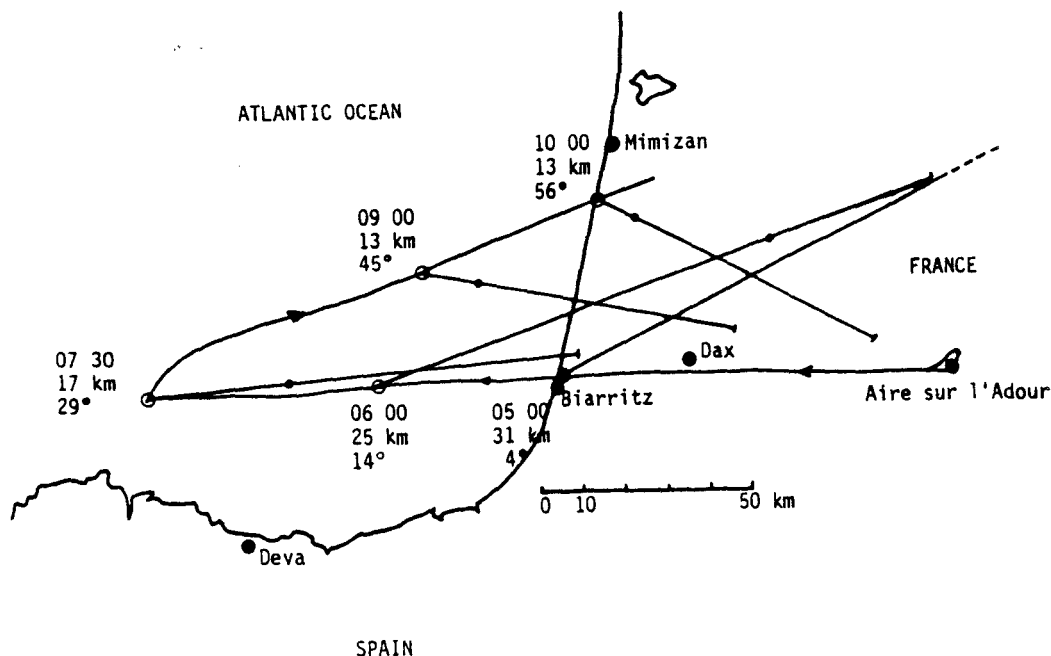
where  $E_s(\lambda)$  is the solar irradiance and  $R(\lambda)$  the spectral response. The equivalent radiance corresponds here to an equivalent monochromatic value weighted by the spectral response for an incoming irradiance equal to  $\pi$ . The dynamic range in equivalent radiance is  $(10^{-4}, 10)$ . A maximum of 10 allows measurements of the radiance in the sunglint. For the expected values of several percent of the radiance, the accuracy on the polarization ratio should be about 0.0025.

The polarimeter is set up horizontally, and to observe the radiation reflected by the Earth-atmosphere system, we added a mirror which scans in a vertical plane. The plane mirror is tilted by  $45^\circ$

and is attached to a rotation axis. The spin rate is 1 rpm, and only the range  $(-80^\circ, +80^\circ)$  for the zenithal viewing angle is investigated. The polarization induced by the silvered mirror depends on the direction of the polarization plane. The mirror influence was measured and was accounted for as a function of the scanning angle (Balois, 1985). This calibration was done for partially polarized incident light, with linear polarization either parallel or perpendicular to the scanning plane, as it must be for the planned measurements in the principal plane. The overall accuracy on the polarization ratio should be 0.01.

A sun pointer allows the gondola to be stabilized at a given azimuth. For this experiment, we chose to observe in the principal plane and the radiometer was set up for this goal. The azimuth of the scanning plane is controlled by a two-axis magnetometer. On the other hand, an inclinometer provides complementary data concerning the gondola stability. All the geometrical conditions (zenithal and azimuthal viewing angles, gondola inclination) are transmitted to the ground as a function of the time, given by an internal clock. At last, the CNES provides minute by minute the balloon position. Local time and position are then used to compute the solar azimuth and zenith angles.

Figure 2. Balloon trajectory. For several points, the GMT time, the balloon altitude, and the solar elevation have been pointed. The bars show the direction and the amplitude of the scans, towards the coast, and the dots indicate the location of the target corresponding to the specular reflection.



### Flight Conditions

The main goal of the experiment was the aerosol remote sensing. To avoid large contamination of the signal by the surface, sea observations were planned. The CNES base for balloon launch is located at Aire sur l'Adour, S.W. of France. For a flight over the Atlantic Ocean, the early summer presents the best atmospheric conditions both to encounter cloud-free conditions and to realize the required flight trajectory. Then, above about 14 km or 150 mb, the wind blows from the east, and below this neutral altitude eastward winds allow to come back over the land.

The experiment was planned in July 1985, and during this period, ground-based measurements were performed near the coast line, at Mimizan, in order to characterize the aerosols. The launch decision was taken on 5 July 1985, after the analysis of the midnight Meteosat picture. The flight trajectory is reported in Fig. 2. The launch was at 2 a.m. Two hours were necessary to reach the 7 mb ceiling level. From 4 a.m., a slow descent was conducted to reach the neutral altitude, at about

150 mb. At 8 a.m., the furthest point over the ocean was reached, and then the balloon altitude was stabilized at 130 mb to find the eastward winds and come back. The coastline was reached at 10 a.m. and the measurements then were stopped. For several points of the trajectory, in Fig. 2, the GMT time, the balloon altitude and the solar elevation have been noted. Moreover, bars indicate which points of the surface were scanned toward the east, within the maximum observation zenithal angle of  $80^\circ$ ; this illustrates the land or oceanic nature of the corresponding observation. Finally, dots on the bars indicate the points which corresponded or should have corresponded to specular reflection.

The inclinometer data proved that the gondola was stabilized within  $0.2^\circ$  except for some sharp deviations which occurred during short unbalanced periods. The magnetometer data showed a systematic departure of about  $8^\circ$  of the scan plane from the principal plane, which resulted from a default in the setting up of the sun pointer. Otherwise, the gondola was well stabilized in azimuth



*Figure 3.* NOAA-6 image in Channel 2, at 7.35 a.m. The thermal band indicated a 5 K difference between the sea surface and the cloud top temperatures, which locates the cloud top altitude at about 1 km, in agreement with the Biarritz weather station data.

Table 1. Ranges of UT time ( $t$ ), Solar Elevation ( $h_s$ ), Solar Azimuth ( $\varphi_s$ ), and Balloon Altitude ( $z$ ) for Each Sequence

Sequence	$t$	$h_s$	$\varphi_s$	$z$ (km)
(a)	4 h 59 min–5 h 28 min	3.8–8.3°	62–66°	31.4–27.7
(b)	5 h 36 min–8 h 05 min	9.6–36°	87.3–91.5°	27.3–14.4
(c)	9 h 22 min–10 h 17 min	49.7–59°	107–124°	13.1–12.8

except during the previously mentioned unbalanced periods, where the sun was lost by the sun pointer. We also noticed scans 50° apart from the principal plane, during half an hour around the sunrise; then the solar irradiance was too low to assure a good aiming.

Some idea about the encountered cloud coverage is provided by the AVHRR of NOAA 6 at 7.35 a.m., in Fig. 3. Over the south part of the Bay of Biscay, the sky was nearly cloud-free, but a large cloud deck covered France. This stratus deck was overflowed mainly during the end of the experiment, when coming back to the coast. On the other hand, Fig. 3 shows that residual cumulus were present in the middle of the clear area, and Fig. 2 indicates that the balloon drifted unfortunately over these clouds during the first part of the experiment. In fact, color pictures taken from the balloon show that we permanently overflowed this broken cumulus field until we joined the continuous stratus deck. According to the polarimeter field of view, and depending on the altitude of the balloon, the ground foot print ranged from 0.5 to 1 km; that was nearly the typical size of the broken clouds, as shown by the color pictures.

## PRESENTATION OF THE MEASUREMENTS

For clarity, the whole experiment may be separated into three main sequences, where the observations exhibit very different features. Table 1 gives the ranges of time, solar elevation, solar azimuth, and balloon altitude corresponding to these sequences. Sequence a) is just after overpassing the coast line; solar elevations are low; the backscattering directions correspond to sea observations while the scan in forward scattering directions is partially concerned with land observations (see Fig. 3), so that no sunglint is present in the measurements. Sequence b) corresponds to sea observations perturbed by the presence of small cumulus and where the sunglint is present. Finally,

sequence c) corresponds to the overflight of the stratus deck at the end of the experiment.

The measurements corresponding to these three sequences are shown in Fig. 4, for the wavelength 850 nm. We removed from the raw data only those measurements corresponding to zenithal viewing angles larger than 80° or to azimuthal viewing angles more than 10° from the mean scanning plane (within 8° from the principal plane). The radiance  $L(\theta)$ , and the polarization ratio  $P(\theta)$ , have been graphed vs. the scattering angle  $\theta$ . Radiance and polarization ratio mainly depend on this parameter, so that we can by this way crudely compare measurements corresponding to different air masses and observation geometries. The only problem is to discriminate the two symmetrical positions, in backscattering, around the incident direction. By convention, we decided to ascribe a scattering angle

$$\theta^* = 360^\circ - \theta$$

to those measurements with a zenith viewing angle  $\theta_v$  larger than the solar zenith angle  $\theta_s$ . Note that the scattering angle is limited in forward directions by the solar elevation angle  $h_s$  ( $h_s = 90^\circ - \theta_s$ ), and that the lack of measurements in backscattering directions corresponds to the 8° deviation of the scan plane from the principal plane.

The qualitative interpretation of the measurements is quite simple. In sequence a), the radiance mainly mimics a phase function whose forward scattering is large, and the polarization ratio shows a maximum around  $\theta = 100^\circ$  and a neutral point in backward scattering. The dispersion of the measurements from these main features clearly may be attributed to the cumulus, whose contamination increases the radiance and depolarizes the signal. The aerosol signature therefore corresponds to the lower boundary of the cluster of measured radiances, and to the upper one for the polarization ratios. Moreover, the discontinuity in the polarization measurements, for scattering angles smaller than about 60°, is related to the fact that these

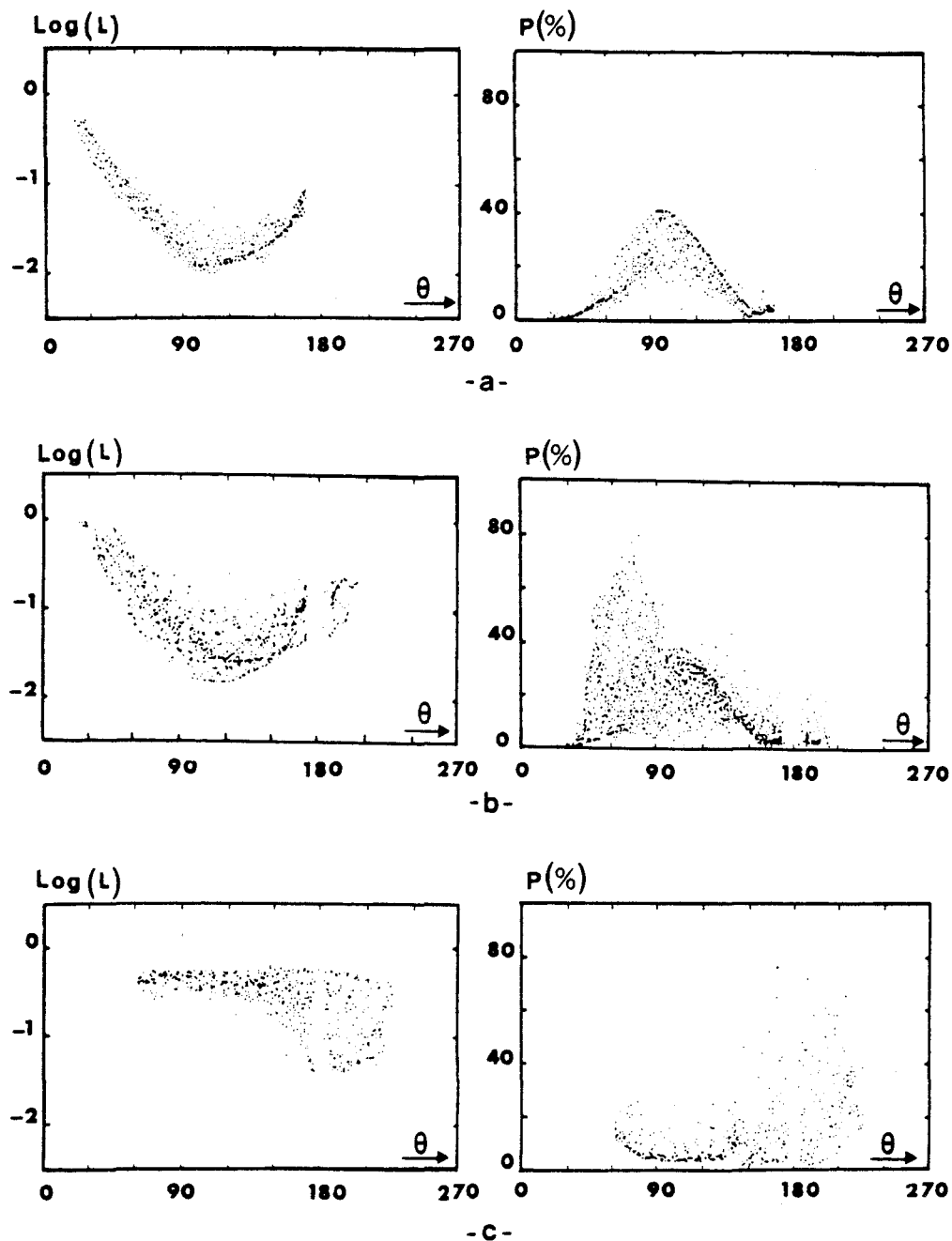


*Figure 4.* Radiance and polarization measurements versus the scattering angle  $\theta$ , for  $\lambda = 850$  nm. The convention on  $\theta$ , for backscattering directions, is explained in the text. Polarization ratios are in percent. All the measurements have been reported, provided that the azimuths of the viewing plane and of the principal plane did not depart by more than  $10^\circ$ . The whole flight has been decomposed in three main sequences, a), b), and c), as described in the text; figures a), b), and c) show the measurements performed during the corresponding sequence.

measurements correspond to land observations (see Fig. 2) which exhibit much smaller polarization than the sunglint.

In sequence b), the perturbation by the cumulus is more pronounced, but the envelopes of the radiances and of the polarization ratios are very

similar to those of sequence a). The main difference appears for observations around the specular direction. Due to the large dispersion of the measurements, the sunglint is difficult to discern in the radiance diagrams, but it is obvious in the polarization diagrams, as a result of the large polariza-

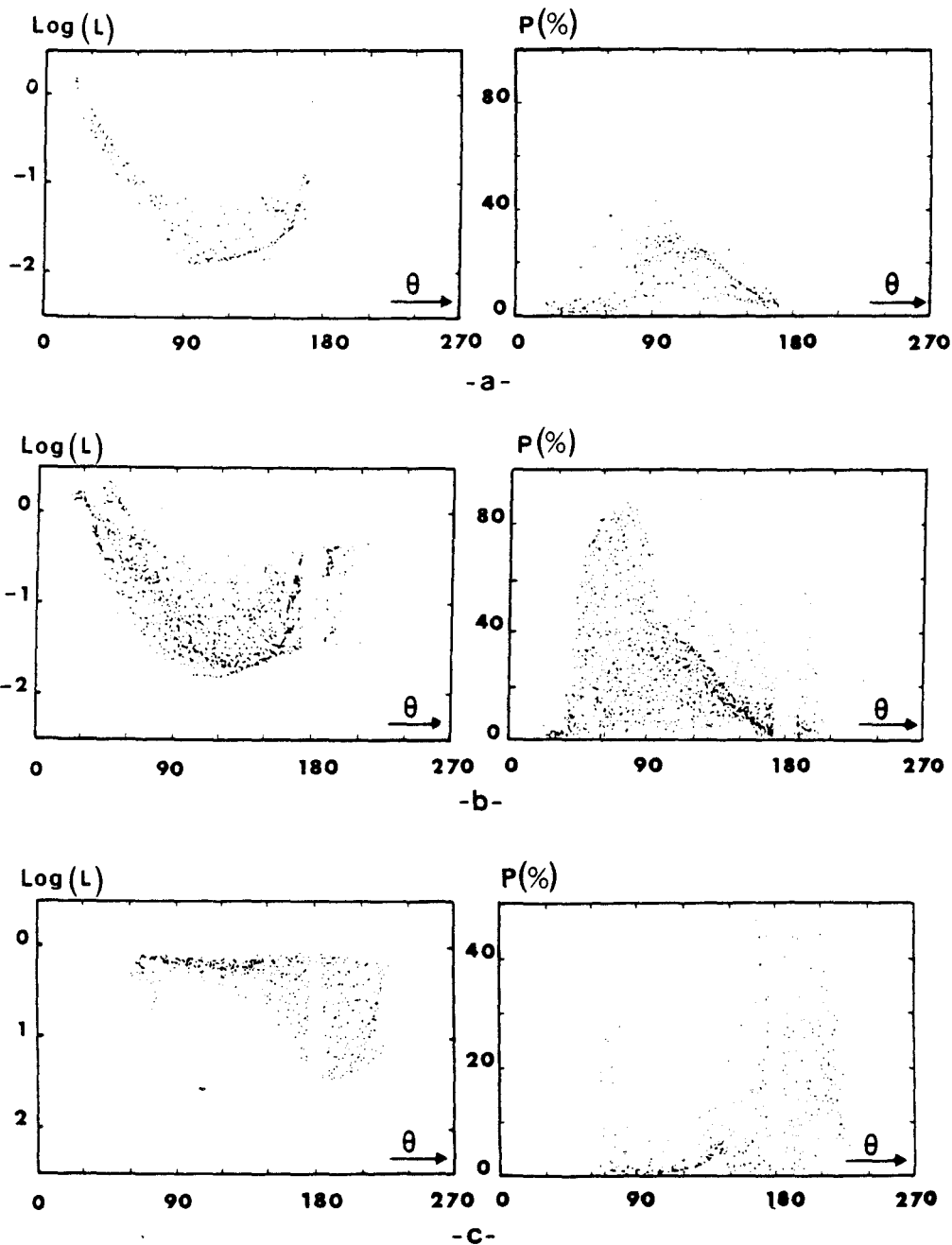


Figure 5. Same legend as Fig. 4, but for  $\lambda = 1650$  nm.

tion of the reflected light for solar zenith angles close to the Brewster angle.

Finally in sequence c), with total cloud coverage, the upward radiance is quite isotropic and the polarization ratio is generally small. The measurements are more dispersed in forward scattering, where we probably observed the edge of the cloud deck (see Figs. 2 and 3). High polarization ratios exist in backscattering directions only, which must correspond to the rainbow of large particles.

Figure 5 presents the same plots for the observations at 1650 nm. The main characteristics are the same. Except over the stratus cloud, the observed radiance decreases from 850 to 1650 nm, due to the decrease of atmospheric optical thickness with wavelength. We notice also that the maximum of the polarization ratio decreases slightly from 850 to 1650 nm, because of the decreased contribution of Rayleigh scattering. Finally, in the sunglint, the polarization is somewhat

larger at 1650 nm, which is consistent with better transmission and less depolarization by the atmosphere at this wavelength.

## ANALYSIS OF THE MEASUREMENTS

### Characterization of the Clouds

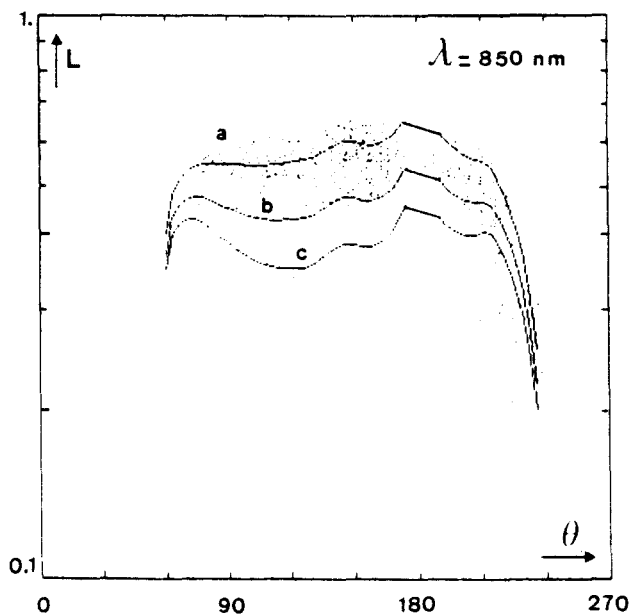
Let us first analyze the measurements of sequence c), which corresponds to cloudy conditions. Then the modeling is simple, on account of the weak dependence of the cloud optical properties both with respect to the observation wavelength and with respect to the droplet size distribution, for which we used here the C1 model of Deirmendjian (1964). The size distribution is a gamma standard law,

$$n(r) = Ar^6 \exp(-3r/2),$$

and the refractive index at 850 nm is  $m = 1.33$ . Moreover, given the homogeneity of the measurements, the cloud deck will be considered as a plane parallel layer.

Figure 6 shows the radiance measured at 850 nm during a limited range of the sequence c),

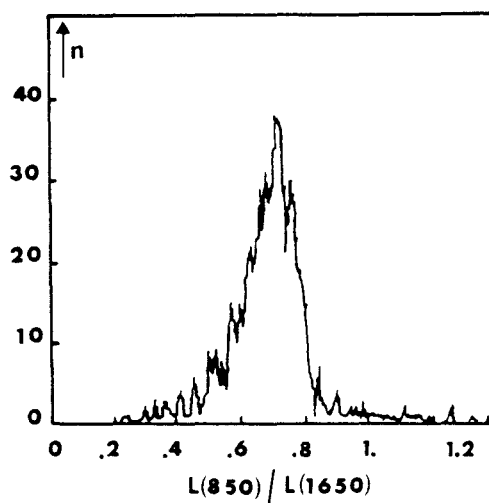
Figure 6. Dots: radiance measurements performed over the cloud deck [Sequence c)], at  $\lambda = 850$  nm, vs.  $\theta$ . (—) Radiance diagrams calculated for a plane parallel cloud, with the C1 model for the droplet size distribution, and with different values of the optical thickness:  $\tau_c = 8, 11, 20$  (c), b), a), respectively].



corresponding to solar elevations varying from  $56.7^\circ$  to  $58.9^\circ$ . Given the high radiances, the Rayleigh scattering contribution is negligible and the only parameter is the cloud optical thickness,  $\tau_c$ . For the cloud model previously defined, we computed the upward radiance for three values of  $\tau_c$ : 8, 11, and 20. The solar elevation was taken equal to  $58^\circ$ ; moreover, considering the sea water properties, the runs were performed for an assumed black surface at the cloud bottom. Figure 6 shows that calculations corresponding to  $\tau_c = 20$  match correctly the observations. We can also notice that we retrieve the large decrease of the radiance towards the limb, typical of planiform clouds.

The lamp irradiance was not given by the manufacturer for wavelengths larger than  $1 \mu\text{m}$ , and its value at 1650 nm was extrapolated from the data for smaller wavelengths (Balois, 1985). In order to check the preflight calibration, we assume no spectral dependence of the cloud radiance. Figure 7 shows the histogram of the observed ratio  $L(850)/L(1650)$ , where the radiances correspond to consecutive measurements. We used a threshold method to select the cloud radiances, and, to avoid bidirectional effects, we removed the grazing angles. Nevertheless, the dispersion of the histogram likely corresponds to aims of the edge of the cloud deck. According to Fig. 7, the radiances measured at 1650 nm have been corrected in the remaining analysis by a multiplicative factor 0.7.

Figure 7. Histogram of the ratio,  $L(\lambda = 850 \text{ nm})/L(\lambda = 1650 \text{ nm})$ , of the radiances observed in the two channels over the cloud deck. The expected radiances should be nearly the same. This *in situ* calibration shows that the estimated radiances, at  $\lambda = 1650$  nm, have to be corrected systematically by a factor 0.7.



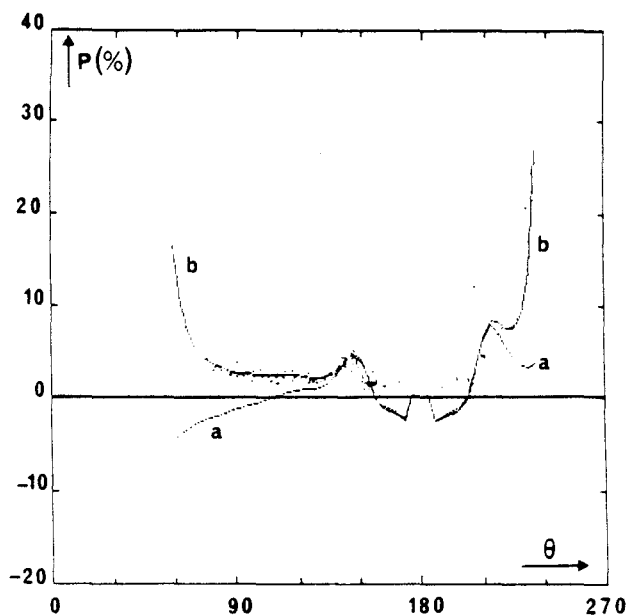


Figure 8. Dots: polarization ratio measurements performed over the cloud deck [Sequence c)], at  $\lambda = 850$  nm, vs.  $\theta$ . (—) Polarization diagrams calculated for a plane parallel cloud, with the C1 model for the droplet size distribution and with  $\tau_c = 20$  for the optical thickness. a) Molecular atmosphere above the cloud neglected into the calculations. b) Molecular contribution taken into account in the calculations.

Then consider polarization. The measurements at 850 nm have been reported in Fig. 8, for the same observations as in Fig. 6. These observations were first compared with calculations corresponding to the previous stratus model of optical thickness  $\tau_c = 20$ , ignoring again the residual Rayleigh atmosphere above the cloud. The results, labeled a) in Fig. 8, match poorly the measurements. Assuming a typical altitude of 1 km for the cloud top, we computed the Rayleigh scattering optical thickness above the stratus deck. When taking into account the Rayleigh atmosphere above the clouds [curve labeled b)], the agreement is improved. The increase of the polarization ratio for grazing viewing angles is retrieved, and the predicted polarization remains positive up to a scattering angle of about  $150^\circ$ , in accordance with the observations. In the same manner, the polarization ratios measured at 1650 nm have been compared in Fig. 9 with computations performed, first without taking into account [curve a)] and then taking into account [curve b)] the Rayleigh atmosphere above the stratus cloud. The two calculations mainly differ at large viewing angles, where the influence of the clear atmosphere is emphasized by the large air mass. Clearly, by taking into account the

Rayleigh scattering, the agreement with the measurements here also is improved. Note that in directions near  $\theta = 140^\circ$ , whereas the measurements are very similar at the two wavelengths, the model predicts a slight spectral effect, with the polarization maximum, in the rainbow direction, moving towards backscattering directions at 1650 nm. Although such a refinement was not investigated, some improvement of the cloud size distribution probably should be possible.

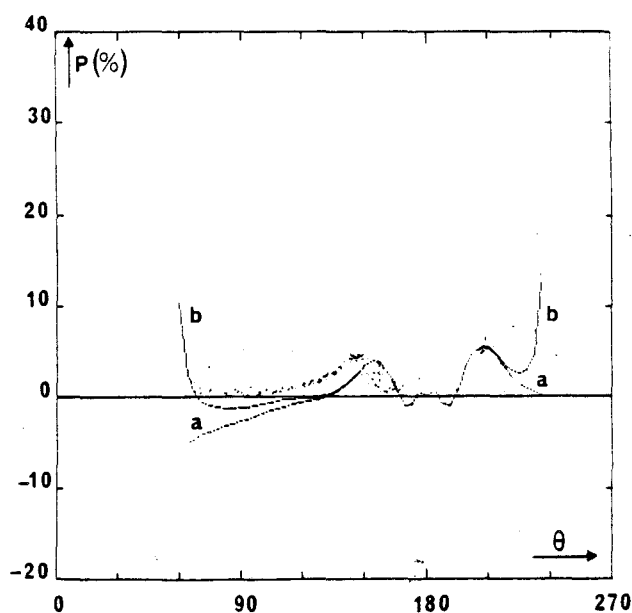
The analysis of sequence c) shows therefore that polarization measurements may provide information on the cloud top level and may be on droplet size distribution. However, the experiment was not designed for cloud remote sensing and these informations are only indicative. As suggested by Hansen (1972), characterization of the cloud droplet size distribution should be better using larger observation wavelengths, of the order of magnitude of the droplet radius, and determination of the cloud top level should need shorter wavelengths, in order to emphasize the molecular scattering influence. To a lesser extent, the results of the experiment confirm these two opportunities.

### Characterization of the Aerosols

#### Clear-Sky Observations. Sunlight

Despite the contamination of the measurements by cumulus clouds in sequences a) and b), we already pointed out that the envelopes of the radiance and

Figure 9. Same legend as Fig. 8, but for  $\lambda = 1650$  nm.



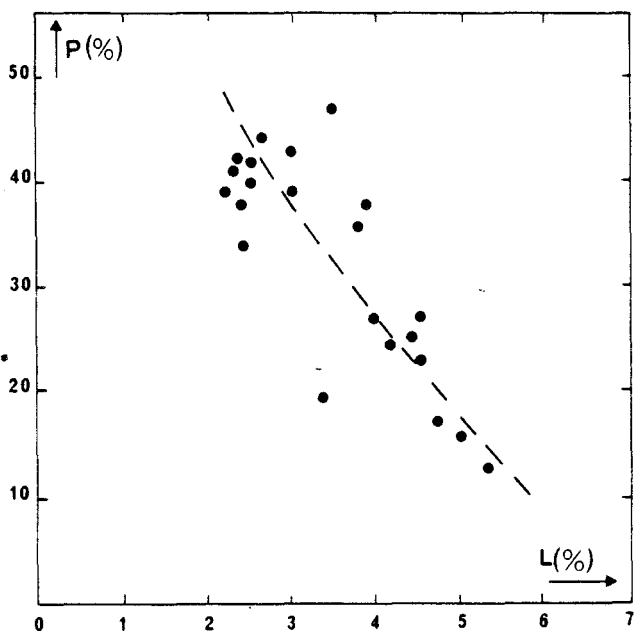
of the polarization measurements should correspond to the aerosol signature. In effect, the clouds tend to increase the radiance, but, except in the rainbow direction, they exhibit weak polarization. Therefore, the presence of clouds within the radiometer field of view must lead to depolarization of the signal and to increase of the radiance. As an example, we selected the observations performed at  $\lambda = 850$  nm, between 7h03 and 7h22, with a scattering angle ranging from  $90^\circ$  to  $100^\circ$ . Figure 10 shows that the correlation between the measured radiances and polarization ratios supports this idea.

To ensure that clear-sky measurements exist in sequences a) and b), we analyzed the possibility of observing the sunglint, which must correspond to direct sun-sea-balloon cloudless paths. As pointed out previously, the sunglint detectivity is better in the polarization measurements than in the radiance ones. We therefore considered the observed polarized radiance, i.e.,

$$L_p(\theta) = L(\theta)P(\theta).$$

Figure 11 shows the values of  $L_p(\theta)$  measured at 850 and 1650 nm, for a solar zenith angle near from  $58^\circ$ . In the sunglint, the polarized light comes almost from the direct reflection of the solar beam, just attenuated by the atmosphere on the direct

Figure 10. Correlation between the polarization ratio  $P(\theta)$  and the radiance  $L(\theta)$ , measured from 7.03 to 7.22 a.m. at  $\lambda = 850$  nm. Larger radiances correspond to smaller polarization ratios, in accordance with the expected effect resulting of a variable contamination of the field of view by small clouds.



sun-sea-balloon path. The corresponding polarized radiance may be estimated from the Fresnel reflection coefficients, by taking into account the wave slope distribution established by Cox and Munk (1954), and parametrized as a function of the wind speed. We plotted in Fig. 11 the polarized radiance predicted by this way for two values of the wind speed,  $v = 2$  and  $5 \text{ ms}^{-1}$ , and for  $\phi_c - \phi_s = 8^\circ$ . We reported also computations corresponding to  $v = 5 \text{ ms}^{-1}$  and  $\phi_c - \phi_s = 0^\circ$ , the measured difference in azimuth between the scan plane and the principal plane. The atmospheric transmission was calculated for assumed aerosol optical thicknesses  $\tau_a = 0.2$  at  $\lambda = 850$  nm and  $\tau_a = 0.1$  at  $\lambda = 1650$  nm, corresponding to mean conditions (i.e., a meteorological visibility of 23 km for a continental model). Actual values of the aerosol optical thicknesses will be derived later from the polarization analysis, but analysis of the radiance behavior around the specular direction does not require accurate estimates of the aerosol optical thickness. Considering the dispersion of the measurements resulting from the gondola stabilization and possible variations of the sea surface roughness from place to place, the calculations corresponding to the  $5 \text{ ms}^{-1}$  wind speed match correctly the upper values of  $L_p(\theta)$ . An assumed wind speed of  $2 \text{ ms}^{-1}$  seems to give a too sharp behavior, and we note that  $5 \text{ ms}^{-1}$  is the wind speed observed by the Biarritz weather station.

Figure 11 thus confirms that cloudless observations exist in sequences a) and b), from which the aerosol characterization is possible. As explained previously, this analysis will be conducted using the lower boundary of the radiances and the upper boundary of the polarization ratios. These envelopes will be compared to calculations of the atmospheric signal for cloudless conditions. These calculations will take into account the well-known Rayleigh component, and an aerosol component whose optical thickness, refractive index, and size distribution will have to be defined. Although this is a secondary effect in the modeling process, the aerosol vertical distribution is assumed to be logarithmic with a 2 km scale height. The boundary condition at the bottom of the atmosphere will correspond to the rough sea surface, modeled according to the model of Cox and Munk (1954) for a  $5 \text{ ms}^{-1}$  wind speed, and the signal will be calculated by the successive order of scattering method.

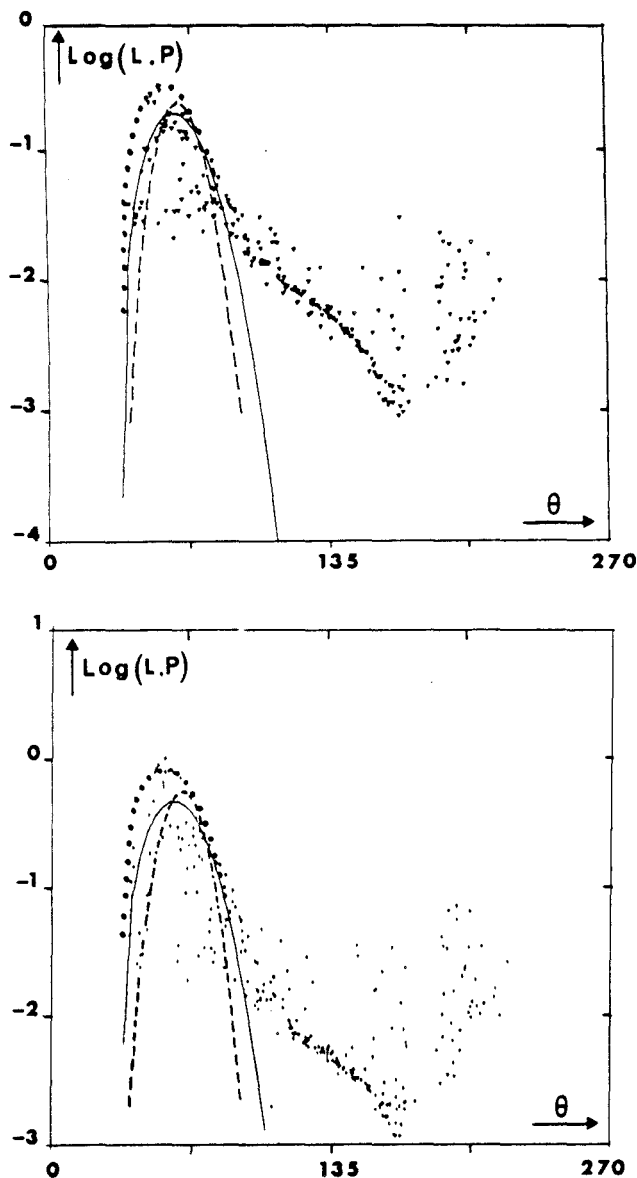


Figure 11. Dots: Polarized radiances [i.e.,  $P(\theta)L(\theta)$ ], measured at  $\lambda = 850$  nm (upper figure) and at  $\lambda = 1650$  nm (lower figure). The measurements are taken from sequence b). Continuous curves: polarized radiance corresponding to the light reflected, from the direct solar beam, upon the sea surface (sunglint). The sea surface is modeled according to the wave slope distribution of Cox and Munk (1954). Computations have been done for  $v = 5$   $\text{ms}^{-1}$ ,  $\phi_o - \phi_s = 8^\circ$  (—),  $v = 5$   $\text{ms}^{-1}$ ,  $\phi_o - \phi_s = 0^\circ$  ( $\cdots$ ), and  $v = 2$   $\text{ms}^{-1}$ ,  $\phi_o - \phi_s = 8^\circ$  (---).

Since, during the campaign, a ground station was based at the coast, at Mimizan (see Fig. 2), we will first examine the results of these observations. They will provide a first estimate of the aerosol component for which the atmospheric signal will be calculated and will be compared with the balloon measurements.

#### Ground-Based Measurements

During the campaign, a ground station based near the coast, at Mimizan, provided on clear days measurements of the extinction of the direct solar beam, from 400 to 2200 nm, and of the radiance and the polarization of the diffuse sky light, at 850 and 1650 nm. The weather conditions on 5 July morning (see AVHRR image, Fig. 3) prevented the ground truth measurements from being made at the time of the balloon overpass, but two sets of measurements were available on 4 July and on 5 July in the afternoon. For these two sets, both the behaviors of the solar beam extinction and of the sky light polarization are very similar and then show a good stability of the aerosol properties, so that the aerosol model derived from these measurements should be representative of the aerosols prevailing during the balloon experiment.

The analysis of this kind of ground measurements has been reported by Deuzé et al. (1987). First, the aerosol optical thicknesses  $\tau_a(\lambda)$  are obtained from the extinction measurements at different wavelengths  $\lambda$  ranging from 0.4 to 2.2  $\mu\text{m}$ , and from  $\tau_a(\lambda)$  the aerosol size distribution is deduced by using the inversion method of King et al. (1978). On the other hand, the radiance and the polarization ratio of the sky light—obtained from a polarimeter similar to the balloon-borne instrument—are measured in the principal plane. The scans are performed for low solar elevations, in order to provide measurements in the backscattering directions, where the polarization is more sensitive to the particle refractive index. These measurements provide independent information about the aerosols, which is tested against the results derived from the extinction data.

The aerosol optical thicknesses  $\tau_a(\lambda)$ , measured on 5 July afternoon are graphed in Fig. 12a), and the aerosol size distribution retrieved from these measurements is shown in Fig. 12b). The size distribution shows a large abundance of small particles, and also a mode of larger particles, which corresponds to the positive concavity of the  $\tau_a$  vs.  $\lambda$  curve [Fig. 12a)] towards near infrared wavelengths.

The aerosol size distribution derived from  $\tau_a(\lambda)$  does not depend on the particle refractive index, but the polarization measurements of the diffuse sky light can be used to estimate this parameter. The radiance and the polarization ratios observed from the ground on 5 July afternoon have been

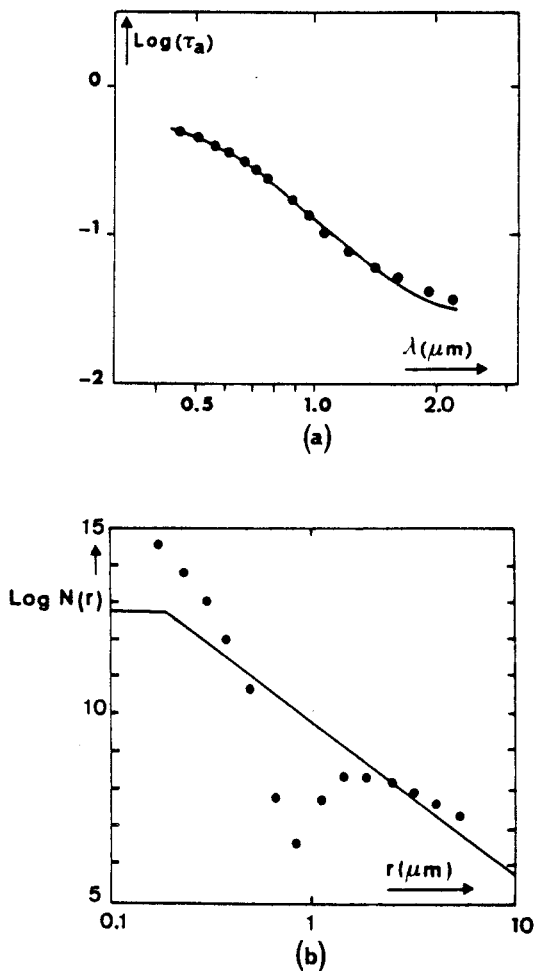


Figure 12. a) Aerosol optical thickness  $\tau_a(\lambda)$ , derived from the solar beam transmission measured at Mimizan, on 5 July 1985 afternoon; the measurements (●) are compared with the optical thicknesses (—) calculated *a posteriori*, from the retrieved aerosol size distribution. b) Aerosol size distribution  $N(r)$ , retrieved from the inversion of  $\tau_a(\lambda)$ , according to the method of King et al. (1978) (●). We also reported (—) the inverted size distribution for the balloon-borne polarization measurements.

reported in Fig. 13. For different guesses of the particle refractive index  $m$ , we calculated the scattering characteristics of the aerosol component and then derived, from the successive order of scattering code, the radiance and the polarization of the downward diffuse sky light, for the conditions corresponding to the observations. The best fit was obtained for  $m = 1.55$ , which is typical of continental aerosols. The results are compared with the observations in Fig. 13. The agreement is rather good for the polarization diagrams. The ground-based photopolarimeter was not calibrated in radiance but the aerosol optical thicknesses are here directly derived from the transmission measure-

ments. For the radiance comparison, we just fitted the measurements at the scattering angle  $\theta = 100^\circ$ ; the angular distribution of the radiance is retrieved by the model.

Then, with this model as input in the radiation code, the upward atmospheric signal above the ocean was calculated and was compared with the balloon observations. Two sets of balloon measurements were selected from sequences a) and b); the corresponding radiances and polarization ratios, at 850 and 1650 nm, are reported in Fig. 14. The radiation code was run for the boundary condition corresponding to the Fresnel reflection over the sea surface, with the Cox and Munk (1954) wave slope distribution defined for a wind speed of  $5 \text{ ms}^{-1}$ . According to Figs. 2 and 3, the small gap observed on the polarization ratio at  $\theta = 60^\circ$  [Figs. 14 and 15, but also Figs. 4a) and 5a)] corresponds to the coast line view. The computations were then also performed for a boundary condition corresponding to a Lambertian reflector with a typical radiance for vegetation of 0.5. Since the measurement corresponded to low solar elevations, the contribution of the ground is quite negligible. The difference between the two runs lies in the Fresnel reflection which brings a significant contribution to the polarization when aiming the ocean.

Figure 14 shows that, at 850 nm, the predicted radiances agree with the observed ones; meanwhile the model predictions slightly overestimate the observed polarization. But the main disagreements occur at 1650 nm. The aerosol optical thickness derived from the ground measurements seems too small at this wavelength, so that the model leads to a large underestimate of the scattered light observed from the balloon; in the glitter spot, on the contrary, it overestimates the reflected light as a result of the overestimate of the atmospheric direct transmission. On the other hand, the predicted polarization ratios are too high compared with the measurements. These two defects are consistent with the hypothesis that the aerosol particles observed at the coast are smaller than those observed from the balloon.

As a conclusion, although the comparison in Fig. 14 is not too bad, the systematic discrepancies suggest that the two sets of observations may bear upon different particles, and that the self-consistency of the balloon measurements may be searched for within an aerosol model different from that deduced from the coast measurements.

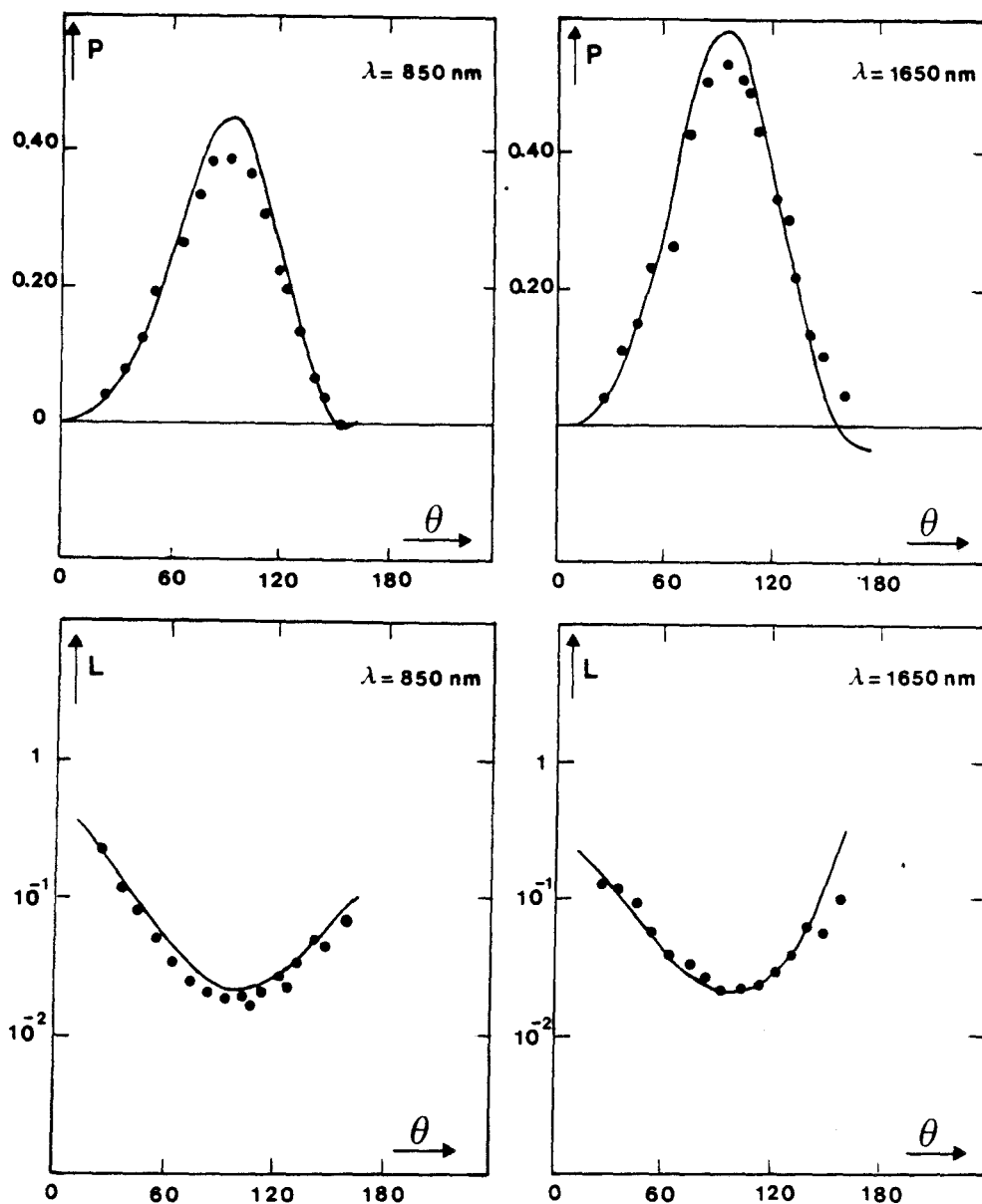


Figure 13. (●) Polarization ratios (upper figure) and radiances (lower figure), measured at Mimizan on 5 July 1985 afternoon vs. the scattering angle  $\theta$ . (—) Signals calculated by using for the aerosol component: the inverted size distribution reported in Fig. 12b), the refractive index  $m = 1.55$ , and the measured optical thicknesses, i.e.,  $\tau_a(\lambda = 850 \text{ nm}) = 0.20$  and  $\tau_r(\lambda = 1650 \text{ nm}) = 0.05$ . The measurements correspond to a scan in the principal plane, at a solar elevation  $h_s = 18^\circ$ .

#### Inversion of the Balloon Measurements

We therefore looked to invert the balloon measurements independently of the ground measurements. The inversion scheme was performed as follows. The aerosol size distribution was assumed to be a modified Junge law, in the form

$$n(r) = C, \quad \text{for } r < r_0$$

$$n(r) = C(r/r_0)^{-\nu}, \quad \text{for } r > r_0$$

with the slope  $\nu$  and the lower radius  $r_0$  as free parameters.

Given the aerosol refractive index, estimates of  $\nu$ ,  $r_0$ , and of  $\tau_a(\lambda)$  were first derived from the observations performed at  $\theta = 100^\circ$ . This inversion step was run according to the scheme described by Santer et al. (1983). Since the scheme is developed within the single scattering approximation, the multiple scattering influence in the measurements was crudely accounted for, by using an approximate estimate of the resulting depolarization effect (Santer, 1984). Then, with this first guess as input in the radiation code, the atmospheric signals were

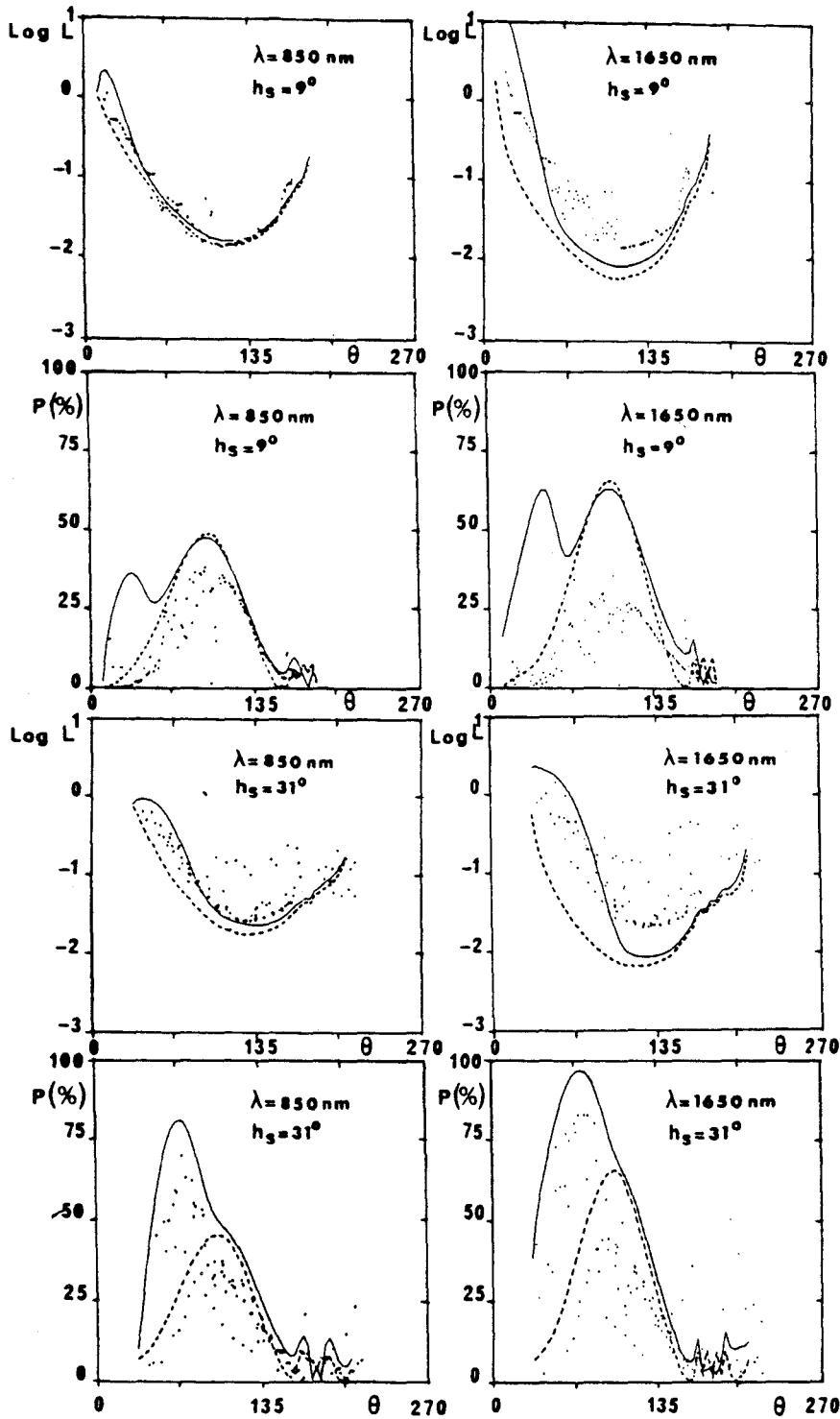


Figure 14. Dots: radiances and polarization ratios measured from the balloon, at  $\lambda = 850 \text{ nm}$  and  $\lambda = 1650 \text{ nm}$ , vs.  $\theta$ . The two sequences correspond to solar elevations  $h_s = 9^\circ$  (upper figure) and  $h_s = 31^\circ$  (lower figure). Curves: signals calculated by using for the aerosol component the model derived from the ground-based measurements (with  $m = 1.55$ ), and with the boundary condition corresponding to the sea surface reflection, for  $\nu = 5 \text{ ms}^{-1}$  (—). Calculations corresponding to a black surface as the boundary condition are shown also (---), to be compared with measurements concerned with land observations (see text).

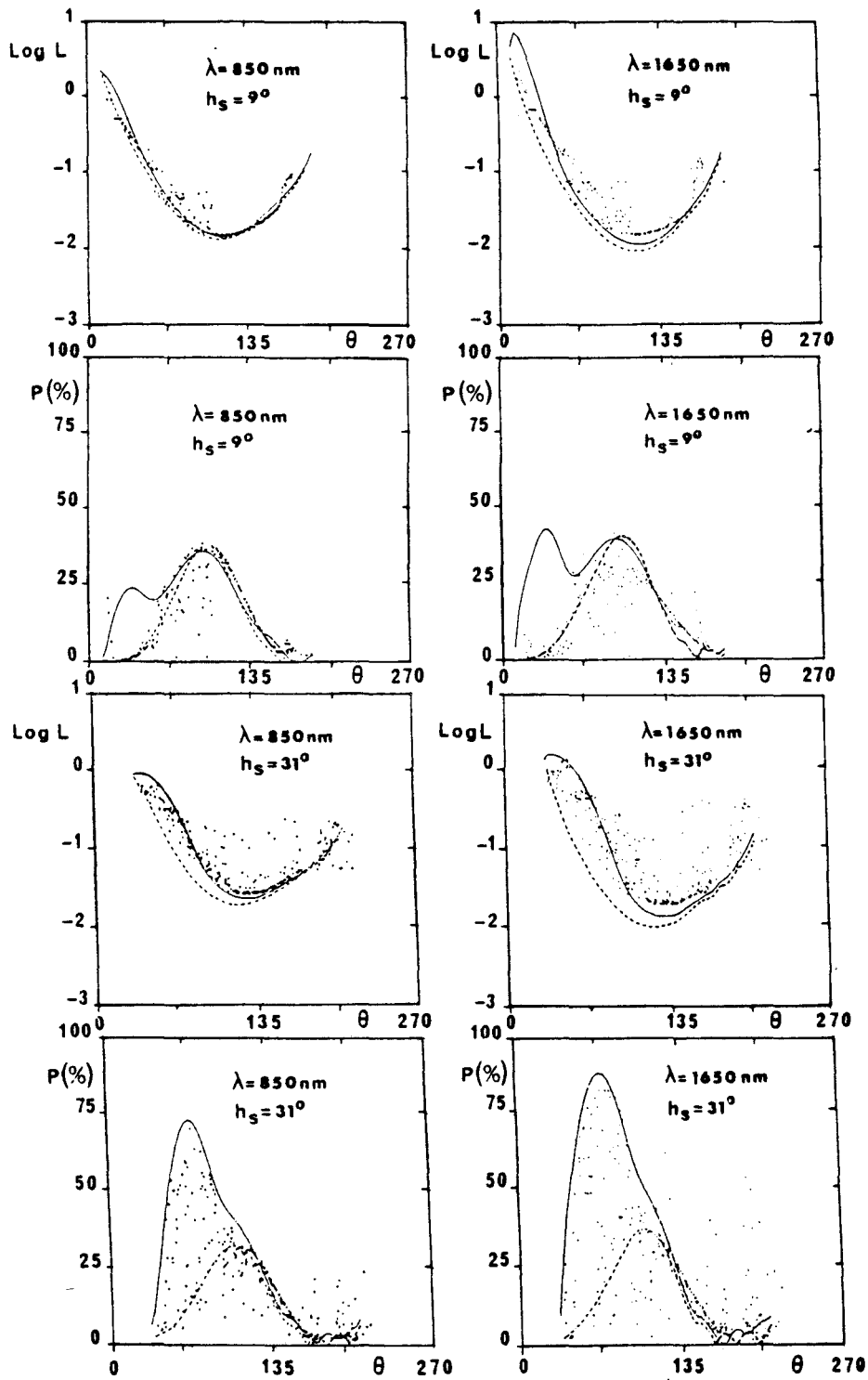


Figure 15. Same legend as for Fig. 14, but the calculated signals now correspond to the aerosol model inverted from the balloon measurements.

calculated and compared to the whole set of measurements, resulting in an improved aerosol model.

The whole scheme was applied for a set of refractive index values. Since the maritime aerosols are reputed to be nonabsorbing, the imaginary part of the refractive index was assumed to be zero.

The best fit was obtained by this way for a refractive index  $m = 1.40$ , with  $r_0 = 0.18 \mu\text{m}$ ,  $\nu = 4.09$ ,  $\tau_a(\lambda = 850 \text{ nm}) = 0.24$  and  $\tau_a(\lambda = 1650 \text{ nm}) = 0.12$ . We notice that the aerosol optical thicknesses are closed from those used in the sunglint analysis.

The accuracy on the refractive index is estimated to be about  $\Delta m = 0.05$ . Since the aerosol properties are well defined from the polarization inversion, the accuracy on the aerosol optical thickness is directly dependent on the radiance calibration quality; with  $\Delta\tau_a(\lambda = 850 \text{ nm}) \approx 0.03$  and  $\Delta\tau_a(\lambda = 1650 \text{ nm}) = 0.02$ .

The inverted Junge size distribution is graphed in Fig. 12b) for comparison to the size distribution derived from the ground-based measurements. The polarization is not sensitive enough to detect bimodalities. As expected, the aerosols remoted at Mimizan seemed to present a larger amount of small particles.

The corresponding predicted signals are compared with the measurements in Fig. 15. Clearly, the agreement is much better than in Fig. 14. As the inversion scheme is mainly based on the polarization measurements at  $\theta = 100^\circ$ , the fit is particularly good around this direction, but the agreement is correct over all the scans, and the retrieved model is able to fit the two chosen sequences, despite the very different solar elevations ( $h_s = 9^\circ$  and  $31^\circ$ ).

The previous analysis is certainly limited. We ignored the indirect influence of the clouds into the measurements, i.e., the light scattered from the clouds, which is partly reflected on the sea surface and scattered by the aerosols. Modeling of these effects, however, is rather difficult. We also ignored the contribution of the white caps in the signal, but, for a  $5 \text{ ms}^{-1}$  wind speed, it seems that the expected white cap coverage is quite null, according to Koepke (1984).

On the other hand, the analysis was based on Mie theory. A major question about the aerosol retrieval is the adequacy of the spherical hypothesis. Microscopic investigations have shown from a

long time that nonspherical-shaped aerosols exist. However, the exact weight of such particles in the signal was unknown. Observations of nonspherical particles in the atmospheric signal, in dust storm conditions, have been recently reported by Nakajima et al. (1988). We only can point out that the Mie theory allows us to fit our measurements. Since polarization is known to be sensitive to the particle shape, we probably observed spherical particles, corresponding to hydrated aerosols.

At last, it seems from Fig. 15 that the retrieved aerosol model is valid. It does not agree accurately with the model derived from the ground-truth experiment, but it is quite possible that the aerosol characteristics vary from the coast to the open sea. In fact, the mode of large particles which appears in Fig. 12b) should correspond to a maritime haze component, whose concentration could increase from the coast towards the open sea. Concerning the rather low refractive index found from the balloon measurements, it should be indicative of a large amount of water soluble components, but this last result is certainly questionable on account of the limited quality of the measurements and of the analysis.

Therefore, despite the limitations of the analysis, mainly related to the semicloudy conditions, and the lack of agreement with the ground-truth experiment, the balloon measurements are largely successful. They look self-consistent and clearly show that polarization measurements from space may provide valuable information about the tropospheric aerosols.

## CONCLUSIONS

A first attempt to observe the aerosols from space by using polarization measurements was done from a stratospheric balloon, on 5 July 1985. The overflight of the Bay of Biscay was chosen, in order to avoid contamination of the measurements by the surface. The experiment was largely successful, and the main problems result from the presence of clouds. Over the large cloud deck overflowed at the end of the experiment, we got information about the bidirectionality of the radiances, and the polarization measurements proved to be able to provide indications about the droplet dimensions. During the first part of the flight, aerosol signatures were present in the envelopes of the signals. The ground

truths were unable to validate definitively the balloon measurements, but the lack of agreement may come from the different times and locations of the two experiments. An inversion scheme of the atmospheric signals was developed and allowed us to retrieve an aerosol model which was consistent with both the polarization and radiance measurements. At last, observations of the sunglint selected from the measurements allowed us to test successfully the Cox and Munk (1954) model of the wave slope distribution, with respect to the predicted polarization of the reflected light.

Another polarimeter has now been designed. It will use a CCD array camera, allowing us to observe a given target in different directions, and avoiding the necessity of working over homogeneous sites like the ocean surface. This device should permit us to observe ground targets and to investigate the ability of polarization measurements concerning remote sensing, on a more general ground.

## REFERENCES

- Ahmad, Z., and Fraser, R. S. (1982), An iterative radiative transfer code for ocean-atmosphere system, *Appl. Opt.* 39:656-665.
- Balois, J. Y. (1985), Mise au point, essais, étalonnage et intégration d'un radio-polarimètre infrarouge embarquable à bord d'une plate-forme stratosphérique, Conservatoire National des Arts et Métiers, Lille, France.
- Coulson, L. K., and Whitehead, V. S. (1986), Polarized views of the earth from orbital altitude, *SPIE* 637:35,41.
- Cox, C., and Munk, W. H. (1954), The measurement of the roughness of the sea surface from photographs of the sun glitter, *J. Opt. Soc. Am.* 44:838-850.
- Deirmendjian, D. (1964), Scattering and polarization properties of water clouds and hazes in the visible and infrared, *Appl. Opt.* 3:187-196.
- Deuzé, J. L., Devaux, C., Herman, M., Santer, R., and Tanré, D. (1987), Saharan aerosols over south of France. Characterization derived from satellite data and ground-based measurements, *J. Appl. Meteorol.* 27:680-686.
- Dollfus, A., Deschamps, M., and Ksanfomaliti, L. V. (1983), The surface texture of the martian soil from the spacecraft Mars-5 photopolarimeters, *Astron. Astrophys.* 23:225-237.
- Egan, G. W. (1985), *Photometry and Polarization in Remote Sensing*, Elsevier, Amsterdam.
- Hansen, J. E. (1972), Information contained in the intensity and polarization of scattered sunlight, unnumbered report.
- Hansen, J. E., and Hovenier, J. W. (1974), Interpretation of the polarization of Venus, *J. Atmos. Sci.* 28:120-125.
- Herman, M., Balois, J. Y., Gonzalez, L., Lecomte, P., Lenoble, J., Santer, R., and Verwaerde, C. (1986), Stratospheric aerosol observations from a balloon-borne polarimetric experiment, *Appl. Opt.* 15:3573-3584.
- Kattawar, G. W., Plass, G. N., and Guinn, J. A. (1973), Monte Carlo calculations of the polarization of radiation in the Earth's atmosphere-ocean system, *J. Phys. Oceanogr.* 3:353-372.
- King, M. D., Byrne, D. M., Herman, B. M., and Reagan, J. A. (1978), Aerosol size distributions obtained by inversion of spectral optical depth measurements, *J. Atmos. Sci.* 35:2153-2167.
- Koepke, P. (1984), Effective reflectance of oceanic white caps, *Appl. Opt.* 23:1816-1824.
- Nagaraja Rao, C. R. (1969), Balloon measurements of the polarization of the light diffusely reflected by the Earth's Atmosphere, *Planet. Space Sci.* 17:1307-1309.
- Nakajima, T., Tanaka, M., Yamano, M., Shiobara, M., and Arao, K. (1988), Aerosol optical characteristics in the yellow sand events of May 1982 in Nagasaki, *J. Meteorol. Soc. Jpn.*, forthcoming.
- Plass, G. N., Kattawar, G. W., and Guinn, J. A. (1975), Radiative transfer in the earth's atmosphere and ocean: influence of ocean waves, *Appl. Opt.* 14:1924-1936.
- Prosch, T., Hennings, D., and Raschke, G. (1982), Studies on polarization of light over water surfaces, *Ann. Meteorol.* 18:113.
- Santer, R. (1984), Caractérisation des aérosols à partir du rayonnement solaire diffusé. Applications aux atmosphères de la Terre, de Vénus et de Saturne, Thèse d'Etat, Université de Lille, France.
- Santer, R., Herman, M., and Lenoble, J. (1983), Retrieval of aerosol characteristics from polarization measurements of reflected solar radiation above the oceans, *Adv. Space Res.* 2:65-70.
- Santer, R., Deschamps, M., Ksanfomaliti, K. L. V., and Dollfus, A. (1985), Photopolarimetric analysis of the Martian atmosphere by the Soviet Mars-5 Orbiter, *Astron. Astrophys.* 150:217-228.
- Santer, R., Deschamps, M., Ksanfomaliti, L. V., and Dollfus, A. (1986), Photopolarimetry of Martian aerosols, II—Limb and terminator measurements, *Astron. Astrophys.* 158:247-258.
- Takashima, T., and Masuda, K. (1985), Degree of radiance and polarization of the upwelling radiation from an atmosphere-ocean system, *Appl. Opt.* 24:2423-2429.
- Vanderbilt, V. C., and Grant, L. (1984), Light polarization measurements: a method to determine the specular and diffuse light-scattering properties of both leaves and plant canopies, in *II Coll. Int. Signatures Spectrales D'objets en Télédétection*, INRA, Bordeaux.
- Walraven, R. L., and Coulson, K. L. (1972), Measurements of the light properties of gypsam sand, *Contrib. to Atmos. Sci.*, N. 17, University of California, Davis.

## FOURIER SERIES EXPANSION OF THE TRANSFER EQUATION IN THE ATMOSPHERE–OCEAN SYSTEM

J. L. DEUZÉ, M. HERMAN, and R. SANTER†

Laboratoire d'Optique Atmosphérique, Université des Sciences et Techniques de Lille,  
59655 Villeneuve d'Ascq Cedex, France

(Received 6 April 1988; received for publication 12 December 1988)

**Abstract**—We consider radiative transfer in a plane-parallel atmosphere bounded by a rough ocean surface. The problem is solved by using a Fourier series decomposition of the radiation field. For the case of a Lambertian surface as a boundary condition, this decomposition is classically achieved by developing the scattering phase matrix in a series of Legendre functions. For the case of a rough ocean surface, we obtain the decomposition by developing both the Fresnel reflection matrix and the wave facet distribution function in Fourier series. This procedure allows us to derive the radiance field for the case of the ruffled ocean surface, with a computation time only a few percent larger than for the case of a Lambertian surface.

### INTRODUCTION

Remote sensing from satellites allows frequent observations with a wide coverage of the Earth. In the visible range, the measured upward radiance is very sensitive to atmospheric and surface parameters and may provide information about these parameters. An impressive amount of work has been done to compute the satellite data as a function of these parameters which is obviously necessary to retrieve this information. In these computations, however, the lower boundary condition generally corresponds to a Lambert reflector. This approach is valid for land observations. But simulations of the satellite signal for the case of a bi-directional reflectance are interesting for some land observations (for example, for water or ice surfaces) and for oceanic observations for which the bi-directional reflectance is related to the Fresnel reflection on the sea surface. Moreover, the percent polarization of the radiation field, which may be valuable information, generally is not taken into account in these computations.

Fraser and Walker<sup>1</sup> assumed a simple model of the ocean–atmosphere system (a standard gas on a smooth ocean) and reported the intensity and degree of polarization. For the same case of a smooth sea surface, Dave<sup>2</sup> and Katawar et al<sup>3</sup> conducted computations for more realistic atmospheric models. For a rough sea surface exhibiting the true complexity of the boundary conditions, Raschke,<sup>4</sup> Plass et al<sup>5</sup> and Quenzel and Kaestner<sup>6</sup> solved the problem, but neglected the polarization of diffuse radiation in the atmosphere as well as polarization of the reflected radiation. Ahmad and Fraser<sup>7</sup> and Takashima and Masuda<sup>8</sup> performed complete calculations accounting for the degree of polarization and also presented some limited comparisons.

The difficulty of exact radiative transfer calculations for rough-ocean reflection is mainly numerical. Most radiative transfer calculations are made tractable by using Fourier series decomposition of the radiation field as a function of the azimuth. For the case of a Lambertian ground or of a smooth sea surface, the boundary condition is compatible with this series expansion. On the other hand, this approach is not easy to follow for the case of a rough ocean because of the complexity introduced by the wave slopes. Here, we solve this problem, taking into account radiation-field polarization.

†To whom all correspondence should be addressed.

## THEORETICAL BACKGROUND

*Formal transfer equation for the s Fourier component*

The radiative transfer equation in a plane-parallel finite atmosphere can be written as

$$\mu \frac{\partial \tilde{I}(\delta, \mu, \phi)}{\partial \delta} = \tilde{I}(\delta, \mu, \phi) - \frac{\omega_0}{4\pi} \int_0^{2\pi} \int_{-1}^{+1} \tilde{P}(\delta, \mu, \phi, \mu', \phi') \tilde{I}(\delta, \mu', \phi') d\mu' d\phi' - \frac{\omega_0}{4\pi} \exp(\delta/\mu_s) \tilde{P}(\delta, \mu, \phi, \mu_s, \phi_s) \tilde{E}_s, \quad (1)$$

where  $\delta$  is the optical depth,  $\omega_0$  the albedo for single scattering,  $\mu$  the cosine of the zenith angle,  $\phi$  the azimuth angle, the  $E_s$  the solar irradiance; the subscript  $s$  refers to solar quantities. The components of the four-vector  $\tilde{I}$  are the Stokes parameters  $I$ ,  $Q$ ,  $U$ , and  $V$ , with the meridian plane as reference. In Eq. (1), the kernel  $\tilde{P}(\delta, \mu, \phi, \mu', \phi')$  is given by

$$\tilde{P}(\mu, \phi, \mu', \phi') = \tilde{L}(-\chi) \tilde{P}(\cos \Theta) \tilde{L}(\chi'), \quad (2)$$

where  $\tilde{P}(\cos \Theta)$  is the phase matrix, with the scattering plane as reference and  $\Theta$  the scattering angle. We have omitted for convenience the dependence of the phase matrix on the optical depth. The matrices  $\tilde{L}(-\chi)$  and  $\tilde{L}(\chi')$  are required to rotate the meridian planes before and after scattering onto the scattering plane.<sup>9</sup> Here,

$$\tilde{L}(\chi) = \begin{pmatrix} 1 & 0 & 0 & 0 \\ 0 & \cos 2\chi & \sin 2\chi & 0 \\ 0 & -\sin 2\chi & \cos 2\chi & 0 \\ 0 & 0 & 0 & 1 \end{pmatrix}. \quad (3)$$

A usual procedure for solving the transfer equation is to consider a Fourier series expansion in azimuth for the radiance. If we consider an atmosphere illuminated by the solar beam [with Stokes parameters  $(E_s, 0, 0, 0)$ ] and with symmetrical boundary conditions with respect to the incident plane, then

$$\begin{pmatrix} I(\delta, \mu, \phi) \\ Q(\delta, \mu, \phi) \\ U(\delta, \mu, \phi) \\ V(\delta, \mu, \phi) \end{pmatrix} = \sum_{s=0}^{\infty} (2 - \delta_{0,s}) \begin{pmatrix} I^s(\delta, \mu) \cos s(\phi - \phi_s) \\ Q^s(\delta, \mu) \cos s(\phi - \phi_s) \\ U^s(\delta, \mu) \sin s(\phi - \phi_s) \\ V^s(\delta, \mu) \sin s(\phi - \phi_s) \end{pmatrix}. \quad (4)$$

If the phase matrix terms are expanded in the same manner in a Fourier series, then the complete problem separates into the following set of independent equations:

$$\mu \frac{\partial \tilde{I}^s(\delta, \mu)}{\partial \delta} = \tilde{I}^s(\delta, \mu) - \frac{\omega_0}{2} \int_{-1}^{+1} \tilde{P}^s(\mu, \mu') \tilde{I}^s(\delta, \mu') d\mu' - \frac{\omega_0}{4\pi} \tilde{P}^s(\mu, \mu_s) \exp(\delta/\mu_s) E_s. \quad (5)$$

A major advantage of Fourier series expansion of the transfer equation lies in the simplicity of the corresponding transfer code, since integrations on  $\phi$  and  $\theta$  are separated. Moreover, only the zeroth term provides answers to interesting problems such as flux computations or radiance estimates in the nadir-viewing direction, as involved in LANDSAT or SPOT observations; according to the reciprocity principle, nadir-radiance for any solar zenith angle  $\theta_s$  may be derived from radiance at the viewing angle  $\theta_s$  for null solar zenith angle, which requires only calculation of the zeroth term of the Fourier series.

The  $\tilde{P}^s(\mu, \mu_s)$  term in Eq. (5) may be derived numerically, but a more powerful approach involves the use of circularly polarized states for the light representation. By assuming that the terms of the phase matrix are developed in Legendre polynomials  $P_l$  and associated functions  $P_l^2$  in the form

$$\tilde{P}(\cos \Theta) = \begin{pmatrix} \Sigma_{l=0}^L \beta_l P_l(\cos \Theta) & \Sigma_{l=2}^L \gamma_l P_l^2(\cos \Theta) & 0 & 0 \\ \Sigma_{l=2}^L \gamma_l P_l^2(\cos \Theta) & \Sigma_{l=0}^L \beta_l P_l(\cos \Theta) & 0 & 0 \\ 0 & 0 & \Sigma_{l=0}^L \delta_l P_l(\cos \Theta) & -\Sigma_{l=2}^L \epsilon_l P_l^2(\cos \Theta) \\ 0 & 0 & \Sigma_{l=2}^L \epsilon_l P_l^2(\cos \Theta) & \Sigma_{l=0}^L \delta_l P_l(\cos \Theta) \end{pmatrix}, \quad (6)$$

it may be shown<sup>10-13</sup> that the kernel  $\tilde{P}(\mu, \phi, \mu', \phi')$  in Eq. (1) may be expanded into the form

$$\tilde{P}(\mu, \phi, \mu', \phi') = \sum_{s=0}^L (2 - \delta_{0,s}) [\cos s(\phi - \phi') \tilde{P}_c^s(\mu, \mu') + \sin s(\phi - \phi') \tilde{P}_s^s(\mu, \mu')], \quad (7)$$

where

$$\tilde{P}_c^s(\mu, \mu') = \begin{pmatrix} \Sigma_{l=s}^L \beta_l P_l^s P_l^{s'} & \Sigma_{l=s}^L \gamma_l P_l^s R_l^{s'} & 0 & 0 \\ \Sigma_{l=s}^L \gamma_l R_l^s P_l^{s'} & \Sigma_{l=s}^L (\alpha_l R_l^s R_l^{s'} + \zeta_l T_l^s T_l^{s'}) & 0 & 0 \\ 0 & 0 & \Sigma_{l=s}^L (\alpha_l T_l^s T_l^{s'} + \zeta_l R_l^s R_l^{s'}) & -\Sigma_{l=s}^L \epsilon_l R_l^s P_l^{s'} \\ 0 & 0 & \Sigma_{l=s}^L \epsilon_l P_l^s R_l^{s'} & \Sigma_{l=s}^L \delta_l P_l^s P_l^{s'} \end{pmatrix}, \quad (8)$$

and

$$\tilde{P}_s^s(\mu, \mu') = \begin{pmatrix} 0 & 0 & \Sigma_{l=s}^L \gamma_l P_l^s T_l^{s'} & 0 \\ 0 & 0 & \Sigma_{l=s}^L (\alpha_l R_l^s T_l^{s'} + \zeta_l T_l^s R_l^{s'}) & -\Sigma_{l=s}^L \epsilon_l T_l^s P_l^{s'} \\ -\Sigma_{l=s}^L \gamma_l T_l^s P_l^{s'} & -\Sigma_{l=s}^L (\alpha_l T_l^s R_l^{s'} + \zeta_l R_l^s T_l^{s'}) & 0 & 0 \\ 0 & -\Sigma_{l=s}^L \epsilon_l P_l^s T_l^{s'} & 0 & 0 \end{pmatrix}. \quad (9)$$

In these equations,  $P_l^s, R_l^s, T_l^s$  stand for  $P_l^s(\mu), R_l^s(\mu), T_l^s(\mu)$  and  $P_l^{s'}, R_l^{s'}, T_l^{s'}$  stand for  $P_l^s(\mu'), R_l^s(\mu'), T_l^s(\mu')$ ;  $R_l^s(\mu)$  and  $T_l^s(\mu)$  are linear combinations of the generalized Legendre functions  $P_{2,2}^s(\mu)$  and  $P_{2,-2}^s(\mu)$ , which are defined in the Appendix.

When substituting Eqs. (4), (7), (8), and (9) into Eq. (1), it separates immediately into the set of independent Eqs. (5) with

$$\tilde{P}^s(\mu, \mu') = \begin{pmatrix} \Sigma_{l=s}^L \beta_l P_l^s P_l^{s'} & \Sigma_{l=s}^L \gamma_l P_l^s R_l^{s'} & -\Sigma_{l=s}^L \gamma_l P_l^s T_l^{s'} & 0 \\ \Sigma_{l=s}^L \gamma_l R_l^s P_l^{s'} & \Sigma_{l=s}^L (\alpha_l R_l^s R_l^{s'} + \zeta_l T_l^s T_l^{s'}) & -\Sigma_{l=s}^L (\alpha_l R_l^s T_l^{s'} + \zeta_l T_l^s R_l^{s'}) & \Sigma_{l=s}^L \epsilon_l T_l^s P_l^{s'} \\ -\Sigma_{l=s}^L \gamma_l T_l^s P_l^{s'} & -\Sigma_{l=s}^L (\alpha_l T_l^s R_l^{s'} + \zeta_l R_l^s T_l^{s'}) & \Sigma_{l=s}^L (\alpha_l T_l^s T_l^{s'} + \zeta_l R_l^s R_l^{s'}) & -\Sigma_{l=s}^L \epsilon_l R_l^s P_l^{s'} \\ 0 & -\Sigma_{l=s}^L \epsilon_l P_l^s T_l^{s'} & \Sigma_{l=s}^L \epsilon_l P_l^s R_l^{s'} & \Sigma_{l=s}^L \delta_l P_l^s P_l^{s'} \end{pmatrix}. \quad (10)$$

The required order  $L$  for the developments in Eq. (6) depends mainly on the dimension of the scattering particles. It is known that  $L = 2$  for molecular scattering; scattering by terrestrial aerosols typically requires about  $L = 48$ . The set of coefficients  $\beta_l, \gamma_l, \delta_l$ , and  $\epsilon_l$  may be computed by using orthogonality relations for Legendre functions and polynomials (see the Appendix for details);  $\alpha_l$  and  $\zeta_l$  are linear combinations of  $\beta_l$  and  $\delta_l$  as follows:

$$\sum_{l=0}^L (\beta_l + \delta_l) P_l(\mu) = \sum_{l=2}^L (\alpha_l + \zeta_l) P_{2,2}^l(\mu), \quad (11)$$

$$\sum_{l=0}^L (\beta_l - \delta_l) P_l(\mu) = \sum_{l=2}^L (\alpha_l - \zeta_l) P_{2,-2}^l(\mu). \quad (12)$$

*Boundary condition; reflection matrix for the rough ocean*

We now consider the atmosphere-ocean system. The boundary condition corresponding to the radiation scattered from the sea water is routinely accounted for by a Lambertian condition. Since

Fourier-series expansion of the radiation field raises no problem for such a condition, we will ignore this term and will limit ourselves to the surface-reflection problem.

Should the sea surface be horizontal, an incident beam would be reflected in the specular direction and the boundary condition at sea level becomes

$$\tilde{I}(\delta_1, -\cos \omega, \phi) = \tilde{R}(\omega)\tilde{I}(\delta_1, \cos \omega, \phi), \tag{13}$$

where  $\delta_1$  is the optical thickness of the atmosphere,  $\omega$  the incident angle, and  $\tilde{R}(\omega)$  the Fresnel matrix, expressed as a function of the complex Fresnel coefficients by<sup>14</sup>

$$\tilde{R}(\omega) = \frac{1}{2} \begin{pmatrix} r_l r_l^* + r_r r_r^* & r_l r_l^* - r_r r_r^* & 0 & 0 \\ r_l r_l^* - r_r r_r^* & r_l r_l^* + r_r r_r^* & 0 & 0 \\ 0 & 0 & r_l r_r^* + r_r r_l^* & r_l r_r^* - r_l r_l^* \\ 0 & 0 & r_l r_r^* - r_r r_l^* & r_l r_r^* + r_l r_l^* \end{pmatrix}. \tag{14}$$

Here,  $r_l$  and  $r_r$  depend on  $\omega$  and on the sea water complex refractive index  $m$ , according to

$$r_l = \frac{\sqrt{m^2 - \sin^2 \omega} - m^2 \cos \omega}{\sqrt{m^2 - \sin^2 \omega} + m^2 \cos \omega}, \tag{15}$$

$$r_r = \frac{\cos \omega - \sqrt{m^2 - \sin^2 \omega}}{\cos \omega + \sqrt{m^2 - \sin^2 \omega}}. \tag{16}$$

For visible and near-infrared wavelengths, the imaginary part of  $m$  is negligible<sup>15</sup> so that  $R_{3,4} = R_{4,3} = 0$ .

For the case of a rough surface, given an arbitrary observation direction  $(\mu, \phi)$  and the downward direction  $(\mu', \phi')$ , water facets exist with the normal direction  $N(\mu_n, \phi_n)$  such that they can reflect downward radiance towards the observer. The reflection geometry is shown in Fig. 1. According to Eq. (13), the resulting contribution  $d\tilde{I}(\delta_1, \mu, \phi)$  in  $\tilde{I}(\delta_1, \mu, \phi)$  from the downward radiance  $\tilde{I}(\delta_1, \mu', \phi')$  will be given by

$$d\tilde{I}(\delta_1, \mu, \phi) = f(\mu_n, \phi_n) \tilde{L}(-\chi) \tilde{R}(\omega) \tilde{L}(\chi') \tilde{I}(\delta_1, \mu', \phi') d\mu' d\phi'; \tag{17}$$

$\tilde{L}(-\chi)$  and  $\tilde{L}(\chi')$  have been introduced to take into account the required rotations of the meridian planes into the reflection plane, which is no longer a vertical one, and  $f(\mu_n, \phi_n)$  stands for the required weighting of  $\tilde{R}(\omega)$  by the density of water facets with the convenient inclination.

Using analysis of aerial photographs of the glitter, Cox and Munk<sup>16</sup> investigated the probability distribution of water facet normals. They showed that it is nearly independent of  $\phi_n$ . When

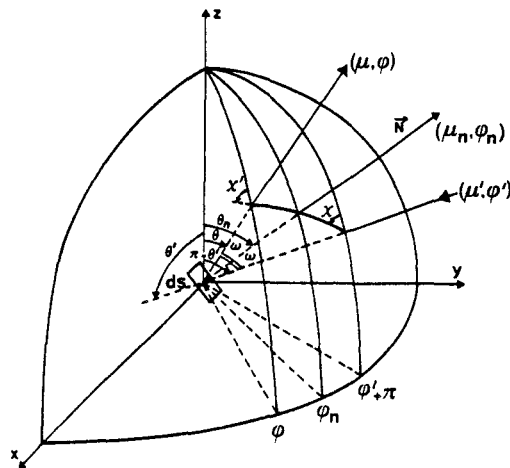


Fig. 1. Geometry of the reflection on a wave facet.

accounting for the transformation of this normal probability distribution into the energetic balance for reflection, it may be shown<sup>16</sup> that  $f(\mu_n, \phi_n)$  is given by

$$f(\mu_n, \phi_n) = \frac{1}{4\mu\mu_n} \frac{1}{\pi\sigma^2} \exp\left(-\frac{1-\mu_n^2}{\sigma^2\mu_n^2}\right). \quad (18)$$

In Eq. (18),  $\sigma$  is related to the wind speed  $v$  by

$$\sigma^2 = 0.003 + 0.00512v. \quad (19)$$

On the other hand, given the directions  $(\mu, \phi)$  and  $(\mu', \phi')$ , convenient normals  $\mathbf{N}$  are such that

$$\mu_n = \frac{|\mu - \mu'|}{2 \cos \omega} \quad (20)$$

and the resulting reflection angle  $\omega$  is given by

$$\cos 2\omega = -\mu\mu' - \sqrt{1-\mu^2} \sqrt{1-\mu'^2} \cos(\phi - \phi'). \quad (21)$$

Equations (18)–(21) determine the problem. Clearly,  $f(\mu_n, \phi_n)$  and  $\tilde{R}(\mu, \phi, \mu', \phi')$  [or  $\tilde{L}(-\chi)\tilde{R}(\omega)\tilde{L}(\chi')$ ] depend only on the azimuth difference  $(\phi - \phi')$ . By introducing the reflection matrix

$$\tilde{M}(\mu, \phi, \mu', \phi') = f(\mu_n, \phi_n)\tilde{R}(\mu, \phi, \mu', \phi'), \quad (22)$$

the boundary condition at sea level is given by

$$\tilde{I}(\delta_1, \mu > 0, \phi) = \tilde{M}(\mu, \phi, \mu_s, \phi_s)E_s \exp(\delta_1/\mu_s) + \int_0^{2\pi} \int_0^{+1} \tilde{M}(\mu, \phi, \mu', \phi')\tilde{I}(\delta_1, \mu', \phi') d\mu' d\phi'. \quad (23)$$

#### FOURIER-SERIES EXPANSION OF THE REFLECTION MATRIX

In order to preserve the Fourier-series expansion of the transfer equation, we need developments of the  $M_{ij}$  terms in cosine or sine series of the azimuth, according to the parity of the Stokes parameters involved. These developments may be derived directly by numerical methods. Such a solution requires, however, impressive data storage and is very time consuming. On the other hand, we note the similarity between  $\tilde{R}(\omega)$  and  $\tilde{P}(\cos \Theta)$  when considering  $(\pi - 2\omega)$  as the scattering angle  $\Theta$ . Therefore, Fourier-series expansion of  $\tilde{R}(\mu, \phi, \mu', \phi')$  may be achieved in the same manner as for the case of the scattering matrix. Since this term does not depend on the sea-surface roughness, this calculation is only needed once. Then, by expanding the scalar term  $f(\mu_n, \phi_n)$  into the Fourier series of  $(\phi - \phi')$ , the expected developments will be obtained as a mixture of the two developments.

First, in parallel with Eq. (6), we expand the terms of  $\tilde{R}(\omega)$  in a series of appropriate Legendre functions of  $\Omega = \pi - 2\omega$  into the form

$$\tilde{R}(\omega) = \begin{pmatrix} \Sigma_{l=0}^L b_l P_l(\cos \Omega) & \Sigma_{l=2}^L g_l P_l^2(\cos \Omega) & 0 & 0 \\ \Sigma_{l=2}^L g_l P_l^2(\cos \Omega) & \Sigma_{l=0}^L b_l P_l(\cos \Omega) & 0 & 0 \\ 0 & 0 & \Sigma_{l=0}^L d_l P_l(\cos \Omega) & -\Sigma_{l=2}^L e_l P_l^2(\cos \Omega) \\ 0 & 0 & \Sigma_{l=2}^L e_l P_l^2(\cos \Omega) & \Sigma_{l=0}^L d_l P_l(\cos \Omega) \end{pmatrix}. \quad (24)$$

Then, Fourier-series expansion of  $\tilde{R}(\mu, \phi, \mu', \phi')$ , will be given by equations similar to Eqs. (7), (8) and (9), but with  $a_l, b_l, g_l, d_l, e_l$ , and  $z_l$ , respectively, in place of  $\alpha_l, \beta_l, \gamma_l, \delta_l, \epsilon_l$ , and  $\zeta_l$ , with  $a_l$  and  $z_l$  derived from combinations of  $b_l$  and  $d_l$ , similar to those introduced in Eqs. (11) and (12).

All of these coefficients may be obtained by appropriate (e.g., Gaussian) numerical quadratures by using orthogonality relations in the Legendre basis. The only problem is to develop to an adequate order  $N$  the Fresnel matrix  $\tilde{R}(\omega)$ . The convergence of this development is correct for  $N = 48$ , as is illustrated in Fig. 2 for the term  $r_1 = R_{1,1} = R_{2,2}$ , and in Fig. 3 for  $r_2 = R_{2,1} = R_{1,2}$ . Figure 2 shows that slight difficulties occur for grazing incidences, where  $r_1$  increases quickly. However, as a result of the vanishing irradiance for grazing incidences, the resulting error should

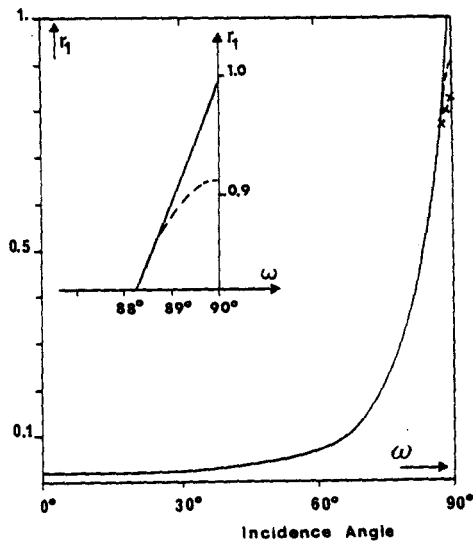


Fig. 2. Development of the reflection coefficient  $r_1$  in series of Legendre polynomials. The exact coefficient (—) is compared with results obtained from a series development of order  $N = 24$  ( $\times$ ) and of order  $N = 48$  (---). The range of grazing incidence angles is zoomed in the upper corner.

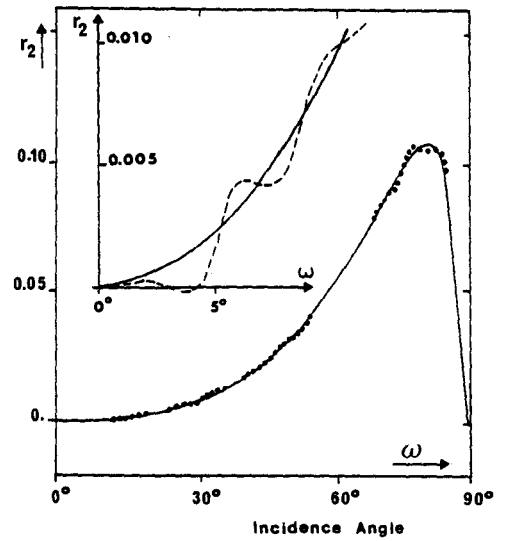


Fig. 3. Development of the reflection coefficient  $r_2$  in series of Legendre polynomials. The exact coefficient (—) is compared with results obtained from a series development of order  $N = 48$  ( $\bullet$ ). The range of near-nadir incidence angles is zoomed in the upper corner for the exact case (—) and the development of order  $N = 48$  (---).

be negligible. In Fig. 3, slight oscillations appear in  $r_2$  around the nadir, but they are unimportant. These directions generally correspond to low polarization ratios. Moreover, these oscillations may be smoothed when integrating Eq. (23). Therefore, we write

$$\bar{R}(\mu, \phi, \mu', \phi') = \sum_{n=0}^{N=48} (2 - \delta_{0,n}) [\cos n(\phi - \phi') \bar{R}_c^n(\mu, \mu') + \sin n(\phi - \phi') \bar{R}_s^n(\mu, \mu')], \quad (25)$$

where  $\bar{R}_c^n(\mu, \mu')$  and  $\bar{R}_s^n(\mu, \mu')$  are given by Eqs. (8) and (9), respectively, but with  $a_l, \dots, z_l$  in place of  $\alpha_l, \dots, \zeta_l$ .

According to the symmetry of  $f(\mu_n, \phi_n)$ , we can write

$$f(\mu_n, \phi_n) = \sum_{k=0}^K (2 - \delta_{0,k}) F_k(\mu, \mu') \cos k(\phi - \phi') \quad (26)$$

with

$$f_k(\mu, \mu') = \frac{1}{2\pi} \int_0^{2\pi} \cos k(\phi - \phi') f(\mu_n, \phi_n) d\phi'. \quad (27)$$

Since this function is very sharp around the specular direction, especially for low wind speeds and for grazing incidences, a Gaussian quadrature is no longer valid in Eq. (27), and we used trapezoidal quadratures restricted to intervals  $\Delta\phi = \phi - \phi'$  such that  $f(\Delta\phi_{\max})/f(\Delta\phi = 0) = 10^{-4}$ . The integration step was defined by using a dichotomy method with a convergence test at  $10^{-4}$ . For not too large incident and emergent angles, regardless of the wind speed,  $K = 96$  provides a fairly good restitution of  $f(\mu_n, \phi_n)$ , as is shown in Fig. 4 for  $\theta = 32.5^\circ$  and  $\theta^* = 21.3^\circ$  ( $\theta^*$  will stand for the supplement of  $\theta$ ). But, for grazing angles and small wind speeds, as a result of the sharp feature of the glitter, 1500–2000 terms would be needed to retrieve  $f(\mu_n, \phi_n)$  within the planned  $10^{-4}$  accuracy (see for example Fig. 5, where  $\theta = \theta^* = 88.4^\circ$ ). Fortunately, the Fourier-series decomposition of the radiation field requires much lower order expansions, so that such extensive developments of  $f(\mu_n, \phi_n)$  will prove to be useless when introducing the boundary conditions.

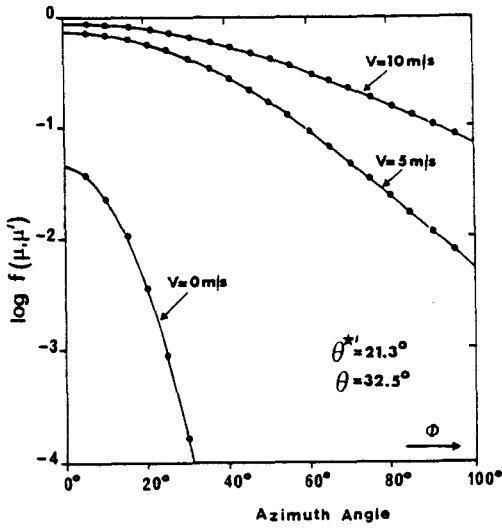


Fig. 4. The function  $f(\mu_n, \phi_n)$  is shown as a function of the azimuth difference  $\phi = \phi - \phi'$  for  $\theta^* = 21.3^\circ$  and  $\theta = 32.5^\circ$ . For three wind speeds, exact computations (—) are compared with Fourier-series expansion (●) according to Eq. (26).

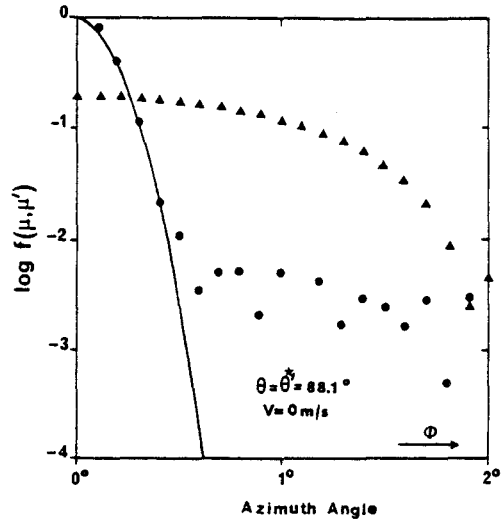


Fig. 5. The same as in Fig. 4 but for a wind speed equal to zero and for grazing angles ( $\theta = \theta^* = 88.4^\circ$ ). The probability function is retrieved by using 1624 terms. The 96 ( $\Delta$ ) and 1000 ( $\bullet$ ) terms developments are also compared with the exact result.

Finally, we substitute Eqs. (25) and (26) into Eq. (22). Since the series products may be written as

$$\sum_{n=0}^N \sum_{k=0}^K (2 - \delta_{0,n})(2 - \delta_{0,k}) \cos n(\phi - \phi') \cos k(\phi - \phi') f^k \tilde{R}_c^n = \sum_{p=0}^{K+N} (2 - \delta_{0,p}) \cos p(\phi - \phi') \tilde{M}_c^p \quad (28)$$

$$\sum_{n=1}^N \sum_{k=0}^K 2(2 - \delta_{0,k}) \sin n(\phi - \phi') \cos k(\phi - \phi') f^k \tilde{R}_s^n = \sum_{p=1}^{K+N} 2 \sin p(\phi - \phi') \tilde{M}_s^p, \quad (29)$$

the reflection matrix will be obtained in the required form

$$\tilde{M}(\mu, \phi, \mu', \phi') = \sum_{p=0}^P (2 - \delta_{0,p}) [\cos p(\phi - \phi') \tilde{M}_c^p(\mu, \mu') + \sin p(\phi - \phi') \tilde{M}_s^p(\mu, \mu')]. \quad (30)$$

By simple rearrangements,  $\tilde{M}_c^p(\mu, \mu')$  and  $\tilde{M}_s^p(\mu, \mu')$  may be written as

$$\tilde{M}_c^p(\mu, \mu') = f^p(\mu, \mu') \tilde{R}_c^0(\mu, \mu') + \sum_{n=1}^N [f^{p+n}(\mu, \mu') + f^{|p-n|}(\mu, \mu')] \tilde{R}_c^n(\mu, \mu'), \quad (31)$$

$$\tilde{M}_s^p(\mu, \mu') = \sum_{n=1}^N [f^{p+n}(\mu, \mu') - f^{|p-n|}(\mu, \mu')] \tilde{R}_s^n(\mu, \mu'). \quad (32)$$

These  $4 \times 4$  matrices are in the same form as  $\tilde{P}_c^n(\mu, \mu')$  and  $\tilde{P}_s^n(\mu, \mu')$ ; they may be partitioned into four  $2 \times 2$  submatrices, with zero submatrices on the trailing diagonal of  $\tilde{M}_c^p(\mu, \mu')$  and zero submatrices on the leading diagonal of  $\tilde{M}_s^p(\mu, \mu')$ . By substituting Eqs. (4) and (30) into Eq. (23), the boundary condition will clearly preserve the separation of the Fourier components and, on account of the particular form of  $\tilde{M}_c^p(\mu, \mu')$  and  $\tilde{M}_s^p(\mu, \mu')$ , the Stokes parameter parity will also be preserved. Finally, the boundary condition may be expressed by

$$\tilde{I}^s(\delta_1, \mu) = \tilde{M}^s(\mu, \mu_s) E_s \exp(\delta_1/\mu_s) + 2\pi \int_{-1}^0 \tilde{M}^s(\mu, \mu') \tilde{I}^s(\delta_1, \mu') d\mu' \quad (33)$$

by writing

$$\tilde{M}^p(\mu, \mu') = \tilde{M}_c^p(\mu, \mu') + \tilde{M}_s^p(\mu, \mu') \tilde{D}, \quad (34)$$

where  $\tilde{D} = \text{diag}(1, 1, -1, -1)$ .

The boundary condition requires integration of the diffuse downward radiance. An idea about the functions to integrate is given by the plots of Figs. 6 and 7. Two sets of  $M_{1,1}^s(\mu, \mu')$  terms are shown as functions of the incident angle  $\theta'$  for the two viewing zenith angles  $\theta = 2.8$  and  $84.4^\circ$ . The wind speed is 5 m/sec. For nadir observations, the glitter spot is obviously almost independent of the azimuth; therefore, the zeroth Fourier-series term is the main term of the expansion and follows the sharp peak of the sunglint. A major advantage of the Fourier-series expansion is observed for grazing angles. Since the glitter spot is very narrow, the Fourier-series convergence is slow. However, Fig. 7 shows that the behaviour of the  $M_{1,1}^s(\mu, \mu')$  terms as functions of the incident zenith angles is smooth enough to apply a classical Gaussian quadrature. To check this statement, we considered an isotropic incident source and computed the reflected radiance for several viewing directions; the wind speed was 5 m/sec. For nine viewing zenith angles, Table 1 shows the exact results, derived from a very accurate trapezoidal quadrature, as well as results obtained by using a Gaussian quadrature with 24 angles. The two results agree within 1%. Although this computation involves only the zeroth term, Fig. 7 shows that the integration problem would be the same for the other terms of the Fourier-series.

Although the Fourier-series expansion of  $\tilde{M}(\mu, \phi, \mu', \phi')$  may require very large orders  $P$ , the expansion of the scattered part of the radiation field is of order  $L$  of the  $\tilde{P}(\theta)$  expansion. Therefore, we limit the analysis to this order  $L$  in the Fourier-series expansions of  $\tilde{I}(t, \mu, \phi)$  and  $\tilde{M}(\mu, \phi, \mu', \phi')$ . We let  $\tilde{M}^L(\mu, \phi, \mu', \phi')$  stand for the approximate reflection matrix thus obtained. By solving this  $L$ -term problem, the resulting error will involve only that part of the radiation field corresponding to light reflected from the direct sunbeam and then directly transmitted through the atmosphere, i.e., the sunglint term. But this term, say  $\tilde{I}_{tr}^{ex}(\delta, \mu, \phi)$ , may be calculated without any Fourier series expansion, from

$$\tilde{I}_{tr}^{ex}(\delta, \mu, \phi) = [\exp(\delta - \delta_1)/\mu] f(\mu_n, \phi_n) \tilde{L}(-\chi_s) \tilde{R}(\omega_s) E_s \exp(\delta_1/\mu_s), \quad (35)$$

where  $\omega_s$  and  $\chi_s$  stand for  $\omega$  and  $\chi$  when the incident direction is the sun direction. Since the boundary condition will provide for this light the erroneous counterpart

$$\tilde{I}_{tr}^{err}(\delta, \mu, \phi) = [\exp(\delta - \delta_1)/\mu] \tilde{M}^L(\mu, \phi, \mu_s, \phi_s) E_s \exp(\delta_1/\mu_s), \quad (36)$$

the results of the code must be corrected by  $\tilde{I}_{tr}^{ex}(\delta, \mu, \phi) - \tilde{I}_{tr}^{err}(\delta, \mu, \phi)$ , the calculation of which raises no particular problem.

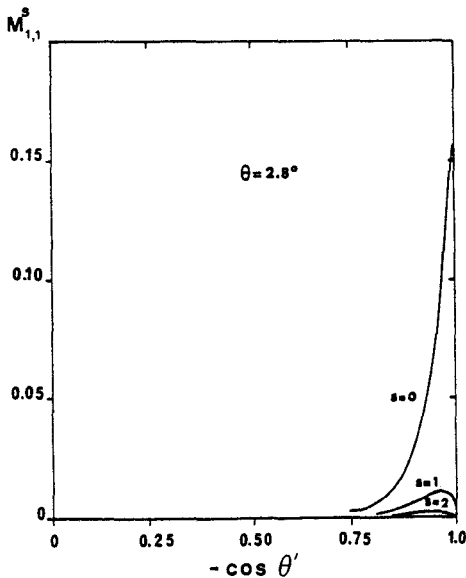


Fig. 6. The Fourier-series terms  $M_{1,1}^s(\mu, \mu')$ , vs the cosine of the incident zenith angle, for a viewing zenith angle of  $\theta = 2.8^\circ$ .

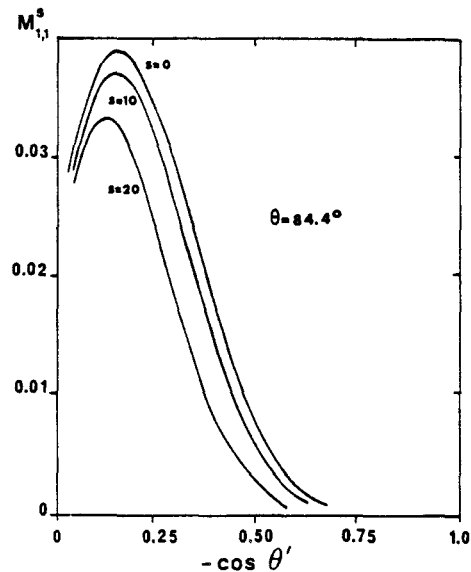


Fig. 7. The same as in Fig. 6 but for a viewing zenith angle of  $\theta = 84.4^\circ$ .

Table 1. Upward radiances observed at sea level for isotropic incident irradiance. The boundary condition of Eq. (33), for a wind speed of 5 m/sec, is integrated by using a Gaussian quadrature with 24 angles. These results are contrasted with the exact results derived from a suitable trapezoidal method (last column).

$\cos \theta$	$I_1$	$I_2$
0.99877	0.02006	0.02008
0.97059	0.02019	0.02020
0.80766	0.02349	0.02349
0.57722	0.04551	0.04552
0.40869	0.09170	0.09176
0.28736	0.1520	0.1522
0.16122	0.2589	0.2594
0.09700	0.3708	0.3716
0.03238	0.8409	0.8368

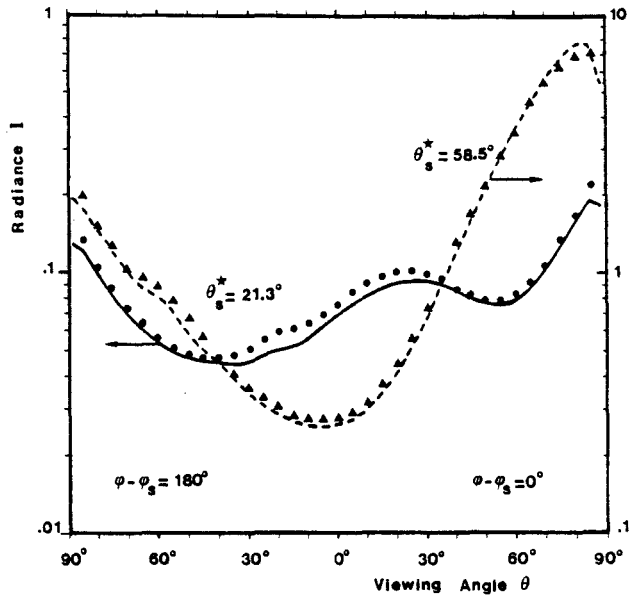


Fig. 8. The radiance  $I(\theta)$  leaving the top of the atmosphere-ocean system, as defined by Ahmad and Fraser (see text), has been calculated for solar zenith angles  $\theta_s^*$  - 21.3 and 58.8° at the wavelength  $\lambda = 0.7 \mu\text{m}$ . The results correspond to upward directions in the principal plane. Our computations (— and ---) are compared with the results reported by Ahmad and Fraser<sup>7</sup> (● and ▲).

APPLICATION

As an example, we will now see how the specified scheme may be used in successive orders of the scattering code. With this method,<sup>17,18</sup> we use the radiative transfer equation in its integral form and estimate the  $n$ -times scattered light  $\tilde{I}_{(n)}(\delta, \mu, \phi)$  from  $\tilde{I}_{(n-1)}(\delta, \mu, \phi)$ , with  $\tilde{I}_{(1)}(\delta, \mu, \phi)$  given by the known primary scattering from the direct sunbeam. For the case of a black background, the resulting equations for each term of the Fourier series expansion of  $\tilde{I}_{(n)}(\delta, \mu, \phi)$  are, therefore,

$$\tilde{I}_{(1)}^s(\delta, \mu > 0) = \frac{1}{4\pi\mu} \int_{\delta}^{\delta_1} \omega_0(\delta') \exp[-(\delta' - \delta)/\mu] \bar{P}^s(\mu, \mu_s) E_s \exp(\delta'/\mu_s) d\delta'; \quad (37)$$

for  $n > 1$ ,

$$\tilde{I}_{(n)}^s(\delta, \mu > 0) = \frac{1}{2\mu} \int_{\delta}^{\delta_1} \omega_0(\delta') \exp[-(\delta' - \delta)/\mu] \left[ \int_{-1}^{+1} \bar{P}^s(\mu, \mu') \tilde{I}_{(n-1)}^s(\delta', \mu') d\mu' \right] d\delta'. \quad (38)$$

These equations apply to the upward directions ( $\mu > 0$ ); the corresponding equations for the downward directions ( $\mu < 0$ ) are obtained with 0 in place of  $\delta_1$ , as the integral upper bound. In order to take into account the boundary condition, it is sufficient to keep the previous expressions unchanged for downward radiances and to add to the expressions for upward radiances as follows. In Eq. (37), the light reflected from the direct sunbeam and transmitted to the level considered in the specified direction is proportional to

$$[\exp - (\delta_1 - \delta)/\mu] \tilde{M}^s(\mu, \mu_s) E_s \exp(\delta_1/\mu_s). \quad (39)$$

In Eq. (38), the radiance reflected from  $\tilde{I}_{(n-1)}^s(\delta, \mu)$  and transmitted to the level considered in the specified direction is proportional to

$$2\pi [\exp - (\delta_1 - \delta)/\mu] \int_{-1}^0 \tilde{M}^s(\mu, \mu') \tilde{I}_{(n-1)}^s(\delta_1, \mu') d\mu', \quad (40)$$

which involves consideration of one reflection on the sea-surface as equivalent to one scattering event in the ( $n$ ) enumeration.

The  $\tilde{I}^s(\delta, \mu)$  terms are calculated at discrete levels  $\delta_i$  and for discrete directions  $\theta_j$ , which are Gaussian points of a Gaussian quadrature of order  $L$ , with  $L/2$  upward and  $L/2$  downward directions. Therefore, the  $L(4 \times 4)$  matrices  $\tilde{M}^p(\mu, \mu')$  must first be calculated from Eqs. (31) and (32) for  $(L/2)^2$  couples  $(\theta_j, \theta_k)$ , that is about  $4L^3$  terms. Next, the successive order code may be started, and the results are finally corrected for the error in the sunglint term, as was indicated previously.

In order to test the validity of the scheme, the radiance and polarization of the light leaving the top of the atmosphere were calculated for a model of the ocean-atmosphere system close to that used by Ahmad and Fraser.<sup>7</sup> The molecular component was fixed according to the US 62 standard atmosphere. The aerosols were spherical particles with refractive index  $m = 1.50 - 0.0i$  and size distribution of the form

$$n(r) = C \text{ for } 0.03 < r < 0.1 \mu\text{m}; n(r) = C(0.1/r)^4 \text{ for } 0.1 < r < 5.0 \mu\text{m}, \quad (41)$$

which were distributed vertically according to Elterman's distribution.<sup>19</sup> A wind speed of 10 m/sec was considered for surface-roughness modelling and calculations were performed for solar zenith angles of 21.3 and 58.5° at a wavelength  $\lambda = 700$  nm. Figures 8 and 9 show the resulting radiances and polarization ratios as a function of the zenith viewing angle for upward directions in the principal plane. The agreement with the results of Ahmad and Fraser is quite good and it is worthwhile to note that, compared with calculations for a black background as boundary condition, the computation time increased only by about 2% when taking into account the sea-surface reflection.

### CONCLUSIONS

We consider the radiative transfer of polarized light in a plane-parallel atmosphere bounded by a rough ocean surface, with wave slope orientations governed by a distribution function. We use Fourier-series decomposition of the radiation field. In order to preserve the separation of the problem into a set of independent problems for each Fourier component, the Fresnel matrix for reflexion and the distribution function for slope orientations are both decomposed by Fourier-series of the azimuth.

For the Fresnel matrix, this development is derived from a preliminary development in a series of Legendre functions or polynomials of the reflection angle. These series need to be computed only once and only for a few wavelengths because of the weak spectral variation of the sea-water refractive index. The wave-slope distribution depends only on the wind speed. The numerical

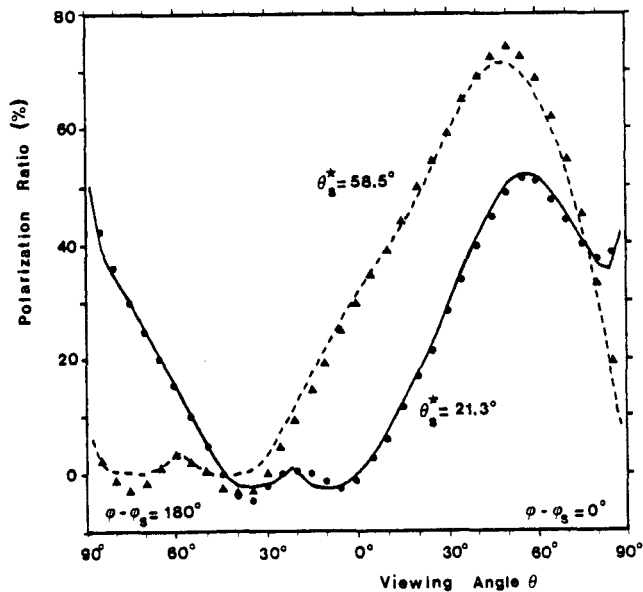


Fig. 9. The same legend as in Fig. 8 but for the polarization ratio.

difficulties encountered in its Fourier-series expansion, which are related to the sharp angular feature around the specular direction, have been investigated. Next, the Fourier-series decomposition of the reflexion matrix corresponding to the boundary condition is obtained as a mixture of the two developments.

Accurate restitution of the reflection matrix generally requires a very large order in the Fourier-series expansion. However, separate calculation of the sunglint term, which raises no particular problem, allows us to solve the rough ocean-problem with Fourier-series expansion of the radiation field of the same order as for the Lambertian boundary condition. The resulting radiation code takes account of reflection on the rough sea-surface with computation times that are only few percent longer than for a black background condition.

Reflection mechanisms, including noticeable polarization effects, are also exhibited by vegetation canopies, as shown by Vanderbilt and Grant,<sup>20</sup> or by natural surfaces, as shown by Coulson et al.<sup>21</sup> The generalization of our previous scheme to such boundary conditions will be examined in the future.

## REFERENCES

1. R. S. Fraser and W. H. Walker, *JOSA* **58**, 636 (1968).
2. J. V. Dave, Tech. Report, Contract No. NAS5-21680, NASA-Goddard Space Flight Center, Greenbelt, MD (1972).
3. G. W. Kattawar, G. N. Plass, and J. A. Guinn Jr., *J. Phys. Ocean.* **3**, 353 (1973).
4. E. Raschke, *Beitr. Phys. Atmos.* **45**, 1 (1972).
5. G. N. Plass, G. W. Kattawar, and J. A. Guinn Jr., *Appl. Opt.* **14**, 1924 (1975).
6. H. Quenzel and M. Kaestner, *Appl. Opt.* **19**, 1338 (1980).
7. Z. Ahmad and R. S. Fraser, *J. Atmos. Sci.* **39**, 656 (1982).
8. T. Takashima and K. Masuda, *Appl. Opt.* **24**, 2423 (1985).
9. S. Chandrasekar, *Radiative Transfer*, Dover, New York, NY (1960).
10. I. Kuscer and M. Ribaric, *Optica Acta* **6**, 42 (1959).
11. J. Lenoble, *C.R. Acad. Sci. Paris* **252**, 3562 (1961).
12. C. E. Siewert, *JQSRT* **31**, 177 (1984).
13. J. W. Hovenier and C. V. M. Van der Mee, *Astron. Astrophys.* **128**, 1 (1983).
14. D. Tanré, Thesis, University of Lille, France (1977).
15. M. W. Irvine and J. B. Pollack, *Icarus* **8**, 324 (1968).
16. C. Cox and W. H. Munk, *JOSA* **44**, 63 (1954).
17. J. L. Deuzé, Thesis, University of Lille, France (1974).
18. J. Lenoble, *Radiative Transfer in Scattering and Absorbing Atmospheres: Standard Computational Procedures*, Deepak, Hampton, VA (1985).
19. J. Elterman, *Appl. Opt.* **3**, 745 (1984).
20. V. C. Vanderbilt and L. Grant, *Jee Trans. Geosci. Remote Sensing* **GE23**, 722 (1985).
21. K. L. Coulson, E. L. Gray, and G. M. Bouricius, Report R64SD74, NASA-Godard Space Flight Center, Greenbelt, MD (1964).
22. I. M. Gel'fand and Z. Ya. Sapiro, *Am. Math. Soc. Transl.* **2**, 207 (1956).

## APPENDIX

### *Complements about the Phase Matrix Development*

The generalized Legendre functions, introduced by Gel'fand and Sapiro,<sup>22</sup> are defined by

$$P_{m,n}^l(\mu) = A_{m,n}^l (1-\mu)^{-(n-m)/2} (1+\mu)^{-(n+m)/2} \frac{d^{l-n}}{d\mu^{l-n}} [(1-\mu)^{l-m} (1+\mu)^{l+m}], \quad (\text{A1})$$

where

$$A_{m,n}^l = \frac{(-1)^{l-m}}{2^l (l-m)!} \sqrt{\frac{(l-m)!(l+n)!}{(l+m)!(l-n)!}}. \quad (\text{A2})$$

These functions are normalized by  $2/(2l+1)$ .

The Legendre polynomials correspond to  $m = n = 0$  and the associated Legendre functions to  $m = 2$  or  $-2$  and  $n = 0$ . All of these functions can be computed by using recurrence relations.

The set of coefficients  $\beta_l$ ,  $\gamma_l$ ,  $\delta_l$ , and  $\epsilon_l$  may be derived from the  $P_{i,j}$  terms of the phase function according to

$$\beta_l = 2/(2l + 1) \int_{-1}^{+1} P_{1,1}(\mu)P_l(\mu) d\mu, \quad (\text{A3})$$

$$\delta_l = 2/(2l + 1) \int_{-1}^{+1} P_{3,3}(\mu)P_l(\mu) d\mu, \quad (\text{A4})$$

$$\gamma_l = 2/(2l + 1) \int_{-1}^{+1} P_{1,2}(\mu)P_l^2(\mu) d\mu, \quad (\text{A5})$$

$$\epsilon_l = 2/(2l + 1) \int_{-1}^{+1} P_{3,4}(\mu)P_l^2(\mu) d\mu. \quad (\text{A6})$$

The functions  $R'_s$  and  $T'_s$  used in Eq. (8) are given by

$$R'_s(\mu) = [P'_{s,2}(\mu) + P'_{s,-2}(\mu)]/2, \quad (\text{A7})$$

$$T'_s(\mu) = [P'_{s,2}(\mu) - P'_{s,-2}(\mu)]/2. \quad (\text{A8})$$

# **Polarization of the solar light scattered by the Earth-Atmosphere system as observed from the US Shuttle.**

J.C. Roger, R. Santer, M. Herman and J.L. Deuzé

Laboratoire d'Optique Atmosphérique  
Université des Sciences et Techniques  
de Lille-Flandres-Artois  
59655 Villeneuve d'Acqs Cédex, France

## **ABSTRACT**

During the four American space Shuttle missions of year 1985, the crew members took pictures of the Earth in polarized light. This data set is a unique experiment involving extensive measurements in polarization. The results that have been already reported in the literature illustrate different potential applications on a qualitative basis. We examine here the possibilities to achieve quantitative analysis of the images. A first step was to validate the experiment. Different problems have been encountered : calibration, uncertainties on the direction of polarization, induced polarization by the Shuttle window, non-linearity of the film response...

The second part of the paper is devoted to the analyze of a set of selected images. The consistency of the calibration is proven for snow or sand observations for which ground measurements, reported in the literature, can be used for comparison with respect to the spatial homogeneity of the target. The potential of polarization for agriculture inventory use is then illustrated by relating space observations to existing ground measurement. Finally, during an atmospheric contamination event, the analysis of the polarization allows us to characterize the origin of the pollution as forest fire smoke.

## 1. INTRODUCTION

Since the beginning of space exploration, cameras have been set up aboard the spacecraft. Despite the multitude of satellite sensors, the use of these photographs is not restricted to an artistic view of the Earth. All the pictures taken from American spacecraft are archived by NASA at Sioux Falls and are available on request for scientific purposes. To take pictures from space has also become a favorite exercise of the crew members of the Shuttle. In the early eighties, some people at Johnson Space Center in Houston thought to take pictures in polarized light using two bore-sighted cameras equipped with polarizers. Qualitative use of these data have been reported; for example, some spectacular structures within the water are observed over oceans in the sunglint spot. The polarization ratio is quite directly derived from a digitized pair of images with the obvious advantage of avoiding any calibration. A first review of the observed degrees of polarization is reported by Coulson et al. (1986). Some other limited observations have been reported by Egan and Whitehead (1989) and Duggin et al. (1990). A study of an area of the Hawaiian islands has been also described by Egan et al. (1991).

A more extensive use of the Shuttle data involves first to investigate all the experimental procedure: criticism of the principle of the experiment, evaluation of the polarization induced by the Shuttle window and by the optics of the camera, linearity of the film response. We describe the procedures to transform the photographs into a pair of overlapped digitized images, to evaluate the uncertainties on direction of polarization and the polarization induced by the windows.

On the other hand, since the signal is basically the sum of the atmospheric scattering and of the ground reflectance, we need to separate the two contributions. For this purpose, calibrated values are required both in total and polarized radiance. In lack of any calibration and since no ground-based calibration was available, we developed in-flight calibration methods based on observations over the sea, for which the signal or its spectral dependence can be predicted. This calibration takes into account the non linearity of the film response.

Different topics are investigated in the last section because they are well documented (high reflective targets such as sand and snow). The series of

stereoscopic views taken over the Hawaiian islands is used to illustrate the bidirectionality of the reflectance and to observe the high polarization at the Brewster condition both over sea and land. Finally, during a turbid situation, the polarization will be used to characterize the aerosol.

## 2. MEASUREMENTS

### 2.1 Principle of the measurements.

The solar radiance up welling reflected from the Earth-Atmosphere system is described by four Stokes parameters. The ellipticity of the vibration is likely to be quite negligible (Kawata, 1978). Therefore, the characterization of the radiance is reduced to three independent parameters. The signal  $I_{tot}$  is the sum of natural (unpolarized) light of intensity  $I_{nat}$  and of a rectilinear vibration (polarized) characterized by its intensity  $I_{pol}$  and its direction of vibration.

If we analyze this vibration by a perfect polarizer, the outgoing intensity is expressed by

$$I(\alpha) = \frac{I_{nat}}{2} + I_{pol} \cos^2(\alpha) \quad (1)$$

where  $\alpha$  is the angle between the direction of the polarizer and the direction of the rectilinear vibration.

The experimental design consists of two bore-sighted Hasselblad cameras equipped with two cross-polarizers. The operator rotates the hand-held dual camera mount about their common optics axis to obtain the maximum of intensity for one camera. The physical parameters to be derived are then the direction of polarization  $\chi$  (directly provided by the orientation of the image), the maximum and the minimum of intensity written respectively  $I_{max}$  and  $I_{min}$ . According to equation (1), we get

$$I_{tot} = I_{max} + I_{min} \quad (2)$$

$$I_{pol} = I_{max} - I_{min} \quad (3)$$

### 2.2 Spectral responses.

A KODAK black and white film was used during the first flight. Its sensitivity is quite constant from 350 nm to 680 nm and drops above. As our computations suppose a monochromatic approximation, we defined an effective wavelength of the bandpass as

$$\bar{\lambda} = \frac{\int_0^{\infty} \lambda T(\lambda) \delta(\lambda) E_s(\lambda) d\lambda}{\int_0^{\infty} T(\lambda) \delta(\lambda) E_s(\lambda) d\lambda} \quad (4)$$

where  $E_s(\lambda)$  is the solar irradiance at the top of the atmosphere,  $\delta(\lambda)$  the spectral response of the film and  $T(\lambda)$  the transmittance of the optics. The film response, provided by the manufacturer, is plotted in Figure 1. We also reported in Figure 1 the transmittance curve of the Shuttle window (Anthon, 1975). The resulting effective wavelength is 549 nm. For the three other missions (June 85, August 85 and November 85), color films KODAK 5036 and 5017 were used. The Blue-Green-Red components were selected using KODAK filters 47b, 61 and 29. The effective wavelengths were then 439 nm, 542 nm and 647 nm.

### 2.3 Geometry of the experiment.

For each mission, a catalogue reports some basic information on the scene: the scene reference, the date, the time (provided by a clock incorporated to the camera mount), the nature of the scene, the percentage of clouds and the navigation parameters of the Shuttle (altitude and location of the sub-spacecraft point). Moreover, where geographical features were identified on the image, the position of the center point of the image is provided. At last, depending on the mission, two focal distances (100 mm and 250 mm) were used which give respectively a scene size of about 80 and 200 km for a nadir view.

Some extra information need to be computed. The geometrical parameters are illustrated in Figure 2. First, a more accurate determination of the location of the scene is done by carefully selecting tie points. The latitudes and longitudes of these points and of the sub-Shuttle point allow determination of the viewing conditions  $\theta_v$  (zenith angle) and  $\varphi_v$  (azimuth angle). The time, the latitude and the longitude of the tie points allow computation of the solar zenith angle  $\theta_s$  and the solar azimuth angle  $\varphi_s$ . A derived value is also the scattering angle  $\Theta$  or the phase angle  $180^\circ - \Theta$ .

#### *2.4 Data selection.*

We just selected one image from the black and white film, the Horn of Africa, already digitized by NASA, in order to compare to our digitization. For the second mission (June 85), the film was quite under-exposed. We then selected images among the two pairs of color films (100 pictures each) taken during the two missions of the fall of 1985.

We processed a first stereoscopic series of the Hawaii island. A group of pictures was selected to perform the in-flight calibration. This set corresponds to oceanic observations both of the sunlint and of the atmosphere. Therefore, we selected homogeneous surfaces (snow and sand), in order to compare to results published for these kinds of targets. We also chose scenes of vegetation to check the potential of the polarization data for agricultural inventory use. At last, we selected a scene taken over Kraskino (close to Vladivostok) which presented a large atmospheric contamination to try an aerosol remote sensing. The characteristics of the chosen scenes are reported in Table 1.

### 3. DATA REDUCTION

We describe here the procedure used to transform the data into a pair of overlapped digitized images. We then examine the data quality with respect to the principle of the experiment and the instrumental polarization.

#### *3.1 Digitization.*

The raw data consisted of 55mm  $\times$  55mm slides and the first step was to digitize these pictures. We used equipment set up at the "Institut d'Optique" of the University of Orsay (Paris). A description of the instruments is given in Figure 3. The size of the incident beam is limited by selected apertures. A Perkin-Elmer micro-densitometer measures the light transmitted through the film. A color filter wheel allows to decompose the light in its basic components. The output voltage is then amplified and converted in 12 bits in the density range of 0 to 4. The density zero corresponds to the light transmitted through the unexposed edges of the film; the density four, to the dark area. The procedure is then repeated for the whole film and for any user.

The support of the film is moved by a step-by-step motor. The step of the scan is adjusted to suit the aperture. We chose to build images of 512  $\times$  512 pixels using 140  $\mu\text{m}$   $\times$  140  $\mu\text{m}$  aperture for a step of 106  $\mu\text{m}$ . Taking into account the mean altitude of the Shuttle (about 300 km), the spatial resolution is 150 m for a focal distance (of the camera) of 250 mm and at nadir view. At last, a mean time of 2<sup>h</sup>30' was necessary to digitize one scene (3 filters  $\times$  2 images).

The optical axes of the two cameras were adjusted to be parallel as well as possible. But a pair of images is not directly comparable. For example, during the two last missions, the two images were shifted by a 1/8 of a scene. Then, the first step consisted to overlap the two images of a scene.

It is quite difficult to estimate the uncertainties due to the overlap procedure. Artificial polarization is expected for high-contrast areas such as coast lines or cloud edges. The quality of the overlap was directly related to the number of tie points we selected. Additional tie points were selected until we canceled any apparent artificial polarization. An alternative is to degrade the spatial resolution.

### 3.2 Direction of polarization.

The camera mount was rotated about the optic axis to obtain the maximum of intensity. Then, the direction of the polarizer provides the direction of the polarized vibration integrated over the whole scene. The direction of the polarization varies over the image and may differ from the measured mean value. Of course, the total radiance is not affected by this departure but both the polarized radiance and the degree of polarization have to be corrected, according to equation (1), by  $\cos(2\delta)$ , where  $\delta$  is the difference between the mean direction and the actual local value.

Let us assume that the image corresponds to a target uniform with respect to the radiance and degree of polarization and that the center of the image is at nadir. The geometrical conditions are given by the solar zenith angle  $\theta_s$ , where the principal plane corresponds to the central line of the image and the center of the image. The direction of polarization, excepted around the neutral points, is perpendicular to the scattering plane (as for example for the Rayleigh scattering) or is parallel to this plane. The direction of polarization is then defined by the geometrical conditions. For a Rayleigh polarization, the direction of the polarization at the image center is vertical and represents the mean measured value. We computed for the whole image  $\cos(2\delta)$ , which is the correction factor in polarization. Figure 4 reports the results for different solar angles. In practice, to account for the local variation of the direction of polarization, we should divide by the factors reported in Figure 4. Nevertheless, since the correction was computed under simplified assumptions, Figure 4 mainly suggests when related problems may exist. In the principal plane, the correction is null. The full image corresponds to a focal distance of the camera of 100 mm, while the white circle limits to a 250 mm focal distance. In this last case, for solar zenith angles larger than  $30^\circ$ , the correction is quite negligible and remains acceptable for high sun except on the edge of the image. The problem is more critical for a higher FOV where for small solar zenith angles at the edge of the image the measurements are no longer significant.

In this ideal case, we can define a correction factor by assuming that the center of the image is representative. In practice, taking into account the non uniformity of the scene, the correction is quite questionable. Then, we need to restrict the selection to a 100 mm focal distance data or to low solar elevation observations. For future missions, NASA has planned to use a third camera in order to cancel any uncertainty on this topic.

### 3.3 Polarization induced by the windows.

The calibration process will refer to the Rayleigh scattering and to the sunglint. In order to emphasize these two contributions, we will need to work with off-nadir observations. Most of the pictures were taken from the overhead windows of the cabin. Since the Shuttle is quite stabilized in orbit on its back, the off-nadir observations correspond to non perpendicular light to the window surface which induces polarization.

For a given state of the incident beam and knowing the geometrical conditions (incident  $i$  and refractive  $r$  angles), it is possible to predict the transfer through the window. For example, Figure 5 reports the degree of polarization  $P_{wd}$  induced by the window, as computed for a double parallel glasses and for an unpolarized incident beam (Bruhat, 1965):

$$P_{wd} = \frac{I_{//} - I_{\perp}}{I_{//} + I_{\perp}} = \frac{1 - \cos^8(i-r)}{1 + \cos^8(i-r)} \quad (5)$$

where  $I_{//}$  and  $I_{\perp}$  are respectively the intensities of the parallel and perpendicular components to the plane of incidence.

The terrestrial clouds strongly polarized in the rainbow, but, in a large scattering angle range, their polarization remains weak. Theoretical computations (Hansen and Hovenier, 1974) as well as reliable observations (Deuzé et al, 1989) indicate the low polarization observed over clouds for scattering angles that range from 90-120°. These geometrical conditions corresponded to cloud observations on an image, digitized by NASA, taken over the Seychelles Islands. The center of the image corresponded to a view angle of 42°, while the scattering angle was 96°. Clouds were present at the two edges of the image. Taking into account the 15° FOV, the corresponding viewing angles were 34° and 52°. In red, the degree of polarization was respectively 9% and 25%, values which fit the induced polarization as plotted in Figure 5.

For a polarized incident beam, the expression of the induced polarization is more complex. If the direction of the vibration is parallel with one of polarizers, the measurements give

$$I_{tot}^* = I_{tot} + I_{pol} P_{wd} \cos(2\chi) \quad (6)$$

$$I_{pol}^* = I_{pol} \left\{ \cos^2(2\chi) + \sin^2(2\chi) \sqrt{1 - P_{wd}^2} \right\} + I_{tot} P_{wd} \cos(2\chi) \quad (7)$$

The induced polarization by the windows affects little the total intensity and a little more the polarized intensity for the small view angles. The effect of the windows becomes important when the view zenith angle is large. In order to avoid this problem, we mainly selected quite nadir images. The correction has to be applied for images involved in the calibration process and will be included in the error budget.

## 4 CALIBRATION

No preflight calibration was performed. Moreover some basic information was missing: on the linearity of the film response, on the duration of the film processing, on the optical characteristics of the Shuttle windows... We need then to perform an in-flight calibration based on scenes for which the signal is predictable.

KODAK provides (Figure 6) the characteristic curve of the film response. This figure does not represent the actual response of the film but illustrates the standard behavior of the film response. All exposures were set up at 1/250 seconds and recommendations were given to the crew to adjust the f/stop in order to be in the linear part of the film response.

In a first time, the calibration process will then be conducted in the hypothesis assuming that the film response to be linear. But the characteristic curve is linear in a limited range and we already pointed out that the measured maximum radiance was saturated for several observations (sunglint and clouds for example). Then, we developed a method which takes into account the non-linearity of the film response.

### 4.1 Basic equations.

What we know for sure is the characteristic curve of the film response (Figure 6) but we ignore how this curve has been modified during the film process.

We have determined the relation between the optical density and the exposure (before the film process) by a polynomial fit,  $f(D)$ , with an order of 5.

Figure 7 shows the typical evolution of film response versus the duration  $t$  of the film processing (Gaudart, 1989). Above  $t_c$  contrasts are saturated. If  $t < t_c$  we assume that, at a first order, the processing time acts linearly. Under these circumstances, the response will be specified through the determination of two flexible parameters called  $a_\lambda$  and  $b_\lambda$ . Then, the observed radiance  $L$  (linked to the exposure and then to the intensity) is related to the density or the digital counts,  $DC$ , by

$$L_\lambda = n a_\lambda (f(DC_\lambda) + b_\lambda) \quad (8)$$

where  $n$  depends upon the selected  $f$ /stop ( $n=1, 2, 4, 8, 16 \dots$ ).

Since the two films were identical and have been processed in the same way,  $a$  and  $b$  are supposed to be identical for each film. Then we define the total radiance ( $L_{max} + L_{min}$ ) for each channel from

$$L_{tot} = a \left( n_{max} \{f(DC_{max}) + b\} + n_{min} \{f(DC_{min}) + b\} \right), \quad (9)$$

the polarized radiance ( $L_{max} - L_{min}$ ) from

$$L_{pol} = a \left( n_{max} \{f(DC_{max}) + b\} - n_{min} \{f(DC_{min}) + b\} \right) \quad (10)$$

and the degree of polarization ( $L_{pol} / L_{tot}$ ) from

$$P = \frac{n \{f(DC_{max}) + b\} - \{f(DC_{min}) + b\}}{n \{f(DC_{max}) + b\} + \{f(DC_{min}) + b\}} \quad (11)$$

where  $n = \frac{n_{max}}{n_{min}}$  can be different to 1.

The principle of the calibration is then to correctly predict  $L_{max}$  and  $L_{min}$  or any derived values. In order to determine  $a$  and  $b$  we used the Rayleigh scattering and sunglint. The degree of polarization depends only upon  $b$  and we used  $P$  for this determination. The second parameter  $a$  was found by using the total radiance and the polarized radiance.

Notice that all radiances (total and polarized) reported in this paper are defined assuming the solar irradiance  $E_s$  is equal to  $\Pi$ . Therefore, the relation between the reflectance and the radiance is

$$\rho = \frac{L}{\cos(\theta_s)}. \quad (12)$$

#### 4.2 Rayleigh scattering calibration.

Several authors (Fraser and Kaufman, 1984; Vermote et al, 1992a) used the Rayleigh scattering as a reference for the calibration. The molecular component is emphasized when dealing with short wavelength oceanic

observations outside of the sunglint and for large atmospheric paths. In fact, the method refers to a signal including standard contamination by aerosols and standard boundary conditions for the sea surface, both with respect to the wind speed and to the diffuse reflectance of the water. We will use this method with priority for the blue filter and residually for the green filter.

An error budget was calculated for the mean geometrical conditions of the observations:  $\theta_v = 40^\circ$ ,  $\theta_s = 50^\circ$  and  $\varphi_s - \varphi_v = 40^\circ$ . The reference model was defined by an aerosol maritime model (Deirmendjian, 1954) with a standard visibility of 23 km, wind speed of 2 m/s, and diffuse reflectance of the sea water corresponding to clear water ( $\rho_{\text{wat}} = 0.02$ ) (Viollier, 1980). As extreme conditions for this reference case, we assumed an extreme wind speed of 15m/s, a "black" water ( $\rho_{\text{wat}} = 0.00$ ) and an aerosol continental model with a visibility of 10 km. In lack of ground truth, the range between the two cases is believed to represent the actual situation.

The resulting error budget on the total radiance, on the polarized radiance and on the degree of polarization is reported in Table 2. The best accuracy is obtained when dealing with the polarized radiance. The Rayleigh scattering is highly polarized (100% for  $\Theta=90^\circ$ ) and since the diffuse reflectance of water is Lambertian, no polarization is generated by the water.

#### 4.3 Sunglint calibration.

The Fresnel reflection of the solar beam on the sea surface is well modeled. The wind speed modifies the distribution of the wave slopes around the specular direction (Cox and Munk, 1954). The radiance in the sunglint is then strongly dependent on the wind speed. Since the Fresnel reflection is independent of the wavelength, the method is suitable for an interband calibration. This method has been already used by Holben and Kaufman (1991) and Vermote et al. (1992b) to inter-calibrate the channels 1 and 2 of AVHRR. On the other hand, the atmospheric paths alter the information on the Fresnel reflection mainly at short wavelengths. This method is then suitable for the ratio of green/red.

The error budget is reported in Table 3, for the same conditions as in Table 2, but for specular observations in the Brewster conditions ( $\theta_v = \theta_s = 54^\circ$ ) where the degree of polarization is high. In this case, the expected accuracy on the green/red ratio is better than 10 %, both on the total radiance and on the polarized radiance, and the method is quite ideal on the degree of polarization.

#### 4.4 Calibration results

We already defined  $b$  as the result of the predicted degree of polarization retrieval:  $b$  is determined in the blue and green bands using Rayleigh scattering. For the red channel,  $b$  is deduced for an interband calibration on the sunglint. The determination of  $a$  is the mean result of comparison of the measurements in total and polarized radiances both on the Rayleigh scattering and sunglint. In Table 4 we report the coefficients  $a$  and  $b$  for each channel.

The final result is plotted in Figure 8, which gives the non-linear relation between digital counts and radiances for the three channels.

We finally compare the converted measurements in total reflectance and degree of polarization to the computations, Table 5, for the Rayleigh scattering. The same comparisons are achieved, Table 6, for the sunglint. The computations correspond to mean conditions for the atmosphere while the measurement results of the conversion of the digital count. Of course, in average, there is a correspondence between the measurements and the computations since the calibration is mainly based on these computations. But not solely, because additional information is required. For example, through equation (8), the analytical expression of the first response. So, the comparison first justifies the calibration but also, through the discrepancies between the two sets, gives an estimate of the calibration uncertainty. The overall accuracy of the calibration is around 20%.

The stereoscopic series of the Hawaii islands offer the opportunity to check the calibration. For the two last pairs, this scene is viewed under the same geometrical conditions. The main change between the two pairs lies in the change of the  $f$ /stop for the images of the maximum by a factor of 2. After calibration, the total radiance of the maximum component  $L_{max}$  for Hawaii 3 is 0.049, 0.022, 0.014 respectively for the blue, green and red channels. For Hawaii 4, we measured 0.086, 0.045, 0.027. According to the very small differences between the two scenes, due to a small change in the geometrical conditions, we retrieved the  $f$ /stop ratio.

## 5. PRELIMINARY ANALYSIS OF THE MEASUREMENTS

We will analyze the last set of shuttle images chosen for nadir view in order to avoid polarization by the window. The first goal was to retrieve for typical targets published characteristics in polarization. The theoretical description of the sunglint is already justified by the coherency of the calibration. In the same way, the calibration confirms the mean atmospheric signature. We then selected homogeneous natural surfaces (snow and sand). In another respect, we will try to investigate the polarization of the canopy. Finally, we will devote a sub-section to an atmospheric pollution event.

### *5.1 Polarization of the natural surfaces.*

The purpose of this section is specific to homogeneous targets: snow and sand. This homogeneity is used to do a calibration of the sensor: cross-calibration with an other satellite, equalization of the detectors for future array detectors... For large field of view sensors, the contamination of the radiance by instrumental polarization may raise some difficulties, mainly if the incident radiance is highly polarized. Some selected scenes are supposed to give some information on this topic.

Two opportunities for snow field observation occurred over O-Ling-Mu Lake (China) and Chili ( $\Theta=132^\circ$  and  $85^\circ$  respectively). In both cases, the total reflectance is over 0.50 and the polarized reflectance less than 0.02 as reported in Figure 9 for the O-Ling-Mu Lake scene. The observed polarization of the snow field is very low and the polarized signal has atmospheric origin. These results confirm the measurements done by Egan (1985) over the Antarctic from an aircraft.

We also have two scenes of sand ( $\Theta$  is equal about  $130^\circ$ ). The first, Yabrai Shan, corresponds to a dune area in the Gobi desert. The total reflectances observed (Figure 10) in the blue, green and red channels are 0.37, 0.32 and 0.33 respectively (in the same order with the AVHRR data over the western American desert). The polarized reflectances are small and partially of atmospheric origin. We obtained the same results over the second scene: Brahmaputra (India). These results confirm that in this particular geometry (outside the specular direction or hot spot) the polarization of the sand is quite small. Of course, the atmospheric scattering contributes to the signal, but compared to the signal reflected by snow (figure 9) this component is quite

negligible. If we assume no spectral dependence for the sand, the higher reflectance measured in the blue (figure 10) corresponds to the additional contribution of the atmosphere mainly by the Rayleigh scattering. Conversely, the atmosphere reduce the polarized reflectance. The overall effect of the atmosphere on polarization is to depolarize. Nevertheless, even if we account for atmospheric effects, the intrinsic polarization of sand remains low.

### *5.2 Polarization of the canopy.*

The specular reflection at the surface of the leaves can be highly polarized if the observation corresponds to the Brewster angle. Vanderbilt and Grant (1985) studied this effect and Rondeaux and Herman (1991) reported some ground-based measurements over different kinds of canopies. We want to see if this information is still present in space observations i.e. with a different spatial scale and with the influence of the atmosphere. Since this information is of the same nature as for the sunglint over ocean, the near-Brewster observation seems suitable. The Hawaii1 and Hawaii2 scenes corresponded to this situation according to the geometrical condition reported in Table 1. Notice that there is just 15 seconds between the two scenes, the Hawaii1 scene (Figure 11) being close to the Brewster condition. As observed in this figure, the sunglint occupied the upper part of the image. The transect 1 scans the specular regions both for the ocean and land. Inversely, the transect 2 is supposed to provide mainly the atmospheric radiance over the sea. Over land, differences between transects result on the specular reflection mostly present in transects 1.

Measurements (total reflectances and polarized reflectances ) along the transect 1 are reported in Figure 12 for the two scenes. For Hawaii1, the left part of transect 1 intercepts a cloud with a peak reflectance over 0.40 followed by a shaded region. As expected, the polarized reflectance observed over the cloud decreases. Then, the sky is clear over the sea. The high reflectance is white, indicating the major weight of the specular reflection. For the near Brewster geometrical conditions, the polarized reflectance is high corresponding to a degree of polarization of 50 %. We can notice that the polarized reflectance is smaller in the blue. The direct to direct atmospheric path depolarized the Fresnel reflection. The attenuation by the atmosphere is more effective on the polarized reflectance for which the decrease of the

reflectance is counterbalanced by the atmospheric scattering. For Hawaii2, the total and polarized reflectances decrease more rapidly over the sea than over the land.

Figure 13 refers to the transect 2. We observe, for Hawaii1, a residual component of the sunglint over the sea both for the total reflectance and polarized reflectance. But for Hawaii2, the contrast between land and sea is quite absent on the total reflectance in blue. The slight increase along the transect is simply related to the small variations in  $\cos(\theta_v)$ . In the green and red, the presence of land is not deeply marked. According to the 5S code (Tanré and al, 1987), the observed reflectances over the sea correspond to a visibility of 100 km. On the polarized reflectance, the land observations exhibit an additional weak contribution to the atmosphere.

According to canopy models, the polarization is induced by the reflection on the surface of the leaves. It is less confined near the specular direction than the sunglint over the sea, the geometry of the leaves slopes being less smooth than the wave slopes. The transect 2 over Hawaii2 mainly provided the contribution of the atmosphere. Taking into account the  $5^\circ$  FOV and the smoothness of the atmospheric scattering versus the scattering angle, this contribution can be removed in a first approximation from the observations of transect 1. The results of this atmospheric correction are:

- the total reflectances over the land are small in the middle of the island corresponding to a mountain region,
- the measured reflectances along the coast correspond (according to 5S) to observations over vegetation,
- and the most significant result is the presence of a large amount of polarized light reflected by the ground. The spectral component is white, expressing its specular origin.

The specular nature of the canopy polarization is illustrated Figure 14 where we plotted at  $\lambda = 650 \text{ nm}$  the observed degree of polarization versus the phase angle. The comparison with the measurements done by Rondeaux and Herman (1991) is indicative of the origin of the measured polarization from the Shuttle. As a matter of fact, this comparison has to be looked at with care. The Rondeaux's measurements are ground-based while the Shuttle measurements included the atmosphere. Moreover, the spatial scales are quite different. Despite of this, the identity of the geometrical distribution of the degree of polarization assesses the common origin of the polarization by reflection.

### 5.3 Aerosol remote sensing.

Several conditions for aerosol loading have been introduced in the calibration procedure. Slight variations of the aerosols in nature or abundance are then included in the looseness of the calibration. But one scene taken over Kraskino (Korea-China border, close to Vladivostok) presented in Figure 15, shows a large atmospheric contamination with a low contrast between land and sea and the presence of white wreath of smoke probably emitted by forest fires.

Figure 16 reproduces the total reflectance and the degree of polarization. The observed peak corresponds to the presence of a plume of smoke. The degree of polarization presents an unusual behavior. For a clear atmosphere, at an observed scattering angle of  $\Theta = 90^\circ$ , the Rayleigh scattering should dominate in the blue channel with a high degree of polarization. Inversely, the polarization increases toward the red channel.

We suppose that the atmospheric contamination is produced by an unique mode of particles of reflective index  $m$  and the well known gamma standard size distribution given by

$$n(r) = r^{\frac{1-3v_{eff}}{v_{eff}}} e^{-\frac{r}{R_{eff} v_{eff}}} \quad (13)$$

with two flexible parameters : the effective radius  $R_{eff}$  of the particles and  $v_{eff}$  the effective variance. The particle abundance is directly related to the aerosol optical thickness.

From studies of planetary atmospheres, it is well known that, even for a dense atmosphere, the degree of polarization in the primary approximation is quite representative of the diffuse regime. Under this assumption, we computed the polarization ratio for a set of aerosol optical thicknesses (0.5, 1.0, 1.5, 2.0), refractive indexes (1.33, 1.50, 1.75 for an imaginary part of 0.01) and two values of the effective variance (0.07 and 0.30). These small values of the variance for terrestrial aerosols are suitable if we wish to retrieve the large spectral dependence of the measurements. Figure 17 provides the plots of the computed degrees of polarization versus the effective radius for  $v_{eff}=0.07$ . For a given aerosol model, the degree of polarization decreases sharply from the Rayleigh Gans regime. This regime, corresponding to  $(m-1)R_{eff} \ll \lambda$ , is the more persistent for  $m=1.33$ . For larger particles, their polarization is quite

null. This remark is applied to the red observations for which the Rayleigh scattering is absent.

The measurements correspond to the horizontal lines and a retrieval is obtained for aerosols with  $R_{eff} \approx 0.15 \mu m$ ,  $v_{eff} = 0.07$ ,  $m = 1.75$  and for an optical thickness  $\delta = 1.5$ . For  $m = 1.75$ , the measurements retrieval is no longer possible if  $v_{eff} = 0.30$ , Figure 18. In the primary scattering approximation, the polarization measurements indicated a well defined solution. We just need to include the multiple scatterings. The successive order of scatterings method provided the computations reported in Table 7 which are quite in agreement with the measurements according to their accuracies.

For comparison, the smoke aerosol is composed of graphitic carbon and organic particles. The graphitic carbon has an refractive index of  $2.00 - 0.66i$  (Ackerman and Toon, 1981) with an effective radius less than  $0.10 \mu m$ . For the organic particles, the refractive index is  $1.43 - 0.0035i$  (Kaufman et al, 1990) and the effective radius is about  $0.15 \mu m$ . On the other hand, several aircraft measurements of size distribution of fires showed particles of effective radii between  $0.1 \mu m$  and  $0.2 \mu m$  (Radke et al., 1978; Stith et al., 1981; Andreae et al., 1988; Kaufman et al., 1991). These results published are similar to our present measurements. The results are also supported by the observations on the image of plumes of smoke originating from the coast.

## 5. CONCLUSIONS

This work reviews the problems encountered by the Shuttle experiment in polarized light. Some warnings are given to the users concerning the polarization induced by the window and by the shift due the spatial variation of the direction of polarization. Future projects should use the Space Shuttle bay in order to avoid the windows and also a third camera should be added.

The polarization experiment conducted from the Space Shuttle was quite unprepared with an absence of calibration. A part from that we defined a calibration strategy available for photo-polarimetric experiments. The final accuracy of the calibration procedure applied to the Space Shuttle is expected to be around 20%.

In a second step, we first verified the low degree of polarization met for natural surfaces (snow and sand). But over vegetation, mainly in the absorption band of the chlorophyll at 650 nm, the measurements exhibit a large degree of polarization for the Brewster condition, confirming the presence of a specular term and the potential of the polarization data for crop classification. Finally, for the Kraskino scene, we produced an example of aerosol remote sensing using the degree of polarization with an accurate determination of the aerosol nature.

On a quantitative base, a more promising experiment called POLDER is under development (Deschamps et al., 1990). This experiment uses a new instrument devoted to the observation of the polarization and directionality of the solar radiation reflected by the Earth-atmosphere system. It is based on the concept of a matrix array CCD detector and a wide field of view optics of 144°. It will allow to observe a single point of the Earth's surface under different viewing angles during the same orbit, and then determine the reflectance and polarization properties from one or several orbits.

## ACKNOWLEDGMENTS

The authors wish to express their thanks to M Leroy and to acknowledge the financial support from CNES under contract 833/CNES/88/5527/00. They are particularly grateful to Eric Vermote and George Vassiliou of Goddard Space Flight Center for their useful discussions and the revision of the manuscript. They would like to thank M. Equilbey for his helpful discussions about the digitization of the images performed at the "Institut d'Optique" (Orsay-France). At least, they express their appreciations to M. Whitehead and the NASA Johnson Space Center that have provided the Shuttle data.

## REFERENCES

Anthon, E. (1975), Optical properties of coated space shuttle windows. Optical Coating Laboratory, Inc. Report, SS0016, Santa Rosa, California, USA.

Bruhat, G. (1965), *Optique* (Masson & Cie Eds.), Paris, pp 384-394.

Coulson, K.L., Whitehead, V.S., and Campbell, C. (1986), Polarized views of the Earth from orbital altitude. *Ocean Optics VIII*, Proc. SPIE, Vol 637:35-41.

Cox, C., and Munck, W.H. (1954), The measurements of the roughness of the sea surface from photographs of the sun glitter, *J. Opt. Soc. Am.*, 44(11):838-850.

Deirmendjian, D. (1954), *Electromagnetic scattering on spherical polydispersions* (Elsevier Ed.), New-York.

Deschamps, P.Y., Herman, M., Podaire, A., Leroy, M., and al. (1990), A spatial instrument for the observation of polarization and directionality of Earth reflectance: POLDER, *IGARS'90 Conference Proceedings*, Washington D.C., USA.

Deuzé, J.L., Devaux, C., Herman, M., Santer, R., and al. (1989), Photopolarimetric observations of Aerosols and clouds from balloon. *Remote Sens. Environ.*, 29:93-109.

Duggin, M.J., Israel, S.A., Whitehead, and al. (1990), Use of polarization methods in Earth resources investigations. *Polarization Considerations for Optical Systems II*, Proc. SPIE, Vol 1166, 11-21.

Egan, W.G. (1985), Airborne observation of polarization and photometry of terrestrial surfaces. Nineteenth International Symposium on Remote Sensing Of Environment, Ann Arbor, October 21-25, Michigan, USA.

Egan, W.G., and Whitehead, V. (1989), Polarization imagery of terrestrial areas obtained during Space Shuttle missions. *International Radiation Symposium'88: Current Problems in Atmospheric Radiation*, Lille, France, on August 18-24 1988. A. Deepak Pub, pp. 561-563.

- Egan, W.G., Johnson, W.R., and Whitehead, V.S. (1991), Terrestrial polarization imagery obtained from the Space Shuttle: characterization and interpretation. *Appl. Opt.*, 30(4):435-442.
- Fraser, R.S., and Kaufman, Y.J. (1984), Calibration of satellite sensors after launch. *Appl. Opt.*, 25(7):1177-1184.
- Gaudart L. (1987), Densitométrie monochrome, *Bulletin de l'union des physiciens*, 697:1033-1049.
- Holben, B.N., and Kaufman, Y.J. (1991), Calibration of AVHRR visible and near-IR bands by atmospheric scattering, ocean glint and desert reflection. *J. Appl. Meteo.*, in press.
- Hansen, J.E., and Hovenier, J.W. (1974), Interpretation of the polarization of Venus. *J. Atmos. Sci.*, 31:1137-1160.
- Kaufman, Y.J., Setzer, A., Ward, D., Tanré, D., and al. (1991), Biomass burning airborne and spaceborne experiment in the amazonas (Base A). Accepted for publication in *Int. J. Remote Sens.*.
- Kawata, Y. (1978), Circular polarization of sunlight reflected by planetary atmospheres. *Icarus*, 33:217-232.
- Radke, L.F., Stith, J.L., Hegg, D.A., and Hobbs, P.V. (1978), Airborne studies of particles and gases from forest fires, *J. Air Poll. Cont. Ass.*, 28:30-34.
- Rondeaux, G., and Herman, M. (1991), Polarization of light reflected by the crop canopies. *Remote Sens. Of Environ.*, 38:63-75.
- Tanré, D., Deroo, C., Duhaut, P., Herman, M., and al. (1986), Simulation of the satellite signal in the solar spectrum (5S), Users Guide, available from Laboratoire d'Optique Atmosphérique, Université de Lille I, 59655 Villeneuve d'Ascq, France.
- Vanderbilt, V.C., Grant, L., Biehl, I., and Robinson, B.F. (1985), Specular diffuse and polarized light scattered by two wheat canopies, *Appl. Opt.*, 24:2408-2418.

Vermote, E., Santer, R., Deschamps, P.Y., and Herman, M. (1992a), In-flight calibration of large field of view sensors at short wavelength using the Rayleigh scattering. *Int. J. Remote Sens.*, in press.

Vermote, E. F., Vassiliou, G. D., Kaufman, Y. J. and Holben, B. N. (1992b), Calibration of the AVHRR Visible and Near IR Channels using radiances measured over remote ocean areas. International Geoscience and Remote Sensing Symposium (IGARSS), 1 IEEE, pp. 9-11.

Viollier, M. (1980), Télédétection des concentrations en Seston et pigments chlorophylliens dans l'océan, Thèse d'état, available from Laboratoire d'Optique Atmosphérique, Université de Lille I, 59655 Villeneuve d'Ascq, France.

## TABLE CAPTIONS

Table 1

Characteristics of the selected images.

Table 2

Error budget of the Rayleigh scattering calibration for the blue channel.

Table 3

Error budget for the glitter calibration for the ratios Blue/Green and Green/Red.

Table 4

Coefficients of a and b.

Table 5

Comparison for the Rayleigh scattering between the measurements (M) and the computations (C).

Table 6

Comparison for the sunglint between the measurements (M) and the computations (C).

Table 7

Restitution of the measurements of the Kraskino scene by particles of  $R_{\text{eff}}=0.15\mu\text{m}$ ,  $v_{\text{eff}}=0.07$ ,  $m=1.75$  and  $\delta=1.5$ .

Table 1 : Characteristics of the selected images  
(for the feature: SG=Sunglint, RA=Rayleigh, VG=vegetation).

date	GMT	location	feature	Geometry at the center of the image			
				$\theta_s$	$\theta_v$	$\varphi_s - \varphi_v$	$\Theta$
11 nov 84	6.946	Horn of Africa	SG	30.2°	30.1°	89.3°	138.6°
30 aug 85	18.674	Hawaii 1	SG-RA-VG	55.0°	52.6°	167.0°	73.3°
30 aug 85	18.678	Hawaii 2	SG-RA-VG	55.0°	46.2°	158.5°	81.2°
30 aug 85	18.705	Hawaii 3	stereoscopy	54.1°	53.6°	-60.6°	131.9°
30 aug 85	18.709	Hawaii 4	stereoscopy-VG	54.1°	58.5°	-54.4°	135.1°
1 sep 85	21.697	Easter islands	RA-VG	49.8°	20.0°	85.4°	128.8°
1 sep 85	21.312	Marshall islands	SG-RA	47.9°	36.4°	167.2°	95.7°
1 sep 85	18.624	Chili	snow	46.5°	53.6°	-143.1°	86.6°
5 nov 85	03.606	O-Ling-Mu Lake	snow	55.5°	10.7°	-47.1°	131.4°
5 nov 85	03.630	Yabrai Shan	sand	57.7°	21.4°	-56.6°	131.8°
5 nov 85	03.556	Brahmaputra	sand	52.2°	21.7°	-76.3°	129.7°
5 nov 85	02.147	Kraskino	aerosol	59.0°	34.5°	149.8°	92.0°
5 nov 85	03.700	China	VG	65.5°	14.2°	-34.6°	125.9°

Table 2 : Error Budget of the Rayleigh scattering  
calibration for the blue channel.

	aerosol type	aerosol load	wind speed	water reflectance	total
$L_{tot}$	±7.8%	±16.0%	±2.4%	±4.1%	±18.4%
$L_{pol}$	±2.3%	±1.5%	±1.8%	±0.0%	±3.3%
P	±5.4%	±17.0%	±4.1%	±4.1%	±18.8%

Table 3: Error budget for the glitter calibration for the ratios Blue/Green and Green/Red.

	aerosol type	aerosol load	wind speed	water reflectance	total
Bleu/Green ratio					
$L_{tot}$	$\pm 7.3 \%$	$\pm 2.4 \%$	$\pm 12.9 \%$	$\pm 0.8 \%$	$\pm 15.0 \%$
$L_{pol}$	$\pm 7.4 \%$	$\pm 2.6 \%$	$\pm 10.2 \%$	$\pm 0.0 \%$	$\pm 12.9 \%$
P	$\pm 0.2 \%$	$\pm 0.8 \%$	$\pm 2.7 \%$	$\pm 0.7 \%$	$\pm 2.9 \%$
Green/Red ratio					
$L_{tot}$	$\pm 5.6 \%$	$\pm 5.9 \%$	$\pm 5.0 \%$	$\pm 0.2 \%$	$\pm 9.6 \%$
$L_{pol}$	$\pm 5.6 \%$	$\pm 6.4 \%$	$\pm 3.7 \%$	$\pm 0.0 \%$	$\pm 9.3 \%$
P	$\pm 0.1 \%$	$\pm 0.2 \%$	$\pm 1.4 \%$	$\pm 0.2 \%$	$\pm 1.5 \%$

Table 4 : Coefficients a and b in each channels.

	Blue	Green	Red
a	0.052	0.063	0.081
b	3.351	3.084	2.650

Table 5 : Comparison for the Rayleigh scattering between the measurements (M) and the computations (C).

scene	total reflectance				degree of polarization (%)			
	Blue		Green		Blue		Green	
	C	M	C	M	C	M	C	M
Hawaii1	0.095	0.112	0.047	0.049	22.0	20.1	22.1	18.0
Hawaii2	0.140	0.121	0.100	0.069	21.8	22.8	25.2	25.7
Marshall	0.109	0.110	0.066	0.058	23.7	22.5	23.9	25.7
Easter	0.089	0.098	0.054	0.049	28.5	25.0	30.4	30.8

Table 6 : Comparison for the sunglint between the measurements (M) and the computations (C).

scene	total reflectance				degree of polarization (%)			
	Blue/Green		Green/red		Blue/Green		Green/red	
	C	M	C	M	C	M	C	M
Hawaii1	0.981	1.005	0.971	0.981	0.712	0.779	0.848	1.060
Hawaii2	1.098	1.203	1.007	1.135	0.743	0.734	0.890	0.939
Marshall	1.010	1.021	1.000	0.965	0.755	0.642	0.904	0.845

Table 7 : Restitution of the measurements of the Kraskino scene by particles of  $R_{\text{eff}}=0.15\mu\text{m}$ ,  $v_{\text{eff}}=0.07$ ,  $m=1.75$  and  $\delta=1.5$ .

	Blue	Green	Red
total reflectance			
measured	0.30	0.14	0.09
computed	0.21	0.16	0.11
polarized reflectance			
measured	0.03	0.05	0.04
computed	0.03	0.04	0.04
degree of polarization (%)			
measured	10	30	38
computed	13	27	41

## FIGURE CAPTIONS.

Figure 1

Transmittance curve of the Shuttle overhead window. Black and White film response.

Figure 2

Geometrical conditions of the observation.

Figure 3

Schematic description of digitization system (PERKIN-ELMER micro densitometer).

Figure 4

Correction factor in polarization induced by the variation of the direction of polarization.

Figure 5

Polarization of the Shuttle windows versus the incident angle. The incident light is natural and the induced polarization is computed for a double parallel glasses.

Figure 6

Characteristic curve of KODAK film.

Figure 7

Variation of the film density versus the exposition for different times of process.

Figure 8

Calibration curves of the radiance versus the digital count.

Figure 9

Transects in total and polarized reflectances on the O-Ling-Mu Lake scene.

Figure 10

Histograms in total and polarized reflectances on the Yabrai Shan scene.

Figure 11

Hawaii 1 scene. Location of the transects.

Figure 12

Total and polarized reflectances as measured over Hawaii scenes for the transect 1 defined on Figure 11.

Figure 13

Total and polarized reflectances as measured over Hawaii scenes for the transect 2 defined on Figure 11.

Figure 14

Degree of polarization at 650 nm on the canopy.

Figure 15

Kraskino scene.

Figure 16

Kraskino scene: Total reflectance and degree of polarization over the wreath.

Figure 17

Degree of polarization versus  $R_{\text{eff}}$  (in  $\mu\text{m}$ ) in blue and red channels, for 4 aerosols optical thicknesses (given at 450 nm), 3 refractive indexes and a variance  $v_{\text{eff}}=0.07$ .

Figure 18

Degree of polarization versus  $R_{\text{eff}}$  (in  $\mu\text{m}$ ) in blue and red channels, for 4 aerosols optical thicknesses (given at 450 nm), a refractive index  $m=1.75$  and a variance  $v_{\text{eff}}=0.30$ .

Figure 1 : Transmittance of the Shuttle overhead window. Black and White film response.

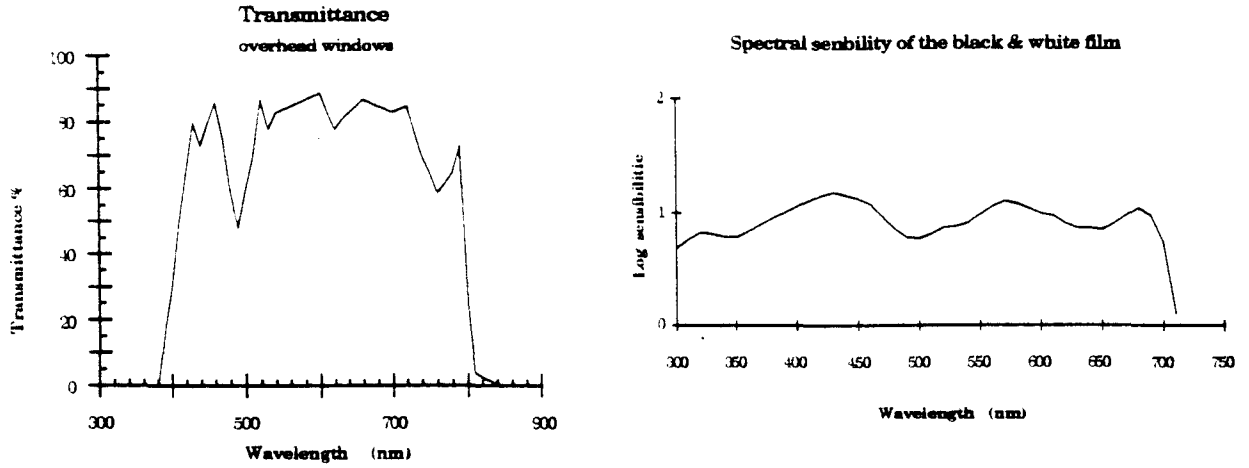


Figure 2 : Geometrical conditions of the observation.

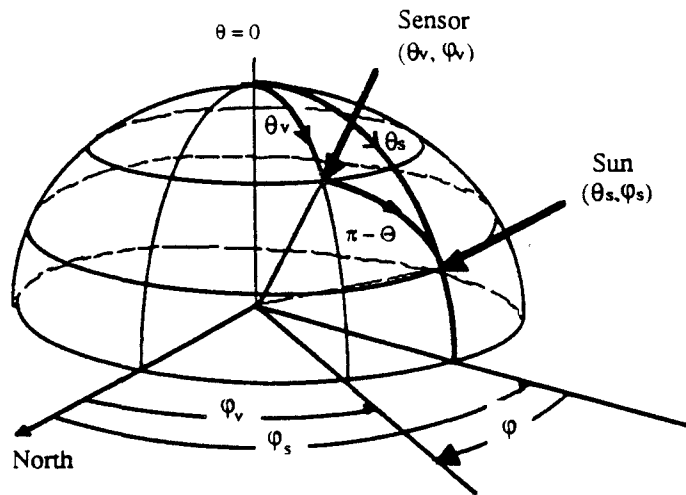


Figure 3 : Schematic description of the digitization system.

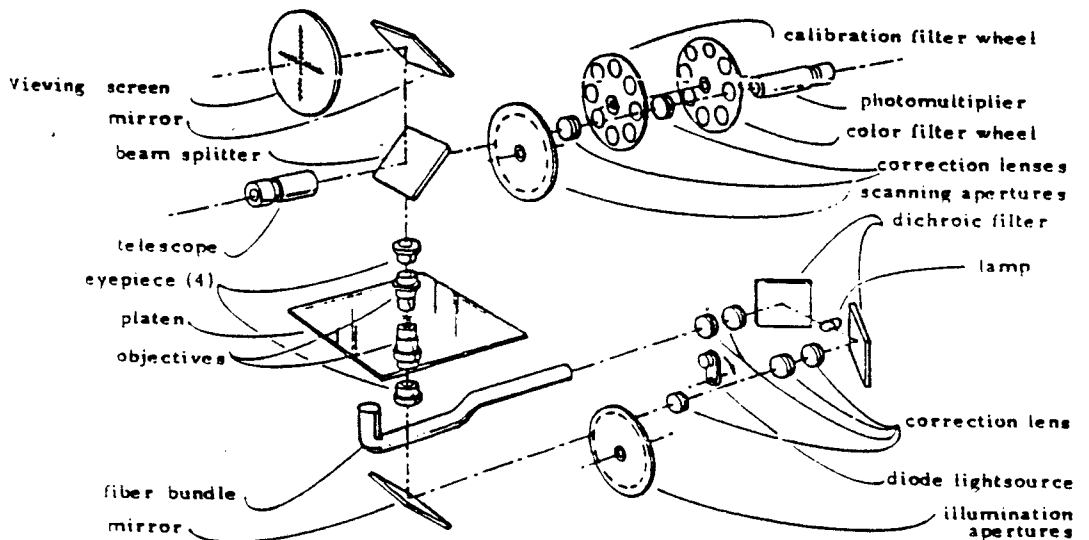


Figure 4: Correction factor  $\cos 2\delta$  in polarization induced by the variation of the direction of polarization.

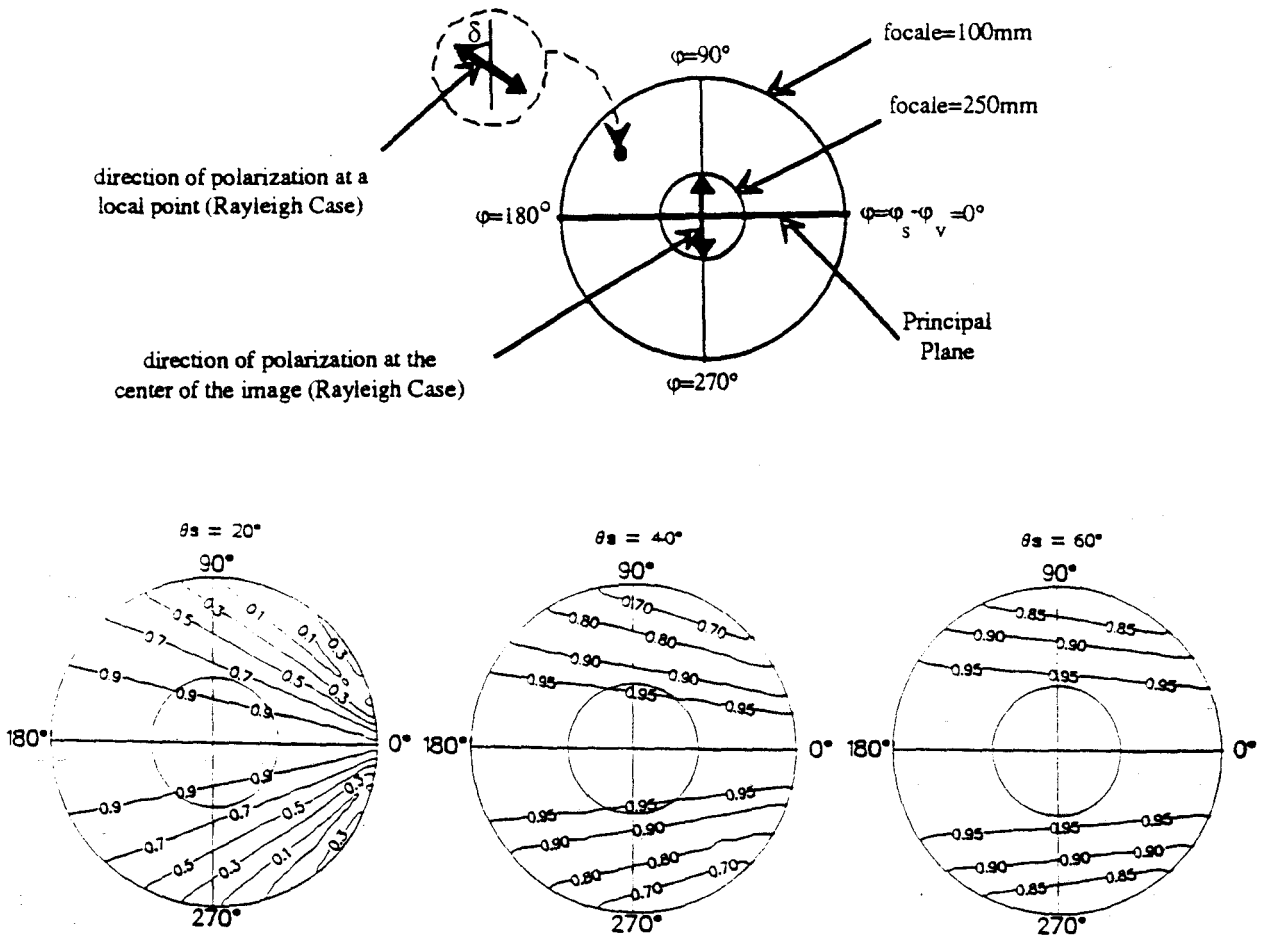


Figure 5 : Polarization of the Shuttle windows versus the incident angle.  
The incident light is natural and the induced polarization is computed for a double parallel glasses.

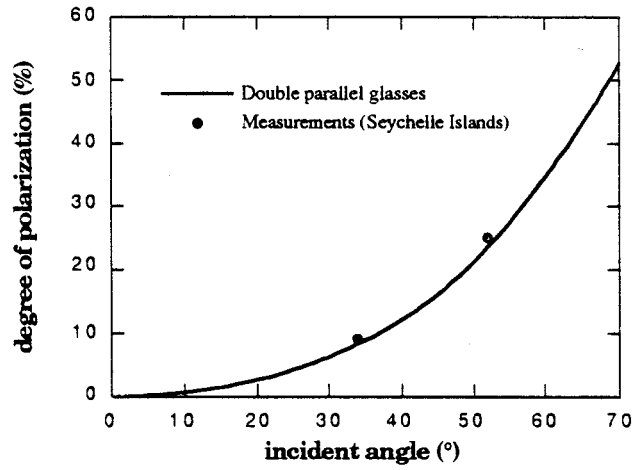


Figure 6 : Characteristic curve of KODAK film.

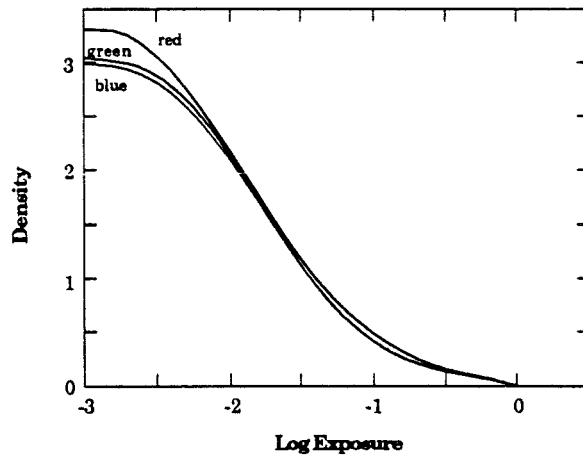


Figure 7 : Variation of the film density versus the exposition for different times of process.

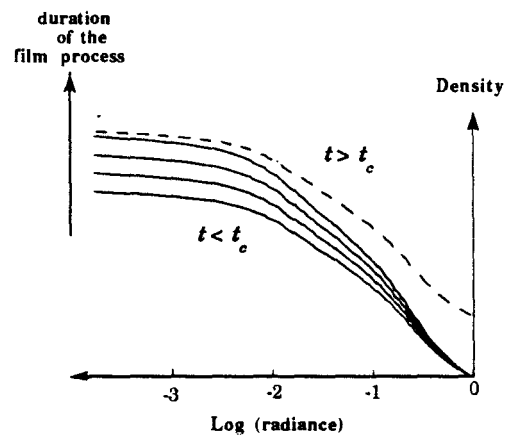


Figure 8 : Calibration curves of the radiance versus the digital counts.

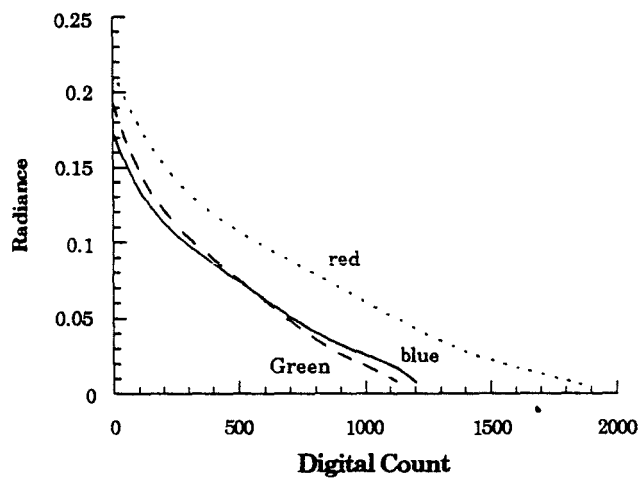


Figure 9 : Transects in total and polarized reflectances on the O-Ling-Mu Lake scene.

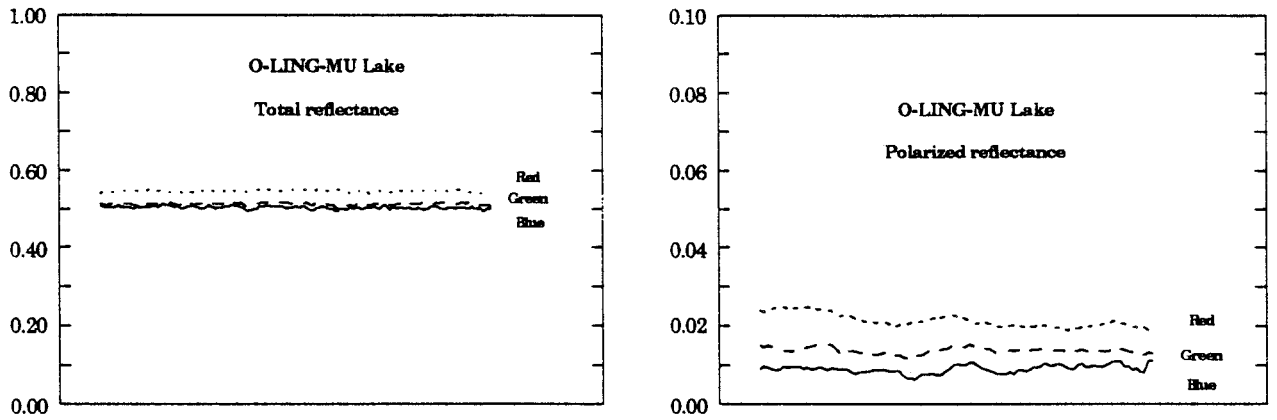


Figure 10 : Histograms in total and polarized reflectances on the Yabrai Shan scene.

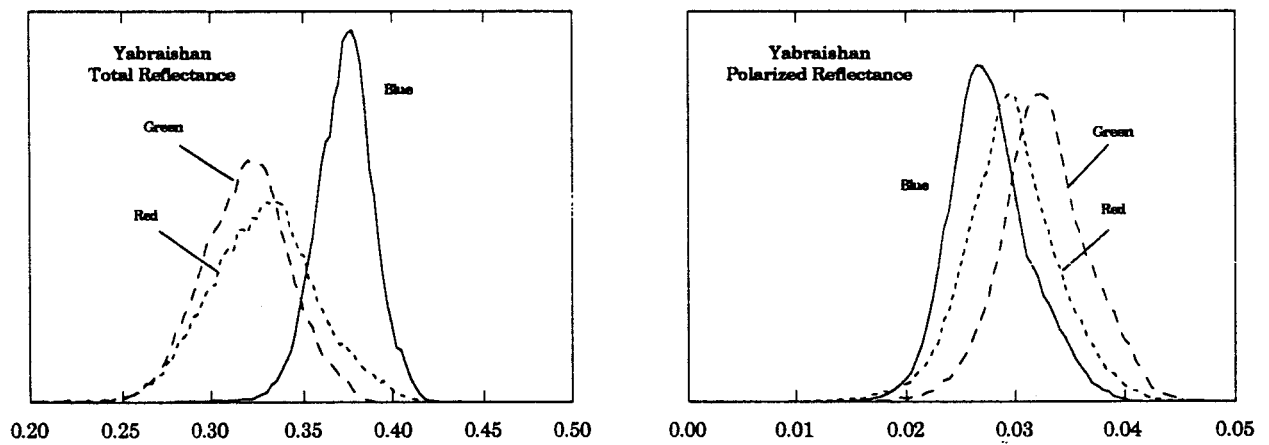


Figure 11 : Hawaii 1 scene. Location of the transects.



Figure 12 : Total and polarized reflectances as measured over Hawaii scenes for the transect 1 defined on Figure 11.

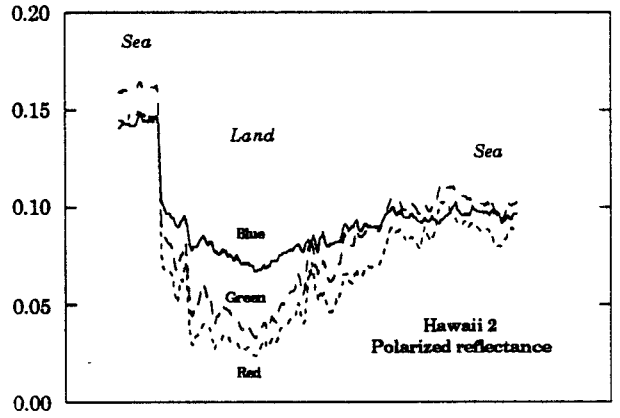
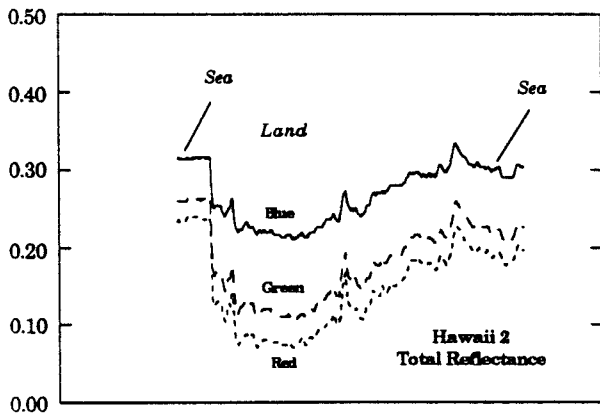
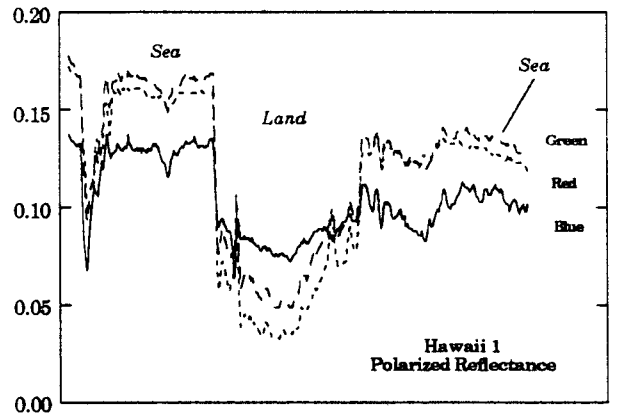
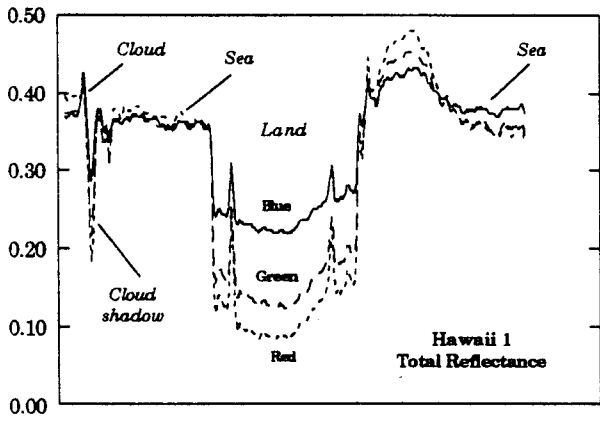


Figure 13 : Total and polarized reflectances as measured over Hawaii scenes for the transect 2 defined on Figure 11.

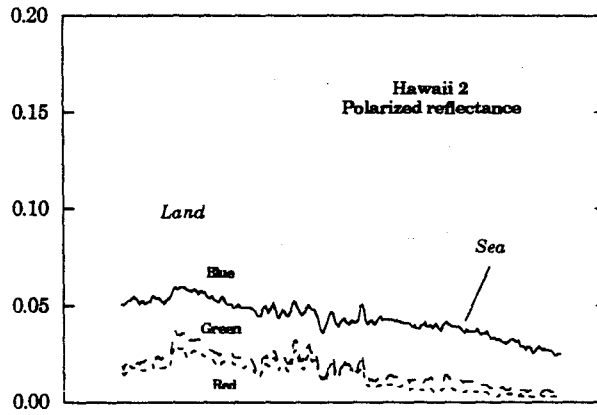
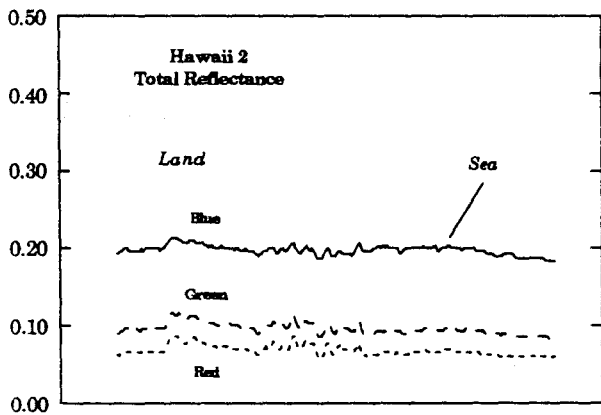
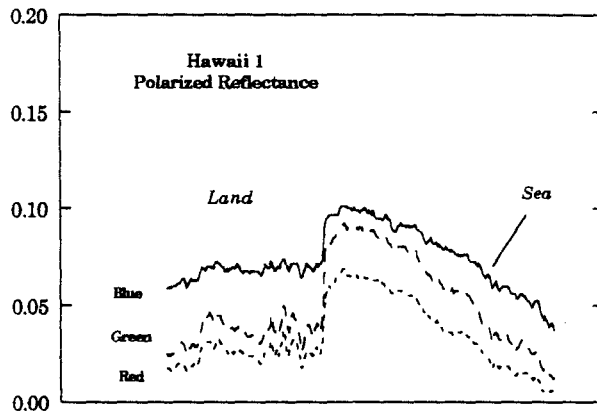
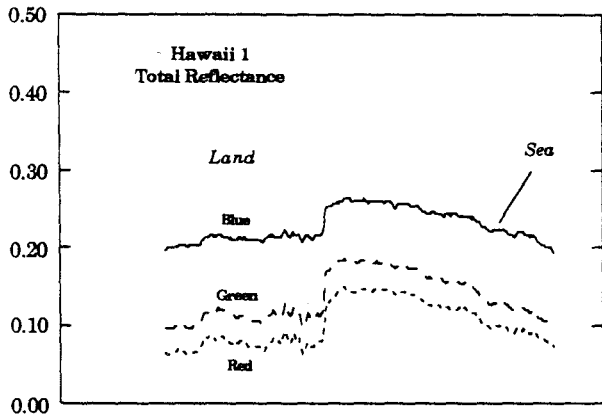


Figure 14 : Degree of polarization at 650 nm on the canopy.

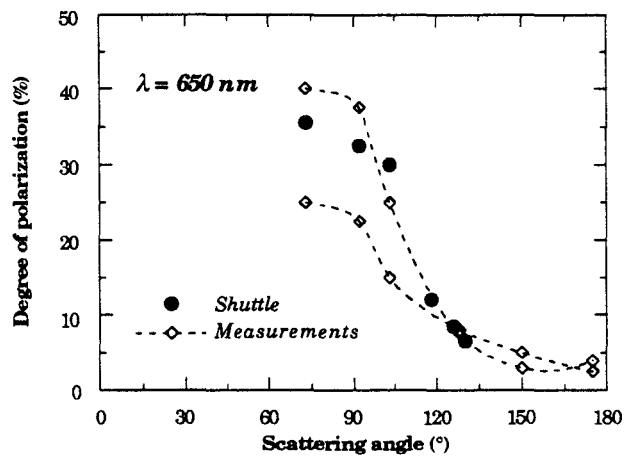


Figure 15 : Kraskino scene.

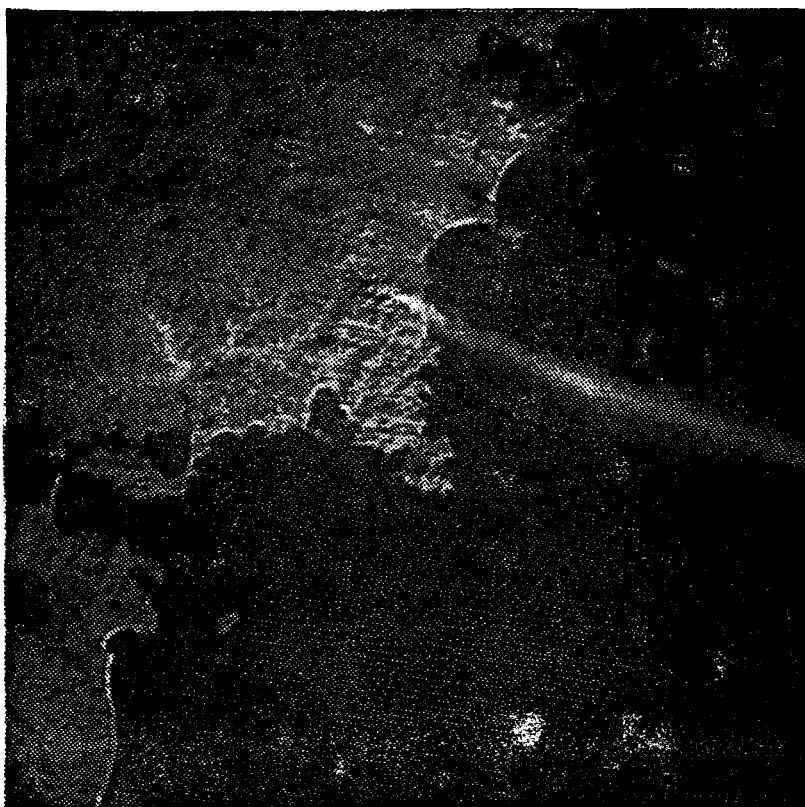


Figure 16 : Kraskino scene: Total reflectance and degree of polarization over the plume of smoke.

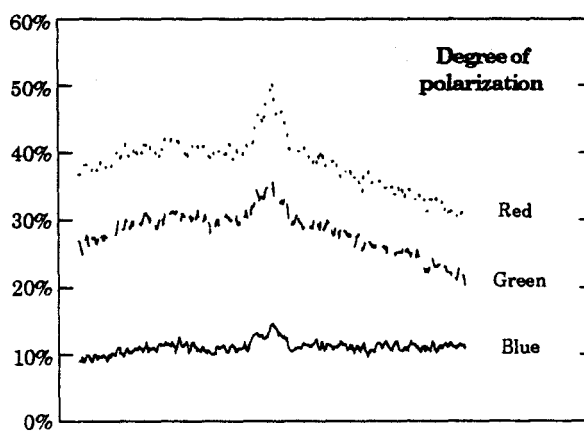
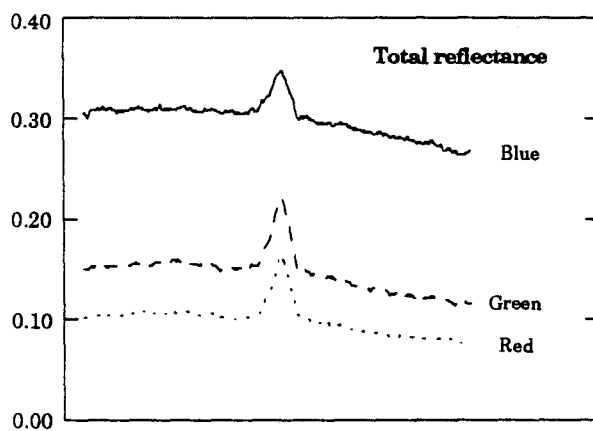
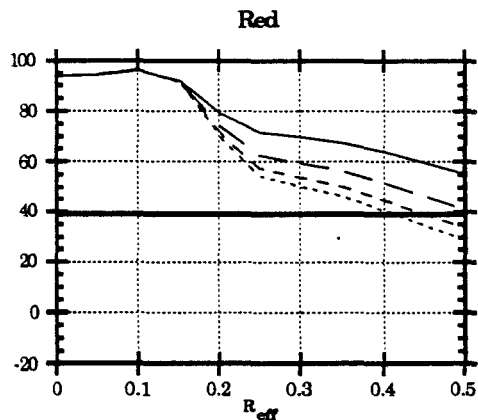
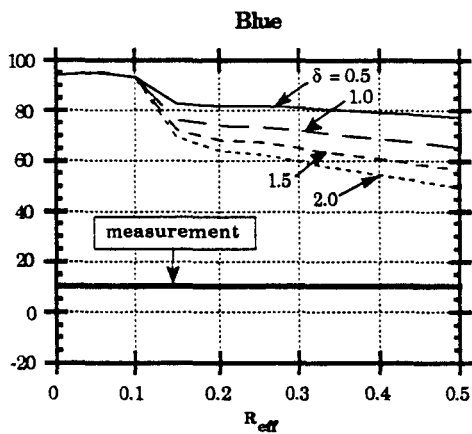
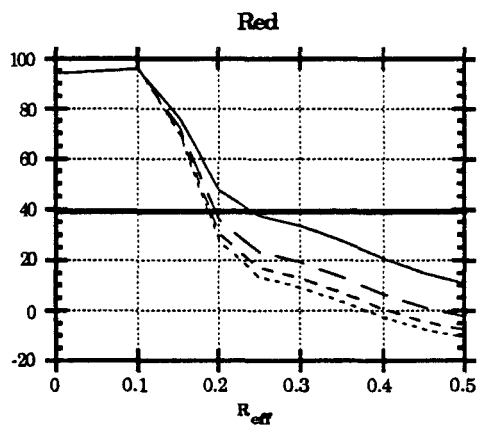
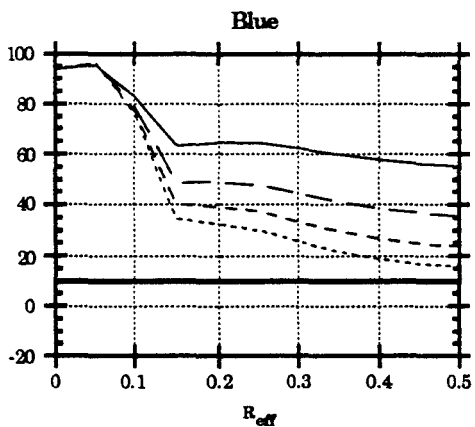


Figure 17 : Degree of polarization versus  $R_{eff}$  (in  $\mu\text{m}$ ) in blue and red channels, for 4 aerosol optical thicknesses (given at 450 nm), 3 refractive indexes and a variance  $v_{eff} = 0.07$ .

$$m = 1.33 - 0.01i$$



$$m = 1.50 - 0.01i$$



$$m = 1.75 - 0.01i$$

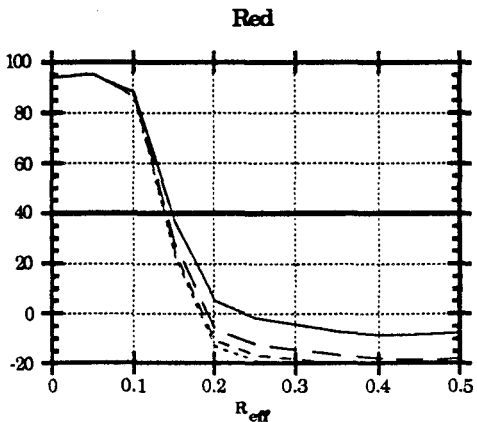
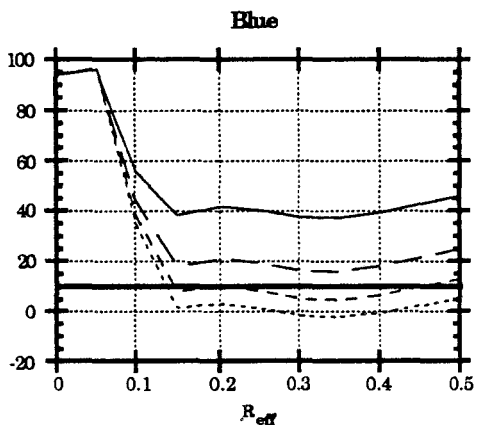
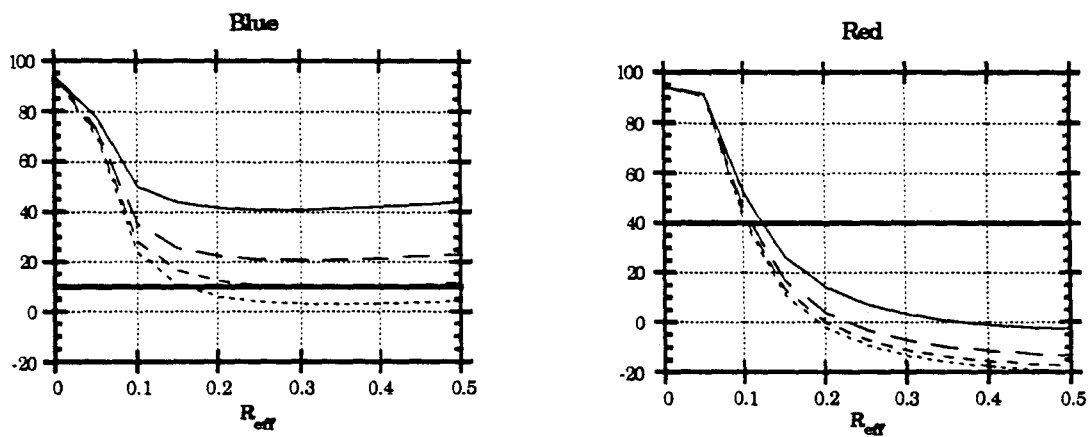


Figure 18 : Degree of polarization versus  $R_{\text{eff}}$  (in  $\mu\text{m}$ ) in blue and red channels, for a refractive index  $m=1.75$  and a variance  $v_{\text{eff}}=0.30$ .



**The POLDER mission: Instrument characteristics  
and scientific objectives**

**F.M. Bréon<sup>1</sup>, A. Bricaud<sup>2</sup>, J.C. Buriez<sup>1</sup>, P.Y. Deschamps<sup>1</sup>,  
J.L. Deuzé<sup>1</sup>, M. Herman<sup>1</sup>, M. Leroy<sup>3</sup>, A. Podaire<sup>3</sup>, G. Sèze<sup>4</sup>**

**1 Laboratoire d'Optique Atmosphérique  
Université des Sciences et Technologies de Lille  
Villeneuve d'Ascq**

**2 Laboratoire de Physique et Chimie Marine  
Villefranche sur Mer**

**3 Centre National d'Etudes Spatiales  
Toulouse**

**4 Laboratoire de Météorologie Dynamique  
Ecole Polytechnique  
Palaiseau**

## Abstract

POLDER (POLarization and Directionality of the Earth's Reflectances) is a new instrument devoted to the global observation of the polarization and directionality of solar radiation reflected by the Earth surface-atmosphere system. The instrument concept has been evaluated using an airborne version, and has been accepted on the Japanese ADEOS platform scheduled to be launched early 1996. The spaceborne POLDER instrument is currently in phase C development at the Centre National d'Etudes Spatiales, the French space agency. It will allow a near-daily coverage of the Earth at a resolution of  $6 \times 7 \text{ km}^2$ .

The original capabilities of POLDER, compared to other current and planned spaceborne instruments are i) its polarized reflectance measurements in the visible and near-infrared part of the solar spectrum; ii) its capability to measure a surface target reflectance from 12 directions during a single satellite pass; and iii) two dynamic modes in order to achieve both a high signal to noise ratio and a wide dynamic range.

Six of POLDER channels have been optimized for the observation of atmospheric aerosols, ocean color and land surfaces. The other two are centered on an  $\text{H}_2\text{O}$  absorption band and an  $\text{O}_2$  absorption band, respectively, for the retrieval of atmospheric water vapor amount and cloud top altitude using differential absorption techniques.

The spaceborne instrument will contribute to climate-related research on aerosol cycling, cloud-radiation interactions, Earth radiation budget, ocean primary productivity and continental biosphere dynamics. These are primary components of the World Climate Research Program (WCRP) and of the International Geosphere and Biosphere Program (IGBP).

## 1. Introduction

Because of the rising concerns for a possible climate change, there are increasing needs and demands for a better understanding of the Earth climate system. The climate system is controlled by the atmosphere and ocean dynamics and the water cycle but also includes the interactions between biosphere and atmosphere. One requirement for the understanding of the climate system and its possible evolution in the context of global change is a global assessment of current exchange processes, their annual cycles, and their modifications related to anthropogenic activities.

The POLDER experiment is a new instrument devoted to the observation on a global scale of the polarization and directionality of solar radiation reflected by the Earth-atmosphere system. This instrument has been selected for the Japanese ADEOS (Advanced Earth Observing Satellite) platform scheduled to be launched early in 1996. ADEOS is a polar satellite dedicated to the observation of the Earth surfaces and atmosphere. Its characteristics are given in Tab. 1. ADEOS will also carry the Ocean Color and Thermal Sensor (OCTS) for the monitoring of ocean color, the Advanced Visible and Near Infrared Radiometer (AVNIR) for surface monitoring with a very high spatial resolution, the NASA Scatterometer (NSCAT) for wind speed and direction retrieval, the Total Ozone Mapping Spectrometer (TOMS) for atmospheric ozone monitoring, the Interferometric Monitor for greenhouse Gases (IMG), the Improved Limb Atmospheric Spectrometer (ILAS) for limb-viewing retrieval of atmospheric microingredients over high latitude areas, and the Retroreflector In Space (RIS).

The POLDER instrument is based on the concept of a matrix array CCD (Charge Coupled Device) detector, a rotating filter wheel and wide field of view optics, along-track and cross-track, with a maximum field of view of  $114^\circ$ . It allows the observation of a given point on the Earth's surface under different viewing angles during the same orbit. These measurements yield the target reflectance and polarization properties, the Bidirectional Reflectance and Polarization Distribution Functions (BRDF and BPDF), from one or several orbits.

Spectral BRDF and BPDF derived from POLDER observations should permit the space-based study of a number of important issues related to the understanding of the biogeochemical cycles and the global energy, water and mass budgets. As such, it should represent a significant contribution to the World Climate Research Program (WCRP) and the International Geosphere Biosphere Program (IGBP).

Except for the ERB instrument on Nimbus-7, most of the past and present space experiments on polar orbiting satellites have a viewing capability limited to the cross-track direction which strongly restricts the bidirectional observations. On the Earth Observing System (EOS), planned to be launched in 1998, the CERES and MISR (Diner et al., 1989) instruments will provide some bidirectional observations, but with only a partial description of the BRDF. Moreover, they will not allow estimates of these effects at a global scale, because of their limited field of view.

Polarization has been used to observe the surface and atmosphere of some planets of the solar system (Hansen and Hovenier, 1974). A few polarized pictures of the Earth have been shot during space shuttle flights and analyzed in terms of reflectance (Coulson et al, 1986; Roger et al., 1992). They have emphasized the potential of polarization for aerosol parameter estimates. The first alternative instrument currently planned to measure the polarized reflectance from space is the Earth Observing Spectrometer Polarimeter (EOSP) (TRAVIS, 1992), scheduled to be launched in 2003.

There is clearly a need to measure global bidirectionality and polarization effects which is not satisfied by the present and planned instruments. The POLDER instrument will satisfy this need.

In the following, we first describe briefly the POLDER instrument concept (§2) and observation principles (§3), then provide a detailed description of the instrument characteristics (§4) and the mission objectives (§5), and finally present the data processing (§6).

## 2. Instrument concept

The POLDER radiometer is based on the simple concept of the association of a CCD matrix detector, a rotating wheel carrying polarizers and filters, and a wide field of view (FOV) telecentric optics (Fig. 1).

The telecentric optics, a key component of POLDER, is a major improvement relative to classical lenses. Within the optics, one of the lens is aspherical, reducing the effect of the incidence angle on the entrance pupil area, and providing a nearly perpendicular incidence of the optical rays on the filters. The optics have a focal length of 3.57 mm, are opened at  $f:4.5$  and have a maximum FOV of  $114^\circ$ .

The CCD array sensor is manufactured by Thomson-CSF, in France. It is composed of 242 by 548 photoelements of size  $27 \mu\text{m} \times 16 \mu\text{m}$ ; the pixels are actually binned two by two, resulting in 242 by 274 independent sensitive areas. The total size of the matrix array detection unit is, therefore, 6.5 by 8.8 mm which, according to the lens focal ratio, corresponds to along track and crosstrack FOVs of  $\pm 43^\circ$  and  $\pm 51^\circ$ , respectively, and to a diagonal FOV of  $\pm 57^\circ$ . The CCD array is equipped with an antiblooming device which prevents the image from degradation when the incident radiance is above the sensor dynamical range. This may occur rather frequently over water surfaces, at low wind speed, around the specular direction. The spectral sensitivity of this CCD array extends between 400 and 1050 nm.

The rotating wheel supports the interference filters and polarizers for the selection of spectral bands and polarization directions. It carries 16 slots with one of them as an opaque filter in order to estimate the CCD detector "dark current". The remaining 15 slots carry 6 unpolarized and 9 polarized filters (3 polarization directions for each of 3 different wavelengths). The selected wavelengths are given in Tab. 2. The wheel rotates steadily with a period of 4.9 s.

### 3. Observation principle

Onboard the heliosynchronous ADEOS satellite at 800 km altitude, the POLDER crosstrack swath is about 2200 km, which allows a nearly complete daily coverage of the Earth. This naturally excludes polar regions when the sun remains below the horizon. The coverage frequency is minimum at the Equator where it is, on the average, 4 days of observations over a 5 day period. On the other hand, surface points located poleward of  $37^\circ$  may be observed several times from consecutive orbits during the same day. This obviously does not account for cloudiness and the above figures are reduced according to cloud cover.

The bidimensional characteristics of the CCD matrix permits observation of any target within the instrument swath under different directions, and then estimation of some of its bidirectional reflectance properties. The 16 channel sequence is repeated every 19.6 s which corresponds to 4 rotations of the filter wheel. During this time interval, a given point on the surface, initially at nadir viewing, has moved by about  $9^\circ$  relative to the satellite (Fig. 2). This point is then still within the POLDER field of view and its bidirectional reflectance can be inferred. As the satellite passes over the target, about 12 radiance measurements are performed aiming at that point. These measurements thus provide a sampling of the target BRDF and BPDF.

The next day or so, the satellite is again in a position to observe the target. Since the orbital cycle is 41 days (subcycle of 4 days), the satellite ascending longitude has changed and the azimuth angles of observation are different. The 12 "snapshots" then provide a new sampling of the BRDF. After a few days, the successive orbits provide a complete coverage of the target BRDF (Fig. 3).

The POLDER observations are acquired for solar zenith angles lower than  $75^\circ$ , which implies that the geographic zones covered by POLDER change according to the season of acquisition. However, the performances of the POLDER instrument, both geometrical and radiometrical, are warranted for solar zenith angles lower than  $60^\circ$ .

## 4. Instrument characteristics

### 4.1 Spectral bands

Table 2 gives the spectral bands of the POLDER instrument on the ADEOS satellite. The 15 channels are defined by their central wavelength, spectral width, dynamic range and the direction of polarization when applicable. The spectral band selection is obviously closely related to the mission requirements, and is described in detail in §5. The dynamic range is given in normalized radiance, i.e. the maximal spectral radiances divided by the solar spectral irradiance at nadir and multiplied by  $\pi$ . The dynamic reflectance range is then obtained by dividing the range given in Table 1 by  $\cos(\theta_s)$ , where  $\theta_s$  is the solar zenith angle.

Two possible dynamic ranges per channel have been considered (See Tab. 2) for the following reason. The cloud and radiative budget missions require a large dynamic range, and the ocean color objective needs a very good radiometric resolution at low signal values. This leads to a high signal to noise ratio and the two missions appeared to be in conflict during the definition phase. It was therefore decided, for a few channels, to make use of two dynamic ranges by changing the time of exposure to the incident photons. Among three successive spectral measurements, two will be performed with the larger dynamic range, optimized for cloud observation and ERB measurements, and one with the smaller dynamic range, which is optimized for the ocean color mission (Fig. 4).

Note also that, owing to the signal to noise requirements for ocean color measurements, the 443 nm channel had to be split into one polarized band (3 channels) and one unpolarized band (1 channel). The 3 polarized channels have a large dynamic range, whereas the unpolarized channel has a low dynamic range optimized for the ocean color mission.

#### 4.2 Polarization measurements

Multiple, as opposed to single, scattering/reflection processes induce elliptic polarization. Radiative transfer simulations show that the fourth component of the Stokes vector of the light at the TOA is negligible compared to the others. It means that the polarization is mostly linear for the conditions which prevail in the atmosphere. In consequence, the POLDER instrument only senses the *linear* polarization of the radiance reflected by the Earth system.

Three of the eight spectral bands (443, 665 and 865 nm) are polarized in order to assess the degree of linear polarization and the polarization direction. These parameters are derived from the combination of measurements in three channels with the same spectral filters but with polarizers having their polarization axis turned by steps of  $60^\circ$ . The three polarized measurements in a spectral band are not simultaneous but successive. There is a total time lag of 0.6 s between the first and the third (last) measurement. In order to compensate for spacecraft motion during this time lag and to register the three measurements, a small angle wedge prism is implemented in each polarizing assembly. As a result, the matrix is apparently translated in the focal plane to compensate for the satellite motion, and the three polarization measurements are obtained for an apparently fixed target.

#### 4.3 Geometry / Spatial Resolution

The ground size of a pixel of the POLDER-ADEOS instrument measurements will be  $6 \times 7 \text{ km}^2$  at nadir. In contrast to mechanically scanning radiometers such as the Advanced Very High Resolution Radiometer (AVHRR), the POLDER design does not suffer any degradation of this resolution on the swath edges when viewing a flat surface. Due to Earth curvature, the observation angle at the surface is larger than that in the satellite coordinates (Fig. 5). Satellite viewing angles ( $\theta_v$ ) of  $10^\circ$ ,  $20^\circ$ ,  $30^\circ$ ,  $40^\circ$  and  $50^\circ$  correspond to incidence angles ( $\theta_i$ ) of  $11.3^\circ$ ,  $22.6^\circ$ ,  $34.1^\circ$ ,  $45.7^\circ$  and  $57.8^\circ$ , respectively. This leads to a slight degradation of pixel size, corresponding to an increase of 21% for a viewing incidence angle of  $60^\circ$ .

## 4.4 Calibration

The POLDER science team has defined high standards for the calibration of spaceborne data. An absolute calibration accuracy of 2 % is required for the shorter wavelength channels ( $\lambda \leq 565$  nm) and of 3% for the longer wavelengths. The goal for the intercalibration accuracy between the spectral channels is 1 %.

The prelaunch calibration in terms of spectral radiances is performed using an integrating sphere available in France as a CNES facility. An accuracy between 4% and 7 % is expected from this pre-launch calibration procedure. This is not sufficient for POLDER scientific objectives and more precise in flight calibration methods are needed. A prelaunch intercalibration of POLDER and OCTS is also planned. An accuracy of 2% is expected.

There is no internal source in the POLDER instrument for in flight onboard calibration. Calibration will be ensured and validated in the post launch phase by viewing specific targets of known reflectance signatures.

### 4.4.1 Absolute calibration

Two methods are planned for the in flight absolute calibration of POLDER. The evaluation of highly reflecting and stable targets such as White Sands (New Mexico) or La Crau (S.E. of France) is a classical method already used for sensors such as the AVHRR and SPOT HRV (Holben et al., 1990; Santer et al., 1992). The absolute calibration of POLDER will also be assessed on the atmospheric Rayleigh scattering (Vermote et al., 1992). Over cloud free ocean surfaces and for the shorter visible wavelengths, the top of the atmosphere (TOA) measured radiance is dominated by the reflectance from molecular scattering. The Rayleigh scattering can be modelled very accurately. The major uncertainties on the TOA reflectance result from the water column reflectance and the aerosol signal. Numerical simulations have shown that, provided that the oceanic target is carefully chosen for its low aerosol loading, an absolute calibration of the order of 2 % is achievable by this method for the 443 nm band. This absolute calibration can then be transferred to the other channels with an interband calibration procedure.

### 4.4.2 Intercalibration

The interband calibration of POLDER channels will be achieved by comparing the spectral measurements over spectrally flat targets such as clouds and the ocean glitter. The basic idea behind this method is to minimize the relative contribution of scattering/reflectance processes for which the spectral dependence is unknown.

For the shorter wavelengths of the POLDER instrument, the clouds are non absorbing and their spectral reflectance is flat. The uncertainties on the radiance spectral signature at the instrument level result from radiance transmitted by the cloud and reflected at the surface, and radiance reflected by the atmosphere above the cloud. In order to minimize the relative contribution from the surface, thick clouds over the ocean are preferred. The contribution from the atmosphere will be minimized by considering only high clouds.

There are some uncertainties on the cloud absorption for the longer wavelengths of POLDER (Stephens and Tsay, 1990). Therefore, cloud targets may not be suitable for the intercalibration of the longer and shorter wavelength bands of the POLDER instrument.

On the other hand, the glitter is spectrally neutral over the POLDER wavelength range. It will be preferred for the intercalibration of the longer and shorter wavelength bands. When viewing the glitter, the spectral variations at the TOA result mostly from the atmospheric transmission. The scattering by the molecules is stable and can be modelled easily. There is some uncertainty resulting from the aerosol transmission. Numerical simulations show that the 1 % accuracy goal for the intercalibration appears feasible with this method.

The use of specific desertic areas of Sahara and South Arabia, known to have an excellent temporal and directional stability, is an alternative approach of intercalibration (Staylor, 1990). The principle of this method is to select desertic zones with approximately 100 km size which satisfy a number of criteria (uniformity, temporal variability at various time scales, cloud cover, relief...), and to provide a preflight calibration of their spectral BRDF spatially averaged over each zone. This method can potentially be used for multitemporal and interband calibration, and possibly also for monitoring the equalization of sensitivities of the CCD detectors.

The 763 nm channel measurement is much more affected by O<sub>2</sub> absorption than other POLDER bands. As a result, over bright spectrally stable targets such as clouds and the glitter, the expected radiance is very different to that of spectrally close POLDER channels. However, when viewing the glitter, the ratio of the 763 nm and 765 nm bands depends only on the clear atmosphere transmission. This ratio can be accurately determined with the help of a line-by-line radiative transfer code if the surface pressure is known. Therefore, the intercalibration of the 763 nm and 765 nm POLDER bands can be performed over the glitter.

The 910 nm channel (water vapor absorption band) cannot be calibrated with the above described methods because it is sensitive to an uncontrolled atmospheric parameter: the water vapor amount. An intercalibration over the glitter with the 865 nm band is possible provided that the scene is clear and that a concomitant accurate estimate of the atmospheric water vapor amount is provided. The calibration plan has not yet been finalized for this channel. The procedure will make use either of operational water vapor measurements over small islands in the Pacific or specific campaigns dedicated to the 910 nm band calibration.

The multiangular intercalibration of the CCD pixels corrects the photoelement sensitivity variations and the lens transmission effects. The high frequency variations (i.e. for pixels located close together on the CCD matrix) results from the CCD photoelements differential sensitivity. Low frequency variations (i.e. the large scale variations over the CCD matrix) are more likely to result from the lens and filters transmittance. The high frequency intercalibration

will be performed by averaging a large number of cloud observations. Any high frequency reflectance variation in the results is an indication of differing photoelement sensitivity that shall be corrected accordingly. The low frequency intercalibration will be performed over targets of known angular reflectance signatures, such as desertic areas.

## 5. Mission objectives

### 5.1 International programs context

The WCRP, initiated in 1979, has instituted three majors projects to investigate climate change processes. The Global Energy and Water Cycle Experiment (GEWEX) project is one of them and aims at quantifying the energetic processes of the Earth's climate system, and the forcing functions on ocean, land, ice and vegetation. GEWEX is particularly demanding in its requirements for satellite data, requiring simultaneous measurements of properties of the upper atmosphere (cloud tops, Earth radiation budget), and underlying vertical profiles of temperature, moisture and clouds.

Initiated in 1986, the IGBP intends to describe and understand the interactive physical, chemical and biological processes that regulate the Earth system, the changes that are occurring in this system, and the way they are influenced by human activities. The initial operational phase of this programme focuses on several key questions, which include i) the regulation of the chemistry of the global atmosphere and the role of biological processes in producing and consuming trace gases, ii) the influence and response of biochemical processes to climate change, and iii) the way global change affects global ecosystems.

It is clear that these projects need measurements over the long term (decades), in particular observations from space, for a large number of variables related to the physical state of the atmosphere, land surfaces and oceans; chemical changes in the atmosphere, oceans and land; and the biological state of land cover and the upper layer of the oceans.

The POLDER experiment on the ADEOS satellite, with its capabilities for determining the bidirectional reflectance and polarization distribution functions, contributes significantly to the objectives of the WCRP and IGBP. Its mission is focused on :

- the characterization of atmospheric aerosols, their sources and transport, and their influence on the Earth radiation budget,
- the determination of cloud properties, and especially cloud top height, cloud phase and cloud type, the determination of integrated water vapor amount, and the estimation of the Earth radiation budget,
- the estimation of ocean color and its role in the carbon cycle,
- the characterization of land surfaces and their vegetation cover.

These scientific objectives are further presented in the following sections.

## 5.2. Aerosols

The IGBP program has clearly identified the biogeochemical cycle of aerosols as an important study objective, particularly the generation of aerosols at the surface, their rise and transport, and their interaction with other biogeochemical cycles. One objective of the POLDER mission is therefore to globally map the type and concentration of tropospheric aerosols.

Aerosol property retrieval from remotely sensed observations is necessary at two levels. First, because of the aerosol potential effects on the Earth radiation budget (Charlson et al., 1992), the phytoplankton primary productivity (Martin and Fitzwater, 1988), and the vegetation growth (Swap et al., 1992), there is a need to better understand their biogeophysical cycle; second, aerosols are the largest perturbation on shortwave remote sensing of the surface. The aerosol effect correction is of uppermost importance for ocean color monitoring since the aerosol reflectance is often larger than the sought after ocean reflectance. Similarly, in the visible spectrum, the vegetation reflectance and the atmospheric aerosol reflectance have the same order of magnitude. An accurate correction of the aerosol optical effects is therefore necessary for monitoring the vegetation cover. The POLDER concept provides new opportunities for the retrieval of aerosol parameters and, subsequently, the correction of remotely sensed data.

### 5.2.1 Over the oceans

In the near infrared, the ocean is almost "black" and the aerosol reflectance constitutes the main contribution to the radiance measurement. After correction for molecular scattering and specular reflection, the measurement provides an estimate of the product of the aerosol optical thickness by their phase function. A set of spectral measurements in the near infrared yields the spectral dependency of the aerosol optical thickness, which is an indication of their size distribution. Measurements have shown that the aerosol optical thickness varies as a power of the wavelength (Deuzé et al., 1988). This property is used, for ocean color monitoring, to extrapolate the near-infrared estimates of the aerosol contribution to the shorter wavelengths for a correction of the atmospheric effects. POLDER spectral bands centered on 665, 765 and 865 nm allow a correct description of the spectral signature of the aerosols over the oceans.

The retrieval of aerosol type and amount can be improved by POLDER relatively to other ocean color instruments. First, its multidirectional measurements provide a 12 points sampling of the phase function. Furthermore, its measurements describe some polarization characteristics of the atmospheric aerosols, which are very sensitive to the aerosol type (size distribution and refractive index). Fig. 6, which shows the result of a radiative transfer simulation over the ocean, illustrates that the polarization measurements allow differentiation between different aerosol types which would be very difficult to distinguish with reflectance measurements alone. POLDER multidirectional and polarized measurements allow a full retrieval of the aerosol amount and type over the ocean. These will improve the aerosol reflectance extrapolation toward shorter wavelengths and thus permit a better correction of visible reflectance measurements for ocean color estimates.

### 5.2.2. Over land

The retrieval of aerosol optical properties over land is difficult because the radiance from the surface and that from the aerosols are ambiguously mixed (Tanré et al., 1988). In the near infrared spectral region, radiance from the surface is generally much larger than that generated by aerosol scattering. In the visible, over vegetated areas, they are of the same order of magnitude.

Several methods have been proposed for the estimate of aerosol parameters from spaceborne sensors such as the AVHRR. At present, however, none is applicable globally for the retrieval of aerosol optical thickness, let alone their Ångström coefficient or phase function. A method exists that derives the aerosol reflectance from that of a target of known reflectance (Kaufman and Sandra, 1988; Kaufman et al., 1990). This method requires the existence of such a target on each remotely sensed image and assumes the spatial homogeneity of atmospheric aerosol content. Another method determines the aerosol atmospheric loading from the reduction in the image contrast that results from scattering by the aerosols (Tanré et al, 1988). This method is clearly only applicable over steady targets, and is not satisfactory over vegetated areas that exhibit a noticeable seasonal cycle. Moreover, as over the ocean, the current instruments provide only one reflectance measurement which does not allow to infer the aerosol phase function.

The POLDER system provides a new opportunity for the estimate of atmospheric aerosol content over land surfaces. Radiance reflected by most land surfaces is little polarized. On the other hand, the radiance scattered by the molecules and aerosols is strongly polarized. Thus, the TOA polarized reflectance originates mostly from the atmosphere. Polarized reflectance measurements provide, therefore, an opportunity to infer some aerosol properties. After correction of the molecular signal, the polarized reflectance measurements at 443, 665 and 865 nm yields the aerosol spectral behavior, which gives an indication of their type.

Results from the first airborne campaign of POLDER have validated the polarized reflectance usefulness over land surfaces (Deuzé et al., 1992), as shown in Fig. 7. This figure plots the polarized reflectance corrected for the optical path (see Deuzé et al., 1992 for details) as a function of the scattering angle for many viewing directions (viewing zenith angle between  $0^\circ$  and  $60^\circ$ , all azimuth angles). A given scattering angle corresponds to many different viewing zenith angle and surface types. Fig. 7 demonstrates that the polarized reflectance is mainly driven by the scattering angle, and therefore the aerosol phase function, and that the surface contribution generates little dispersion of the measurements. Around the  $150^\circ$  scattering angle, the polarized reflectance equals that estimated for a "clear" atmosphere. This shows that the aerosols present in the POLDER field of view exhibit zero polarization for a  $150^\circ$  scattering angle.

From the polarized reflectance measurement, an estimate of the atmospheric aerosol content requires the aerosol phase function and polarization function. It is possible, as a first step, to assume typical functions. Some uncertainty results, however, from the large phase function

variability over space and time. Another, more ambitious, goal of the POLDER mission is therefore a full inversion of the polarized measurements for the retrieval of aerosol type and amount. Since a single satellite overpass will provide 12 bidirectional measurements for each of the three polarized channels, the inversion seems feasible, although it has not yet been fully verified.

### 5.3. Earth radiation budget

Clouds-radiation interactions or, in a more general way, the water cycle and its impact on the Earth radiation budget, is one of the major causes of uncertainty on the response of the climate system to the forcing induced by the increase of anthropogenic greenhouse gases. The understanding of these phenomena has been identified by GEWEX as one of the major subjects of interest.

Earth Radiation Budget (ERB) studies are of primary importance in order to understand better the energy transport within the atmosphere and the ocean, to quantify the cloud forcing, to detect any large scale modification and to provide a validation dataset for General Circulation Models (GCMs).

Several dedicated spaceborne experiments have been achieved, such as the Nimbus 7 Earth Radiation Budget (Jacobowitz et al., 1984) and the Earth Radiation Budget Experiment (ERBE) (Barkstrom, 1984), and others are planned for these objectives, such as CERES (Clouds and the Earth's Radiant Energy System) and ScaRaB (Scanner for Radiation Budget). Solar radiation budget studies have also been achieved using shortwave sensors onboard geostationary and polar satellites (Moser and Rashke, 1984).

However, the anisotropy of the radiation field remains one of the main causes of uncertainty in the determination of ERB, the other ones being the instrument calibration accuracy and the temporal variability of ERB. Indeed, most ERB instruments provide a radiance measurement, as opposed to a flux. Since the solar radiation field reflected by the Earth system is not isotropic, the reflected flux can only be estimated with the a-priori knowledge of the BRDF.

In the ERBE experiment, the required BRDF have been derived empirically by averaging a large number of bidirectional measurements (Suttles et al, 1988; Taylor and Stowe, 1984). These measurements were non-synchronous and the empirical BRDF are only valid on a statistical basis. POLDER provides quasi simultaneous multidirectional radiance measurements. These allow a new determination of the Earth system BRDF for various surface coverages and cloud types and amounts.

Note that POLDER does not provide broadband measurements. A method has to be developed to derive a BRDF valid for the whole solar spectrum from the POLDER spectral measurements. This method would take advantage of the 443, 665 and 865 nm spectral bands, which permit a good sampling of the visible and the near-infrared spectral domains, and of the 763 and 910 nm absorption bands, which allow to take into account the oxygen and water vapor absorption bands. This combination of spectral bands requires good multispectral, multiangular and absolute calibrations.

The spatial resolution of POLDER ( $6 \times 7 \text{ km}^2$ ) is better than that of ERB dedicated instruments (typically 40 km) and is therefore adequate to describe structures of smaller scales.

#### 5.4. Clouds

Significant progress is expected in the understanding of the cloud cover retroaction on the climate thanks to a better knowledge of the climatology of different cloud types, of their optical properties and of their conditions of formation. Recent simulation experiments (Cess et al., 1989; Cess et al, 1990; Mitchell et al., 1989) have outlined the complexity of the mechanisms involved and the uppermost importance of the characterization of the type, the optical properties and the localization of the clouds. The International Satellite Cloud Climatology Project (ISCCP) represents the first approach for a cloud climatology at a global scale (Rossow and Schiffer, 1991).

Since cloud top temperature, which is related to its pressure level, is a major driver of the cloud radiative forcing, this parameter is needed for a characterization of cloud cover and for climate studies. Two techniques will be evaluated for the determination of cloud top pressure from POLDER measurements.

The first method relates the measured polarized radiance to the atmospheric molecular optical thickness above the cloud, assuming that the polarization of the radiance originating from the cloud is negligible, or may be estimated from multi-spectral measurements. This assumption may not be true in some viewing directions such as that of the rainbow, which should therefore be avoided. In the other viewing directions, the measured polarized reflectance is generated by the atmosphere and is nearly proportional to the molecular optical thickness above the cloud. This relationship thus leads to an estimation of cloud top pressure. Since molecular scattering polarization is maximal at  $90^\circ$  scattering angle, this viewing direction shall be preferred. Some uncertainty results from the aerosols above the cloud layer which could also produce some perturbing polarized radiance. Note, however, that the bulk of atmospheric aerosol is contained in the boundary layer and, therefore, below the cloud layer. The measurements of polarization at 443 nm will be used for this first method because the contribution to the measurement of molecular scattering, relative to the other contributions, is maximal at this wavelength.

The second method for cloud top pressure retrieval is a differential absorption technique. It makes use of the ratio of radiances measured in a narrow oxygen absorption band, centered at about 763 nm and 10 nm wide, and in a broadband centered at 765 nm and 40 nm wide (Table 1). This ratio is sensitive to the oxygen amount along the optical path. Since oxygen is evenly distributed in the atmosphere, this path is clearly related to the cloud top pressure. However, some uncertainty results from the radiance path within the cloud. With this method, an accuracy of a few tens of mb is expected for the estimate of cloud top pressure, provided that the cloud layer has a spatial extent significantly larger than the pixel size.

Cloud type determination and atmosphere thermodynamics studies require to recognize the cloud phase. POLDER polarized measurements make this parameter accessible. Radiative transfer simulations have shown that the polarization of radiance reflected by clouds in specific directions is very sensitive to cloud phase, either ice or liquid water (Masuda and Takashima, 1992). The foreseen method makes use of the 865 nm polarized channel since it is the least polluted by molecular scattering.

Another cloud related objective is the analysis of the BRDF observed by POLDER to retrieve a 3D characterization of the cloud layer. Fig. 8, reproduced from Bréon (1992), shows that the BRDF of a plane parallel cloud differs greatly from that of a broken cloud field. Further research is needed on this subject, but some information on the ratio of a typical height scale to a typical horizontal scale of the cloud field may be gained from the measured BRDF.

### 5.5. Atmospheric water-vapor amount

Atmospheric water vapor is a key climatologic variable. Water vapor is a major driver of the exchanges of energy both between ocean and atmosphere, and within the atmosphere, through the release of latent heat. The feedback between temperature and water vapor amount is theoretically largely positive, and an atmospheric warming must be linked to an increase of the total water amount. Moreover, the water-vapor is the atmospheric gas that exhibits the largest spatial and temporal variations. It potentially drives a large positive feedback in the prospect of global warming. In this context, and as stressed by GEWEX, there is a need for an accurate global mapping of atmospheric water vapor amount.

Rawinsonde provide the profile, as well as the total amount, of atmospheric water vapor. These are unfortunately unevenly distributed over the globe. Moreover, there are concerns on their accuracy. Atmospheric water vapor estimates are obtained from space either from microwave radiometers (e.g. SSM/I) or from thermal infrared sensors (e.g. TOVS). The former cannot provide useful estimates over land areas because of land emissivity variability. The advantage of the latter is its global coverage (over clear areas) and its ability to provide a three layer "profile". The accuracy, however, is not better than 20 % and the IR water vapor estimates sometimes do not show any correlation with the surface measurements (Holben et al., 1991). An explanation is that the TOVS water vapor channels are only weakly sensitive to the lower atmospheric layers that contain a large fraction of the total water vapor amount. Moreover, the IR measurements are sensitive to the water vapor concentration, but also to the atmospheric temperature. Thus, the measurements are not directly related to the atmospheric water vapor amount.

POLDER provides a new opportunity for the retrieval of total atmospheric water vapor amount with a differential absorption technique (Frouin et al., 1990). The 910 nm -20 nm width- channel is centered on a water vapor absorption band. The radiance measured at this wavelength is compared to that measured at 865 nm, where the water vapor absorption is very weak. The ratio of these two radiances is related to the amount of atmospheric water vapor.

Uncertainties result from the aerosol scattering and surface reflectance variations between the two wavelengths. A global accuracy on the order of 10 % is expected for this method.

### 5.6. Ocean color

International programs, WOCE and primarily JGOFS, have clearly specified their needs for space observations of ocean color to contribute to the global study of the ocean dynamics and of the interactions between climate and the marine biosphere. A global assessment of marine production is requested, first in order to evaluate the marine biosphere resources, and second to study its role in the global carbon cycle. On the other hand, pigments affect the heating rate of the surface layer, which has some impact on its stability. Moreover, as the phytoplankton or terrigen materials behave, as a first approximation, like passive tracers, ocean color may be used to visualize specific features like eddies, plumes and meanders.

The POLDER instrument, complementary to the OCTS onboard the ADEOS platform, contributes to satisfy the scientific needs for ocean color observation expressed above.

The spectral signature of solar radiation reflected by the upper ocean is driven by the concentrations of different particulate and dissolved materials present in the waterbody by increased absorption and scattering. In the open ocean, the main optically active components, besides water molecules, are the living phytoplankton cells and the associated detrital matter (particulate and dissolved). Because of their chlorophyll and carotenoid pigments, phytoplanktonic cells primarily absorb the blue radiations, with a maximum around 435-445 nm. The biogenous detrital matter absorbs radiations increasingly toward shorter wavelengths. Therefore, an increase of the phytoplankton concentration lowers ocean reflectances below 500 nm because absorption by living cells and associated detritus is the dominant process. Conversely, in the green part of the spectrum, the reflectance is only weakly affected by the variations in phytoplankton concentration. Thus, the ratio of two marine spectral reflectances, one measured in the blue and another in the green part of the solar spectrum, is taken as an index of the phytoplankton biomass in the oceanic surface layer (Morel, 1988).

This reflectance ratio, e.g.  $R_{443}/R_{565}$ , varies from 7 to 0.5 when chlorophyll concentration is increased from 0.02 to 20 mg Chl  $m^{-3}$ . The quantitative derivation of algal biomass is based on this dependency. The present goal is to determine 10 concentration classes within each order of magnitude (26 percent increase between two successive classes), i. e. about thirty classes over the whole oceanic range of chlorophyll content given above.

When observed from space, the ocean signal is mixed with the signal resulting from atmospheric scattering, which is typically 10 times larger. For any space ocean color mission, it is a challenge to accurately correct for atmospheric effects. Atmospheric reflectance results from molecular (Rayleigh) and aerosol (Mie) scatterings. The molecular scattering is easily computed from a theoretical model with the correct input: geometry, atmospheric pressure, atmospheric ozone amount, central wavelength, and the instrument calibration relative to the sun. The aerosol scattering properties are assessed from space measurements in the near-

infrared region where the ocean is black and molecular scattering is weak. These properties are then extrapolated to the visible channels devoted to the derivation of the chlorophyll content.

The major drawback of POLDER compared to other ocean color missions is its spatial resolution, which is limited to about 6 km by the present technology of the CCD matrix array used in its conceptual design. Ocean color variability relevant to global biogeochemical studies scales at more than 10 km over the open oceans but lower than 1 km over coastal areas. POLDER medium spatial resolution is therefore not a handicap for the mission of monitoring biomass and marine production over the open ocean. This resolution may not be sufficient for coastal water studies, however. For such investigations, POLDER shall be used in synergy with OCTS on ADEOS. Both instruments support each other in their calibration, atmospheric correction, and the validation of derived products.

On the other hand, when compared to other, former or forthcoming, spaceborne instruments dedicated to ocean color observation, POLDER shows a number of benefits. A major benefit specific to POLDER is the improvement of aerosol scattering correction using the aerosol optical properties retrieved from the polarization and bidirectional measurements. A minor benefit specific to POLDER is a multidirectional observation of the water column reflectance. Non specific to POLDER is the benefit we expect from an accurate spaceborne calibration procedure based on the molecular scattering.

The accuracy of the molecular scattering correction is limited by the absolute calibration of the instrument. This calibration shall be understood as a reference, not to a given standard of radiance, but relative to the solar constant, which cannot be measured correctly by the prelaunch ground calibrators, or by inflight onboard devices. The inflight calibration procedure of POLDER using the molecular scattering, as described in 4.4.1, allows an accurate calibration relative to the solar constant.

The new capabilities of POLDER for accurate retrieval of aerosol optical properties were discussed in section 5.2.1. They result from its unique ability to measure the rate of linear polarization, which is very sensitive to the atmospheric aerosol type and amount, and to sample the aerosol phase function for various scattering angles. The accurate retrieval of aerosol optical properties will certainly improve the atmospheric correction and therefore the ocean color retrieval.

The POLDER experiment has the unique original capability to measure the radiance originating from one specific point at the ocean surface, not only at different wavelengths as the other ocean color dedicated experiments do, but also from different directions. One immediate application is controlling the glitter contribution to the signal by successively viewing the same target from several angles relative to the specular direction. Another one is monitoring the bidirectional signature of the radiance originating from the water column.

The bidirectional variability of the radiance originating from the water column has been overlooked, probably because most in-situ ocean color measurements are irradiances rather than

radiances since radiance measurements at sea are extremely difficult to obtain.. Numerical simulations of the radiative transfer within the ocean do show an angular signature large enough to affect the accuracy of the pigment concentration estimate by several tens of percent. Fig. 9 plots the angular variations of the ratio of the reflectances at 443 nm and 565 nm. This simulation was performed with a solar zenith angle of  $45^\circ$  and a phytoplankton concentration of  $0.3 \text{ mg m}^{-3}$ . We neglected all atmospheric effects and we subtracted the specular component from the ocean reflectances. The reflectance ratio ranges from 2.3 to 3.5 and shows a marked minimum in the antispecular direction. According to Morel (1988) relation, such ratios indicate a phytoplankton concentration of 0.30 and  $0.11 \text{ mg m}^{-3}$ . If we eliminate the antispecular direction, the  $R_{443}/R_{565}$  ratio is larger than 2.8 which corresponds to a concentration of  $0.19 \text{ mg m}^{-3}$ . Fig. 9 clearly indicates that the angular signature of the water column reflectance is a source of error for phytoplankton estimate. This difficulty has been overlooked with previous instruments such as the CZCS because the angular signature was seen as a negligible source of noise relative to others. With forthcoming instrument of better accuracy, the reflectance angular variations may be one of the major source of error. Note that the antispecular direction provides the measurement least polluted by the glitter. Unfortunately, it is also the direction where the directional effects are the largest.

The multidirectional viewing capability of POLDER allows a better assessment of the angular variability of the water column reflectance, which can be used to infer the signal corresponding to normalized viewing conditions. There may be some information on the ocean phytoplankton content, for instance its scattering phase function and thus its type, that can be derived from the angular signature of the radiance leaving the water column, but further work is needed to verify this hypothesis.

To satisfy the objectives defined above, ocean color measurements at 443, 490 and 565 nm are requested. The 490 nm band is characterized by an intermediate absorption of chlorophyll-like-pigments, and is useful in high chlorophyll concentrations waters where the sensitivity of the 443 nm band is poor. The scientific objective of distinguishing 10 classes of chlorophyll pigment concentration in every decade requires an estimate of the spectral water reflectance with an accuracy of  $10^{-3}$ . This accuracy must be achieved after atmospheric correction and for a range of solar zenith angle from  $0^\circ$  to  $60^\circ$ . In order to achieve this accuracy, the following Noise Equivalent Differential Reflectance, for a sun at the zenith (NEDRZ) is required:  $4 \cdot 10^{-4}$  in the ocean color channels (443, 490 and 565 nm) and  $2 \cdot 10^{-4}$  in the atmospheric correction channels (665, 765 and 865 nm). The aerosol scattering correction combines 2 channels and introduces an additional  $3 \cdot 10^{-4}$  of NEDRZ in the corrected ocean color channels. As a result, surface water reflectances are derived with  $5 \cdot 10^{-4}$  of NEDRZ, which leads to a noise equivalent reflectance of  $10^{-3}$  for a solar zenith angle of  $60^\circ$ .

The global observation of ocean color will benefit from the synergy of POLDER and OCTS onboard ADEOS. POLDER can provide accurate aerosol parameters for an improved atmospheric correction of the measured reflectances. The greater spatial resolution of OCTS is essential for coastal water studies. Both instruments support each other for their calibration and the validation of their products.

### 5.7 Land surfaces

Like the ocean, the land surfaces are a potential sink of carbon dioxide, through the photosynthesis process. However, in contrast to the ocean case, the carbon dioxide absorbed by terrestrial vegetation is recycled into the atmosphere after the death of vegetation. The potential for a carbon dioxide sink over land surface areas is related to a large scale vegetation growth. Such growth has been observed over the United-States (LaMarche et al., 1987) and western Europe. On the other hand, extended deforestation over the African or Amazonian forests is a source of carbon dioxide, in addition to industrial emissions. In order to better understand the currently measured carbon dioxide variation in the atmosphere, and to better predict that of forthcoming years, there is a need, therefore, to measure the global biomass and the vegetation primary productivity.

Land cover use is partly at the origin of increased atmospheric carbon dioxide. In the context of global change, it may also be a consequence. Land cover may change because of increased CO<sub>2</sub> (fertilization process) or variations in temperature, rainfall and illumination (climatic forcing). A change in vegetation cover is, in areas unperturbed by man, an indication of climate change. In order to detect such variations in vegetation cover, a long term dataset, as well as an accurate and stable calibration, is needed. These are stressed by international programs such as IGBP.

The three major uses of satellite observations for land surface studies are i) the identification of land cover; ii) the detection of change in surface cover related either to anthropogenic activities (e.g. deforestation) or to climate forcing (e.g. reduced rainfall); and iii) the specification of surface parameters for climate modeling studies. At the global scale, such studies have been performed using mainly the shortwave channels of the AVHRR instrument, as well as those onboard the geostationary satellites (GOES and METEOSAT). At the local scale, focused surveys have also been performed using higher resolution sensors such as Landsat or the SPOT HRV.

Shortwave remote sensing of the vegetation makes use of the large difference in spectral signature between the bare soil and the canopy. The chlorophyll absorbs radiation in the visible part of the solar spectrum, but little in the near infrared (Sellers, 1985). Thus, vegetation shows a large variation in reflectance around the 700 nm threshold. On the other hand, the bare soil reflectance is approximately spectrally flat. Thus, the difference in reflectance above and below 700 nm is a quantitative estimate of the vegetation cover. The Normalized Difference Vegetation Index (NDVI), which is the ratio of the difference and sum of the visible and near IR

reflectances of a scene, has been largely used for a quantitative characterization of the vegetation cover. The relationships of the NDVI to the vegetation coverage, the leaf area index (LAI) and the primary productivity, have been quantified (Spanner et al., 1990; Bartlett et al., 1990; Sellers, 1985, Tucker et al., 1986).

The main difficulties for land surface monitoring from space are i) the uncertainties in the relationship between the surface reflectance and the information sought; ii) the correction to the reflectance for atmospheric effects; and iii) the existence of angular effects on the reflectance that are not yet controlled. The first difficulty, relating the surface reflectance spectral and temporal signatures to the land cover parameters, may be solved by additional ground-truth measurement campaigns, such as FIFE or HAPEX-Sahel, and a better identification of the major canopy parameters that control the reflectance. The POLDER instrument design permit to solve the other difficulties.

As discussed in section 5.2, it is difficult, over land areas, to distinguish between surface and atmospheric contributions to the TOA reflectance. Atmospheric effect correction is then difficult with current instruments. The POLDER polarized measurements, however, provide new means for an accurate atmospheric correction.

The observation of land surfaces from spaceborne instruments has shown significant bidirectional effects on the reflectance (Roujean et al., 1992). The importance of these effects has been confirmed by surface measurements (Kriebel, 1978; Kimes, 1983; Kimes et al., 1985) and by numerical radiative transfer simulations (Fig. 10). The empirical solution to this problem has been, so far, to restrict the eligible satellite observations to a limited range of viewing directions (i.e. Duggin et al., 1982). This solution greatly affects the temporal coverage of land surfaces. Moreover, the directional effects exist at all angles and the selected range of viewing directions is, therefore, arbitrary. The alternative provided by POLDER is a multidirectional measurement of the target reflectance. It allows evaluation of the bidirectional effects, and then correct the measurements for them.

The bidirectional signature on the reflectance measured at the TOA has been seen, so far, as a noise that should be corrected. Many models of the surface and/or vegetation bidirectional reflectance have been published in the literature (i.e. Otterman and Weiss, 1984; Pinty et al., 1989; Verstraete et al., 1990; Roujean et al., 1992), some of which are physical (i.e. they express the BRDF as a function of physical parameters) and can be inverted. Thus, there may be some information on the surface and/or the canopy structure to be derived from the BRDF measured at the TOA. As shown in Fig. 3, POLDER provides an extended sampling of the BRDF and is therefore an excellent tool for investigating this hypothesis. Some uncertainties about the feasibility of this approach, are related to the model accuracy and the surface heterogeneity within the POLDER pixel.

Another application of POLDER multidirectional measurements is a better estimate of the land surface spectral albedo. The albedo, rather than the bidirectional reflectance, is the key

parameter for the radiative budget of the surface. An accurate BRDF is needed to accurately determine the surface albedo from satellite bidirectional measurements. The BRDF, and thus the albedo, are provided by POLDER.

Part of the solar radiation incident on the canopy is specularly reflected by the leaf wax (Vanderbilt et al., 1985). This radiance does not interact with the chlorophyll pigments and cannot participate, therefore, to the photosynthesis process. Thus, it should not be considered when computing vegetation indices (Vanderbilt and Grant, 1985). The radiance specularly reflected is partly polarized. Therefore, another potential application of the polarization over land surfaces is to correct the reflectance for the specular component. The POLDER polarized observations may also help to describe the vegetation cover, since these observations are sensitive to the microscale structure of the canopy (Curran, 1982). However, since the TOA polarized reflectance originates mostly from the atmosphere, a very accurate atmospheric correction will be necessary before spaceborne polarized reflectance measurements can be used for vegetation monitoring applications.

In the visible, reflectances measured over land surfaces are highly correlated between the various spectral bands; thus, only one visible and one near-infrared band, i.e. 665 and 865 nm with polarization measurements, are necessary to achieve the mission objectives. A third channel, such as the 443 nm band, allows the use of a vegetation index less sensitive to atmospheric disturbances, as in Kaufman and Tanré (1992).

The POLDER spatial resolution is of the same order as that accessible with the AVHRR Global Area Coverage (GAC) or the geostationary satellites shortwave sensors. It is poorer than that currently accessible for local scale studies with the AVHRR Local Area Coverage (LAC) or the imagers SPOT and Landsat. Some studies evaluating the spatial resolution necessary for a global land surface survey have recommended a resolution on the order of 500 m (Townshend and Justice, 1988). These studies have argued for the choice of the spatial resolutions of the MODerate resolution Imaging Spectrometer (MODIS; King et al., 1992) on the EOS platform, which range from 250 m to 1000 m depending on the spectral band. These are, therefore, significantly better than what POLDER provides. Similarly, the OCTS, a companion instrument of POLDER on the ADEOS platform, has a spatial resolution of 700 m.

However, it is noticeable that many successful land studies have been performed with the AVHRR-GAC mode, which has a resolution comparable to POLDER's. In spite of the fact that the spaceborne POLDER spatial resolution is not optimum for vegetation remote sensing, the capability of POLDER to provide additional information on reflectance bidirectional signatures represents a significant improvement in a global land surface monitoring. It is also clear that other sensor data are needed for the study of local phenomena.

## 6. Data processing

The ground segment is responsible for the calibration, validation, processing and distribution of POLDER data. The raw data are received from the ADEOS ground segment on a regular basis, which is on the order of two weeks. From these raw data three levels of high resolution products and a "Quick look" are generated.

Level 1 processing consists in radiometric and geometric transformation of the data. The radiometric model associated to POLDER measurements allows to compute the three accessible Stokes parameters or, which is equivalent, the radiance, degree of linear polarization and linear polarization direction. For the non polarized channels, only the reflectance is derived from the measurements. The calibration coefficients, determined as in 4.4, are needed for the radiometric processing. Note that the polarization rate measured by the polarized channels will be interpolated for the other channels in order to correct the optics transmission effects.

The geometric processing interpolates POLDER measurements over a fixed grid relative to the Earth. The grid spatial resolution shall be on the same order as that of POLDER raw data, i.e. 7 km. In order to avoid the interpolation degradation near the poles, a constant area grid is preferred (Rossow and Garder, 1984).

Level 1 products consist in geocoded and registered spectral reflectances, polarization rates and polarization directions at the TOA. For each satellite orbit and each accessible grid point, about 12 such directional measurements are generated. A crude cloud mask will be generated from these data and added to the Level 1 products.

From the Level 1 data, a "Quick look" product is easily generated. The Quick look file contains a single spectral measurement. The 443 nm reflectance is selected over oceanic areas, whereas 665 nm is chosen over land surfaces. This yields an optimization of the Quick-look dynamics. Chosen among the 12 directional measurements, the Quick-look contains the observation acquired with the smallest zenith viewing angle. The spatial resolution of this product is degraded to about 35 km through a sampling of the original Level 1 data. A cloud indicator is also generated from the Level 1 cloud mask. It is a function of the cloud masks for 25 Level 1 grid points nearby the Quick look pixel.

Level 2 and 3 products are generated from Level 1 data and ancillary data, either from other ADEOS instruments or climatological fields of parameters. Level 2 products are those which can be generated from a single satellite pass. Level 3 products are obtained through a combination of several orbit measurements. Level 2 and Level 3 processings are divided in three parallel processes: Earth radiation budget and clouds, ocean and marine aerosols, land surfaces and continental aerosols. Currently envisioned global products are atmospheric parameters such as cloud coverage, cloud top altitude, atmospheric water vapor content and aerosol optical thickness, as well as surface reflectances corrected for the atmospheric effects. Higher order geophysical products may be generated from the spectral, temporal and directional

signatures of these surface reflectances, as discussed in §5. A library of angular signature maps for various scenes, such as different cloud types and cover or landscapes, will also be produced by the POLDER mission.

As explained in §5.2, the POLDER instrument provides new means of correcting the measurements for aerosol perturbation but the techniques have not yet been validated. Therefore, two levels of processing will be performed for the generation of land and ocean products. In the first one, a typical aerosol type is assumed; the aerosol optical thickness is estimated from the reflectance and polarization measurements, and a simple aerosol correction is applied to the data. In the second one, a full inversion of the aerosol optical properties is attempted. If successful, the measurements can then be corrected more accurately for the aerosol effects.

## 7. Conclusion

As shown in this paper, the spaceborne POLDER measurements will have many applications and may interest a vast community of researchers involved in the IGBP. There is no doubt that potential applications not listed in the present paper can be found using the forthcoming POLDER data. An announcement of opportunity will be released mid 1993 for scientific investigations using the POLDER data.

In preparation for the spaceborne POLDER mission, several airborne measurement campaigns have been done and others are planned. For the land surface mission of POLDER, measurements have been acquired over various types of land cover, such as cultivated areas and barren ones (La Crau, 1990; 1991), coniferous forests and corn fields (Landes, 1990), and savanas and deserts (HAPEX Sahel, 1992). A participation to the BOREAS experiment over the boreal forest is planned for 1994. For the ocean color mission, measurements have been acquired over the Mediterranean sea (MEDIMAR, 1991) and the Antarctic ocean (RACER, 1992). For cloud investigations, observations of clouds over land (CLEOPATRA, 1991) and stratocumulus over the ocean (SOFIA-ASTEX, 1992) have been acquired. The first results have been described in Deuzé et al. (1992) and Bréon and Deschamps (1992). Airborne POLDER measurements can be made available to interested researchers.

In summary, the POLDER instrument, despite its rather simple design, allows a number of innovative observations of the Earth system. It permits an increase in accuracy for the ocean color monitoring, as compared to those accessible over the CZCS. Similarly, the global monitoring of vegetation, currently achieved mainly with the AVHRR, is improved.

The POLDER mission on ADEOS also permits further investigation of several important concepts for Earth remote sensing, such as the differential absorption technique and the measurement of polarization as an help for aerosol retrieval and atmospheric correction.

## Acknowledgment

Financial support was provided by the Centre National d'Etudes Spatiales and the Centre National pour la Recherche Scientifique. We are very grateful to those who contributed to an in-depth reading of this paper: J.M. André, F. Dulac, Y. Fouquart, J.M. Martinuzzi, B. Millet, J. Perbos, J. Poitou and A. Ratier.

## References

- Ardanuy, P.E., D. Han, and V.V. Salomonson; 1991: The moderate resolution imaging spectrometer (MODIS) science and data requirements. *IEEE Trans. Geosci. Remote Sensing*, 29, 75-87.
- Barkstrom, B.R.; 1984: The Earth Radiation Budget Experiment (ERBE). *Bull. Am. Met. Soc.*, 65, 1170-1185.
- Bartlett, D.S., G.J. Whiting, and J.M. Hartman; 1990: Use of vegetation indices to estimate intercepted solar radiation and net carbon dioxide exchange of a grass canopy. *Remote Sens. Environ.*, 30, 115-128.
- Bréon, F.M., 1992: Reflectance of Broken Cloud Fields: Simulation and Parameterization. *J. Atmos. Sci.* 49, 1221-1232.
- Bréon, F.M. and P.Y. Deschamps; 1992: "Optical and Physical parameter retrieval from POLDER measurements over the ocean using an analytical model". *Remote Sens. Environ.*, Accepted.
- Cess R.D., G.L. Potter, J.P. Blanchet, G.J. Boer, S.J. Ghan, J.T. Kiehl, H. Le Treut, Z.X. Li, X.Z. Liang, J.F.B. Mitchell, J.J. Morcrette, D.A. Randall, M.R. Riches, E. Roeckner, U. Schlese, A. Slingo, K.E. Taylor, W.M. Washington, R.T. Wetherald, and I. Yagai; 1989: Interpretation of cloud-climate feedback produced by 14 atmospheric general circulation models. *Science*, 245, 513-516.
- Cess R.D., G.L. Potter, J.P. Blanchet, G.J. Boer, A.D. Del Genio, M. Deque, V. Dymnikov, V. Galin, W.L. Gates, S.J. Ghan, J.T. Kiehl, A.A. Lacis, H. Le Treut, Z.X. Li, X.Z. Liang, B.J. McAvaney, V.P. Meleshko, J.F.B. Mitchell, J.J. Morcrette, D.A. Randall, L. Rikus, E. Roeckner, J.F. Royer, U. Schlese, D.A. Sheinin, A. Slingo, A.P. Sokolov, K.E. Taylor, W.M. Washington, R.T. Wetherald, I. Yagai, and M.H. Zhang; 1990: Intercomparison and interpretation of climate feedback processes in 19 atmospheric general circulation models. *J. Geophys. Res.*, 95, 16601-16616.
- Charlson, R.J., S.E. Schwartz, J.M. Hales, R.D. Cess, J.A. Coakley Jr, J.E. Hansen, D.J. Hofmann; 1992: Climate forcing by anthropogenic aerosols. *Science*, 255, 423-429.
- Coulson, K.L., Whitehead, V.S., Campbell, C., 1986: Polarized views of the Earth from orbital altitude. *SPIE 637, Ocean Optics VIII*, 35-41.
- Curran P.J., 1982, Polarized visible light as an aid to vegetation classification. *Remote Sens. Environ.*, 12, 491-499.

- Deuzé, J.L., C. Devaux, M. Herman, R. Santer, and D. Tanré; 1988: Saharian aerosols over south of France. Characterisation derived from satellite data and ground based measurements. *J. Appl. Meteor.*, 27, 680-686.
- Deuzé, J.L., F.M. Bréon, J.L. Roujean, P.Y. Deschamps, C. Devaux, M. Herman, and A. Podaire; 1992: Preliminary results of POLDER overland flights. *Rem. Sens. Env.*, in press.
- Diner, D.J., C.J. Bruegge, J.V. Martonchik, T.P. Ackerman, R. Davies, S.A.W. Gerstl, H.R. Gordon, P.J. Sellers, J. Clark, J.A. Daniels, E.D. Danielson, V.G. Duval, K.P. Klaasen, G.W. Lilienthal, D.I. Nakamoto, R.J. Pagano, and T.H. Reilly; 1989: MISR: A multiangle Imaging SpectroRadiometer for geophysical and climatological research from EOS. *IEEE Trans. Geosci. Remote Sensing*, 27, 200-214.
- Duggin, M.J., D. Piwinski, V. Whitehead and G. Ryland; 1982: Evaluation of NOAA-AVHRR data for crop assessment. *Applied Optics*, 21, 1873-1875.
- Frouin, R., P.Y. Deschamps, and P. Lecomte; 1990: Determination from space of total atmospheric water vapor amounts by differential absorption near 940 nm. Theory and airborne verification. *J. Appl. Met.*, 29, 448-460.
- Hansen, J.E. and J.W. Hovenier; 1974: Interpretation of the polarization of Venus. *J. Atmos. Sci.*, 31, 1137-1160.
- Holben, B.N., Y.J. Kaufman, and J.D. Kendall; 1990: NOAA-11 AVHRR visible and near-IR inflight calibration. *Int. J. Remote Sensing*, 11, 1511-1519.
- Holben, B.N., T.F. Eck, and R.S. Fraser; 1991: Temporal and spatial variability of aerosol optical depth in the Sahel region in relation to vegetation remote sensing. *Int. J. Remote Sensing*, 12, 1147-1163.
- Jacobowitz, H., H.V. Soule, H.L. Kyle, F.B. House and the Nimbus 7 ERB Experiment Team, 1984: The Earth radiation budget experiment: An overview. *J. Geophys. Res.*, 89, 5021-5038.
- Kaufman, Y.J., and C. Sandra; 1988: Algorithm for automatic atmospheric corrections to visible and near IR satellite imagery". *Int. J. Remote Sensing*, 9, 1357-1381.
- Kaufman, Y.J., C.J. Tucker, and I. Fung; 1990: Remote sensing of Biomass burning in the tropics. *J. Geophys. Res.*, 95, 9926-9939.
- Kimes, D.S., 1983, Dynamics of directional reflectance factor distributions for vegetation canopies. *Appl. Opt.*, 22, 1364-1372.

- Kimes, D.S., W.W. Newcombe, C.J. Tucker, I.S. Zonneveld, W. Van Wijngaarden, J. De Leeuw, 1985, Directional reflectance factor distributions for cover types of Northern Africa. *Remote Sensing Environ.*, 18, 1-19.
- King, M.D., Y.J. Kaufman, W.P. Menzel and D. Tanré; 1992: Remote sensing of cloud, aerosol, and water vapor properties from the moderate resolution imaging spectrometer (MODIS). *IEEE Trans. Geosci. Remote Sensing*, 30, 2-26.
- Kriebel, K.T., 1978, Measured spectral directional reflection properties for four vegetated surfaces. *Appl. Opt.*, 17, 253-259.
- LaMarche, V.C. Jr., D.A. Graybill, H.C. Fritts, M.R. Rose; 1987: Increasing atmospheric carbon dioxide: Tree ring evidence for growth enhancement in natural vegetation. *Science*, 225, 1019-1021.
- Martin, J.H., and S.E. Fitzwater; 1988: Iron deficiency limits phytoplankton growth in the north-east Pacific subarctic. *Nature*, 331, 341-343.
- Masuda, K., and T. Takashima; 1992: Feasibility study of derivation of cirrus information using polarimetric measurements from satellite. *Remote Sensing of Environment* 39, 45-59.
- Mitchell, J.F.B., C.A. Senior, and W.J. Ingram; 1989: CO<sub>2</sub> and climate: a missing feedback? *Nature*, 341, 1321-134.
- Morel, A., 1988: Optical Modeling of the Upper Ocean in Relation to its Biogenous Matter Content (Case 1 Waters). *J. Geophys. Res.*, 93, C9, 10749-10768.
- Moser, W., and E. Rashke; 1984: Incident solar radiation over Europe estimated from METEOSAT data. *J. Clim. Appl. Meteor.*, 23, 166-170.
- Otterman, J. and G.H. Weiss, 1984: "Reflection from a field of randomly located vertical protrusions". *Applied Optics*, 23, 12, 1931-1936.
- Pinty, B., M.M. Verstraete, and R.E. Dickinson, 1989, A physical model for predicting bidirectional reflectances over bare soil. *Remote Sensing of Environ.*, 27, 273-288.
- Roger, J.C., R. Santer, M. Herman, J.L. Deuzé; 1992: Polarization of the solar light scattered by the Earth-atmosphere system as observed from the US shuttle. *Rem. Sens. of Environment*. Accepted.
- Rossow, W.B., and L. Garder; 1984: Selection of a map grid for data analysis and archival. *J. Clim. Appl. Met.*, 23, 1253-1257.
- Rossow, W.B., and R.A. Schiffer; 1991: ISCCP Cloud Data Products. *Bull. Am. Met. Soc.*, 72, 2-20.

- Roujean, J.L., M. Leroy, P.Y. Deschamps, and A. Podaire; 1992: Evidence of surface bidirectional effects from a NOAA/AVHRR multitemporal dataset. *Int. J. Remote Sensing*, 13, 685-698.
- Roujean, J.L., M. Leroy, P.Y. Deschamps; 1992: A bidirectional reflectance model of the Earth surface for the correction of remote sensing data. *J. Geophys. Res.*, in press.
- Santer, R., X.F. Gu, G. Guyot, J.L. Deuzé, C. Devaux, E. Vermote, and M. Verbrugge; 1992: SPOT calibration at the La Crau test site (France). *Rem. Sens. of Environment*, 41, 227-237.
- Sellers, P.J.; 1985: "Canopy reflectance, photosynthesis and transpiration", *Int. J. Remote Sensing*, 6, 1335-1372.
- Spanner, M.A., L.L. Pierce, S.W. Running, and D.L. Peterson; 1990: The seasonality of AVHRR data of temperate coniferous forests: relationship with leaf area index. *Rem. Sens. of Environment*. 33, 97-112.
- Slater, P.N., S.F. Biggar, R.G. Holm, R.D. Jackson, Y. Mao, M.S. Moran, J.M. Palmer, and B. Yuan; 1987: Reflectance- and radiance-based methods for the in-flight absolute calibration of multispectral sensors. *Rem. Sens. of Environment*. 22, 11-37.
- Staylor, W.F.; 1990: Degradation rates of the AVHRR visible channel for the NOAA 6, 7, and 9 Spacecraft. *J. Atmos. and Ocea Techn.*, 411-423.
- Stephens, G.L., and S.-C. Tsay; 1990: On the cloud absorption anomaly. *Q. J. R. Meteorol. Soc.*, 116, 671-704.
- Suttles, J.T., R.N. Green, P. Minnis, G.L. Smith, W.F. Staylor, B.A. Wielicki, I.J. Walker, D.F. Young, V.R. Taylor, and L.L. Stowe; 1988: Angular radiation models for Earth Atmosphere System. Vol 1, Shortwave Radiation. *NASA Ref. Pub. 1184*, 147 pp, Washington D.C.
- Swap, R., M. Garstang, S. Greco, R. Talbot, and P. Källberg; 1992: Saharan dust in the amazon basin. *Tellus*, 44B, 133-149.
- Tanré, D., P.Y. Deschamps, C. Devaux, and M. Herman; 1988: Estimation of Saharan aerosol optical thickness from blurring effect in Thematic Mapper data. *J. Geophys. Res.*, 93, 15955-15964.
- Taylor, V.R., and L.R. Stowe, 1984: Reflectance characteristics of Uniform Earth and Cloud Surfaces Derived from Nimbus-7 ERB. *J. Geophys. Res.*, 89, 4987-4996.
- Townshend, J.R.G., and C.O. Justice; 1988: Selecting the spatial resolution of satellite sensors required for global monitoring of land transformations. *Int. J. Remote Sensing*, 9, 187-236.

- Travis, L.D.; 1992: Remote sensing of aerosols with the Earth Observing scanning polarimeter. *Conf. Proc., SPIE, July 1992, San Diego.*
- Tucker, C.J., I.Y. Fung, C.D. Keeling and R.H. Gammon; 1986: Relationship between atmospheric CO<sub>2</sub> variations and a satellite derived vegetation index. *Nature*, 319, 195-199.
- Vanderbilt, V.C. and L. Grant, 1985, Plant Canopy Specular Reflectance Model. *IEEE Trans. on Geosciences and Remote Sensing*, 23, 722-730.
- Verhoef, W.; 1984: Light scattering by leaf layers with application to canopy reflectance modeling: The sail model. *Rem. Sens. of Environment.*, 16, 125-141.
- Vermote, E., R. Santer, P.Y. Deschamps, and M. Herman; 1992: In flight calibration of large field of view sensors at short wavelengths using Rayleigh scattering. *Int. J. Remote Sensing*, in press.
- Verstraete, M.M., B. Pinty and R.E. Dickinson, 1990, A physical model for predicting the bidirectional reflectance of vegetation canopies. 1. Theory. *J. Geoph. Res.*, 95, D8, 11755-11765.

Table 1: General characteristics of the POLDER instrument and the ADEOS satellite.

POLDER on ADEOS	
Size (m <sup>3</sup> )	0.8x0.5x0.25
Weight	33 kg
Consumption	42 W
Data Rate	882 Kbit/s
Altitude	800 km
Period	100 min
Local cross. time	10:30
Inclination	98.59°

Table 2: Characteristics of the spectral bands selected on POLDER-ADEOS. There are 3 channels for each polarized band. See text for details.

Central Wavelength	Band width (nm)	Polarization	High dynamic	Low dynamic	Main mission
443 nm	20	no	0 - 0.22	0 - 0.22	Ocean color
443 nm	20	yes	0 - 1.1	0 - 1.1	Aerosols, ERB
490 nm	20	no	0 - 0.17	0 - 0.17	Ocean color
565 nm	20	no	0 - 0.11	0 - 0.11	Ocean color
665 nm	20	yes	0 - 1.1	0 - 0.25	Vegetation, aerosols, ERB
763 nm	10	no	0 - 1.1	0 - 0.25	Cloud top pressure
765 nm	40	no	0 - 1.1	0 - 0.25	Aerosols, CTP
865 nm	40	yes	0 - 1.1	0 - 0.25	Vegetation, aerosols, ERB
910 nm	20	no	0 - 1.1	0 - 0.25	Water-vapor amount

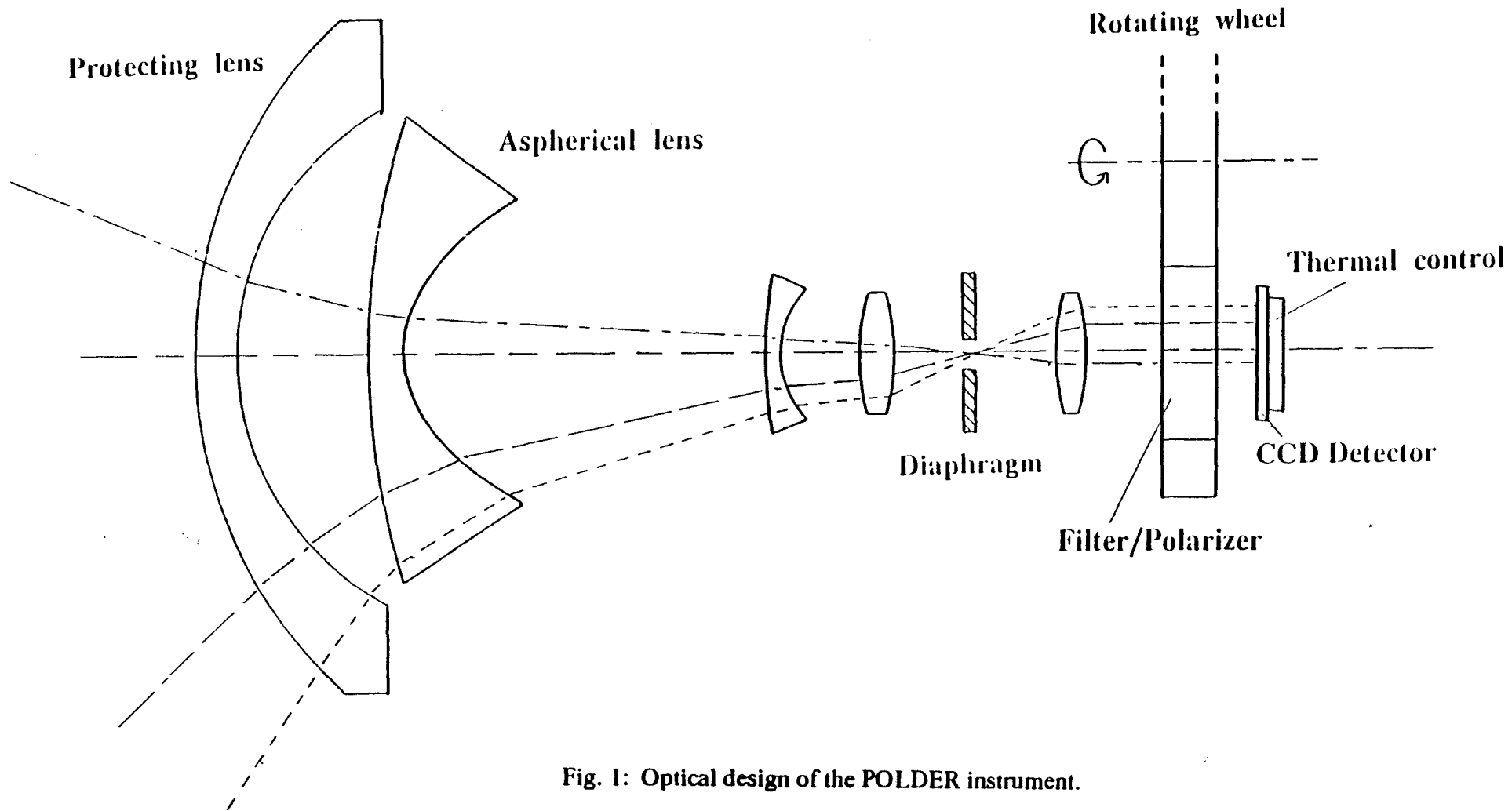


Fig. 1: Optical design of the POLDER instrument.

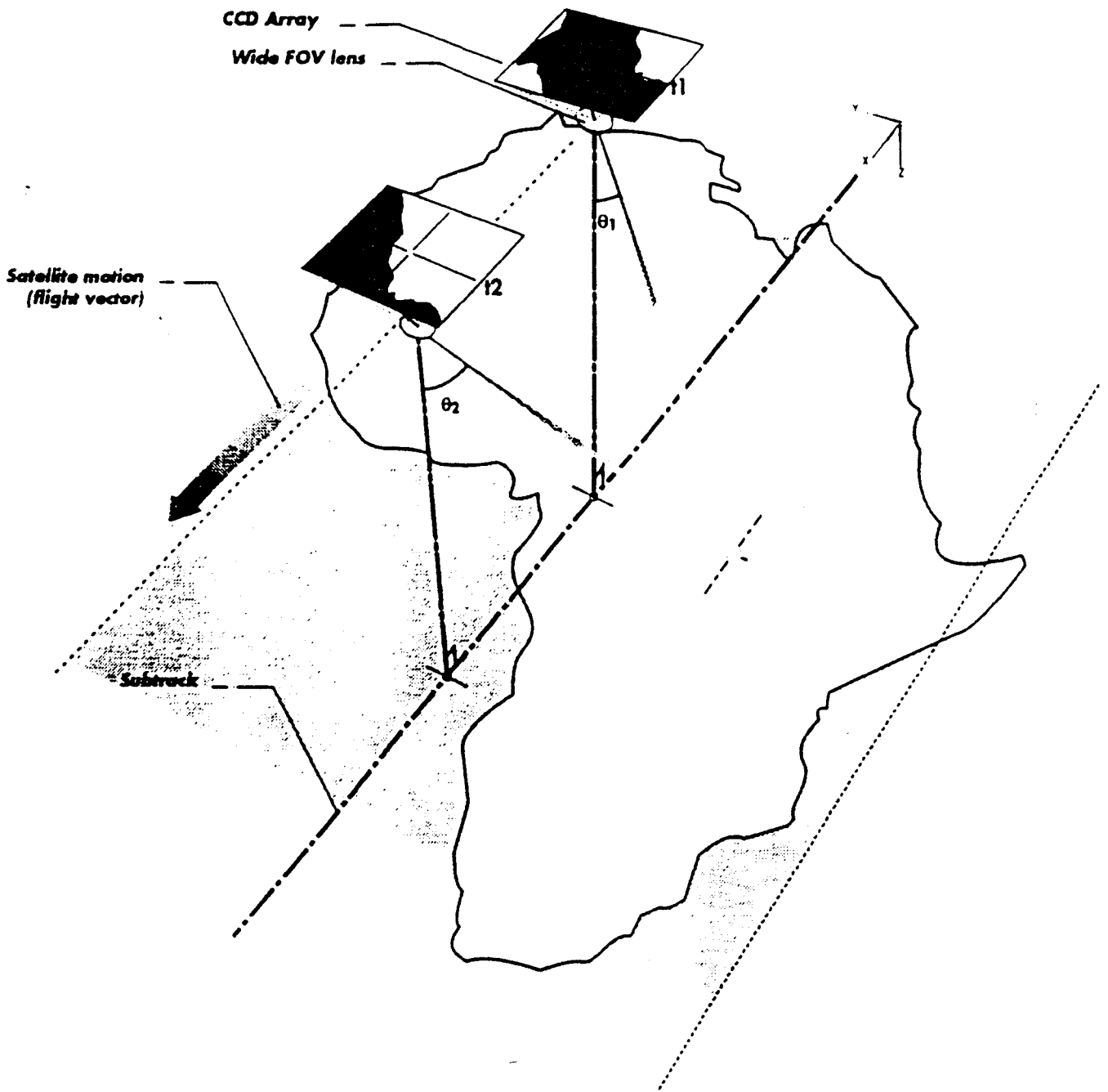


Fig. 2: Imaging mode of the POLDER concept. The CCD matrix is shown for two successive snapshots. The viewing angle of a surface target, and thus its position on the CCD matrix, has changed between the two snapshots. This figure is not on scale.

**POLDER on ADEOS**  
**Latitude: 40°N**  
**March 19th to March 23rd**

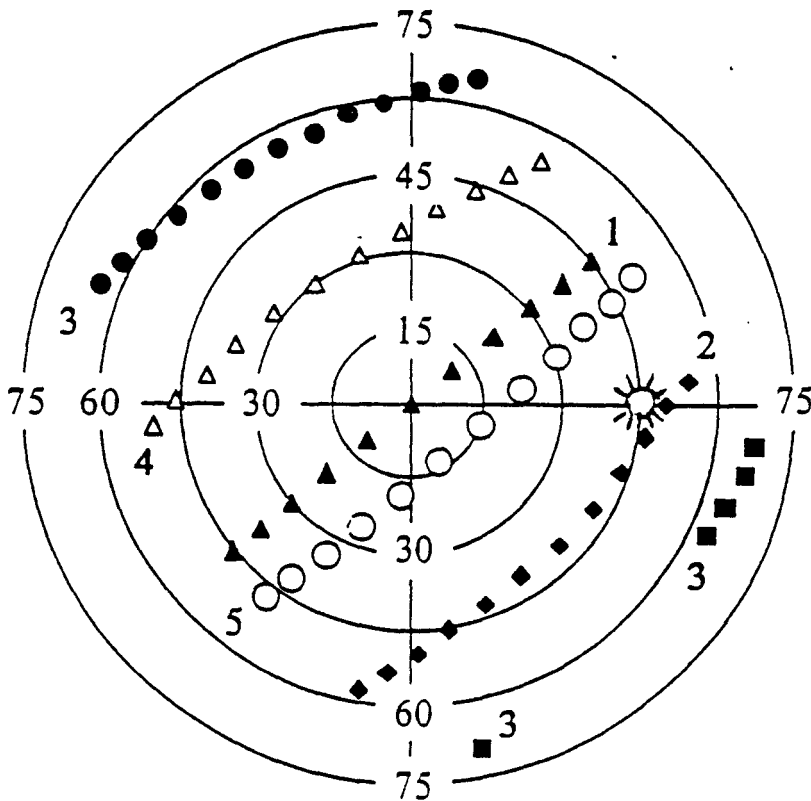


Fig. 3: Typical sampling of a surface target BRDF. The target is located at 40°N and the period of observation is from March 19 to March 23. On this figure, the radius represents the viewing zenith angle and the angle is the azimuth relative to the sun direction. The sun symbol indicates the antispecular direction. Each dot indicates one direction of observation by POLDER. A "line" of dots corresponds to one orbit. The day number beginning on March 19th is indicated. Note that the target is monitored twice during day #3. Note also that, since the BRDF is generally symmetrical with respect to the principal plane, the density of points can actually be doubled.

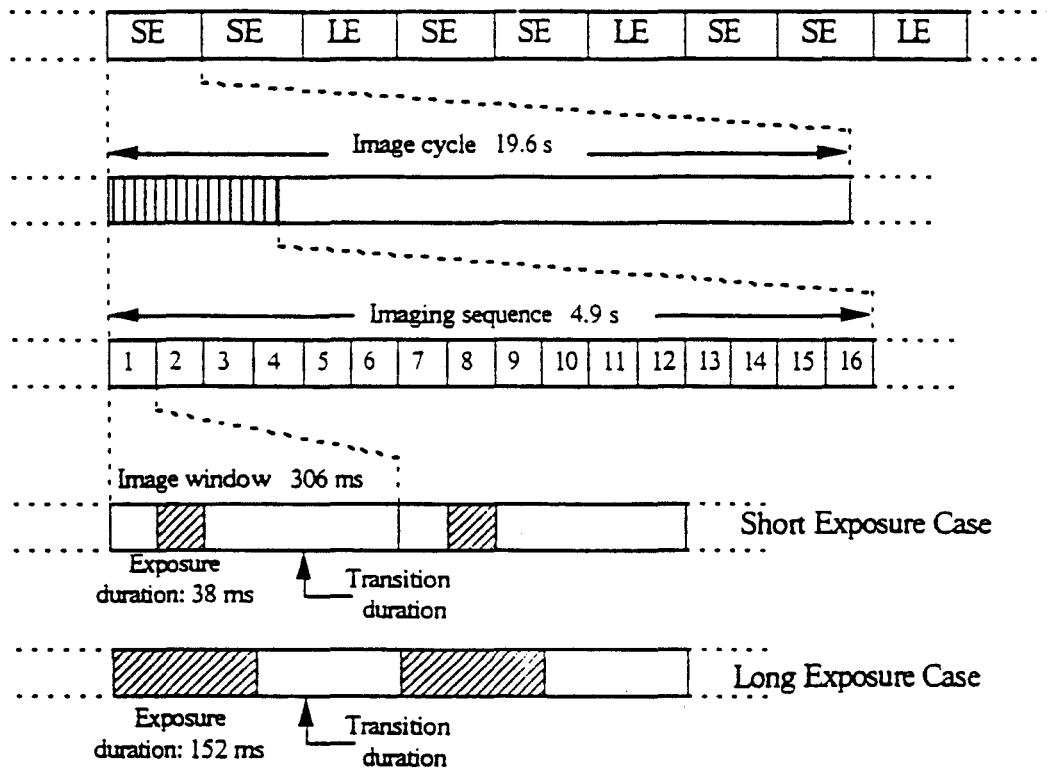


Fig. 4: Image sequencing of POLDER on ADEOS. A cycle, of total duration 58.8 s is composed of three subcycles of equal duration, one adapted to the low dynamic (Long Exposure) and two to the large dynamic (Short Exposure). During each subcycle, the 16 image acquisition is performed during one filter wheel period. No acquisition is performed during the following 3 periods. Exposure and measurement transfer are performed during each image acquisition.

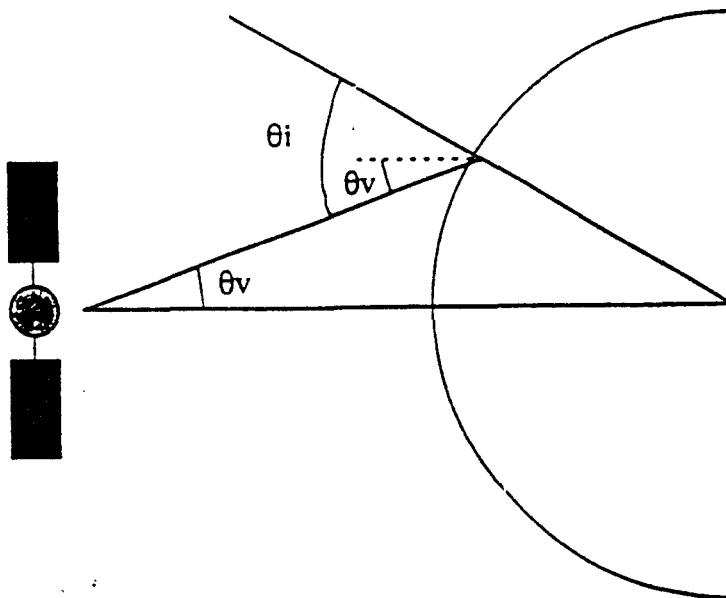


Fig. 5: This Fig. shows how the viewing angle at the surface ( $\theta_i$ ) is larger than that at the satellite level ( $\theta_v$ ).

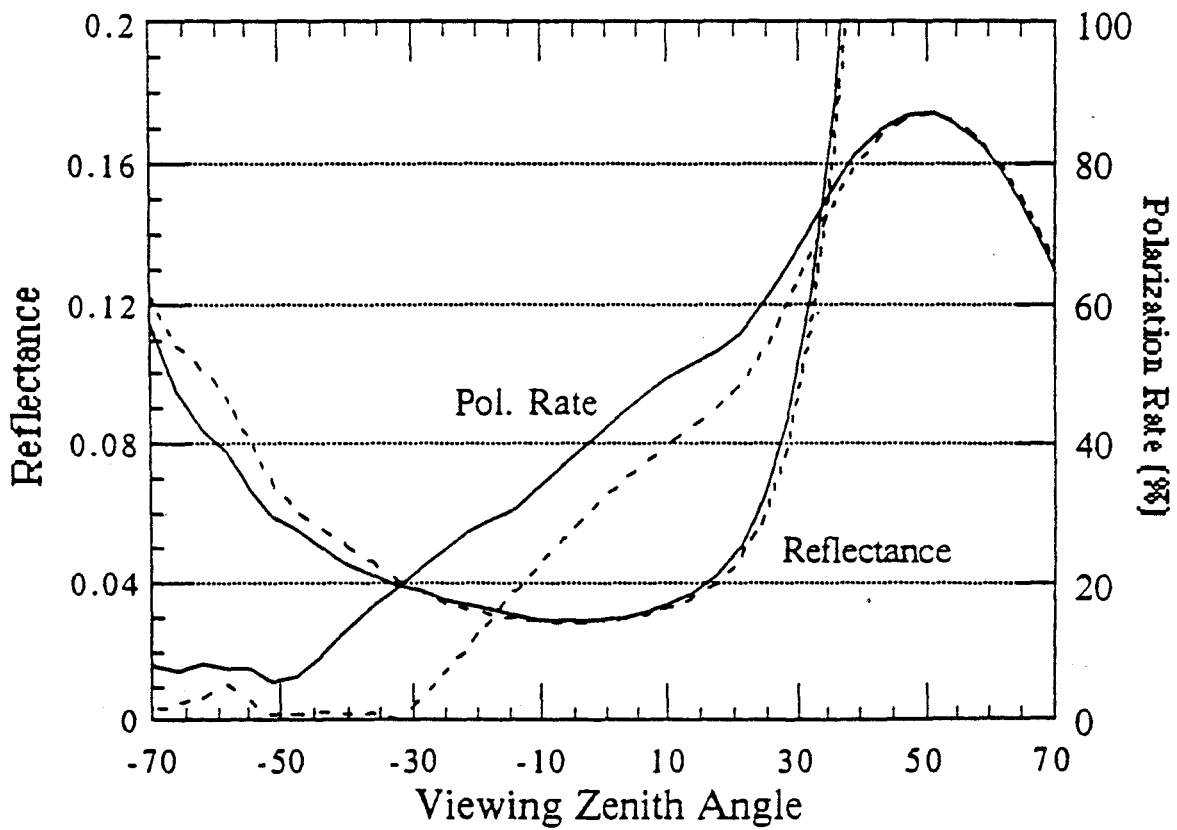


Fig. 6: Radiative transfer simulation of the TOA reflectance and the polarization rate over the ocean in the solar principal plane. The plain curves are for an aerosol of refractive index 1.33. The dashed curves are for the same aerosol model but with a refractive index of 1.55. The right side of the figure corresponds to the glitter direction.

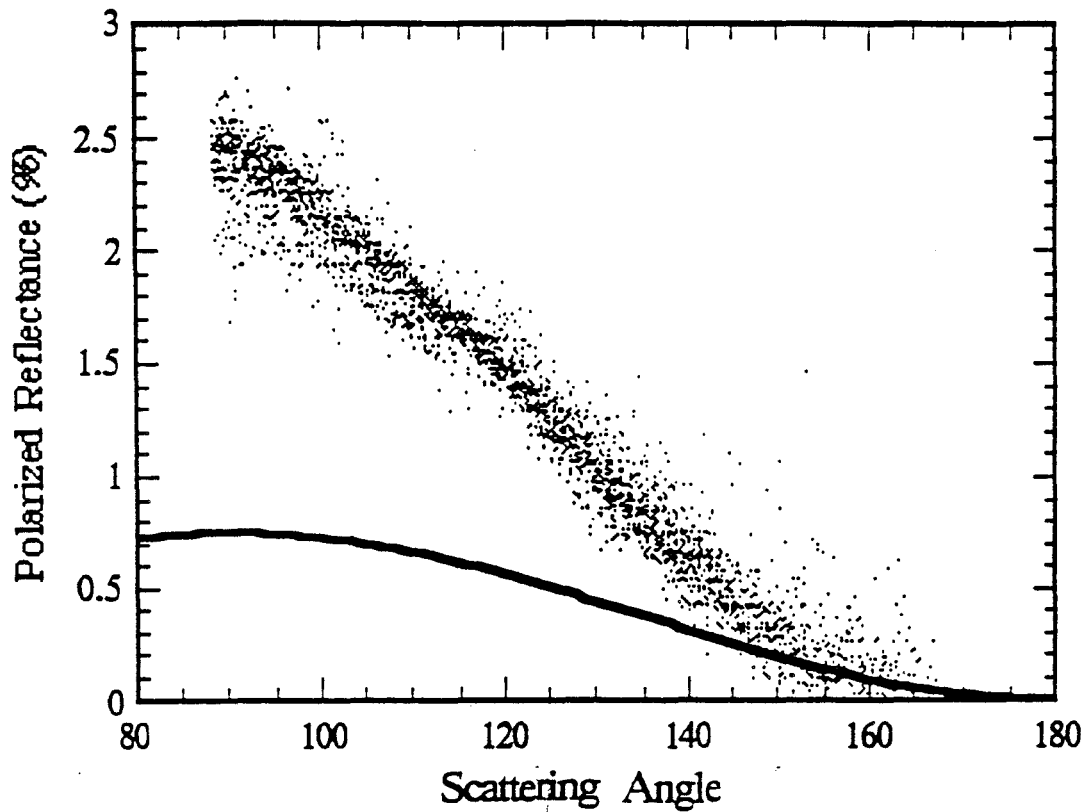


Fig. 7: Polarized reflectance normalized by the optical path as a function of scattering angle (dots). These measurements have been obtained by airborne POLDER over La Crau, France. The line indicates the polarized reflectance expected for an atmosphere without aerosols (Rayleigh scattering only). The gap between the line and the dots corresponds, therefore, to radiance scattered by the aerosols.

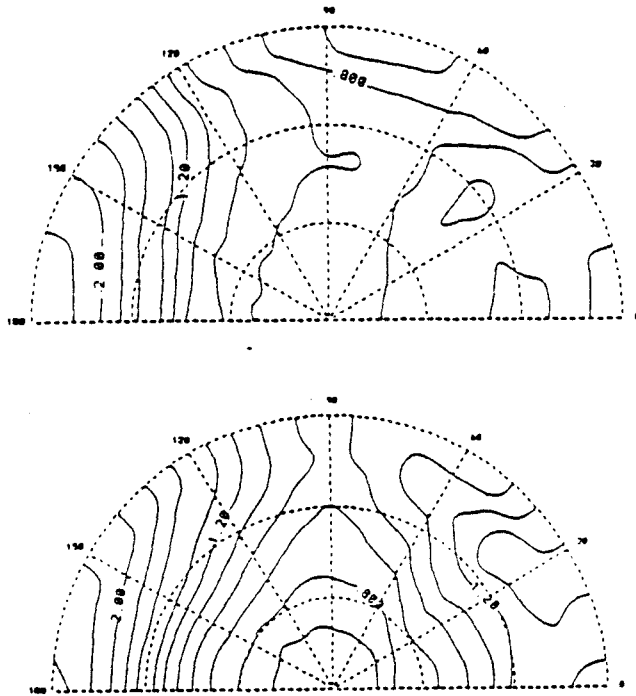


Fig. 8: Monte Carlo simulation of the TOA BRDF for a plane parallel cloud field (Fig. 8a, top) and a broken cloud field (Fig. 8b, bottom) of optical thickness 50. The solar zenith angle is  $60^\circ$ . The mean cloudiness of the broken cloud field is 0.5. Fig. 8a and Fig. 8b have been extracted from Bréon (1992). See this paper for details on the radiative transfer simulations.

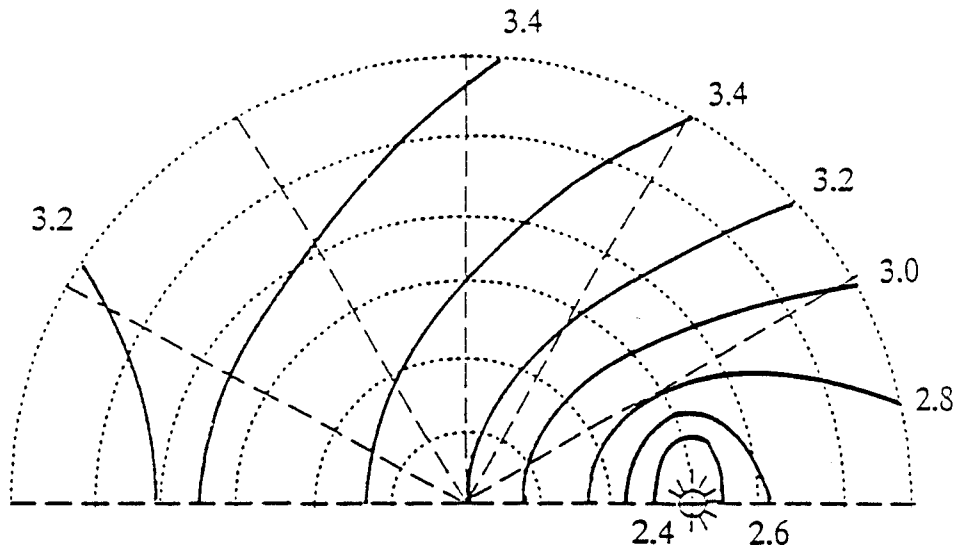


Fig. 9: Ratio of 443 nm and 565 nm ocean reflectances simulated by a Monte Carlo method. The phytoplankton concentration is  $0.3 \text{ mg m}^{-3}$  and the solar zenith angle is  $45^\circ$ .

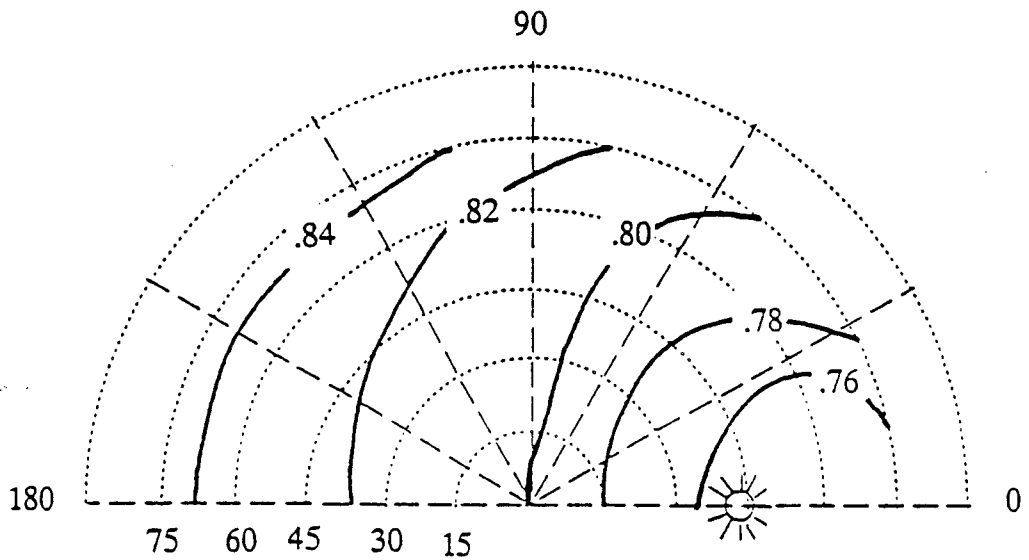


Fig. 10: Bidirectional signature of the NDVI as simulated with the SAIL model for a typical canopy. The solar zenith angle is 45 degrees, the leaf area index is 2 and the leaf orientation distribution is isotropic. In the visible (resp. PIR) the surface reflectance is 0.126 (resp. 0.286); the leaf reflectance is 0.135 (resp. 0.52) and its transmittance is 0.055 (resp 0.44). These are typical values as given by Verhoef (1984).

# Analysis of the POLDER (POLarization and Directionality of Earth's Reflectances) Airborne Instrument Observations over Land Surfaces

J. L. Deuzé, F. M. Bréon, P. Y. Deschamps, C. Devaux,  
and M. Herman

Laboratoire d'Optique Atmosphérique, Université des Sciences et Technologies de Lille, U.F.R. de  
Physique, Villeneuve d'Ascq, France

A. Podaire

Centre National d'Etudes Spatiales, Toulouse, France

J. L. Roujean

Centre National de Recherches Météorologiques, Toulouse, France

**T**he POLDER (POLarization and Directionality of the Earth's Reflectances) instrument provides polarized reflectance measurements that can be used to distinguish atmospheric and surface contributions to reflectance. Polarized reflectance measurements can then be used for an accurate aerosol estimation over land. The POLDER instrument was flown for the first time on 17 June 1990 over the "La Crau" site, in southern France and the results are presented in this article. The POLDER instrument is scheduled for launch in 1995 on the Japanese ADEOS (ADvanced Earth Observing System) platform. Surface based atmospheric optic measurements (spectral optical thickness, sky radiance)

are used to estimate the aerosol refractive index and size distribution. The corresponding aerosol model is then used in a radiative transfer model to simulate POLDER polarized measurements. The correlation between the observations and the simulations is good for the 550 nm and 650 nm wavelengths, but the simulation is biased for the 850 nm wavelength. These results indicate that, compared with the atmospheric contribution to the polarized reflectance, the surface contribution can be neglected at shorter wavelengths, but not so in near infrared wavelengths. The POLDER instrument allows multidirectional reflectance measurements. A surface target bidirectional reflectance, therefore, can be sampled at various viewing angles. In this article, we investigate the angular variations of the surface reflectance of various surface covers. The main observed variations are: i) a limb brightening; ii) a larger reflectance in the backscattering

Address correspondence to J. L. Deuzé, Laboratoire d'Optique Atmosphérique, USTL, Bat. P5, 59655 Villeneuve d'Ascq Cedex, France.

Received 5 February 1992; revised 3 October 1992.

direction; iii) a local maximum in the forward direction for the shorter wavelengths, indicating specular reflection by the leaves. A very simple empirical model is proposed to quantify the main reflectance angular variations.

## INTRODUCTION

Wide field of view sensors, such as the AVHRR (Advanced Very High-Resolution Radiometer), future instruments expected on the polar platforms (i.e., MODIS-N, MOderate-Resolution Imaging Spectrometer-Nadir, MERIS, MEium Resolution Imaging Spectrometer, AMRIR, Advanced Medium-Resolution Imaging Radiometer), or pointable sensors such as SPOT HRV (Système pour l'Observation de la Terre, Haute Résolution Visible), measure the energy reflected by the Earth surface-atmosphere system under a large range of viewing and solar geometries. The radiance measured by spaceborne instruments depends, therefore, on the viewing and solar geometry as well as the bidirectional scattering characteristics of the surface. Numerous field experiments have established the existence and importance of bidirectional and polarization effects in the solar light reflected by vegetation and soils (Coulson et al., 1965; Curran, 1982; Kriebel, 1978; Kimes et al., 1985; Vanderbilt et al., 1985). Moreover, the atmospheric path induces specific bidirectional and polarization effects. The magnitude of these coupled surface and atmospheric effects has been assessed on satellite sensor data (Taylor and Stowe, 1984; Gutman, 1987; Soufflet et al., 1991; Roujean et al., 1991) and by means of numerical simulations (Holben et al., 1986; Tanré et al., 1992).

The existence of a bidirectional and polarization signal from the surface in addition to the atmosphere radiance suggests several questions:

- Is it possible to account for, and correct, the bidirectional effects in order to compare the measurements acquired on the same target under different solar and viewing geometries?
- How much information about the surface can be gained from the reflectance bidirectional signature?

- Is it possible to use the polarized reflectance signal for a characterization of the atmospheric aerosols?

The POLDER (POLarization and Directionality of the Earth's Reflectances) instrument, which has been selected for the Japanese ADEOS satellite payload, has been designed specifically to address these questions. The instrument includes a matrix array CCD detector and a wide field of view optics of 114° along-track and across-track (Deschamps et al., 1990). The spectral bands and polarization states are selected by a rotating filter wheel. In a given channel, the state of polarization is derived from three successive measurements performed with three positions of the wheel, with a polarizer fixed on each filter: the angle between the directions of these three polarizers is 60°. Using the calibration, we obtain the radiance  $L$  and the polarized radiance  $L_p$  from the numerical counts. Then, we have chosen to transform these radiances into total and polarized reflectances as

$$\rho = \pi L / E_s, \quad \rho_p = \pi L_p / E_s,$$

where  $E_s$  is the solar irradiance at the top of the atmosphere. The degree of linear polarization is defined as

$$P = \rho_p / \rho.$$

The bidirectional reflectance and polarization distribution functions, that is, BRDF and BPDF, are obtained from near-simultaneous directional reflectance measurements of a single geographic target.

An airborne version of the POLDER instrument has been built. The first flight of this instrument was conducted over land surfaces in the southern part of France during the spring of 1990. The purpose of this article is to present the first results obtained during this campaign. We provide experimental evidence of bidirectional signatures on the reflectance that result from both the atmosphere and the land surface. We also show that the polarized radiance is mostly generated by the atmosphere (molecules and aerosols). It can be used, therefore, for a characterization of the aerosol amount and type. The BRDF of identified land surfaces are shown, and their trends are fitted and explained using a simple empirical model.

## MEASUREMENTS

### Land Cover Inventory

The measurement campaign was conducted over the 30 km × 15 km "La Crau" test site, centered at (43°30 N, 4°50 E), in the southeast of France (Fig. 1). The site can be divided in two different zones: "Crau sèche" contains dry and bright bare soil, patches of sparse grass and stones; "Crau humide" includes medium sized (e.g., approximately 1 ha) agricultural fields containing primarily grasses, rice, and wheat, which represent respectively 25%, 15%, and 10% of the total surface. Orchards and other crops of marginal importance (corn, sorghum, and sunflower) together with uncultivated land containing low vegetation (e.g., barren and maquis) comprise the remaining land area.

The day of the POLDER flight, the grasslands were green and totally covered the soil, the rice was green but immersed, and the wheat was mature and ready for harvesting. The orchards were in leaf. The spring crops (corn, sorghum, and sunflower) had a small cover. Barren and maquis areas were heterogeneous and had variable cover and greenness.

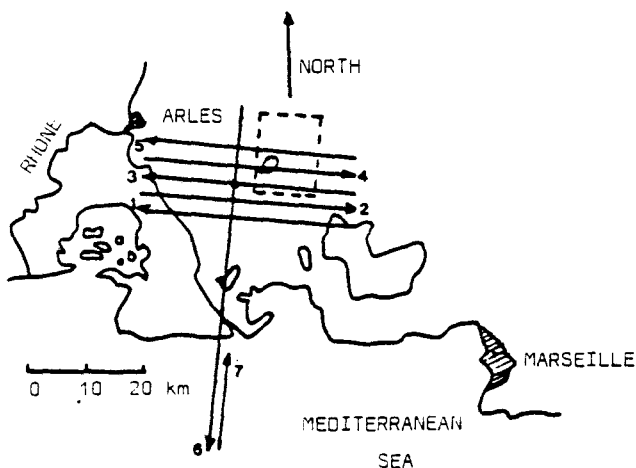
The land cover has been mapped for an area of about 750 km<sup>2</sup> using two approaches for land cover census. In the first, classical maps were

prepared for 76 small area segments, each approximately 0.5 km<sup>2</sup>, and selected by a predefined regular grid. This sample of about 5% of the test area allowed an estimate of the areal extent of each ground cover within the test site. In the second method, the land cover on four large area segments, each arbitrarily selected, was mapped. On three areas, each 4 km<sup>2</sup>, and a fourth area, 16 km<sup>2</sup>, the dominant land cover was grass, rice, and other crops.

The land cover of each segment was mapped during a 5-day period before and after the POLDER overflight. Recorded for each field or delimited ground area within a segment were the type of crop or vegetation, its phenological stage, health, height, coverage, the direction of the rows and the distance between two rows, the soil type, and its hydric state. The survey, relatively easy on cultivated plots where the vegetation is generally homogeneous, was difficult and subjective over natural vegetation, such as barren and maquis, where the type of vegetation and its coverage are often heterogeneous.

The information collected over the segments is qualitative and visual. While sufficient for relating the BRDF and BPDF to the land surface coverage, the recorded information was insufficient to infer the BRDF and BPDF usefulness for surface parameter retrieval.

Figure 1. The experiment area. The plain lines show the six aircraft runs. The dashed rectangle shows the size of one POLDER image from an altitude of 6000 m. The ground measurements were performed at the crossing between lines #3 and #6. The Entressens lake is crossed by line #4.



### POLDER Measurements

The POLDER concept is described in Deschamps et al. (1990), and the specific design of the POLDER airborne version is detailed in Herman et al. (1992). The POLDER system multangular viewing capabilities allow an angular coverage of  $\pm 41^\circ$  in the along track direction and  $\pm 51^\circ$  in the crosstrack direction. The filter wheel rotation allows nine spectral polarized measurements. During the aircraft displacement, the radiance from a given ground pixel is measured for different viewing angles, which leads to a sampling of the ground pixel BRDF.

For this campaign, measurements were performed in polarized mode in three spectral bands of width 40 nm, centered at 550 nm, 650 nm, and 850 nm, corresponding to the SPOT HRV channels (XS bands). POLDER was flown on the French Avion de Recherche ATmosphériques

(ARAT) airplane on 17 June 1990. The flight altitude was about 6000 m and the POLDER footprint was approximately 11 km  $\times$  15 km (see Fig. 1). The resulting images are partitioned in 288  $\times$  384 identical ground pixels of dimensions 37 m  $\times$  37 m. The nine spectral polarized images of each sequence were acquired in 3.7 s, which is the period of the filter wheel. During this period, the aircraft displacement is about 370 m, or 10 pixels. The time interval between two consecutive sequences was 11 s, which corresponds to a total aircraft displacement of 1.1 km. This sequencing provides twelve different viewing geometries for each ground pixel. Approximately 100 image sequences were obtained over the experimental site. The data were processed as explained in Herman et al. (1992). The raw data were corrected for the optical transmission, and, from the flight data, the latitude and the longitude were calculated for each pixel. The spectral and polarized measurements were then processed to estimate the reflectance, the degree of linear polarization and the polarization direction. Typical POLDER images are shown in Figures 6 and 7.

### POLDER Calibration

This article discusses the directional and polarization effects in the data, which are mainly based on relative measurements. An accurate calibration is necessary, however, when analyzing the aerosol influence of estimating corrections from molecular scattering. The POLDER instrument has been calibrated in the laboratory after the experimental flight, using an integrating sphere, as explained in Herman et al. (1992). To validate this calibration from in-flight measurements, we compared selected target radiance measurements from the POLDER and SPOT HRV instruments.

The SPOT HRV image was acquired on 21 June, 4 days after the POLDER flight. The solar conditions were slightly different: The solar zenith angle was 26° during SPOT overflight, and 35.5° during the POLDER measurements used for the intercalibration. To minimize the influence of the observation conditions, we chose the POLDER image so that the target viewing conditions are close to the nadir, matching the SPOT HRV viewing conditions. In these conditions, according to the known BRDF of the SPOT calibration site of La Crau, the bidirectional effects are negligible

for the aiming targets. On the other hand, a difference in the aerosol optical thickness between the SPOT HRV and the POLDER observations is probable. However, because of the high ground reflectance, the reflectances at the top of the atmosphere do not depend strongly on the aerosol content. For example, at the 550 nm wavelength, the ground reflectance is 0.17; for a nadir observation and a solar zenith angle  $\theta_s = 32^\circ$ , the calculated reflectance at the satellite level increases only from 0.211 to 0.229 while the aerosol optical thickness varies from 0.1 to 0.6. The aerosol optical thickness was close to 0.4 during the POLDER flight, and we estimate that the uncertainty resulting from variation of the aerosol loading should be less than 5% at this wavelength. For the 650 nm and 850 nm bands, the results should be better because the ground reflectance is larger while the atmospheric contribution is smaller than for 550 nm.

For the POLDER-SPOT HRV intercalibration in the 550 nm and 650 nm bands, we chose as a target the SPOT calibration site of "La Crau." It is an easily recognizable target on SPOT images thanks to the intersection of a channelized stream and a dirt road. The surface is mostly covered with pebble and stones. Its spectral, spatial, bidirectional, and seasonal characteristics have been well studied (Santer et al., 1991). For the near infrared band (850 nm) intercalibration, we used a vegetation covered target because of its larger reflectance. We chose a site, slightly north of the target for the visible bands, just west of Entresens lake.

The POLDER instrument measured the reflectance from an height of about 6000 m, while SPOT is located at the top of the atmosphere. Because the atmospheric absorption is rather low in the three spectral bands, we expect the radiance measurements from the satellite sensor to be larger than those of POLDER. The differences are estimated (first-order Rayleigh scattering) to be 1.9% at 550 nm, 1% at 650 nm, and 0.3% at 850 nm. After applying these atmospheric contributions to POLDER measurements, we obtain reflectances very similar to SPOT's (Table 1). The differences, expressed as a percentage of the SPOT measurement, are equal to -2%, 5%, and 4%. We do not expect to improve this intercalibration because of uncertainties related to i) HRV calibration, ii) atmospheric effects, and iii) solar

Table 1. SPOT HRV and POLDER Intercalibration<sup>a</sup>

Central Wavelength	550 nm	650 nm	850 nm
$\rho(\text{HRV})$	16.4	18.4	43.7
$\rho(\text{POL})$	14.2	18.4	45.3
$\rho(\text{POL}) + \rho(\text{atm})$	16.1	19.4	45.6

<sup>a</sup> The reflectances  $\rho(\text{POL})$  and  $\rho(\text{HRV})$  (in %) have been measured by the two instruments aiming at selected targets. The last line gives the POLDER reflectance  $\rho(\text{POL})$  added to an atmospheric contribution  $\rho(\text{atm})$  to match SPOT HRV measurement conditions (see text).

conditions. The comparison with SPOT measurements shows that the POLDER postflight calibration accuracy is better than 10%. It does not allow, however, its improvement.

### Flight Plan

The flight plan (Fig. 1) comprised five near east-west flight lines, 3 km apart and about 18 km long, and two bisecting superposed north-south flight lines. The aircraft altitude was 6 km, except for the last north-south flight line (#7), which was conducted at low altitude (200 m). A distance of 3 km was chosen between each parallel flight line so that the radiance of the central area was measured from each flight line. The seven flight lines therefore provide excellent coverage with which to estimate the BRDF.

During most of the flight, the sky was clear, although high clouds moved into the region toward the end of the flight. A light haze covered

the test site. The chronology, the positions of the flight lines and the mean solar zenith and azimuth angles during data collection are given in Table 2. The flight was executed according to plans except for a slight deviation on the third flightline. This was then reflown and identified as 3bis.

### Surface-Based Atmospheric Optic Measurements

To assess the aerosol influence in the POLDER data, ground-based measurements were performed before and during the flight, from the SPOT calibration site (see Fig. 1). They consisted in measurements of i) the direct solar transmission, ii) the solar aureole, and iii) the intensity and polarization of the diffuse sky light.

The direct solar transmission was monitored from 4.75 h UT (Universal Time) to 9.45 h UT, while the flight took place from 7.80 h UT to 9.65 h UT. A radiometer, previously calibrated during stratospheric balloon flights, measured the atmospheric transmission at  $\lambda = 450$  nm. The derived aerosol optical thickness is shown in Figure 2. The atmosphere was rather turbid but stable during the flight because the aerosol optical thickness remained rather constant. After about 9.25 h UT, the appearance of thin cirrus clouds increased the atmospheric optical thickness and modified the irradiance of the site, which perturbed probably the last flight line (#7) data. The atmospheric transmission was also measured at  $\lambda = 450$  nm,

Table 2. Chronology, Position, and Solar Conditions during the Flight<sup>a</sup>

Run No.		GMT Time	Long. = 4° E + ...	Lat. = 45° N + ...	$\theta_s^\circ$	$\varphi_s^\circ$
1	Begin	7.50.21	58'30"	31'06"	50°	94°
	End	7.56.45	33'11"	34'20"		
2	Begin	8.06.46	33'42"	35'49"	48°	97°
	End	8.11.59	58'53"	32'45"		
3	Begin	8.21.17	59'19"	34'20"	45°	100°
	End	8.27.21	34'07"	37'24"		
4	Begin	8.35.40	33'45"	39'06"	43°	104°
	End	8.41.18	59'37"	35'56"		
5	Begin	9.02.13	59'59"	37'32"	38°	109°
	End	9.08.31	33'38"	40'45"		
3 bis	Begin	9.17.09	59'19"	34'20"	35°	113°
	End	9.22.23	34'07"	37'24"		
6	Begin	9.34.49	51'51"	42'13"	33°	118°
	End	9.38.49	49'19"	30'27"		
7	Begin	10.31.57	45'45"	20'53"	24°	140°
	End	10.40.10	51'51"	42'13"		

<sup>a</sup>  $\theta_s$  is the solar zenith angle and  $\varphi_s$  the solar azimuth angle.

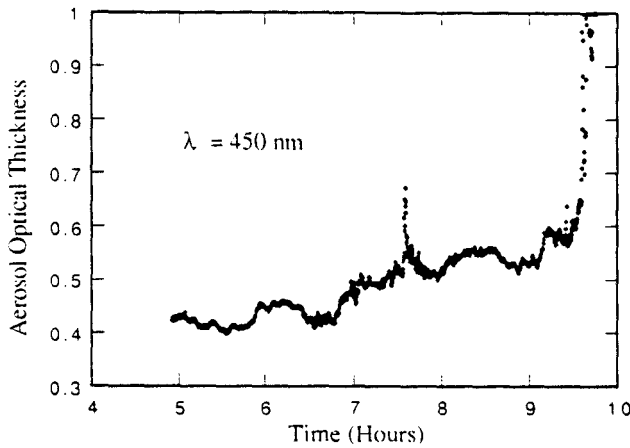


Figure 2. Aerosol optical thickness (dimensionless) at 450 nm from surface measurements as a function of time.

550 nm, 670 nm, 870 nm, 925 nm, 1040 nm, 1250 nm, and 1580 nm by a multichannel radiometer. The derived aerosol optical thicknesses  $\delta_{\text{meas}}(\lambda)$  are reported in Table 3. The estimated absolute error is 0.03. The derived Angström coefficient is about 1.4, which is characteristic of small particle dimension. These measurements were performed at 9 h UT, but no significant variation of the optical thickness spectral dependence was noticeable during the flight.

At 6.75 h UT, the aureole measurements were performed in the almucantar (i.e., by varying the viewing azimuth angle  $\phi_v$ , with viewing zenith angle  $\theta_v$  equal to the solar zenith angle  $\theta_s$ ), at  $\lambda = 850$  nm. When corrected for Rayleigh and multiple scattering effects (Santer, 1984), these

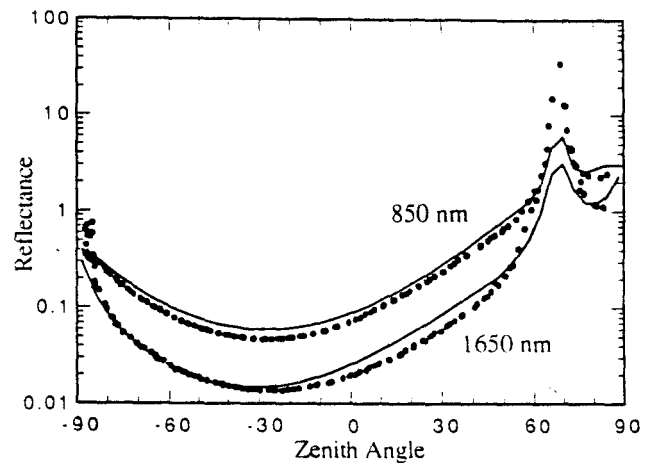


Figure 3. Downward sky reflectance (dimensionless) in the principal solar plane. The results obtained from the inverted model (dots) are compared to the measurements (lines).

measurements allow calculation of the aerosol phase function,  $p_{\text{meas}}(\Theta)$ , for scattering angles  $\Theta$  ranging from about  $2^\circ$  to  $30^\circ$ . The results are reported in Table 4.

The intensity and polarization of the diffuse sky light were scanned in the principal plane by a ground based calibrated polarized radiometer with a  $2^\circ$  field of view. Measurements were limited to wavelengths  $\lambda = 850$  nm and 1650 nm. The solar principal plane was scanned six times from 4.30 h UT to 6.50 h UT, during which the solar zenith angle decreased from  $88^\circ$  to  $66^\circ$ . Such large zenith angles allowed us to observe the aerosol phase function over a large range of

Table 3. Spectral Aerosol Optical Thicknesses as Estimated from Direct Solar Radiance Attenuation,  $\delta_{\text{meas}}$ , and as Restituted from the Inverted Aerosol model,  $\delta_{\text{rest}}$

$\lambda$ (nm)	450	550	680	870	1040	1250	1600
$\delta_{\text{meas}}$	0.500	0.400	0.290	0.201	0.159	0.130	0.084
$\delta_{\text{rest}}$	0.500	0.381	0.280	0.191	0.141	0.103	0.067

Table 4. Aerosol Phase Function for Various Scattering Angles as Estimated from Sky Radiance Measurements,  $p_{\text{meas}}$  and as Estimated from the Inverted Aerosol Model,  $p_{\text{rest}}$

$\Theta^\circ$	2.0	2.3	2.7	3.0	3.3	3.7	4.0	4.3
$p_{\text{meas}}$	26.9	23.7	20.9	18.6	16.8	15.4	14.3	13.5
$p_{\text{rest}}$	27.0	23.7	20.9	18.6	16.9	15.5	14.5	13.7
$\Theta^\circ$	5.0	5.7	6.3	7.7	9.0	11.0	13.3	19.0
$p_{\text{meas}}$	12.3	11.5	10.8	9.6	8.6	7.7	7.0	5.9
$p_{\text{rest}}$	12.4	11.5	10.8	9.5	8.6	7.7	7.1	5.7

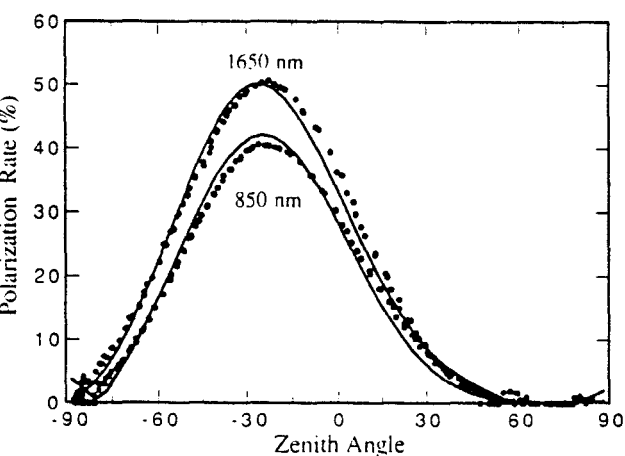


Figure 4. Sky radiance polarization rate measured from the surface in the principal plane. The line is the model estimate. The dots correspond to surface measurements.

scattering angles. Typical results are shown in Figures 3 and 4.

## AEROSOL ESTIMATION

The atmospheric contribution in the POLDER measurements and/or the ground-based sky radiance measurements were estimated by numerical simulations. These simulations were performed by the successive order of scattering method (SOS), described in Deuzé et al. (1989a). This radiative transfer code allows us to take into account rigorously polarization and multiple scattering by molecules and aerosols. In these calculations, it is assumed that the ground is a Lambertian, non-polarizing reflector.

The spectral optical thicknesses and phase function data in Tables 3 and 4 were processed to estimate the aerosol size distribution by using conjugated inversion schemes of King's and Chahine's types, as explained in Devaux et al. (1989). Absorbing spherical particles with complex refractive index  $m = 1.50 - 0.005i$  were assumed. The derived aerosol size distribution,  $n(r)$ , versus the radius  $r$  is shown in Figure 5. The inversion procedure was successful as shown by comparing the predicted and measured values of the spectral optical thickness (Table 3) and the phase function (Table 4). Note that the size distribution for the largest particles ( $r > 1 \mu\text{m}$ ) is mostly derived from the aureole measurements. Since these were conducted at 6.75 h UT, which was 1 h before the beginning of the flight, a different aerosol size

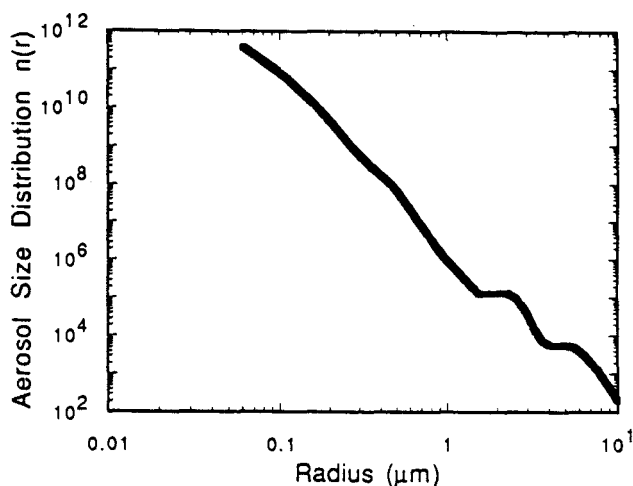


Figure 5. Aerosol size distribution  $n(r)$ , in arbitrary units, estimated from the spectral optical thicknesses and aureole measurements.

distribution possibly affected the POLDER measurements.

Given the aerosol size distribution of Figure 5, the aerosol single scattering properties were calculated for spherical particles with refractive indices ranging from 1.33 to 1.55 for the real part and 0.00 to 0.01 for the imaginary part. These results, together with the known molecular component, the measured aerosol optical thickness and the measured ground reflectance were used as input of the SOS algorithm. The simulated radiances and polarization rates were compared to the sky measurements in the principal plane. The best fit was obtained with an aerosol refractive index of  $1.50 - 0.005i$  for the observations at 850 nm and  $1.45 - 0.008i$  for the observations at 1650 nm. The decrease in the retrieved aerosol refractive index, from 850 nm to 1650 nm, is consistent with the behavior of known tropospheric aerosols (Fen et al., 1985). These materials, on the other hand, are known to exhibit negligible variation of the refractive index from 450 nm to 850 nm. We will therefore assume that, during the POLDER flight, the atmospheric aerosols had a size distribution as in Figure 5 and a constant refractive index  $m = 1.50 - 0.005i$  at 550 nm, 650 nm, and 850 nm. The aerosol layer will be assumed to be invariant over all of the test site.

The corresponding simulated radiances and polarization rates are shown together with the measurements in Figures 3 and 4. The largest

differences between the model results and the remotely sensed measurements are found for a zenith viewing angle close to  $65^\circ$ , which is close to the solar direction. These differences result from parasite light in the skylight measurements because of multiple reflections of the direct sunbeam in the optics. On the other hand, the aureolemeter, whose measurements are used for the aerosol model retrieval, is designed to avoid this problem. The aerosol refractive index determination is essentially based on the polarization measurements. The close agreement between the model results and the measurements, in Figures 3 and 4, suggests that the aerosol model is valid for predicting correctly the aerosol radiative properties.

## POLDER DATA ANALYSIS

### Aerosol Observation from Polarization Measurements

Remote sensing of aerosols over land from spaceborne sensors which measure only radiance is known to be a difficult task because surface radiance is generally much larger than that of aerosols and varies significantly on short spatial scales and on viewing angles, in the absence of any well-defined rules. On the other hand, polarized light is expected to be mostly generated by molecule and aerosol scattering. Over land, measurements of the polarized radiance should then be helpful for aerosol retrieval. One of the scientific objectives of POLDER is to investigate this hypothesis. Aerosol estimation from POLDER measurements, therefore, will be achieved from the analysis of polarized radiance.

We have several reasons to assume that the aerosol properties do not vary within the airborne POLDER field of view during the flight (axis #1–#5): First, the region has no aerosol source around which the aerosol content is very inhomogeneous; then, the aerosol optical thickness  $\delta_a$  at  $\lambda = 450$  nm is quite constant (0.50–0.55); last but not least, the polarized reflectances at  $\lambda = 550$  nm and  $\lambda = 650$  nm do not change on the pictures of the same axis. This fact shows us that the aerosols remain the same and that the land polarization is quite negligible at these shorter wavelengths. So the atmospheric BPDF can be investigated over

the whole POLDER image. Local discrepancies from the mean PPDF signatures in particular directions correspond to surface polarization effects, specially at the 850 nm wavelength.

Figures 6a and 6b display typical POLDER images at  $\lambda = 650$  nm. Figure 6a is the reflectance (total)  $\rho$ , whereas Figure 6b is the polarized reflectance,  $\rho_p$ . Figures 6c and 6d are the polarized reflectances measured in the two other POLDER channels, at  $\lambda = 550$  nm and 850 nm, respectively. In each of these figures, the central column corresponds to observation directions in the solar principal plane. The antispecular direction (i.e., scattering angle  $\Theta = 180^\circ$ , or zero phase angle) is near the top of the images.

Unlike the reflectance image (Fig. 6a), which displays pronounced spatial patterns due to varying ground cover, the polarized reflectance image (Fig. 6b) exhibits a smooth pattern, suggesting that the polarized reflectance represents primarily light scattered by the atmosphere. Further evidence for atmospheric scattering as the main origin of polarized light is given in Figures 6b, 6c, and 6d: from 850 nm to 550 nm, as the molecule and aerosol optical thicknesses increase, the polarized reflectance increases and the relative contribution from the surface decreases.

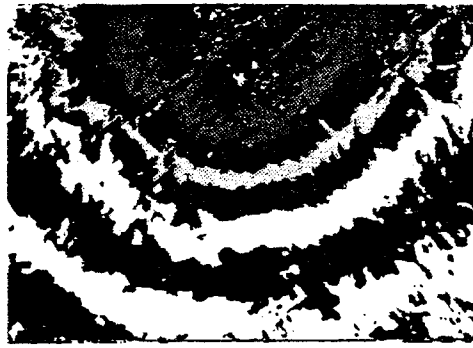
Assuming that the polarized light is mostly generated by primary scattering in the atmosphere, the measured polarized reflectance should be

$$\rho_p = \frac{\delta_m p_m(\Theta) P_m(\Theta) + \delta_a p_a(\Theta) P_a(\Theta)}{4 \cos(\theta_s) \cos(\theta_v)}, \quad (1)$$

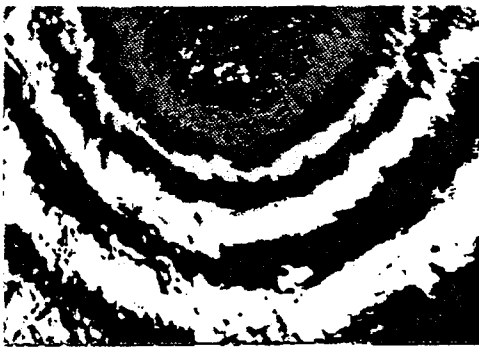
where  $P_m(\Theta)$  and  $P_a(\Theta)$  are the polarization rates for single scattering,  $p_m(\Theta)$  and  $p_a(\Theta)$  are the phase functions, and  $\delta_m$  and  $\delta_a$  are the optical thicknesses of molecules (index  $m$ ) and aerosols (index  $a$ ). The term  $\rho_p \cos(\theta_v)$ , which accounts for the atmospheric air mass, therefore, depends only on the scattering angle  $\Theta$ . This hypothesis is investigated in Figure 7. The continuous curve corresponds to the results expected for single scattering by molecules only (the molecule optical thickness and their polarization behavior are known). The difference between this curve and the mean measured reflectance corresponds to aerosol scattering. The dispersion around the mean measurement is relatively small, which shows that atmospheric scattering is the main contribution to the observations. Around  $\Theta = 150^\circ$  the polarized reflectance equals the molecular one. It shows that the aero-



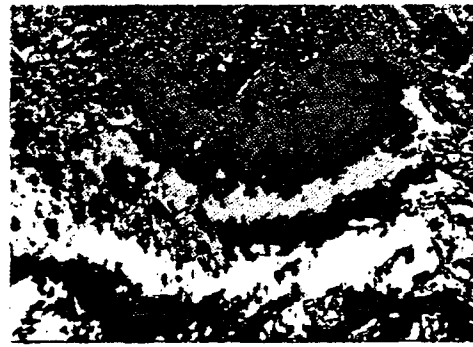
**a**  
Reflectance 650 nm



**b**  
Rpol 650 nm



**c**  
Rpol 550 nm



**d**  
Rpol 850 nm



Figure 6. a) Typical POLDER image of total reflectance. The wavelength is 650 nm. The distance from the image center is proportional to the tangent of the zenith viewing angle. It is  $41^\circ$  ( $51^\circ$ ) on the small (long) axis edges. b) Same as a but for the polarized reflectance (dimensionless). c) Same as b but for  $\lambda = 550$  nm. d) Same as b but for  $\lambda = 850$  nm.

sols exhibit zero polarization for a  $150^\circ$  scattering angle. For larger scattering angles, the aerosol polarization seems to increase again, with the polarization direction now parallel to the scattering plane; however, very few measurements are available in this range of scattering angles because the backscattering direction is not located within the POLDER field of view.

We now compare POLDER measurements to that simulated with the SOS algorithm. Because polarized and total light are mixed ambiguously in the polarization ratio  $P$ , we rather simulate the polarized reflectance  $\rho_p$ , which is nearly additive

with respect to the contributions from molecules, aerosols, and land surfaces. It is then legitimate to compare the respective contributions  $\rho_r^m$ ,  $\rho_r^a$ , and  $\rho_r^s$  from these sources to the POLDER  $\rho_p$  measurements. The measurements shown in Figures 6b, 6c, and 6d were simulated accounting for molecular scattering and for the estimated aerosol model (see the Subsection on POLDER Calibration). According to the aircraft altitude, the simulations were performed with 47% of the molecular atmosphere above the detector level. A 2 km aerosol scale height was assumed, which results in 95% of the total aerosol content below

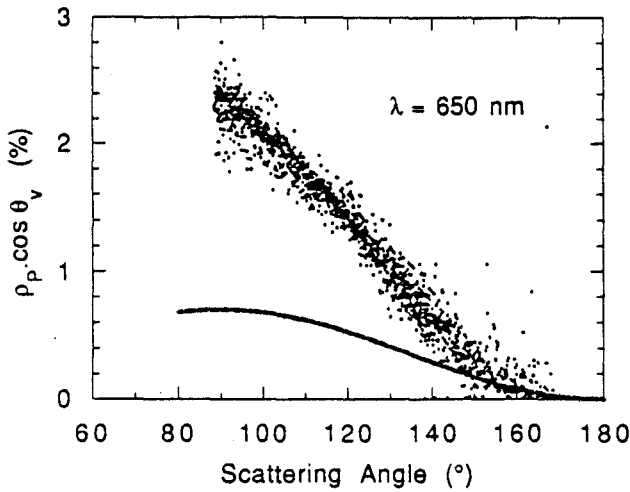


Figure 7. Polarized reflectance normalized by the optical path (see text) as a function of scattering angle. The wavelength is 650 nm. The dashed curve corresponds to the results expected for single scattering by molecules only.

the radiometer. We assumed that the radiance reflected by the surface was not polarized, and we fixed the albedo of the assumed Lambertian surface to the average value of the observed reflectances. Note that the polarized reflectance at the detector level was simulated for a Lambertian, nonpolarizing surface, with albedo ranging from 0 to 0.50; the largest change in the predicted polarized reflectance was only 0.001. Therefore,

Figure 8. Scatter plot of the measurements versus the simulated polarized reflectance. The wavelength is 550 nm and the refractive index  $1.50 - 0.005i$ .

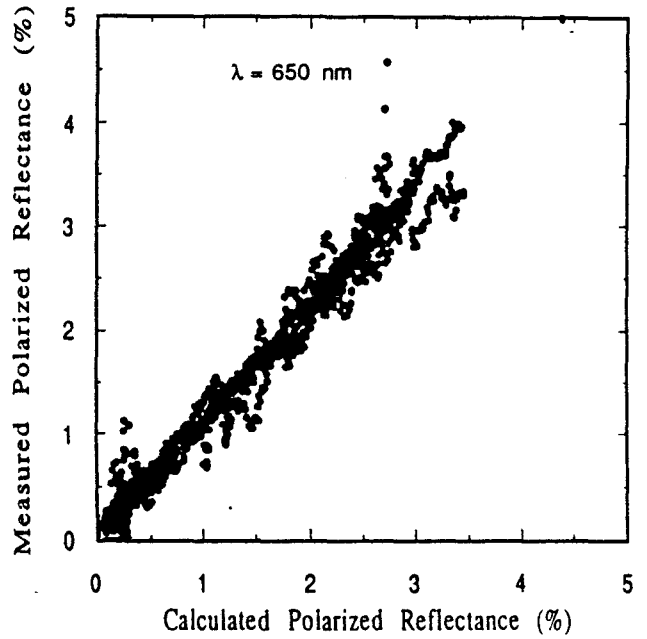
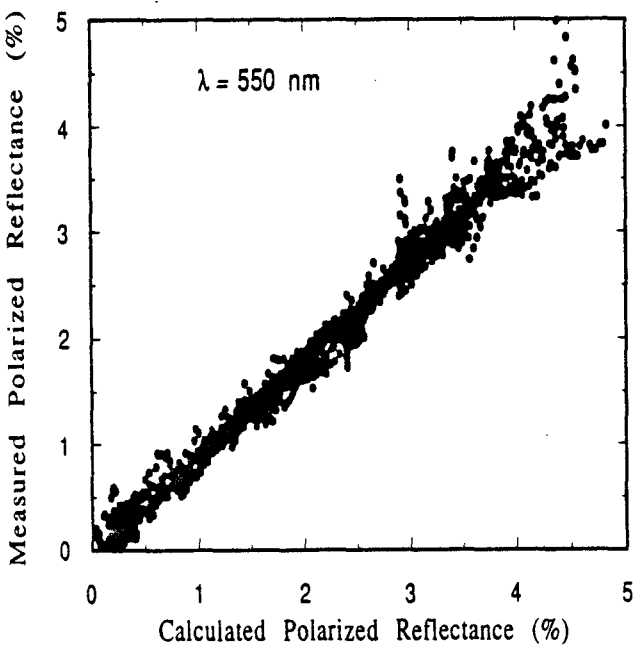
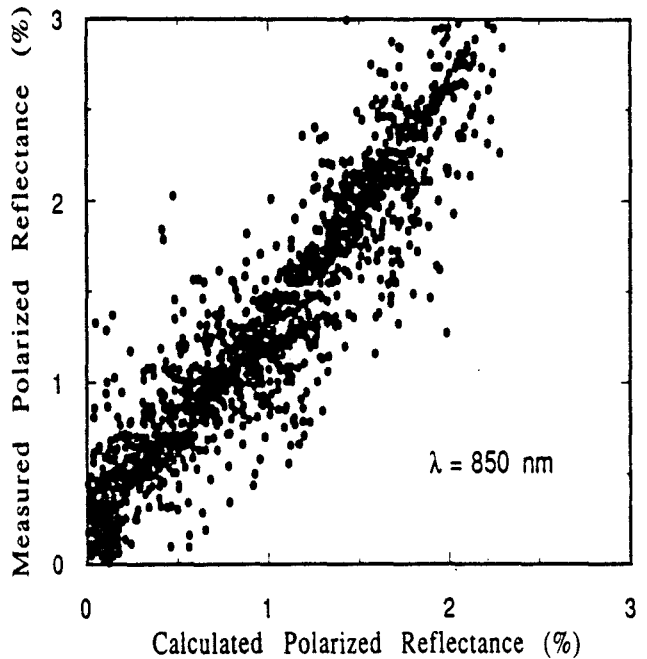


Figure 9. Same as Figure 8 but for  $\lambda = 650 \text{ nm}$ .

the surface albedo does affect the polarized reflectance measurements but by a small amount.

Figures 8, 9, and 10 compare the simulated polarized reflectances to the observations for  $\lambda = 550 \text{ nm}$ ,  $650 \text{ nm}$ , and  $850 \text{ nm}$ , respectively. The aerosol model derived from the ground-based measurements leads to a good agreement for the

Figure 10. Same as Figure 8 but for  $\lambda = 850 \text{ nm}$ .



550 nm and 650 nm wavelengths. For the 850 nm wavelength, the measured polarized reflectance is systematically larger than that predicted by the model. The difference is the largest for limb observations. This result suggests that the surface generates polarized light, as was anticipated from examination of Figure 4d. But this land effect is quite small and is hidden by the atmosphere at the shorter wavelengths.

We have found a good agreement between the measured polarized light and that simulated using a radiative transfer model with a crude surface description. It shows that the polarized reflectance depends little on the surface. It can then be used to retrieve specific information about aerosols over land surfaces. POLDER multiangular capabilities make it possible to estimate the aerosol polarization for many scattering angles. These can then be used for an aerosol model estimation. Inversion of multiangular and multiwavelength measurements of the polarized light scattered from aerosols is a difficult task, but is known to be feasible (Hansen and Hovenier, 1974; Deuzé et al., 1989b). At  $\lambda = 850$  nm, a small surface contribution is ambiguously mixed with the atmospheric signal, which complicates the inversion problem. From our results, however, it seems that the surface contribution to the polarized reflectance is small enough at the shorter wavelengths so that it can be neglected compared to the atmospheric contribution.

Another objective of POLDER polarization measurements is to investigate the polarization properties of land surfaces. According to the previous analysis, this information is probably accessible at  $\lambda = 850$  nm but the polarization of the land cannot be estimated with the present observation set because 1) the surface contribution is significantly smaller than the atmospheric signature and 2) the surface signal is rather noisy. The polarized reflectance here is derived from differences between three polarized measurements. Because of the aircraft displacement, these measurements are acquired over slightly different surface targets, so that the data processing cannot account for all high frequency surface reflectance spatial variations. The technique that is used to measure the polarized reflectance is, therefore, a source of noise over nonhomogeneous land surfaces. The noise shall be reduced with the spaceborne version of POLDER because of i) a better spatial

coherence of the three measurements used for the polarized reflectance estimate and ii) a larger surface pixel, which may smooth out the high spatial frequency of the land surface reflectances.

### Land Surface BRDF

We now consider the total reflectance  $\rho$  without polarization considerations. The multiangular viewing capabilities of the POLDER instrument makes it possible to obtain a BRDF sampling for various surface types. When located within the instrument field of view, a given surface point reflectance was measured from about 10 directions for each of the seven overflights. A small portion of the La Crau experiment area was observed from all overflights providing more than 70 directional reflectance measurements. A larger area has been observed from five or six of the seven overflights, which still provides an excellent sampling of the BRDF within the viewing angle conditions accessible to the airborne POLDER instrument ( $\theta_v < 57^\circ$ ). The east-west airplane passes were broadly directed in the Sun direction, providing a BRDF sampling in the principal plane for surface points located on the subtrace, when the last was performed in a perpendicular direction. Note that, from the first flight line to the last, the solar zenith angle decreased from  $50^\circ$  to  $33^\circ$  and that, therefore, the measurements have been obtained in different solar conditions.

Using the *in situ* observations and some aerial pictures, we selected 33 targets: These targets were chosen in order to have a sampling of the various surface types in the experimental area. Each of them was chosen within the 70 carefully studied zones so that its characteristics would be well known. Moreover, we only selected surface points for which the surface type was homogeneous within a 150 m radius. The corresponding circle also had to look homogeneous on the airplane pictures.

The latitude and longitude of each target was then obtained from a digital map, and, using this information, we extracted all POLDER-derived directional reflectances.

A first step toward deriving surface BRDFs from POLDER observations is to correct the measured reflectance for atmospheric effects. Ideally, the reflectance has to be corrected for the target environment and all atmospheric effects (multiple

Figure 11. Polar diagrams of bidirectional reflectance for six surface coverages. Each dot corresponds to one observation, the color of which defines the reflectance range. The seven color intervals were chosen between the minimal and the maximal reflectance in order to obtain an equipopulation. The quantitative ranges of these reflectance intervals are given in Table 5. In the diagram, the radius is the viewing zenith angle and the angle gives the azimuth. Backscattering conditions are on the right hand side of the diagram. The top half of each diagram is for 850 nm wavelength observations, whereas the bottom part gives 550 nm wavelength results.

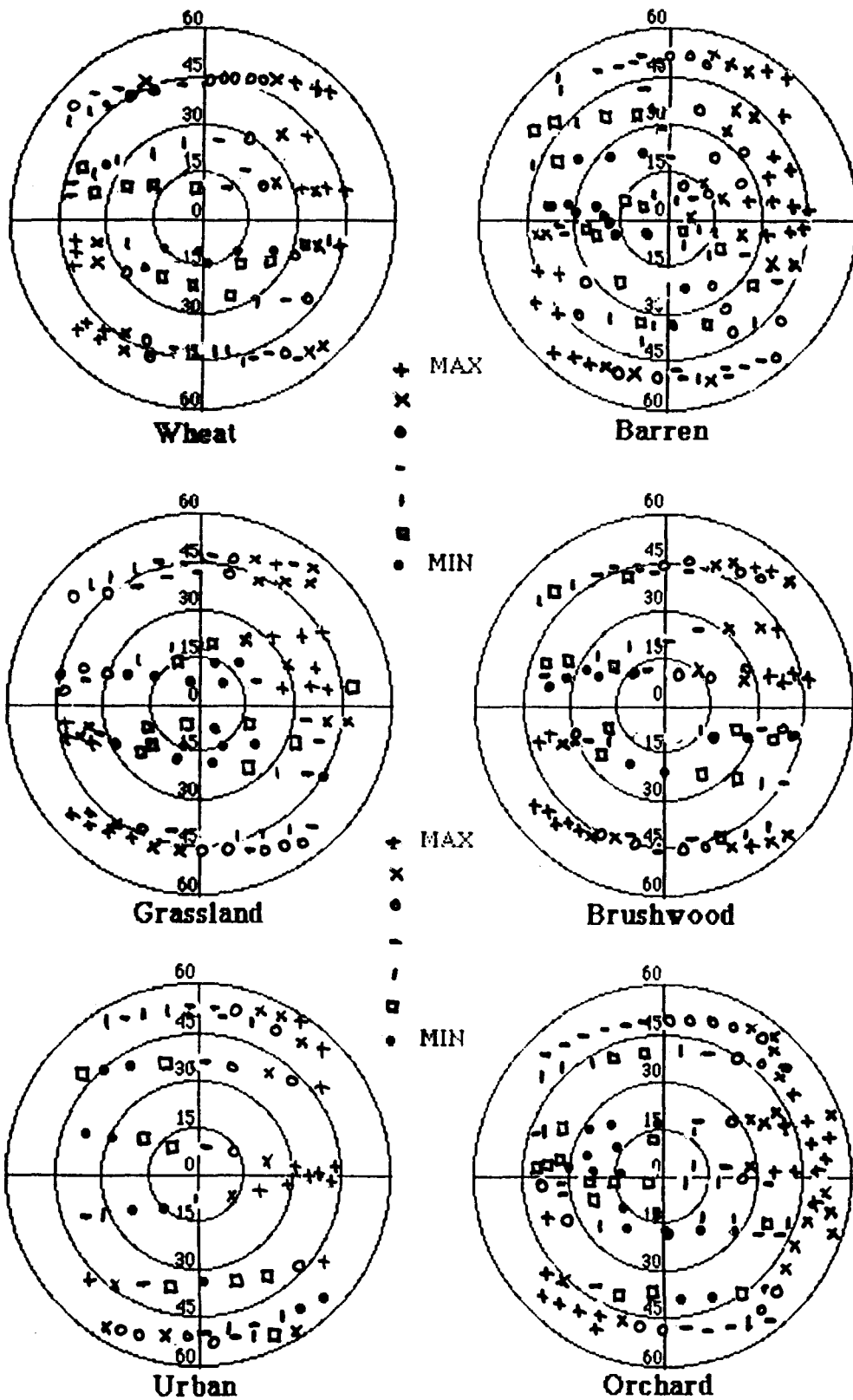


Figure 11. Polar diagrams of bidirectional reflectance for six surface coverages. Each dot corresponds to one observation, the color of which defines the reflectance range. The seven color intervals were chosen between the minimal and the maximal reflectance in order to obtain an equipopulation. The quantitative ranges of these reflectance intervals are given in Table 5. In the diagram, the radius is the viewing zenith angle and the angle gives the azimuth. Backscattering conditions are on the right hand side of the diagram. The top half of each diagram is for 850 nm wavelength observations, whereas the bottom part gives 550 nm wavelength results.

Table 5. Reflectance Intervals (in %) Corresponding to Each of the Seven Color Scales Used in Figure 11<sup>a</sup>

Surface	$\lambda_c$	Black	Dark Blue	Light Blue	Green	Yellow	Orange	Red	
Wheat	850	19.9	21.3	22.1	23.1	23.5	25.3	26.2	30.4
	550	6.3	6.9	7.5	7.7	7.9	8.2	8.8	11.1
Grassland	850	31.8	43.9	46.2	47.0	47.4	48.7	50.2	54.8
	550	5.5	6.4	6.9	7.1	7.9	8.1	8.9	11.6
Brushwood	850	23.3	24.5	25.3	26.2	27.8	30.2	32.3	48.1
	550	3.7	5.1	5.5	5.7	6.3	6.9	7.5	9.9
Orchard	850	10.6	28.4	29.7	31.2	32.7	34.9	37.4	41.9
	550	5.6	6.0	6.2	6.8	7.1	7.6	8.3	10.7
Barren	850	24.9	25.7	26.8	27.5	28.7	29.6	30.9	41.0
	550	7.3	8.8	9.1	9.5	9.7	9.8	10.5	12.0
Urban	850	23.9	24.8	25.7	26.7	28.2	29.3	31.0	38.2
	550	9.4	9.7	9.9	10.1	10.4	10.6	11.3	14.7

<sup>a</sup> Note that these intervals were chosen different for each surface and each central wavelength  $\lambda_c$  of the waveband in order to obtain an equipopulation. The first and last columns give the minimum and maximum reflectance of each target respectively.

order Rayleigh scattering, atmospheric absorption, aerosol absorption, and scattering). We only accounted for the main one, however, that is, first-order Rayleigh scattering, by subtracting to the measured reflectance a term equal to

$$\Delta\rho = \frac{3\Delta\delta}{16} \frac{1 + \cos^2(\Theta)}{\cos\theta_s \cos\theta_v}, \quad (2)$$

where  $\Delta\delta$  is the molecular spectral optical thickness between the ground and the instrument (deduced from that of the whole atmosphere and the airplane altitude), and  $\Theta$  is the scattering angle.

Figure 11 gives a graphic representation of these corrected reflectances for six typical surfaces of the La Crau experimental area for which we had the most measurements. Each dot represents one observation, the color of which defines the reflectance range. The seven color intervals were chosen between the minimal and the maximal reflectance in order to obtain an equipopulation. The quantitative ranges for these reflectance intervals are given in Table 5. The polar diagram should be interpreted as follows: The radius is the viewing zenith angle and the angle gives the azimuth. Backscattering conditions are on the right hand side of the diagram. The top half of each diagram is for the 850 nm wavelength observations, whereas the bottom part gives the 550 nm wavelength results.

It was noted that:

- The main tendency observed over all sur-

faces and for both wavelengths is a reflectance decrease toward the zenith viewing angle. It can be explained by the increased portion of lower canopy layers sensed from nadir viewing conditions; these lower layers being shaded by upper layers (Kimes, 1983).

- Another large effect, but one that is only observed at the 850 nm wavelength, is the larger reflectance observed in the backscattering hemisphere, a result of intershadowing: When looking from a direction opposite to that of the Sun, the relative portion of shadowed surfaces in the sensor field of view is larger than when the sensor is in the direction of the Sun.
- At the 550 nm wavelength, the opposite effect is noticeable: For a given viewing angle, the reflectance are generally larger in the forward hemisphere than in the backward hemisphere. Let us point out that, because of the very large absorption by chlorophyll, most of the 550 nm radiation that penetrates the leaves is absorbed. At this wavelength, specular reflectance on the leaf wax is, therefore, relatively large and shows a clear maximum in the forward direction (Vanderbilt and Grant, 1985). Specular reflectance is, therefore, likely responsible for the feature described in this paragraph.
- A nonnegligible observation noise is detectable on the measured BRDFs, as pre-

Table 6. Result of the Geometrical Model Fit against the Target Observations<sup>a</sup>

Surface	$N_{obs}$	$K_0$	$K_1$	$K_2$	$\sigma_{obs}$	$RMS_{dif}$	$R^2$
	28	20.78	20.82	10.37	2.93	1.40	0.77
Garrigue	16	5.57	1.83	-0.81	0.58	0.38	0.57
03	30	3.86	4.82	0.01	0.77	0.52	0.55
	9	48.62	13.06	18.19	2.59	0.58	0.95
Grassland	28	3.51	6.17	0.48	0.91	0.72	0.37
04	50	5.74	2.95	-0.47	0.87	0.79	0.17
	28	31.89	6.96	9.25	3.05	0.82	0.93
Pebble	28	15.69	1.74	3.35	1.43	1.04	0.47
05	29	10.65	1.53	0.79	0.90	0.86	0.07
	20	57.12	-13.27	8.21	4.32	3.35	0.40
Grassland	26	3.28	7.79	0.23	0.89	0.47	0.73
08	37	3.82	7.16	-0.75	1.03	0.57	0.69
	32	25.07	17.19	9.38	3.34	1.99	0.65
Barren	24	8.49	5.84	1.63	0.93	0.79	0.27
09	43	5.70	3.53	-1.09	1.08	0.92	0.27
	26	25.98	5.65	5.34	1.36	0.47	0.88
Steppe	25	14.01	3.85	2.81	0.79	0.40	0.74
10	25	8.49	2.91	0.03	0.50	0.41	0.33
	49	22.82	11.00	6.28	2.31	1.05	0.80
Wheat	51	7.84	8.59	1.23	1.24	0.89	0.49
11	50	5.20	4.74	-1.13	1.01	0.77	0.42
	47	45.91	12.76	6.44	2.91	2.01	0.52
Grassland	49	3.12	6.73	-0.60	1.06	0.71	0.55
12	50	4.06	6.43	-1.51	1.26	0.81	0.58
	37	29.16	12.48	11.34	4.03	1.41	0.88
Brushwood	46	3.28	6.27	-0.55	0.98	0.63	0.58
13	46	2.67	6.33	-1.47	1.17	0.71	0.63
	56	29.07	21.25	10.32	3.76	1.20	0.90
Orchard	38	5.98	6.16	1.49	1.12	0.92	0.33
14	51	4.46	5.71	-0.20	1.13	0.92	0.33
	68	28.55	12.63	9.08	2.83	1.23	0.81
Barren	68	12.37	5.31	3.14	1.09	0.62	0.68
15	70	8.35	3.45	0.19	0.78	0.66	0.29
	25	21.45	22.20	6.43	2.54	0.84	0.89
Wheat	32	5.89	12.23	0.89	1.08	0.55	0.74
16	46	4.61	6.15	-1.47	1.01	0.75	0.45
	7	19.08	19.60	0.49	1.51	0.39	0.93
Rice	44	2.95	7.73	-1.68	1.21	0.88	0.47
17	46	2.60	6.60	-3.07	1.44	0.90	0.61
	58	22.82	24.58	6.83	3.19	1.62	0.74
Barren	57	12.10	9.81	2.44	1.43	0.98	0.53
18	57	7.64	7.20	-0.55	1.10	0.71	0.59
	35	25.27	27.66	10.30	3.58	0.87	0.94
Swamp	14	2.89	14.60	0.63	1.57	1.10	0.51
19	25	1.73	12.63	-2.00	1.48	1.02	0.52
	33	-1.49	58.86	0.17	5.41	2.25	0.83
Swamp	29	-0.68	13.70	-2.43	1.71	0.55	0.90
20	44	-1.72	14.06	-3.50	1.96	0.69	0.88
	46	15.65	35.61	8.76	4.14	2.01	0.76
Barren	45	5.49	22.90	2.33	1.93	1.15	0.64
21	45	1.45	18.61	-0.99	1.34	0.77	0.67
	26	25.64	13.32	6.02	1.80	0.62	0.88
Barren	30	12.92	6.87	0.73	1.13	0.87	0.41
25	35	7.00	6.81	-1.90	1.21	0.80	0.57
	23	28.44	14.88	11.96	2.67	0.92	0.88

(continued)

Table 6. (continued)

Surface	$N_{obs}$	$K_0$	$K_1$	$K_2$	$\sigma_{obs}$	$RMS_{dif}$	$R^2$
Urban	0						
28	16	9.69	0.73	-0.29	0.37	0.34	0.15
	6	21.07	13.26	3.79	1.84	1.02	0.69
Swamp	35	4.34	4.74	-0.76	0.71	0.51	0.48
29	38	3.90	4.69	-1.64	0.87	0.62	0.49
	20	4.86	54.76	3.46	3.61	0.88	0.94
Rice	13	4.72	11.10	-0.02	0.71	0.44	0.61
32	34	1.76	12.11	-1.20	0.81	0.37	0.79

<sup>a</sup> "Surface" gives the target surface type and the target number used in our classification.  $N_{obs}$  is the number of observations used for the fit.  $K_0$ ,  $K_1$ , and  $K_2$  are the retrieved model parameters.  $\sigma_{obs}$  is the measured reflectances standard deviation (in %).  $RMS_{dif}$  is the RMS difference between the observed and modeled values (in %).  $R^2$  is the fit correlation coefficient.

sented on Figure 11: Some close dots indicate very different reflectance ranges. The solar zenith angle variations may account for part of this "noise," but registration errors that result in the monitoring of a slightly different surface are responsible for the largest variations. It seems that no bidirectional reflectance model can reproduce these variations and, therefore, any model will show a residual error when fitted to the observations.

- The largest variations are observed in the principal plane. The maximal reflectance is generally measured in the "hot-spot" viewing direction, that is, where no shadow surfaces are in the sensor field of view. The minimal reflectance is localized in the principal plane, slightly off the nadir in the forward hemisphere.

From these qualitative results, it is difficult to assess if different surface types can be distinguished from their bidirectional reflectance diagrams. One ought to fit bidirectional reflectance models and analyze the retrieved parameters. Many such models are available in the literature (see, e.g., Hapke, 1981; 1986; Otterman and Weiss, 1984; Deering et al., 1987; Verstraete et al., 1990; Roujean et al., 1991). They differ in complexity and their choices of modeled physical processes.

Figure 11 analysis has shown some noise in the data. This measurement noise makes it impossible to estimate valuable physical parameters from the physical models and will reduce any model capability to fit the directional reflectance

measurement set. It is, therefore, not our purpose here to compare several models ability to fit the observations. We will rather develop our own simple geometric model that reproduces the main BRDF characteristics.

The reflectance is modeled as the sum of an isotropic contribution, a function that accounts for the brightening to the limb viewing ( $F_1$ ), and a function that accounts for the maximum in the direction to the Sun ( $F_2$ ).  $F_1$  depends on the solar and viewing zenith angles whereas  $F_2$  also depends on the azimuth angle. The three coefficients  $K_0$ ,  $K_1$ , and  $K_2$  that describe the relative contributions of these functions are obtained with a least square fit on the observations.  $F_1$  and  $F_2$  are normalized to be zero for  $\theta_s = \theta_v = 0$  so that  $K_0$  is the estimated reflectance for nadir viewing when the Sun is at the zenith. We tried many different definitions for the  $F_1$  and  $F_2$  functions using simple trigonometric functions. The best results (that is the largest mean correlation between model and observation) were obtained with the following definitions:

$$F_1 = 1 - \cos \theta_v \cos \theta_s, \quad (3)$$

$$F_2 = (\text{MIN}(0, \cos \Theta))^2 - 1. \quad (4)$$

Although very simple, these functions comply with the following requirements:

- They are bounded and continuous.
- They follow the principle of reciprocity.
- They are symmetrical over the principal plane.

We present in Table 6 the model result for the targets observed from more than 20 direc-

tions. The number of observations, the three parameters  $K_0$ ,  $K_1$ , and  $K_2$ , are given together with the observation standard deviation, the RMS (root mean square) difference after the fit and the correlation between the observations and the model. For each target, the first line is for 850 nm measurements, the second for 650 nm, and the third for 550 nm. The surfaces that have been selected and whose directional reflectances are presented on Figure 11 are numbers 11 (wheat), 12 (grassland), 13 (brushwood), 14 (orchard), 15 (barren), and 28 (urban).

$K_0$  is the model prediction for the target reflectance with nadir solar and viewing conditions. It indicates the observed reflectance magnitude and, therefore, shows the spectral signature of the target.  $K_0$  values are a good indication of the target vegetation coverage: The highest values at  $\lambda = 850$  nm are obtained with grassland-type cover. These targets are also the only ones to give a  $K_0$  at  $\lambda = 550$  nm larger than that at  $\lambda = 650$  nm, which is expected for the vegetation because of the larger chlorophyll absorption at  $\lambda = 650$  nm. "Pebble," "barren," "steppe," and "urban," because of their low vegetation coverage, show relatively large reflectances in the visible channels. The negative values obtained with target #20 indicate a defective interpolation. Further examination of this target shows that it was only observed from large viewing or solar angles. Nadir observation was therefore poorly constrained. Similar arguments are given for target #32, which shows a very low  $K_0$  at the 850 nm wavelength.

The observation standard deviation  $\sigma_{\text{obs}}$  is generally on the order of 10–20% of  $K_0$ . It is difficult to assess from these figures which surfaces exhibit the largest bidirectional effects since i) the noise contributes to the standard deviation and ii) the observations may not be distributed equally over the angles.

The ratio  $K_1/K_0$  quantifies the target darkening to the nadir viewing. Apart from target #20 whose unusual results are explained above, only one slightly negative value is found for the  $K_1/K_0$  ratio. All surfaces investigated here present, therefore, a tendency to limb brightening. The order of magnitude for the  $K_1/K_0$  ratio is 1, but no clear pattern can be found from the retrieved values.

The ratio  $K_2/K_0$  quantifies the reflectance maximum in the Sun direction, mostly due to

shadowing effects. At  $\lambda = 850$  nm,  $K_2$  values are always positive, which confirms the qualitative observations from Figure 11 for six particular surfaces. The ratio  $K_2/K_0$  is on the order of 0.3, which corresponds to a 30% reflectance relative variation. At both other wavelengths, the ratio  $K_2/K_0$  extends over a broader range. We speculated from Figure 11 that, at the 550 nm wavelength, the reflectance azimuth dependence results from the competition of shadowing effects and specular reflection. The former yields a maximum in the backward hemisphere and is modeled with  $F_2$ , but the latter, which results in a maximum in the forward hemisphere, is not parameterized. The relatively large reflectances in the forward hemisphere leads to negative values for  $K_2$ . As for  $K_1$ , no surface type dependent pattern is clearly depicted.

The RMS difference and the determination coefficient quantify the model ability to reproduce the measured reflectance directional dependence. At  $\lambda = 850$  nm, the model explains about half of the observed reflectance variability and leads to determination coefficients ( $R^2$ ) in the 0.7–0.9 range. For both other wavelengths, the reflectance range is lower which leads to a lower signal to noise ratio. The measurement standard deviation is generally slightly over 1%, and the residual error after the model fit is on the order of 0.8%. This results in a determination coefficient on the order of 0.5.

We also tried to fit the model of Roujean et al. (1991) and that of Verstraete et al. (1990) to our data. We found correlations that are of the same order as that obtained above, and no model performed significantly better than another. It is clear that a meaningful evaluation of the various physically based models can only be done with a less noisy dataset. This should be possible using forthcoming POLDER observations obtained with an improved registration system.

## SUMMARY AND CONCLUSION

This article presents the first results of the POLDER instrument that was flown for the first time in June 1990 over the "La Crau" site, in southern France. The instrument provides polarized reflectance measurements. For most vegetation coverage and observation conditions, land surface

reflectances are little polarized. It has been expected, therefore, that the polarization could help to distinguish, over land, the surface and atmospheric contributions to the reflectance. Over the nonhomogeneous surface coverage of the La Crau site, the *total* reflectance showed large variations associated with different vegetation coverages whereas the *polarized* reflectance was relatively smooth. The main polarized reflectance variations were associated with the viewing zenith angle (atmospheric path) and the scattering angle (phase function). The surface relative contribution to the polarized reflectance is the smallest for the shorter wavelength (550 nm). At this wavelength, the aerosol and molecules contribution to the reflectance is the largest, and the surface reflectance of vegetated areas is very small. Some surface contribution to the polarized reflectance was noticeable at the longest wavelength (850 nm). This contribution was too small and noisy, however, to be quantitatively usable with POLDER measurements acquired during the "La Crau" experiment. Some improvements are expected with forthcoming POLDER airborne campaign and spaceborne observation.

During the experiment, surface-based radiometers performed atmospheric optical measurements. These included the spectral aerosol optical thickness, the aerosol phase function for scattering angles between  $5^\circ$  and  $150^\circ$ , and the aerosol phase function in the forward peak. These measurements were used to derive an estimate of the aerosol refractive index and size distribution. The corresponding aerosol model was then used in a radiative transfer scheme to simulate POLDER polarized measurements. The agreement was good for the 550 nm and 650 nm wavelengths but the measurements were systematically larger than the model estimates for the 850 nm wavelength. These results indicate, as was inferred from POLDER image analysis, that the surface contribution to the polarized reflectance could be neglected at the shorter wavelengths, but not so in the near infrared.

The POLDER instrument allows multidirectional reflectance measurements. During the flight, a surface target bidirectional reflectance, therefore, could be sampled for various viewing angles ( $\theta_s \leq 60^\circ$ ). Owing to the flight plan design, the reflectance of investigated targets were sampled for up to 70 directions distributed in the bidirec-

tional diagram. We investigated the surface reflectance angular variations for various surface coverages. The main variations were: i) a limb brightening owing to an increased contribution of the vegetation upper layers; ii) a larger reflectance in the backscattering direction which results from intershadowing; iii) a local maximum in the forward direction for the shorter wavelengths, indicating specular reflection on the leaves. Because of the measurement positioning uncertainties, some noise was also clearly noticeable on the bidirectional reflectance sampling.

A very simple geometrical model was proposed to quantify the main reflectance angular variations. This model described the angular reflectance as a linear combination of an isotropic term, a function accounting for the limb brightening and a function that described the backscattering maximum. This very simple model was able to reproduce part of the observed reflectance angular variations. The relative importance of the three terms depended on the surface coverage and the wavelength. They could be used for a surface coverage discrimination that accounts for the reflectance spectral and angular signatures. In the present dataset, although the spectral signature was meaningful, the noise was too large to allow a discrimination based on the reflectance angular variation.

The first POLDER campaign has shown this radiometer capabilities for surface and atmospheric remote sensing over land. It also showed a few defects in the campaign design that will be corrected in future experiments. These are mostly related to the necessity for a very accurate ( $\approx 1$  pixel) positioning of POLDER measurements. Improvement is expected with the installation of a Global Positioning System (GPS) onboard the aircraft. Also recommended is a slight change in the POLDER design (rotation of the matrix) so that the angular viewing capabilities of POLDER are extended to  $\pm 51^\circ$  for the subtrace pixels. Further results will be presented in forthcoming papers.

---

*Funding assistance was provided by the Centre National d'Études Spatiales (CNES) and the Programme National de Télédétection Spatiale (PNTS). We are grateful to C. Verwaerde and J.Y. Balois for their excellent work in the assembling of the POLDER instrument and to L. Gonzales and F. Lemire for the processing of POLDER data. Thanks are due to S. De Brisis, H. Lagrange, S. Louahala, and P. Loudjani, the team*

of students who performed the land surface survey and to the Institut Géographique National (IGN), which allowed the flight on the ARAT.

## REFERENCES

- Coulson, K. L., Gray, E. L., and Bourgeois, G. M. (1965), Study of the reflection and polarization characteristics of selected natural and artificial surfaces, Ct N123 (60530) 51172A, Technical Information Service, Space Science Laboratory.
- Curran, P. J. (1982), Polarized visible light as an aid to vegetation classification, *Remote Sens. Environ.* 12:491-499.
- Deering, D. W., Eck, T. F., and Otterman, J. (1987), Bidirectional reflectances of selected desert surfaces and their three-parameter soil characterization, *Agric. Forest Meteorol.* 52:71-93.
- Deschamps, P. Y., Herman, M., Podaire, A., Leroy, M., Laporte, M., and Vermande, P. (1990), A spatial instrument for the observation of polarization and bidirectionality of the Earth reflectances: POLDER, in *Remote Sensing for the Nineties, IGARSS 90*, Washington, DC, Conference Proceedings, Vol. III, pp. 1769-1774.
- Deuzé, J. L., Herman, M., and Santer, R. (1989a), Fourier series expansion of the transfer equation in the atmosphere-ocean system, *J. Quant. Spectrosc. Radiat. Transfer* 41(6):483-494.
- Deuzé, J. L., Devaux, C., Herman, M., et al. (1989b), Photopolarimetric observations of aerosols and clouds from balloon, *Remote Sens. Environ.* 28:93-109.
- Devaux, C., Herman, M., Santer, R., and Tanré, D. (1989), On the complementarity of solar transmission and aureole measurements to derive the aerosol size distribution: application to desert aerosol characteristic retrieval, in *Proceedings of the International Radiative Symposium: Current problems in the Atmospheric Radiation 1988*, Lille, France, A. Deepak, pp. 557-560.
- Fen, R. W., Clough, S. A., Gallery, W. O., et al. (1985), Optical and infrared properties of the atmosphere, *Handbook Geophys.* 18(9):18-25.
- Gutman, G. (1987), The derivation of vegetation indices from AVHRR data, *Int. J. Remote Sens.* 8:1235-1243.
- Hansen, J. E., and Hovenier, J. W. (1974), Interpretation of the polarization of Venus, *J. Atmos. Sci.* 31:1137-1160.
- Hapke, B. (1981), Bidirectional reflectance spectroscopy. 1. Theory, *J. Geophys. Res.* 86(B4):3039-3054.
- Hapke, B. (1986), Bidirectional reflectance spectroscopy. 4. The extinction coefficient and the opposition effect, *Icarus* 67:264-280.
- Herman, M., Balois, J. Y., Bréon, F. M., et al. (1992), The airborne version of the POLDER instrument. Description, calibration plan and data processing, forthcoming.
- Holben, B. N., Kimes, D., and Fraser, R. S. (1986), Directional reflectance response in AVHRR red and near infrared bands for three cover types and varying atmospheric conditions, *Remote Sens. Environ.* 19:213-236.
- Kimes, D. S. (1983), Dynamics of directional reflectance factor distributions for vegetation canopies, *Appl. Opt.* 22:1364-1372.
- Kimes, D. S., Newcombe, W. W., Tucker, C. J., Zonneveld, I. S., Van Wijngaarden, W., and De Leeuw, J. (1985), Directional reflectance factor distributions for cover types of Northern Africa, *Remote Sens. Environ.* 18:1-19.
- Kriebel, K. T. (1978), Measured spectral directional reflection properties for four vegetated surfaces, *Appl. Opt.* 17:253-259.
- Otterman, J., and Weiss, G. H. (1984), Reflection from a field of randomly located vertical protrusions, *Appl. Opt.* 23(12):1931-1936.
- Pinty, B., Verstraete, M. M., and Dickinson, R. E. (1989), A physical model for predicting bidirectional reflectances over bare soil, *Remote Sens. Environ.* 27:273-288.
- Roujean, J. L., Leroy, M., and Deschamps, P. Y. (1991), A bidirectional reflectance model of the Earth surface for the correction of remote sensing data, *J. Geophys. Res.*, forthcoming.
- Santer, R. (1984), Caractérisation des aérosols à partir de la polarisation du rayonnement solaire diffusé. Application aux atmosphères de la Terre, de Vénus, et de Saturne, Thèse, Université de Lille, France.
- Santer, R., Deuzé, J. L., Devaux, C., et al. (1991), In-flight calibration of SPOT1-HRV over La Crau, *Remote Sens. Environ.*, forthcoming.
- Soufflet, V., Tanré, D., Begue, A., Podaire, A., and Deschamps, P. Y. (1991), Atmospheric effects on NOAA AVHRR data over Sahelian regions, *Int. J. Remote Sens.* 12:1189-1203.
- Tanré, D., Holben, B. N., and Kaufman, Y. J. (1992), Atmospheric correction algorithm for NOAA-AVHRR products: theory and application, *IEEE Trans. Geosci. Remote Sens.*, forthcoming.
- Taylor, V. R., and Stowe, L. L. (1984), Reflectance characteristics of uniform Earth and cloud surface derived from Nimbus-7 ERB, *J. Geophys. Res.* 89:4987-4996.
- Vanderbilt, V. C., and Grant, L. (1985), Plant canopy specular reflectance model, *IEEE Trans. Geosci. Remote Sens.* 23:722-730.
- Vanderbilt, V. C., Grant, L., Biehl, L. L., and Robinson, B. F. (1985), Specular, diffuse and polarized light scattered by wheat canopies, *Appl. Opt.* 24:2408-2418.
- Verstraete, M. M., Pinty, B., and Dickinson, R. E. (1990), A physical model for predicting the bidirectional reflectance of vegetation canopies. 1. Theory, *J. Geophys. Res.* 95(D8):11755-11765.

1

# ANALYSIS OF THE POLDER AIRBORNE INSTRUMENT OBSERVATIONS OVER CLOUD COVERS.

Goloub,P., J.L.Deuzé, M.Herman, Y.Fouquart, P.Y.Deschamps

*Laboratoire d'Optique Atmosphérique*

*URA CNRS 713*

*Université des Sciences et Technologies de Lille.*

*U.F.R. de Physique.*

*59655 Villeneuve d'Ascq Cedex. France.*

## **Abstract:**

The POLDER instrument is designed to provide wide field of view bidimensional images in polarized light. During campaigns of the airborne version of the instrument, images of homogeneous cloud fields were acquired in polarized bands centered at 450 and 850 nm. The polarization of these images is analyzed. The bidirectional polarization distribution function measured in the 850 nm band is shown to make evident the liquid phase of the cloud droplets, by the large characteristic polarization of the cloudbows detected in backward scattering directions. The sensitivity of this feature to cloud parameters is discussed. On the contrary, for observation directions at about  $90^{\circ}$ - $100^{\circ}$  from the Sun, the cloud polarization is negligible. In these directions, the polarized light observed in the 450 nm band is characteristic of the molecular scattering above the cloud, which allows to derive the cloud top altitude. The feasibility of the method is analyzed and is tested on cloud pictures acquired at different altitudes above cloud fields.

## **1.INTRODUCTION**

The POLDER instrument is a radiometer designed to measure the directionality and polarization of the sunlight scattered by the ground-atmosphere system (Deschamps et al., 1992). The instrument concept consists in imaging bidimensional pictures of the site on a CCD detector matrix, through a wide field of view telecentric optics. A given ground pixel thus may be observed with different viewing angles in consecutive pictures acquired while the sensor overflows the experimental site. The spectral analysis of the

radiance is provided by a filter wheel. In some spectral bands, 3 filters are equipped with analysors rotated by  $60^\circ$  and the polarization is deduced from combination of the 3 images.

The scientific objectives of the experiment concern remote sensing of aerosols, ocean color and vegetation monitorings and estimate of the cloud impact on the terrestrial shortwave radiative budget (Bréon et al, 1993). Concerning clouds, observation of the bidirectional reflectance distribution function (BRDF) should provide better estimate of their radiative impact and better understanding of their radiative properties as a function of their morphology. Polarization measurements are expected to be useful for cloud altimetry, by the way of the molecular scattering as the barometric signal, and for determination of the cloud phase, ice or liquid, by the way of the cloud particle polarization signature.

POLDER, that has been selected on the Japanese ADEOS payload, is now in phase C study by the Centre National d'Etudes Spatiales (CNES). For preparatory studies, an airborne simulator of the instrument has been developed and experimental campaigns have been conducted. Cloud fields were observed occasionally. The purpose of this paper is to describe the polarization measurements performed over these cloud covers and to investigate the interest of polarization for cloud studies.

## 2. PRINCIPLE

The interest of polarized measurements for cloud studies has been outlined long ago, and airborne or balloon-borne experiments were flown to test this possibility (see e.g. Coffeen and Hansen, 1972; Deuzé et al., 1989). Polarization, however, is really informative when obtained for different viewing conditions. Because these previous experiments consisted in cloud scannings by narrow field of view polarimeters, they were not easy and practically valid only when performed over horizontally homogeneous cloud fields. The present bidimensional POLDER pictures benefit from the ability to observe any cloud pixel with different viewing conditions, according to the sensor displacement during the successive acquisitions, or to acquire the entire bidirectional reflectance or polarization distribution functions (BRDF or BPDF) from one single picture when overflowing homogeneous cloud fields.

Polarization measurements from space, at short wavelengths (say,  $\lambda < 500$  nm), are expected to provide cloud altimetry by the way of molecular scattering. At these wavelengths and for observation conditions corresponding to scattering angles near from  $\Theta = 90^\circ$ , molecules are very efficient for scattering polarized light. Then, considering that the ground and most of the aerosols are screened by the cloud, when neglecting the cloud contribution, the amount of polarized light should yield the optical thickness of the atmosphere above the cloud, i.e. the cloud top altitude. Of course, multi-band observations are preferable. Because of the  $\lambda^{-4}$  dependence of the Rayleigh scattering, near infrared observations (say  $\lambda > 850$  nm) should give the cloud contribution and allow correction of the shortwave data.

Identification of the phase (solid or liquid) of the cloud particles is expected from the angular polarization signature of clouds as measured at near infrared wavelengths. Liquid cloud droplets are known to exhibit a characteristic polarization feature with a large maximum in the range of the rainbow, i.e. for scattering angles near from  $140^\circ$ . The polarization by scattering of ice crystals is more speculative, because the geometry of these particles is probably variable. However, the scattering laws of crystalline particles have been studied for a lot of geometries: cylinders, hexagonal plates or prisms (see e.g. Cai and Liou, 1982; Takano and Jayaweera, 1985; De Haan, 1987; Brogniez, 1992). The predicted polarization diagrams depend on the assumed geometry, but a very general feature is the suppression of the characteristic rainbow maximum for particles departing from spherical geometry.

Within our present knowledge, therefore, mere polarization signatures probably cannot allow direct identification of ice clouds. But the POLDER experiment intends to derive cloud altimetry also by the way of differential absorption measurements in the oxygen band. Combined  $O_2$  altimetry and polarization observation are expected to provide better understanding of ice cloud polarization properties and, finally, to help for discriminating between liquid and ice clouds.

The measurements here reported do not allow to test all of these possibilities. No cirrus clouds were present, or detectable because of the aircraft maximum altitude, so that we were unable to confirm

differences in polarization signatures of liquid and solid cloud particles. Moreover, because the POLDER airborne simulator has only 10 filters instead of the 15 ones planned in the satellite version, simultaneous observations of clouds in polarized light and in the oxygen band were not acquired. These preliminary results, however, prove the possibility to estimate grossly the cloud altitude from Rayleigh scattering barometry and confirm the possibility to identify liquid cloud droplets from the rainbow polarization.

### 3. DESCRIPTION OF THE DATA

#### 3.1 Experimental campaigns

The present cloud observations were obtained occasionally during the various campaigns of the POLDER airborne simulator.

POLDER was first flown aboard the French Avion de Recherches ATmospheriques (ARAT) for campaigns devoted to land surfaces observations, in the Southern of France during the Summer of 1990 (La CRAU and LANDES 90 campaigns) and for a campaign devoted to the ocean color, over the Mediteranean sea in the Summer of 1991 (MEDIMAR campaign). Then, it was flown aboard the Falcon of DLR for a campaign specifically designed to cloud observations, over the Alpes in late 1991 (CLEOPATRA campaign). Finally, POLDER was flown again aboard the ARAT, over the Atlantic Ocean, during the ASTEX-SOFIA campaign in the Summer of 1992. Table 1 sums up some characteristic points concerning these different acquisitions.

#### 3.2 Flight conditions. BRDF acquisitions

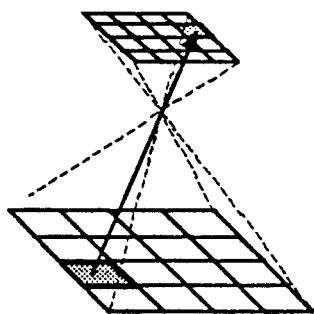


Figure 1a

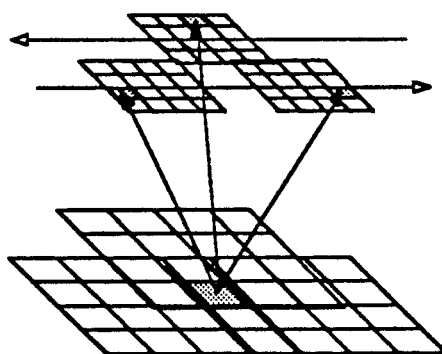


Figure 1b

The POLDER instrument includes a matrix array CCD of 288x384 detectors with dimensions 23x23  $\mu\text{m}$ , in the focal plane of a wide field of view optics with 3.565 mm focal length. This provides an angular coverage with viewing angles  $\theta_v$  of  $\pm 42^\circ$  in the along track direction and  $\pm 51^\circ$  in the crosstrack direction, or inversely depending of the matrix orientation with respect to the aircraft (Fig.1a). For a flight altitude of 5000 m above the ground or the cloud top, for example, the foot print is approximately 9.3x12.3 km and the resulting image is partitioned in 288x384 identical ground or cloud pixels with 32x32 m dimensions.

During the aircraft displacement, the radiance from a given ground or cloud pixel is measured for different viewing angles. For land observations, the flight plans consisted in successive parallel runs (Fig.1b), which allowed to sample the BRDF and BPDF of each ground pixel. For the cloud observations here reported, because of the expected changes in the cloud structure between successive runs, we only flown simple runs over the cloud cover, at nearly constant altitudes (from 3500 to 6000 m with the ARAT, until 11000 m for the Falcon) that are reported in Table 1. In one occasion, during CLEOPATRA, the same extended cloud was overflown by the Falcon at different altitudes.

Given these conditions, we will mainly deserve our analysis to the average gross features of the BPDF of cloud scenes that looked rather homogeneous within the POLDER foot print. The average BPDF, then, will be derived from one single picture. The different pictures acquired along the flight run will be used for testing the cloud homogeneity and/or for averaging the cloud properties.

### 3.3 Polarization and spectral analysis

The filter wheel of the airborne simulator has 10 filter positions. One blind position is used for the measurement of the darkness current. The system therefore allows measurements in 3 polarized spectral bands, or in 2 polarized and 3 unpolarized bands, etc.... For cloud studies in polarized light, the best seems to measure polarization in the shortest and largest POLDER wavelength bands, 450 and 850 nm, as it was retained for the CLEOPATRA campaign. The spectral bands and polarization configurations used for the different campaigns are indicated in Table 1.

A measurement sequence consists in these 9 spectral polarized images. They are acquired in 3.7 seconds, which is the period of the filter wheel. The time interval between two consecutive sequences is 11 seconds. During a sequence acquisition, the aircraft displacement is about 370 m, or about 120 m between the images of a polarized band. Within the sequence time interval, variations in the cloud structure are assumed to be negligible. Then, by processing the 9 images, the spectral and polarization properties of the cloud cover may be retrieved.

### 3.4 Data processing

Because most clouds exhibit significant structure variations at 100 m scale lengths, polarization and multi-spectral measurements necessitate correct image registration.

For land observations, an efficient processing of the POLDER data has been elaborated (Deuzé et al., 1992). However, registration of the data within a 1 pixel accuracy needs that the POLDER attitude with respect to the aircraft inertial system should be estimated, from known landmarks selected in the pictures. As this is not possible over cloud fields, the data processing of cloudy scenes was simplified as follows.

1-The raw data in the 9 channels of each sequence were first corrected from dark current and from the optics transfer function. For unpolarized spectral bands, within the appropriate calibration factor, this correction step provides directly the radiance or the reflectance in entrance of the instrument.

2-In the polarized bands, the 3 images were then corrected for the aircraft translation. Change in the aircraft attitude was neglected and the images were just translated, within 1 pixel, in order to minimize the contrasts between the 3 images.

3-To smooth the residual registration errors, the results were averaged within a 5x5 pixel window.

4-Finally, the entrance radiance and polarization were deduced from the averaged data.

As confirmed by simulations and observations over terrestrial targets, we consider that the light is linearly polarized. The entrance radiance is then given by  $(L_1+L_2+L_3)/3$  where  $L_i$  ( $i=1,2,3$ ) are the 3 polarized measurements corresponding to the same ground pixel, as obtained after the previous step 2, and the

entrance polarized radiance (i.e. the polarized part of the radiance), by  $(\sum_i 2(L_i - L_{i+1})^2/9)^{1/2}$ ; the direction of the polarized vibration (say, the angle  $\xi$  between the polarized vibration and some convenient reference) may be deduced too from the  $L_i$ . The calibration factor is such that the results reported here are expressed in terms of normalized radiances,  $\rho$ , and normalized polarized radiances,  $\rho_P$ , as:

$$\rho = \pi L / (\cos\theta_s E_s) \quad \rho_P = \pi L_P / (\cos\theta_s E_s) \quad (1)$$

where  $L$  is the radiance,  $\theta_s$  the solar zenith angle and  $E_s$  the solar irradiance at the top of the atmosphere. The degree of linear polarization is defined as

$$P = \rho_P / \rho$$

Note that the characterization of the polarized light is provided by  $(\rho, \rho_P, \xi)$ , or, equivalently, by its Stokes parameters  $(\rho, \rho_Q, \rho_U)$ , with

$$\rho_Q = \rho_P \cos 2\xi ; \quad \rho_U = \rho_P \sin 2\xi . \quad (2)$$

As an example, Fig. 2 shows a cloud picture acquired on 18/10/91 during the CLEOPATRA campaign, with the aircraft at about 8000 m above the cloud top. Image A shows the measurements in one of the polarized channels of the 850 nm band, i.e. with the best resolution of POLDER, just corrected from the optics transfer function (step 1). Image B shows the total reflectance in the 850 nm band as derived when processing the 3 polarized images as explained previously. We see that the cloud structure is well preserved by the 5x5 pixel smoothing process. The other features are discussed below.

## 4. CLOUD POLARIZATION FEATURES

### 4.1 Qualitative results

Images 2C and 2D show the polarized reflectances measured above the cloud field in the 850 nm and 450 nm bands respectively. We look at the polarized reflectance rather than at the polarization ratio, because the polarized reflectance is known to be formed in the upper cloud layer (Hansen and Travis, 1974) and to be few

sensitive to the cloud optical thickness or to the properties of the underlying ground.

The most significant feature in these images are the highly polarized arches. The flight direction here was nearly parallel to the sun incident plane, with the antispecular direction (i.e. scattering angle  $180^\circ$ , or zero phase angle) near the top of the pictures, and these highly polarized features correspond to viewing directions  $(\theta_v, \phi_v)$  such that the scattering angle  $\Theta$  is near from  $140^\circ$  (i.e.  $\cos \Theta = \cos \theta_s \cos \theta_v + \sin \theta_s \sin \theta_v \cos \phi_v$ ). This is the angular position of the primary rainbow of large spherical particles, which confirms that the cloud particles are large cloud droplets. The same feature was repeatedly observed over all the cloud fields encountered during the campaigns. As examples, Fig.3 shows cloud pictures obtained respectively over a thin stratocumulus, during ASTEX (images A, B, C) and over a much more heterogeneous cloud, during MEDIMAR (images D, E, F); images 3B and 3E display the polarized reflectances in the 850 nm band, images 3C and 3F, in the 450 nm one. The rainbow signature was a permanent characteristic of these low, very probably liquid clouds, and in the case of thin clouds as for image 3F, secondary cloudbows were even discernable for scattering angles larger than  $140^\circ$

In other viewing directions, the polarized reflectance is rather low. Let us restrict for the moment to the 850 nm band that is more convenient for observing the intrinsic cloud polarization since molecular scattering is negligible. The second characteristic observation is that cloud polarization at  $\lambda=850$  nm tends to vanish for scattering angles near from  $100^\circ$ . To make it clearer, for the case of image 2C, the polarized reflectance  $\rho_p$  and the angle  $\xi$  between the polarized vibration and the scattering plane (i.e. the plane formed by the Sun and the viewing directions) have been reported in Fig.4 and 5 respectively, as a function of  $\Theta$ . For clarity, we only considered pixels corresponding to viewing directions within the solar incident plane (i.e., nearly the central column of image 2C). Because of the radiometric noise and the registration errors (see later), zero polarization is not attained, but  $\rho_p$  is minimum near  $\Theta = 90^\circ-100^\circ$ . On the other hand, Fig.5 shows that the polarized vibration is perpendicular to the scattering plane in backward scattering directions, but parallel to the scattering plane in forward

scattering directions; of course, this change in the direction of the electric field goes through zero by continuity.

#### 4.2 Polarization modeling

Quantitative analysis of these results needs numerical simulations of the cloud polarization. In a first approximation, for cloud pictures like that of Fig.2, it seems reasonable to investigate the mean BPDF over the whole POLDER foot print, regardless of small scale features and assuming plane parallel geometry. We therefore simulated POLDER polarization measurements above plane parallel clouds. Calculations were performed with a code, provided by C.E.Siewert (Garcia and Siewert, 1986), of the Generalized Spherical Harmonics Solution (GSHS) of the radiative transfer problem in polarized light (Siewert, 1986).

The polarized reflectance was calculated for different cloud optical thicknesses  $\delta$ , and for different size distribution functions of the cloud droplets,  $n(r)$ . Table 2 indicates the models used in the calculations and the corresponding cloud type, according to Deirmendjian's classification (Deirmendjian, 1969). The corresponding size distributions are shown in Fig.6. Calculations were performed by neglecting molecular scattering above and within the cloud and by assuming zero reflectance of the underlying ground.

The calculations confirm that the polarized light has negligible ellipticity and may be considered as linearly polarized, with direction along the major axis of the ellipse. To state how the polarized reflectance varies according to the cloud properties: (i) Fig. 7 shows how  $\rho_p$  varies as a function of the cloud optical thickness  $\delta$ , for the case of the cloud model C1 (for comparison, Fig.8 shows the behavior of the corresponding total reflectance), (ii) and Fig.9 shows how  $\rho_p$  varies as a function of the cloud model, for a constant cloud optical thickness  $\delta=15$ . The solar zenith angle is  $60^\circ$ . For simplicity, the results are shown for viewing directions within the solar incident plane. They are reported versus  $\Theta$ . Because of the symmetry exhibited by the solar incident plane,  $\xi$  is exactly either  $0^\circ$  or  $90^\circ$ ;  $\rho_p$  has been reported as negative for  $\xi=0^\circ$  and as positive for  $\xi=90^\circ$ .

As suggested previously, Fig.7 shows that, because the polarized light is formed in the very upper cloud layer, the polarized light scattered by the cloud no more depends on the cloud thickness as soon as the optical thickness is larger than 1. Clearly, the total reflectance, and therefore the polarization ratio, are much more dependent on  $\delta$ . Moreover, even for very small cloud depths ( $\delta=0.1$ ), calculations performed with lambertian reflectance of the ground as large as 1 show that  $\rho_p$  is at all modified, which proves that the polarized reflectance gives a specific cloud information whatever the ground underlying properties.

Figure 9 shows that the primary rainbow near  $\Theta=140^\circ$  and the less intense cloudbow near  $175^\circ$  are features that are nearly insensitive to the cloud droplet dimensions. Similarly, all cloud models exhibit zero polarization for scattering angle near from  $100^\circ$ . Only very small size spectrum as corresponding to models C2 and C3 show departures from these characteristics.

### 4.3 Comparison

From such calculations, given the solar zenith angle and the flight direction, polarized POLDER pictures over plane parallel clouds may be simulated.

For the geometric conditions of Fig.2, image 2E shows the synthetic POLDER picture in polarized light obtained by this way, when assuming a cloud model C1 with an optical thickness  $\delta=15$ . The corresponding values of  $\rho_p$  and  $\xi$  for viewing directions in the solar incident plane have been reported as continuous curves in Figs. 4 and 5. Finally, to compare the results over the entire POLDER picture, we just plotted, in Figs.10 and 11 respectively, the observed and the simulated polarized reflectances for all the pixels of the image, as a function of the corresponding scattering angle  $\Theta$ .

Figure 11 shows that this representation is specially convenient. Moreover, we reported in Fig.11 calculations of  $\rho_p$  for the same cloud, but for different solar zenith angles. It is noteworthy that the entire bidirectional polarized reflectance distribution function of a plane parallel cloud may practically be displayed by a simple bidimensional plot, as a function of the scattering angle  $\Theta$ . This comes from the fact that polarized light is mainly formed by the

single scattering process. In this approximation, for sufficient optical thickness of the layer, we have

$$\rho_P = \frac{p(\Theta)P(\Theta)\cos\theta_s}{4(\cos\theta_s + \cos\theta_v)} \quad (3)$$

where  $p(\Theta)$  and  $P(\Theta)$  are the phase function and polarization ratio for single scattering of the cloud particles, which shows that the polarized light is mainly governed by  $\Theta$ . The large influence of single scattering explains also that calculated values of  $\xi$  (not presented here) are always near from  $0^\circ$  or  $90^\circ$ , since single scattering by spherical particles gives polarization either parallel or perpendicular to the scattering plane.

The reasonable agreement between the histograms of Figs.10 and 11 confirms that POLDER polarized measurements allowed to evidence particles with dimensions typical of liquid cloud droplets. In some conditions, the measurements displayed clearly secondary cloudbows that could correspond to smaller cloud droplets in the uppermost entrainment layer of the cloud. Despite the large dispersion of the results, the observations confirm also that most clouds exhibit, near  $90^\circ$ - $100^\circ$  scattering angle, negligible polarization, which may be useful for the purpose of estimating the cloud top pressure as will be seen now.

## 5 CLOUD ALTIMETRY FROM RAYLEIGH SCATTERING

### 5.1. Multi-band polarization observations

Let us then consider the spectral aspect of polarization measurements over cloud fields. We will limit to pictures acquired during the CLEOPATRA campaign, on account of the reasonable altitude above the clouds allowed by the Falcon of DLR, thus providing sufficient effect of the molecular scattering layer between the cloud and the aircraft.

As shown previously (images 2C and 2D in Fig.2, for example) the rainbow features are very similar in the 450 and 850 nm spectral bands of POLDER, but in other viewing directions, specially around  $\Theta=90^\circ$ , the polarized reflectance is clearly larger at 450 nm than 850 nm. This effect is present in all sequences of all flights. It results from the increasing influence of the intervening molecular

layer at shorter wavelengths. Of course, nothing similar do appear in the reflectance images where the spectral effect varies largely as a function of the underlying ground properties.

On 21/10/91, because of the large extension of the cloud field, the Falcon was able to overflow the cloud at different altitudes, including a first run near the top, at about 3.5 km. Figure 12 shows histograms of  $\rho_p$  vs  $\Theta$  in the 450 nm channel, derived from 3 pictures obtained at about 3.5 km (cloud top), 7.3 km and 11.3 km, with mean solar zenith angle  $\theta_s=60^\circ$ . For clarity, the histograms have been restricted to pixels near from the solar incident plane. Within the range of scattering angles  $80^\circ-100^\circ$ , where polarization by molecular scattering is large, the polarized reflectance increases with the aircraft altitude, i.e. with the thickness of the intervening molecular atmosphere. By contrast, the polarized reflectance at 850 nm is practically unchanged, in accordance with the  $\lambda^{-4}$  dependence of the molecular scattering efficiency. These observations confirm that differences in the polarized reflectance observed at 450 and 850 nm above clouds mainly correspond to molecular scattering, from which the cloud top altitude could be estimated.

To test this possibility, let us consider that the polarized light measured at 450 nm around  $\Theta=90^\circ$  corresponds only to light scattered by the molecular layer, on account of the negligible contribution of the cloud in this direction. Let  $\Delta\delta_m(\lambda)$  be the optical thickness of the molecular layer; because  $\Delta\delta_m(\lambda)$  is small, single scattering approximation of  $\rho_p$ , or  $\rho_{m,p}$ , is valid and

$$\rho_{m,p}(\lambda) = \Delta\delta_m(\lambda) \frac{P_m(\Theta)P_m(\Theta)}{4\cos\theta_v\cos\theta_s} = \frac{3\Delta\delta_m(\lambda)}{16\cos\theta_s\cos\theta_v} (1 - \cos^2\Theta) \quad (4)$$

When reporting in eq(4), in place of  $\rho_{m,p}$ , the mean polarized reflectances measured around  $\Theta=90^\circ$  in Fig.12, the derived estimates of  $\Delta\delta_m$  are respectively  $\Delta\delta_m=0.071$  for  $z_A=7.3$  km and  $\Delta\delta_m=0.098$  for  $z_A=11.3$  km. On the other hand, given the altitudes of the cloud top and of the aircraft,  $z_C$  and  $z_A$ , the expected figures are about

$$\Delta\delta_m = \delta_{0,m} (\exp(-z_C/H) - \exp(-z_A/H)) \quad (5)$$

where  $\delta_{0,m}$  is the total optical thickness of the standard molecular atmosphere and  $H$  the atmospheric scale height. With  $H=8$  km and  $\delta_{0,m}=0.216$  at  $\lambda=450$  nm, eq.(5) gives  $\Delta\delta_m=0.053$  for  $z_A=7.3$  km and  $\Delta\delta_m=0.087$  for  $z_A=11.3$  km, which is not bad, respectively about 35 % and 10 % lower than the polarimetric estimates.

To extend the method to observation directions other than  $90^\circ$ - which is important for enlarging the applicability of the method in satellite pictures- we have to take into account the cloud contribution in the polarized light. Let us assume that the polarized light reflected by the cloud do not depend on the wavelength, because of the large dimension of the cloud droplets, and that the light resulting from multiple interactions between the cloud and the molecular layer exhibits negligible polarization. The expected polarized reflectance then will be

$$\hat{\rho}_P(\lambda) = \hat{\rho}_{m,P}(\lambda) + \exp\left(-\frac{\delta_m(\lambda)}{\cos\theta_s} - \frac{\Delta\delta_m(\lambda)}{\cos\theta_v}\right) \hat{\rho}_{c,P} \quad (6)$$

where  $\delta_m$  is the optical thickness of all molecules above the cloud and  $\rho_{c,P}$  stands for the polarized light at the top of the cloud when directly illuminated by the solar beam; the exponential term accounts for the attenuation by the overlying molecular layer. Note that eq.(6) is written in terms of the reduced 2 terms Stokes' matrices  $\rho = (\rho_Q, \rho_U)$  which are additive, while the simple absolute polarized reflectances may not be, when for example the molecular and cloud components are polarized at right angles.

To simplify eq(6), as  $\delta_m$  and  $\rho_{m,P}$  are negligible at  $\lambda=850$  nm, let us consider that  $\rho_P(\lambda=850)$  provides directly  $\rho_{c,P}$ , and let us neglect the transmission effect. Then, eq.(6) gives

$$\hat{\rho}_P(\lambda = 450\text{nm}) - \hat{\rho}_P(\lambda = 850\text{nm}) \approx \hat{\rho}_{m,P}(\lambda = 450\text{nm}) \quad (7)$$

We note that molecular scattering gives polarization perpendicular to the scattering plane, i.e.  $\xi_m=90^\circ$  or  $\rho_{m,U}=0$  (cf. eq.(2)). The  $\rho_Q$  term of eq(7), therefore, has only to be considered; it provides all the polarized reflectance  $\rho_P$ , so that according to eq(4) it comes

$$\Delta\delta_m(\lambda = 450\text{nm}) = \frac{16\cos\theta_s\cos\theta_v}{3(1-\cos^2\Theta)} \left\{ \left[ \cos 2\xi \cdot \rho_P \right]_{(\lambda=450\text{nm})} - \left[ \cos 2\xi \cdot \rho_P \right]_{(\lambda=850\text{nm})} \right\} \quad (8)$$

from which  $\Delta\delta_m$  and the cloud top altitude may be derived.

To assess the validity of these approximations, the POLDER measurements at 450 and 850 nm were simulated by the GSHS code, by taking into account the molecular scattering at 850 nm, the multiple scattering within the free atmosphere and within the cloud and the spectral variation of the cloud droplet scattering, as derived from Mie theory. We only neglected the influence of molecules mixed with cloud droplets, i.e. we considered an homogeneous cloud; this seems correct since the effective cloud optical depth which the polarized light comes from,  $\delta \approx 2$ , should correspond only to 40 m for a typical cloud scattering coefficient  $50 \text{ km}^{-1}$ .

The calculations were made for different cloud models and for different pressures of the cloud top within a standard atmosphere. We considered satellite measurements (i.e.  $\Delta\delta_m = \delta_m$ ). The cloud optical thickness and the solar zenith angle were fixed ( $\delta=15$  at 850 nm,  $\theta_s=60^\circ$ ) and the measurements were simulated for viewing directions within the whole POLDER pictures. They were reported in eq.(8) and the derived  $\delta_m$  were converted in cloud top pressures.

The results are shown in Fig.13 as a function of the scattering angle; we restricted to  $\Theta$  ranging from  $80^\circ$  to  $100^\circ$  where the molecular polarization is large enough in front of the cloud one. Some improvements (systematic correction of  $\rho_{m,P}$  for multiple molecular scattering and iteration between eqs.(6) and (8) to take into account transmission effect) could reduce the dispersion, but the principal limitation is probably the spectral variation of the cloud polarization, which entails increasing errors in backward scattering directions, for all cloud models, and, in the case of very small particles (C3), systematic error in all observation directions. Figure 13 shows that the crude approximate eq(8) gives, however, correct results with pressure errors no more than 20 hPa for most cloud models; the systematic error increases to 50 hPa for the very small particles of model C3.

The method was then applied to CLEOPATRA images. In order to minimize possible errors due to small scale variations in  $\rho_{c,p}$ , the POLDER pictures in the 2 channels were translated to be superposed; the resulting variation of  $\Theta$ , for the same cloud pixel as seen in the two channels, is negligible. The  $\Delta\delta_m(\lambda=450\text{nm})$  derived from eq.(8) were converted in pressure differences  $\Delta P$  between the aircraft and the cloud top, according to

$$\Delta P = P_C - P_A = P_0 \cdot \Delta\delta_m / \delta_{0,m} \quad (9)$$

where  $P_0$  is the standard pressure at sea level.

As an example, Fig. 14 shows the results for the case of the CLEOPATRA picture of Fig.2. The continuous curve shows the average result and we indicated the expected pressure difference, according to the altitudes  $z_C$  and  $z_A$ . Figure 14 is representative of the scatter in the  $\Delta P$  estimates obtained in all the pictures that we analyzed. In the case of the cloud picture of Fig.12, we only reported in Fig.15 the average estimates, as a function of  $\Theta$ , for 3 altitudes of the aircraft.

Polarization provides the correct order of magnitude and Figs.14 and 15 suggest that cloud altimetry derived by this way could be valid. There is, however, a large dispersion in the estimates and some apparent systematic discrepancy as a function of the viewing direction.

## 5.2. Discussion

The scatter in the results of Fig.14 comes partly from the simplifying assumptions of the method, from probable departures from the assumed plane geometry and maybe from horizontal variations in the particle dimension. According to Fig.13, however, the method error should be quite small, at least for large enough cloud droplet dimensions. On the other hand, Fig.11 shows that polarized light is not sensitive to variations in  $\theta_s$  and  $\theta_v$  so that it is expected that polarized light should not be affected by small departures from plane parallel geometry resulting from the cloud top roughness. It seems therefore very likely that most of the scatter comes from the quality of the measurements, as seen in the histograms of Figs.4 and 12.

The measurement method of polarization in POLDER, by differences between successive images, entails large influence of the radiometric noise and registration errors on the estimated polarized light. It may be shown that the radiometric noise, say  $\Delta\rho$ , leads to a measured polarized reflectance,  $\rho^{\text{est}}_{\text{P}}$ , in the form

$$\left(\rho_{\text{P}}^{\text{est}}\right)^2 = \left(\rho_{\text{P}}\right)^2 + \frac{4}{3}\Delta\rho \cdot \rho_{\text{P}} + \frac{4}{3}(\Delta\rho)^2 \quad (10)$$

The noise equivalent  $\Delta\rho$  of the airborne instrument, however, is only  $5 \cdot 10^{-4}$ , which does not explain the observed dispersion nor the residual polarization, of the order of 0.005, near zero polarization directions. The present principal limitation, therefore, is probably the image superposition, that entails apparent polarization over otherwise unpolarized scene, as soon as the scene exhibits reflectance variations at small scales. This defect ought to be reduced in the satellite version of POLDER, whose the filters will be equipped by prisms for better superposition of the images. This point deserves further study in the airborne version. Improved processing of the data has to be searched for, specially by looking for image registration within better accuracy than the present 1 pixel. Note, however, that during CLEOPATRA condensation occurred on the optics and on the filters, which resulted in small localized defects that could not be corrected by post and pre-flight calibrations. The pictures acquired during the ASTEX campaign prove to exhibit much smaller dispersion; but they were performed from too small altitudes to permit validation of the altimetry method and further study of this point needs principally extended observational data.

In any case, the main dispersion of the data, about 100 hPa in Fig.14, is not too large and encouraging. May be more serious is the second defect in Figs.14 and 15, where the estimated pressure increases systematically for observation directions corresponding to backward scattering. Because the residual aerosol layer, above 3.5 km, is expected to have negligible influence, the only explanation suggested by the present modeling should be the existence of very small cloud droplets in the upper entrainment cloud layer, with spectral dependence no more negligible in eq(6). Indication of such particles might be the secondary cloudbows clearly observed in the ASTEX pictures, but probably discernable also in the CLEOPATRA histograms of Fig.12. Apart from the possible interest of this

detection for cloud studies, this should require that some correction term in eqs.(7) and (8), accounting for the spectral variation of the cloud contribution, be derived from the bidirectional polarization signature at 850 nm. Further analysis of this point needs certainly much better measurements than the present ones.

## 6 CONCLUSION

The POLDER airborne instrument was able to measure in different occasions the bidirectional polarization distribution function of low cloud fields. Over all these clouds, polarized observations made it specially clear the characteristic rainbow of spherical cloud droplets, which is very probably a good indicator of liquid phase. It is noteworthy that the POLDER capability to provide bidimensional pictures makes this feature recognizable whatever the cloud field heterogeneity. Simulations show that the BPDF of homogeneous cloud fields is specially simple in terms of polarized reflectance: quite entirely defined by the only scattering angle and characterized by the polarization of the upper cloud droplets. Position of the cloudbows could give some information about the cloud particle dimension, but this point deserves further study.

The observations confirmed that difference in the polarized reflectance at 450 and 850 nm above clouds mainly corresponds to the residual molecular atmosphere scattering, that may be used as a barometer to estimate the cloud top pressure. Simulations indicate that, because of the small effective cloud depth concerned by the formation of polarized light, the method should lead to a well defined cloud top pressure. The simple scheme proposed for the retrieval of the cloud top pressure should be efficient provided the upper cloud layer is formed of large enough droplets.

The present observations, however, suggest that very small particles near the cloud top might necessitate more elaborate treatment. We no more examined the case of heterogeneous cloud fields, which is clearly a much more complicated problem. Finally, the present lack of cirrus cloud observations prevents definitive conclusion concerning the possibility to identify ice clouds from polarimetry. These important points deserve further studies which require much more complete observations, presently planed in future POLDER campaigns.

**Acknowledgment**

This work was supported by the Centre National d'Etudes Spatiales and by the Centre National de la Recherche Scientifique. The authors are very grateful to Pr. C.Siewert who kindly provided his GSHS code, to F.Parol, Y.Balois and C.Verwaerde who conducted the different campaigns, and to L.Gonzalez and F.Lemire who processed the POLDER data.

## REFERENCES

Bréon, F.M., A.Bricaud, J.C.Buriez, P.Y.Deschamps, J.L.Deuzé, M.Herman, M.Leroy, A.Podaire and G.Sèze, 1992. The POLDER mission: instrument characteristics and scientific objectives. Submitted to IEEE Trans. Geosci. Remote Sensing.

Brognez, G., 1992. Contribution à l'étude des propriétés optiques et radiatives des cirrus. Thèse d'état, Université des Sciences et Technologies de Lille.

Cai, Q. and K.N.Liou, 1982. Polarized light scattering by hexagonal ice crystals: theory. *Ap. Optics*, 21, 3569-3580.

Coffeen, D.L. and J.E.Hansen, 1972. Airborne infrared polarimetry. Proc. of the eighth international symposium of remote sensing of environment. 2-6 Oct. 1972.

Deirmendjian, 1969. Electromagnetic scattering on spherical polydispersions. American Elsevier Publishing Company, Inc New York.

Deschamps, P.Y, M.Herman, A.Podaire, M.Leroy, M.Laporte and P.Vermande, 1990. A spatial instrument for the observation of polarization and directionality of Earth reflectances: POLDER, Proc. IGARSS' 90, Washington D.C., 1990.

De Haan, J., 1987. Effects of aerosols on the brightness and polarization of cloudless planetary atmospheres. Thesis. Free University of Amsterdam. Holland.

Deuzé, J.L., C.Devaux, M.Herman, R.Santer, J.Y.Balois, L.Gonzalez, P.Lecomte and C.Verwaerde, 1989. Photopolarimetric observations of aerosols and clouds from balloon. *Remote sensing of environment*, 29, 93-109.

Deuzé, J.L., F.M.Bréon, J.L.Roujean, P.Y.Deschamps, C.Devaux and M.Herman, 1992. Preliminary results of POLDER overland flights. To appear in *Remote Sensing of Environment*.

Garcia, R.D.M., and C.E.Siewert, 1986. A generalized spherical harmonics solution for radiative transfer models that include polarization effects. *J.Quant.Spec.Rad.Transfer*, 36, p401-423.

Hansen, J.E. and L.D.Travis, 1974. Light scattering in planetary atmospheres. *Space Science Reviews*, 16, 527-610.

Siewert,C.E., 1986, *Astrophysical J.* 245, p1080-1086.

Takano, Y. and K.Jayaweera, 1985. Scattering phase matrix for hexagonal ice crystals computed from ray optics. *Ap. Optics*, 24, 3254-3263.

Campaign	Spectral band	Aircraft	Filght level (km)
CRAU 90	550P, 650P, 850P	ARAT	6 km
MEDIMAR 91	450P,500NP,570NP,670NP,850P	ARAT	4.5 km
CLEOPATRA 91	450P,500NP,570NP,670NP,850P	FALCON	Variable: 0 to 11km
SOPHIA-ASTEX92	450P,763NP,765NP,850P,910NP	ARAT	3.5 km

Table 1 : Some characteristics of the principal POLDER campaigns.  
(P for polarized band and NP for Non Polarized band)

	$\alpha$	b	$\gamma$	a
C1	6.0	1.5	1.0	2.37
C2	8.0	0.0415	3.0	1.08 10 <sup>-2</sup>
C3	8.0	0.333	3.0	5.55
Cumulus	3.0	0.5	1.0	2.604
Altostratus	5.0	1.11	1.0	6.28
Stratocumulus	5.0	0.8	1.0	0.437
Stratus	3.0	0.667	1.0	8.24

Table2 : Size ditribution parameters.

with the size distribution given by  $n(r) = a r^\alpha \exp(-b r^\gamma)$

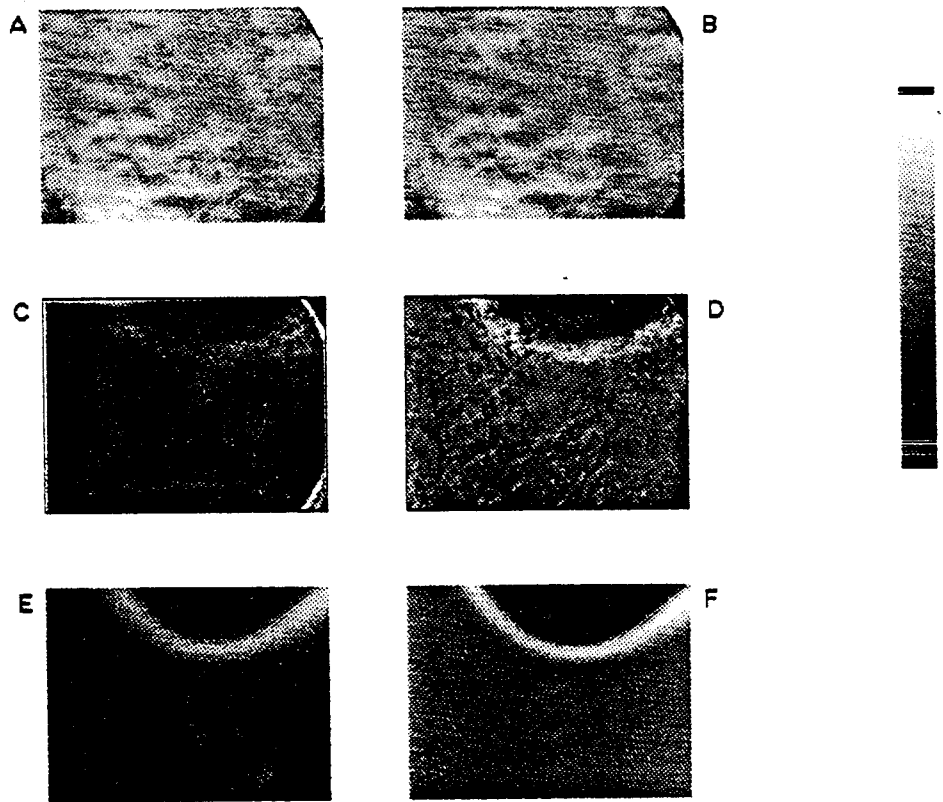


FIGURE 2

Figure 2: POLDER pictures obtained during CLEOPATRA, on 18/10/91, over an extended homogeneous cloud field. Image A shows the observations with full POLDER resolution, in one filter of the 850 nm spectral band. Image B is the reflectance derived from the 3 component images of the 850 nm band, with smoothing processing (see text). The 256 gray levels correspond to reflectances ranging from 0.5 to 1.3 . Images C and D are the polarized reflectances, derived in the 850 and 450 nm bands respectively. Images E and F are synthetic images of C and D respectively, corresponding to plane parallel clouds underlying the molecular atmosphere.

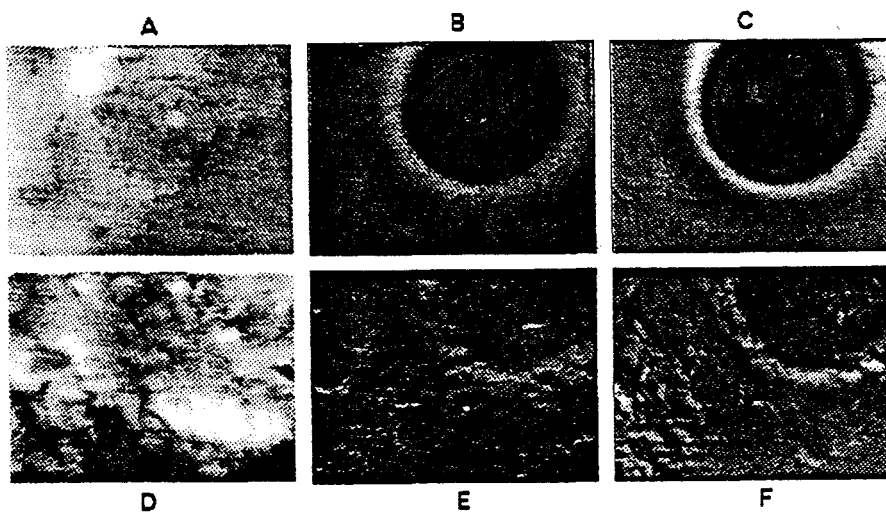


FIGURE 3

Figure 3: POLDER observations over a thin stratocumulus, during ASTEX (images A, B, C) and over an heterogeneous cloud, during MEDIMAR (images D, E, F). Processed images of polarized bands (see text). Images A and D display the reflectance in the 850 nm band, images B and E the polarized reflectance in the 850 nm band, images C and F the polarized reflectance in the 450 nm band.

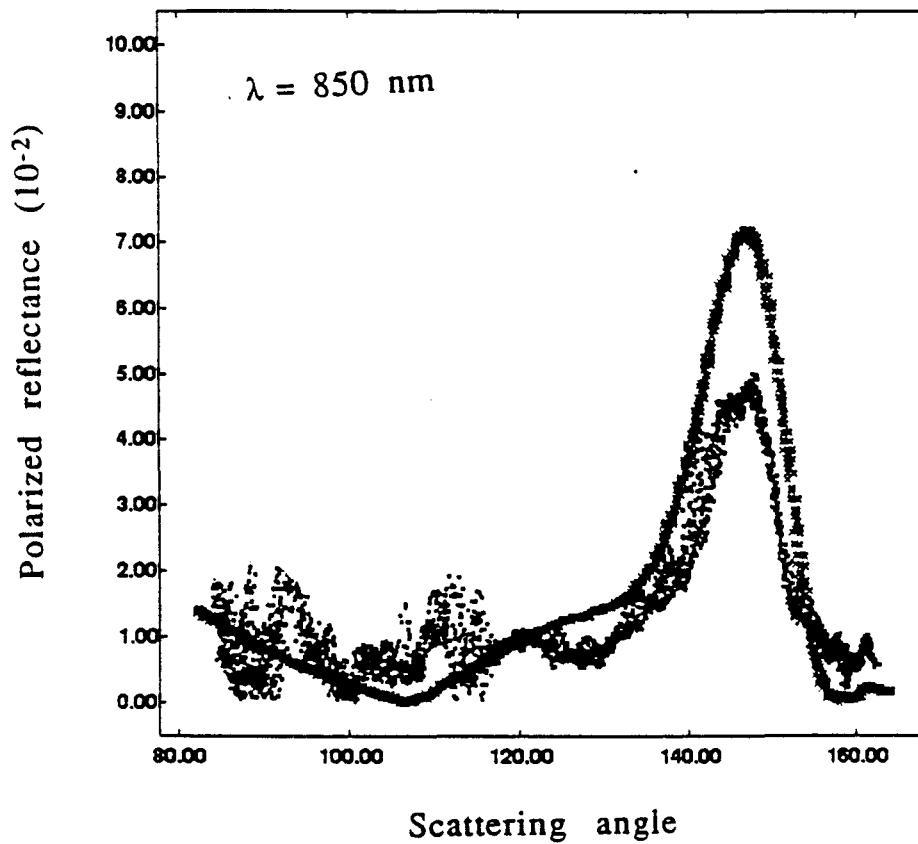


Figure 4: Data points: polarized reflectances measured in the 850 nm band, over the cloud of Fig.2;  $p_p$  is reported only for viewing directions within the solar incident plane, as a function of the scattering angle  $\Theta$ .

Continuous curve: polarized reflectances calculated, for the same geometry, for a plane parallel cloud with optical thickness  $\delta=15$  and with Deirmedjian's model C1 for the droplet size distribution.

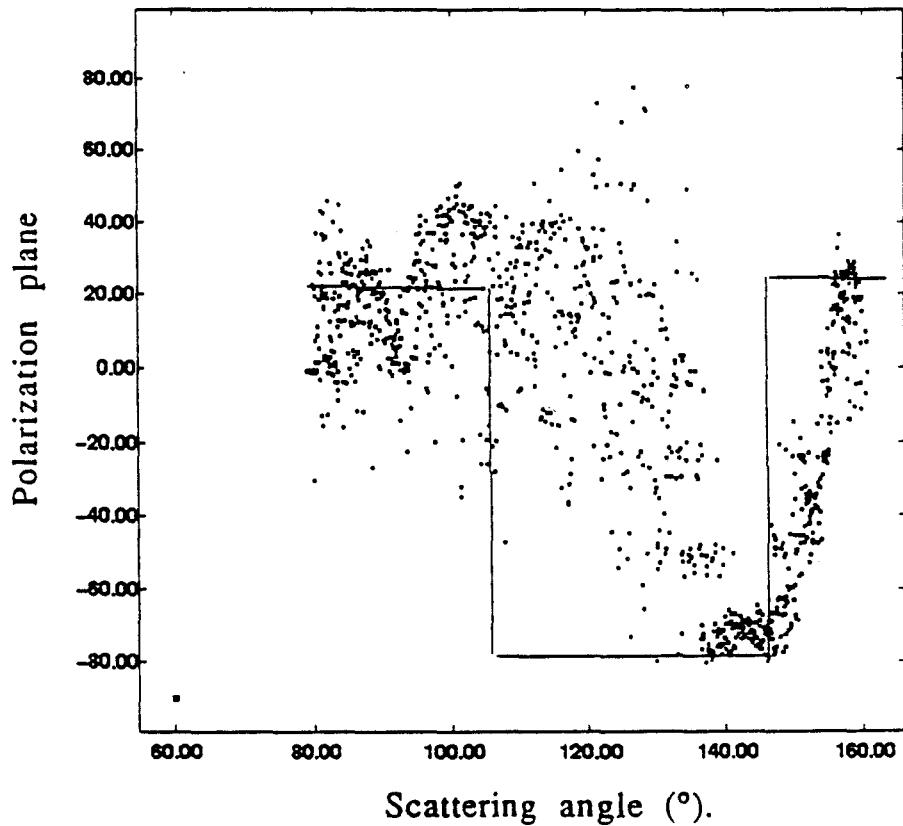


Figure 5: Same legend as Figure 4, but for the angle  $\xi$  between the polarized vibration and the scattering plane.(i.e., here, the solar incident plane).

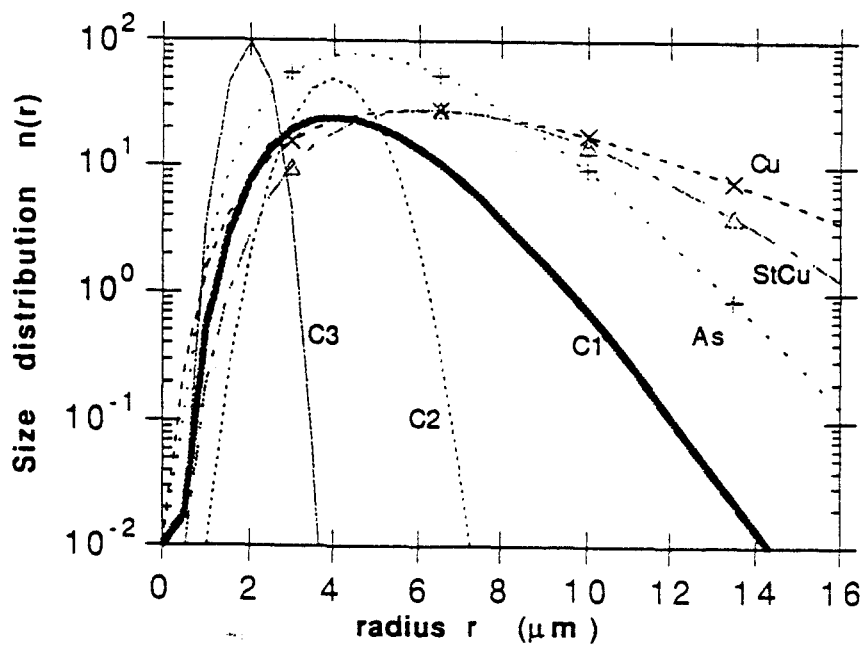


Figure 6: Cloud droplet size distributions used for the calculations.

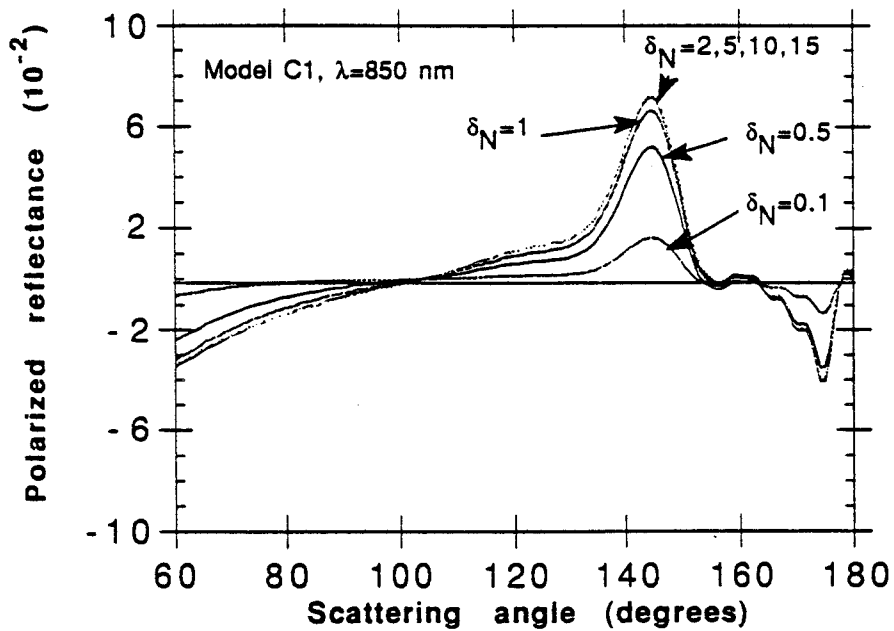


Figure 7: Calculations of the polarized reflectance  $\rho_p$ , reflected by a plane parallel cloud overlying a non reflecting ground, for different optical thicknesses of the cloud. The solar zenith angle is  $60^\circ$ ; the observation direction is within the solar principal plane and  $\rho_p$  is reported as a function of the scattering angle  $\Theta$ . The cloud droplet size distribution is the Deirmendjian's model C1; the observation wavelength is  $\lambda=850$  nm. The molecular scattering is neglected.

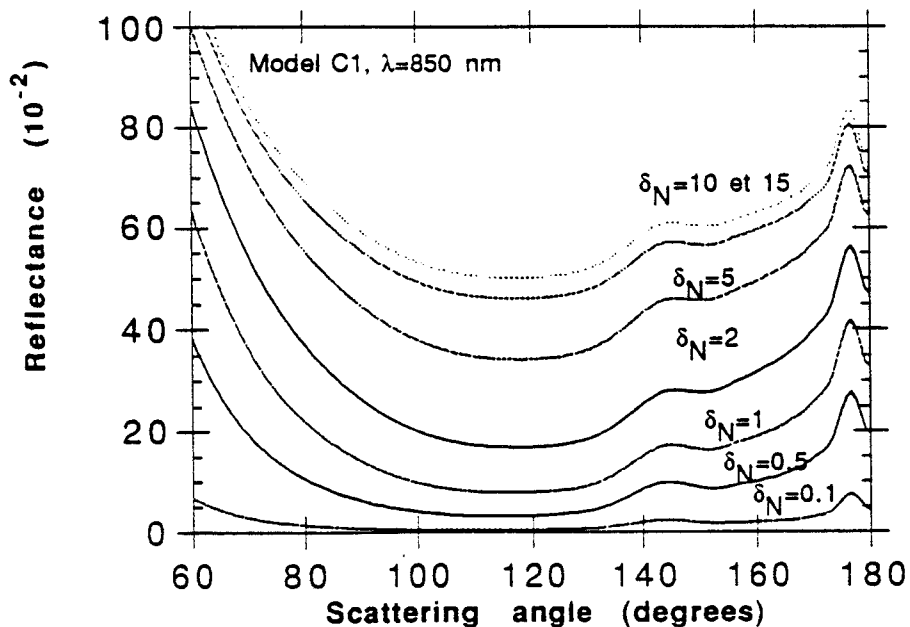


Figure 8: Same legend as Figure 7, but for the total reflectance.

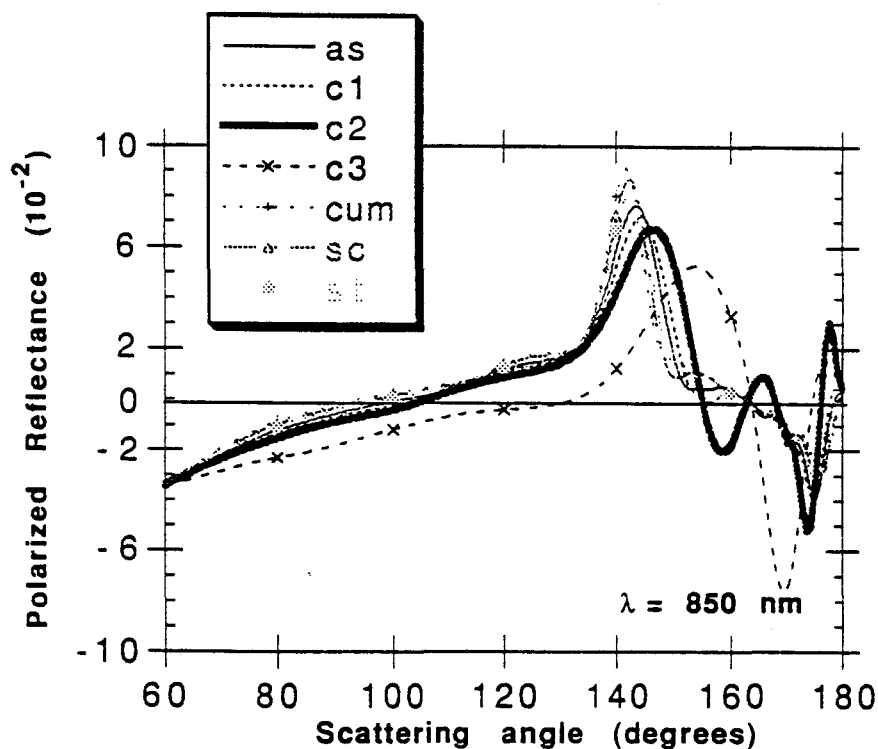


Figure 9: Same legend as Figure 7, but the polarized reflectance is reported for a constant cloud optical thickness ( $\delta=15$ ), for different cloud droplet size distributions (see Table 2).

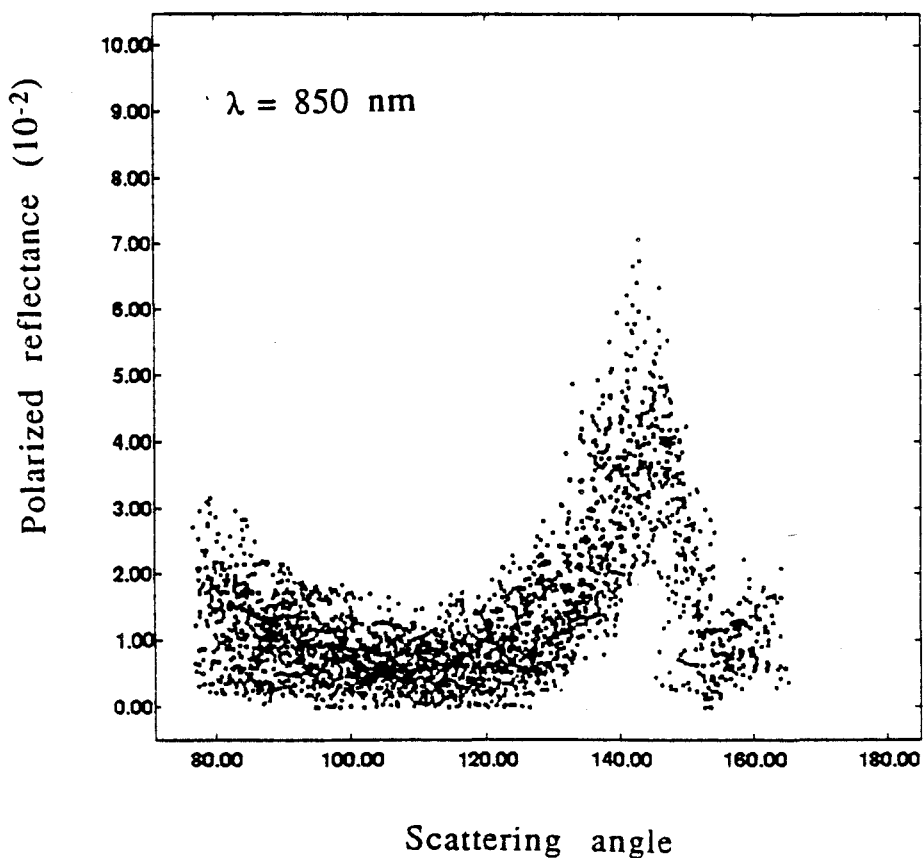


Figure 10: Histogram of the polarized reflectance  $\rho_p$ , measured over cloud field of Fig.2, in the 850 nm band;  $\rho_p$  has been plotted vs the scattering angle  $\Theta$ , for all the pixels of the image. Cloud observations conducted during CLEOPATRA, on 18/10/91, at about 11000 m. altitude, with mean solar zenith angle  $\theta_s=60^\circ$

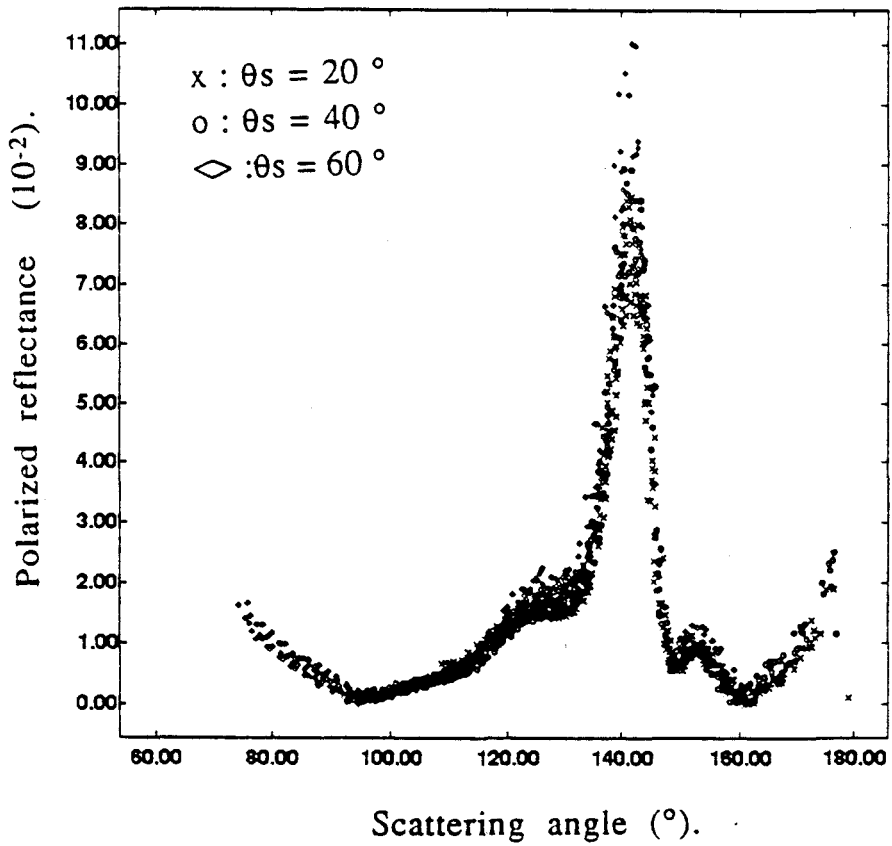
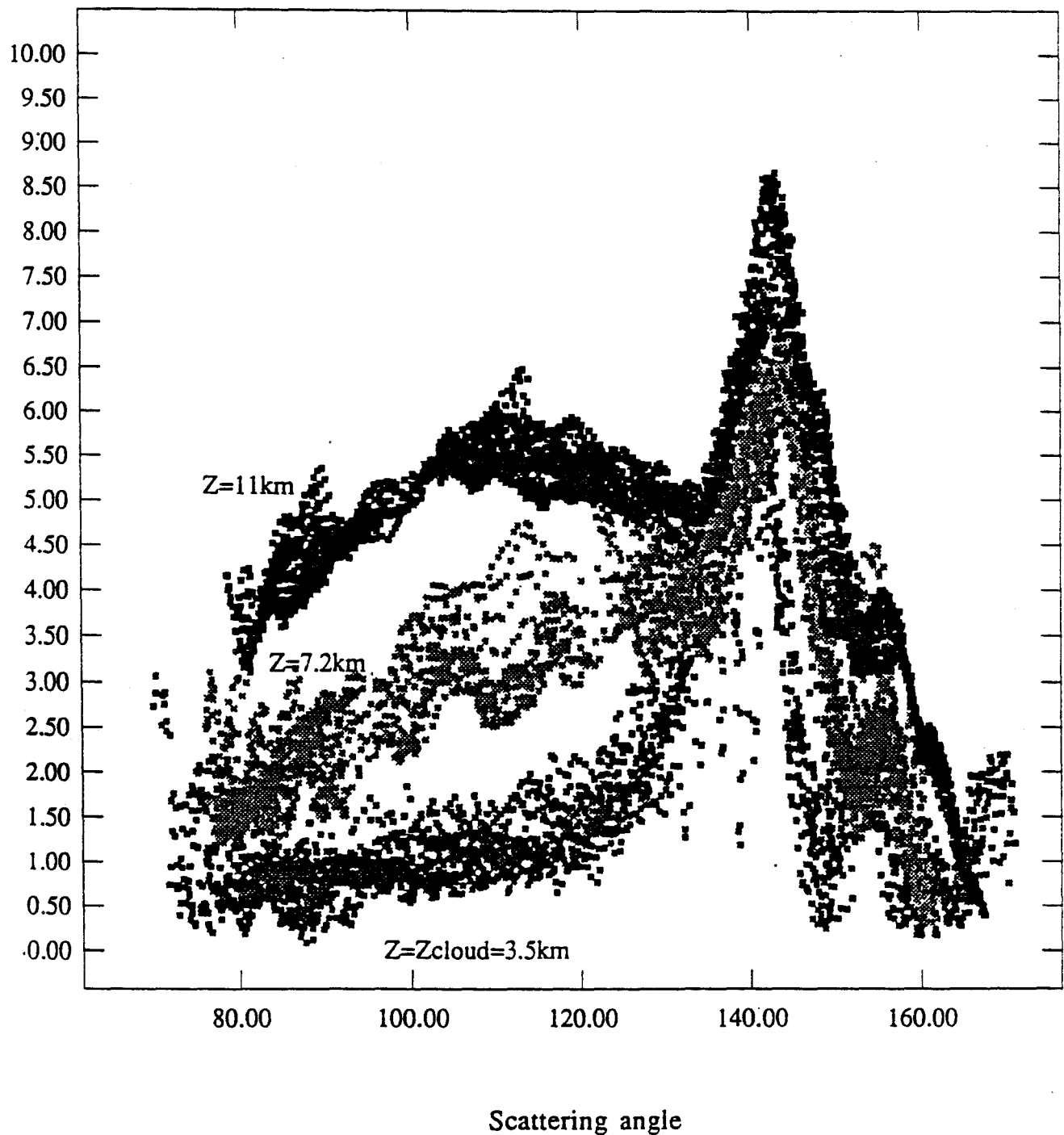
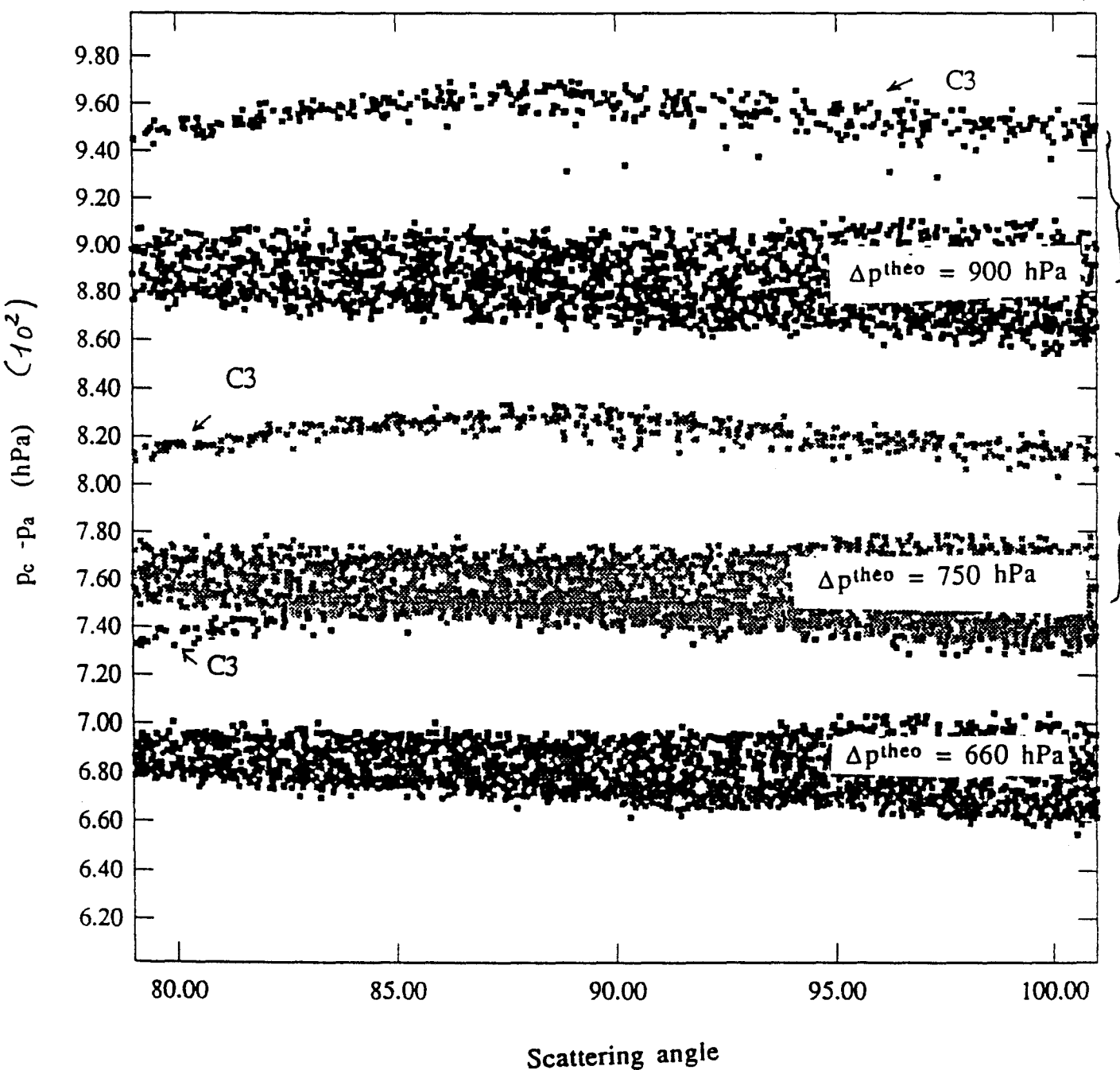


Figure 11: Histogram of the polarized reflectance  $\rho_p$ , calculated for the same geometry ( $\theta_s=60^\circ$ ) and observation wavelength as in Fig.10, for a plane parallel cloud with optical thickness  $\delta=15$  and with Deirmedjian's model C1 for the droplet size distribution. The polarized reflectances calculated for the same cloud but for other solar zenith angles ( $\theta_s=20^\circ, 40^\circ$ ) are indicated by different labels.



**Figure 12:** Histograms of the polarized reflectance  $p_p$ , in the 450 nm channel, vs the scattering angle  $\Theta$ . Cloud observations conducted during CLEOPATRA, on 21/10/91, with mean solar zenith angle  $\theta_s=60^\circ$ . For clarity, only pixels near from the solar incident plane have been reported. The different labels correspond to measurements performed at about 3.5 km (cloud top), 7.3 km and 11.3 km



**Figure 13:** Simulations of the cloud top pressure derived from POLDER measurements at 450 and 850 nm, over plane parallel cloud, by using the proposed approximate inversion method (see text). Measurements have been simulated by the GSHS code, with different assumed models of the cloud droplets and pressures of the cloud top, for viewing directions within the whole POLDER images. The assumed cloud top pressures are indicated. The retrieved pressures have been plotted, with different labels according to the assumed droplet model, vs the scattering angle  $\Theta$  corresponding to the viewing direction. Results are restricted to directions where molecular scattering is large enough. The results are nearly similar, within 20 Hpa, for all cloud models except model C3, for which the cloud top pressure is underestimated by about 50 Hpa.

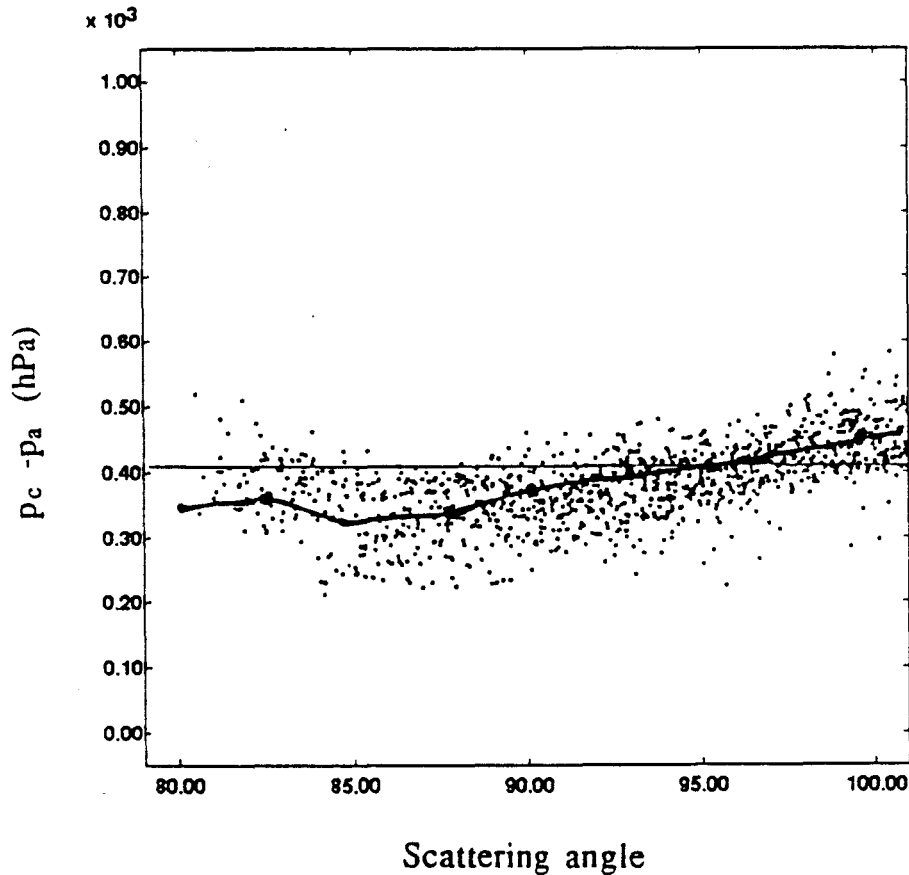


**Figure 14:** Estimates of pressure differences between the cloud top and aircraft levels, derived from the POLDER observations of CLEOPATRA, on 18/10/91 (see Fig. 2). The inversion has been applied only to image pixels corresponding to scattering angles  $\Theta$  ranging from  $80^\circ$  to  $100^\circ$ , and results have been reported vs  $\Theta$ . The continuous curve is the average result. The expected pressure difference (400 hPa) is indicated.

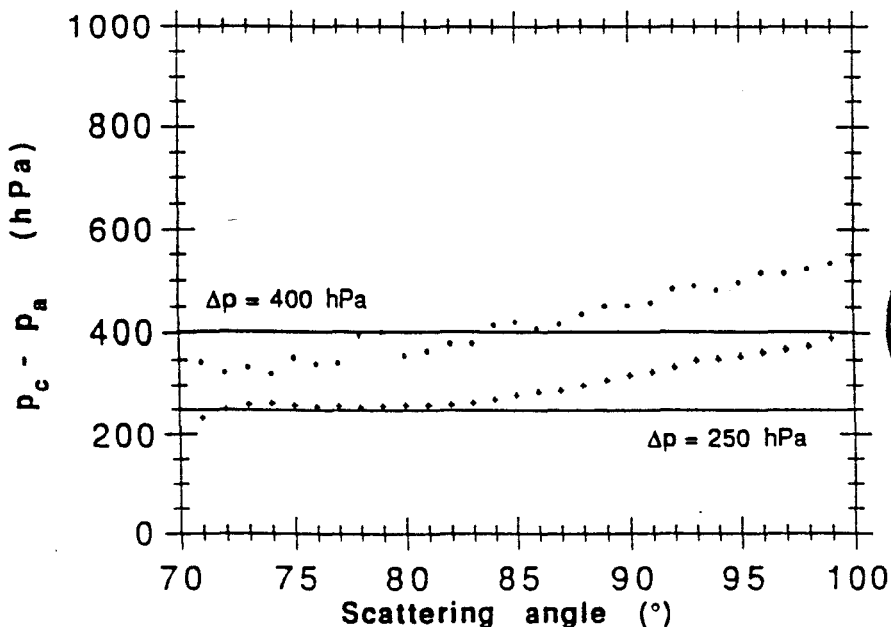


**Figure 15:** Same legend as Fig. 14, but for CLEOPATRA observations on 21/10/91, performed at 2 different altitudes above the same cloud. The average results only have been reported.